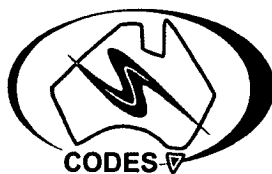

**Geological setting and mineralisation
characteristics of the Long Chieng Track
and Ban Houayxai deposits, Lao PDR**

Takayuki Manaka
B.Sc.
(University of Tsukuba, Japan)



A thesis submitted in partial fulfilment for the
Degree of Master of Science (Exploration Geoscience)



CODES ARC Centre of Excellence in Ore Deposits
University of Tasmania
Australia

November, 2008

Declaration

I declare that this thesis does not contain material which has been accepted for the award of any other degree or diploma in any university; and to the best of my knowledge contains no material previously published or written by any other person, except where due reference is made in the text of the thesis.

Takayuki Manaka

Takayuki Manaka 22/11/2008

Statement of Authority of Access

This thesis is not to be made available for loan or copying for two years following the date this statement was signed. Following that time the thesis may be made available for loan and limited copying in accordance with the Copyright Act 1968.

Takayuki Manaka

Takayuki Manaka 22/11/2008

ABSTRACT

The Long Chieng Track (LCT) Au deposit and Ban Houayxai (BHX) Au-Ag deposits are located in the Phu Bia Contract Area (PBCA), at the confluence of the Loei and Truongson Fold Belts in the northern Lao PDR. The LCT deposit is hosted by an Early Carboniferous sedimentary sequence intruded by Early Permian intrusive rocks, whereas the BHX deposit occurs in the Early Permian volcano-sedimentary sequence. The igneous units occurring at LCT and BHX are geochemically characterised by calc-alkaline affinities, and yield Early Permian age as revealed by the LA-ICPMS U-Pb zircon geochronological study.

Detailed mineralogical and paragenetic studies indicate that the LCT deposit has five mineralisation stages including single syn-mineralisation stage (i.e., stage 2), whereas seven mineralisation stages are recognised at the BHX deposit including three syn-mineralisation stages (i.e., Stages 1, 2 and 3). Alteration is extensively formed at LCT and BHX associated with the Au-rich vein systems, consisting mainly of sericite, chlorite, adularia and quartz assemblages. On the basis of core assay and the electrum fineness data, the vein system of the Stage 2 at LCT and the Stage 1 at BHXT are identified as Au-rich system, whereas the Stages 2 and 3 of BHX are recognised to be Ag-rich vein system. Gold at LCT occurs as electrum and native gold, while the occurrence of electrum, native silver and stephanite is found at BHX. These precious metals are commonly associated with sulphides including pyrite, sphalerite, chalcopyrite, galena and arsenopyrite. The LA-ICPMS analyses of trace elements in pyrites at the both LCT and BHX deposits reveal that the variable amount of gold is hosted in pyrite structure, closely associated with Ag, As, Sb, Tl, Co and Pb elements.

The obtained fluid inclusion data for the Au-rich vein system and Ag-rich vein system indicate discrete and different characteristics, having homogenisation temperature ranges from 175 to 215 and from 240 to 415°C respectively, and the salinity values are form 1.7 to 8.3 and 2.7 to 13.0 NaCl wt. % equiv. respectively. The isotope analyses of sulphur of the sulphides in syn-mineralisation stages at LCT and BHX indicate that the sulphur has a magmatic source. The oxygen and hydrogen isotopic compositions of the LCT and BHX show a mixing nature of the

magmatic water and meteoric water. The lead isotopic compositions suggest the metals were mainly derived from crustal source at the LCT and BHX deposits.

The present integrated field, mineralogy, paragenesis, fluid inclusions and isotopic studies indicate that the Au-rich vein system occurring at the both LCT and BHX deposits are comparable to the deeper part of the low-sulphidation epithermal model of Buchanan (1981), whereas the Ag-rich structurally-hosted vein system at BHX may be comparable to the middle to deeper part of the Ag-rich Mexican epithermal model of Albinson et al. (2001). However, the presence of CO₂ and CH₄ gases in fluid inclusions at LCT as detected by Laser Raman spectrometric analysis cannot rule out the intrusive-related style for the LCT deposit.

CONTENTS

ABSTRACT	i
LIST OF FIGURES	vii
LIST OF TABLES	xi
ACKNOWLEDGEMENTS	xii

CHAPTER 1 INTRODUCTION

1.1. Preamble.....	1
1.2. Location, access and geographical backgrounds.....	2
1.3. Previous mining activity, exploration and geological study.....	4
1.4. Aims of this study.....	5
1.5. Methodology.....	5

CHAPTER 2 TECTONICS AND METALLOGENY OF THE INDOCHINA TERRANE

2.1. Introduction.....	7
2.2. Tectonic evolution of mainland SE Asia.....	9
2.2.1. Rifting.....	9
2.2.2. Drifting.....	9
2.2.3. Amalgamation.....	10
2.2.4. Post-amalgamation.....	11
2.3. Metallogeny of Indochina Terrane.....	12
2.3.1. Loei Fold Belt.....	12
2.3.2. Truongson Fold Belt.....	14
2.4. Phu Bia Contract Area.....	15
2.4.1. Southern section of the Phu Bia Contract Area.....	15
2.4.2. Northern section of the Phu Bia Contract Area.....	17

CHAPTER 3 LOCAL GEOLOGY

3.1. Introduction.....	18
3.2. Local geology of the LCT and BHX deposits.....	18
3.2.1. Introduction.....	18

3.2.2. Sedimentary units at LCT.....	18
3.2.3. Intrusive igneous units at LCT.....	26
3.2.4. Volcano-sedimentary units at BHX.....	29
3.2.5. Intrusive units at BHX.....	32
3.2.6. Red bed units at BHX.....	33
3.3. Geochronology.....	34
3.3.1. Introduction.....	34
3.3.2. Analytical methods.....	34
3.3.3. Geochronological results.....	35
3.3.4. Geochronological interpretation.....	36
3.4. Whole rock geochemistry.....	38
3.4.1. Introduction.....	38
3.4.2. Analytical methods.....	38
3.4.3. Geochemical results.....	38
3.4.3.1. Major elements.....	38
3.4.3.2. Trace elements.....	44
3.4.3.3. REE.....	44
3.4.3.4. Geochemical classification.....	47
3.5. Discussion and summary.....	47
3.5.1. Discussion.....	47
3.5.2. Summary.....	51

CHAPTER 4 MINERALISATION CHARACTERISTICS

4.1. Introduction.....	52
4.2. Analytical methods.....	52
4.2.1. Mineralisation and ore mineral description.....	52
4.2.2. Gold fineness and FeS variation in sphalerite.....	52
4.3. Mineralisation.....	53
4.3.1. LCT observation, drill hole logging, macroscopic and microscopic investigation.....	53
4.3.2. BHX observation, drill hole logging, macroscopic and microscopic investigation.....	61
4.4. Ore minerals.....	71
4.4.1. LCT ore minerals.....	71
4.4.2. BHX ore minerals.....	73
4.5. Gold fineness.....	77
4.6. Sphalerite geochemistry.....	79
4.7. Discussion.....	82
4.8. Summary.....	85

CHAPTER 5 PYRITE GEOCHEMISTRY

5.1. Introduction.....	86
5.2. Analytical methods.....	86
5.3. Pyrite morphology and occurrence.....	87
5.4. Result.....	88
5.4.1. Au and Ag concentration in pyrite.....	91
5.4.2. Correlation of elements.....	92
5.4.3. Trace element variation in different textural types of pyrite.....	95
5.4.4. Trace element variation in the mineralised veins and the wall rock.....	95
5.5. Discussion.....	100
5.5.1. As contribution to Au concentration in pyrite.....	100
5.5.2. Au/Ag ratio in pyrite.....	101
5.5.2. Origin of pyrite.....	103
5.6. Summary.....	104

CHAPTER 6 FLUID INCLUSION STUDY

6.1. Introduction.....	105
6.2. Analytical methods.....	105
6.3. Inclusion petrography.....	106
6.4. Microthermometric results.....	108
6.5. Laser Raman Spectrometric data.....	112
6.6. Discussion.....	113
6.7. Summary.....	117

CHAPTER 7 SULPHUR, OXYGEN AND HYDROGEN ISOTOPES

7.1. Introduction.....	118
7.2. Analytical methods.....	118
7.2.1. Sulphur isotope.....	118
7.2.2. Oxygen and hydrogen isotopes.....	119
7.3. Sulphur isotope data.....	120
7.4. Oxygen and hydrogen isotope data.....	122
7.5. Discussion.....	124
7.5.1. Source of sulphur.....	124
7.5.2. Source of ore-forming fluids.....	125
7.6. Summary.....	127

CHAPTER 8 LEAD ISOTOPES

8.1. Introduction.....	128
8.2. Analytical methods.....	128
8.3. Lead isotope data.....	129
8.4. Discussion.....	133
8.5. Summary.....	135

CHAPTER 9 DISCUSSION AND CONCLUSIONS

9.1. Introduction.....	136
9.2. Formation of vein stages.....	136
9.3. Origin of the LCT and BHX deposits.....	139
9.4. Deposit models.....	142
9.5. Conclusions.....	148
9.6. Implications for mineral exploration.....	150

References.....	151
------------------------	------------

Appendices

Appendix I Sample catalogue

Appendix II LA-ICPMS zircon U-Pb geochronological data

Appendix III XRD results

Appendix IV Sphalerite geochemical data

Appendix V LA-ICPMS pyrite geochemical data

Appendix VI Fluid inclusion data

LIST OF FIGURES

CHAPTER 1

- Fig. 1.1. Location map of Lao PDR in mainland SE Asia, including Phu Bia Contract Area and Sepon District..... 2
- Fig. 1.2. Location map of the deposits in the Phu Bia Contract Area in northern Lao PDR, including Phu Kham, Ban Houayxai, Long Chieng Track, Phu He and KTL deposits... 3
- Fig. 1.3. Views in and around the Phu Bia Contract Area in northern Lao PDR..... 4

CHAPTER 2

- Fig. 2.1. Tectonic setting of mainland SE Asia.....8
- Fig. 2.2. Reconstruction maps of the Gondwanaland-derived terranes from Early Carboniferous to Late Permian..... 10
- Fig. 2.3. Location of Phu Bia Contract Area and Sepon Mineral District in Lao PDR and Chatree and Phu Thap Fa deposits in Thailand, with distribution of Loei and Truongson Fold Belts in mainland SE Asia 13

CHAPTER 3

- Fig. 3.1. Geological map of the LCT deposit..... 19
- Fig. 3.2. Interpreted geological cross-section of the LCT deposit..... 20
- Fig. 3.3. Geological map of the BHX deposit..... 21
- Fig. 3.4. Interpreted geological N-S cross-section of the BHX deposit..... 22
- Fig. 3.5. Interpreted geological stratigraphy of the LCT and BHX deposits..... 23
- Fig. 3.6. Representative hand specimen samples of sedimentary units at the LCT deposit..... 25
- Fig. 3.7. Representative hand specimen sample and thin-section images of igneous units at the LCT deposit..... 27
- Fig. 3.8. Representative samples of volcano-sedimentary sequence units at BHX deposit..... 30
- Fig. 3.9. Representative sample of aphyric mafic dyke unit at BHX deposit..... 33
- Fig. 3.10. Representative samples of red bed units at the BHX deposit..... 34
- Fig. 3.11. Representatives of zircon cathodoluminescence image and zircon concordia diagrams of the selected rock units from the LCT and BHX deposits..... 36
- Fig. 3.12. Summary of geochronological data of the BHX, LCT and Phu Kham deposits..... 37
- Fig. 3.13. Major element vs SiO₂ bivariate diagrams for major igneous units of the LCT and BHX deposits, with incorporated data of Phu Kham granitoids..... 43

Fig. 3.14.	Trace element vs SiO ₂ bivariate diagrams for major igneous units of the LCT and BHX deposits, with incorporated data of Phu Kham granitoids.....	45
Fig. 3.15.	Chondrite-normalised REE patterns of major igneous rock units of the LCT and BHX deposits.....	46
Fig. 3.16.	Geochemical discrimination diagrams for the igneous units of the LCT and BHX deposits.....	48
Fig. 3.17.	Tectonic discrimination diagrams for igneous units of the LCT and BHX deposits.....	49

CHAPTER 4

Fig. 4.1.	Summary of mineralisation and paragenesis of the LCT deposit, Lao PDR.....	54
Fig. 4.2.	Stage 1 mineralisation facies of the LCT deposit.....	55
Fig. 4.3.	Stage 2 mineralisation facies of the LCT deposit.....	56
Fig. 4.4.	Stage 3 mineralisation facies of the LCT deposit.....	58
Fig. 4.5.	Stage 4 mineralisation facies of the LCT deposit.....	60
Fig. 4.6.	Stage 5 mineralisation facies of the LCT deposit.....	60
Fig. 4.7.	Summary of mineralisation and paragenesis of the BHX deposit, Lao PDR.....	62
Fig. 4.8.	Stage 1 mineralisation facies of the BHX deposit.....	63
Fig. 4.9.	Schematic diagram of syn-mineralisation stage vein occurrences at the BHX deposit.....	64
Fig. 4.10.	Stage 2 mineralisation facies of the BHX deposit.....	65
Fig. 4.11.	Stage 3 mineralisation facies of the BHX deposit.....	66
Fig. 4.12.	Stage 4 mineralisation facies of the BHX deposit.....	68
Fig. 4.13.	Stage 5 mineralisation facies of the BHX deposit.....	69
Fig. 4.14.	Stage 6 mineralisation facies of the BHX deposit.....	69
Fig. 4.15.	Stage 7 mineralisation facies of the BHX deposit.....	70
Fig. 4.16.	Ore minerals of the LCT deposit.....	72
Fig. 4.17.	Ore minerals of the BHX deposit.....	75
Fig. 4.18.	Histogram of gold fineness values of electrum, native gold and native silver in the syn-mineralisation stages of the LCT and BHX deposits.....	77
Fig. 4.19.	Histogram of FeS mole % sphalerite from the LCT and BHX deposits, Lao PDR.....	79
Fig. 4.20.	Plot of FeS mole % in sphalerite and gold assay (g/t) of the sample from LCT and BHX deposits, Lao PDR.....	81
Fig. 4.21.	Plot of FeS mole % in sphalerite and silver assay (g/t) of the sample from LCT and BHX deposits, Lao PDR.....	81

CHAPTER 5

Fig. 5.1.	Example of different pyrite textures in the LCT and BHX deposits.....	89
Fig. 5.2.	Range and average of pyrite trace element contents in mineralised veins and wall rock at the LCT and BHX deposits.....	90
Fig. 5.3.	Histogram of Au concentration in the pyrite from the LCT and BHX deposits.....	91
Fig. 5.4.	Histogram of Ag concentration in the pyrite from the LCT and BHX deposits.....	91
Fig. 5.5.	Bi-plots of the selected elements in pyrites from the LCT and BHX deposits.....	94
Fig. 5.6.	Time chart of the selected LA-ICPMS line analyses of pyrite with multiple overgrowth zone texture from the BHX deposit.....	96
Fig. 5.7.	Time chart of the selected LA-ICPMS line analyses of pyrite with multiple overgrowth zone texture from the BHX deposit.....	97
Fig. 5.8.	Time chart of the selected LA-ICPMS line analyses of wall rock pyrite with sponge core with euhedral rim texture from the BHX deposit.....	98
Fig. 5.9.	Comparison of average values of trace elements in pyrite from the LCT and BHX deposits.....	100
Fig. 5.10.	Au-As plot of pyrite geochemistry at the LCT and BHX deposits.....	101
Fig. 5.11.	Au-Ag correlation in the pyrite from Stage 2 vein at the LCT and from Stages 1 and 3 veins at BHX.....	102

CHAPTER 6

Fig. 6.1.	Fluid inclusion characteristics of the LCT and BHX deposits.....	107
Fig. 6.2.	Histograms of homogenisation temperatures of fluid inclusions in syn-mineralisation stages at the LCT and BHX deposits.....	110
Fig. 6.3.	Histograms of salinity data from fluid inclusions in syn-mineralisation stages at the LCT and BHX deposits.....	111
Fig. 6.4.	An example of Laser Raman spectral profile of CO ₂ and CH ₄ gas compositions in fluid inclusion from the Stage 2 mineralisation of the LCT deposit.....	112
Fig. 6.5.	Plots of salinity vs homogenisation temperatures from fluid inclusions in syn-mineralisation stages at the LCT and BHX deposits.....	115

CHAPTER 7

Fig. 7.1.	Histograms of δS^{34} values for sulphides at the LCT and BHX deposits, Lao PDR.....	120
Fig. 7.2.	Histogram of the calculated $\delta^{18}O$ compositions of the Stage 2 vein at LCT and Stage 1 vein and sericitised wall rock samples at BHX.....	123
Fig. 7.3.	Histogram of the measured δD compositions of the Stage 2 vein at LCT and Stage 1 at BHX.....	123

Fig. 7.4.	Comparison of δS^{34} values in syn-mineralisation stages at the LCT and BHX deposits with the igneous and bacteriogenic ranges.....	124
Fig. 7.5.	Comparison of δS^{34} value ranges between the LCT and BHX deposits and the major VHMS deposits occurred throughout Phanerozoic time.....	125
Fig. 7.6.	Calculated $\delta^{18}O$ and δD values of the ore-bearing fluids at the LCT and BHX deposits, with fields of modern geothermal systems and primar magmatic water.....	126

CHAPTER 8

Fig. 8.1.	Lead isotopic composition of $^{207}Pb/^{204}Pb$ vs $^{206}Pb/^{204}Pb$ ratios of the LCT and BHX deposits.....	132
Fig. 8.2.	Lead isotopic composition of $^{208}Pb/^{204}Pb$ vs $^{206}Pb/^{204}Pb$ ratios of the LCT and BHX deposits.....	132
Fig. 8.3.	Plots of lead isotope fields of the LCT and BHX deposits and those of other deposits and granites in mainland SE Asia	134
Fig. 8.4.	Plots of lead isotope fields for metallogenic styles and granites of mainland SE Asia ...	134

CHAPTER 9

Fig. 9.1.	Schematic diagram showing mineralisation stages of the LCT deposit.....	137
Fig. 9.2.	Schematic diagram showing syn-mineralisation stages of the BHX deposit.....	138
Fig. 9.3.	Three dimensional ore model of the BHX deposit, looking NE.....	145
Fig. 9.4.	Low-sulphidation epithermal model in comparison with the LCT mineralisation.....	146
Fig. 9.5.	Ag-rich Mexican epithermal model in comparison with the BHX mineralisation.....	147

LIST OF TABLES

Table 2.1.	Geological characteristics of different Cu-Au deposits in the Phu Bia Contract Area, northern Lao PDR.....	16
Table 3.1.	Summary of previous geochronological data of LCT and BHX deposits, Lao PDR.....	34
Table 3.2.	LA-ICPMS U-Pb zircon ages of major igneous and sedimentary units from the LCT and BHX deposits, Lao PDR.....	37
Table 3.3.	Major, trace and rare earth elements geochemistry of the igneous rocks from the LCT deposit.....	39
Table 3.4.	Major, trace and rare earth elements geochemistry of the igneous rocks from the BHX deposit.....	41
Table 4.1.	Summary of microprobe analysis of gold- and silver-bearing ore minerals from the LCT and BHX deposits, Lao PDR.....	78
Table 4.2.	Summary of microprobe analysis of average FeS mole % composition in sphalerite with gold and silver grade of diamond drill core samples from the LCT and BHX deposits.....	80
Table 5.1.	Au and Ag core assay data with Au/Ag ratio of samples analysed for pyrite trace element geochemistry.....	102
Table 6.1.	Summary of fluid inclusion microthermometric data of syn-mineralisation stages at the LCT and BHX deposits, Lao PDR.....	109
Table 6.2.	Summary of Laser Raman spectrometric data of fluid inclusions from the LCT and BHX deposit, Lao PDR.....	113
Table 7.1.	Summary of δS^{34} isotope data of the LCT and BHX deposits, Lao PDR.....	121
Table 7.2.	Oxygen and hydrogen isotope data with calculated oxygen data at the LCT and BHX deposits, Lao PDR.....	122
Table 8.1.	Lead isotope data of the LCT and BHX deposits, Lao PDR.....	131
Table 9.1.	Summary of the geological, mineralogical and geochemical characteristics of the LCT and BHX deposits, Lao PDR.....	140
Table 9.2.	Comparison of the geological, geochemical and mineralisation characteristics of the LCT deposit with typical low-sulphidation epithermal deposits and the epithermal Au-Ag deposits of Hauraki Goldfield in New Zealand.....	143
Table 9.3.	Comparison of the geological, geochemical and mineralisation characteristics of the BHX deposit with the Mexican Ag-rich epithermal and the Santo Nino epithermal deposits.....	144

ACKNOWLEDGEMENTS

Firstly, I would like to thank my supervisor, Associate Professor Khin Zaw, for providing me with a great project and the opportunity to undertake research and fieldwork in Lao PDR. Khin Zaw has given me motivation, advice, constructive criticism and full logistical support throughout my Masters program at CODES. I would also like to thank my co-supervisor, Dr Sebastien Meffre, for his helpful comments and for reviewing drafts of my thesis. This study was undertaken with financial and logistical support from Khin Zaw's ARC Loei Linkage Grant.

Secondly, I would like to thank Pan Australian Resources Ltd for giving me access to my field areas and for providing support during my fieldwork in Lao. Previous and present Pan Australian geologists including Dr Ralph Child, Ben Tucker, Andrew Rowe, Jono Lawrence, Richard Hague, Aaron McLeod, Paul Merriner, and Ross Faichney, helped me to become familiar with the general geological setting in my study area. I also thank the local Loatian staff of Phu Bia Mining Company for their help and assistance.

Many thanks go to the staff at CODES, University of Tasmania. They include Sarah Gilbert, Simon Stephens, Katie McGoldrick, Phil Robinson, Wally Herrmann, Peter Cornish, Izzy, Dianne Madden, and Grace Cumming. Thanks to Christine Cook and Karsten Goemann at the Central Science Laboratory for helping with analyses.

My colleagues at CODES provided physical and mental supports during my study. I offer my sincere thanks to Lee Robson, Abhisit Salam (Masoe), Teera Kamvong, Bronto Sutopo, Paul Cromie, Weerapan Srichan (Bee), Wojciech Zukowski, Victor Galvan, Yansan Jamyambaatar, Liezl Cuison, Sang Dinh, Adam Bath, Corrie Chamberlain, and Cesar Mascarelli.

Finally, I would like give special thanks to my family in Japan, who provided financial support for my studies in Hobart. I couldn't have finished my study at CODES without their kind contribution.

CHAPTER 1 INTRODUCTION

1.1. Preamble

Lao People's Democratic Republic (Lao PDR) is a land-locked country in mainland SE Asia with an area of approximately 237,000 km². It borders China, Vietnam, Cambodia, Thailand and Myanmar to the north, east, south, west and northwest respectively (Fig. 1.1). The country has a history of mining and exploration for gold resources, and small-scale gold panning has been conducted at many streams throughout the country (ESCAP, 1990). In recent years, the Phu Bia Contract Area (PBCA) and Sepon Mining District (SMD) have been recognised as hosting significant gold and copper resources and have attracted considerable international attention from mining companies.

The PBCA and SMD were granted the title of Mineral Exploration and Production Agreement area (MEPA) by the Lao PDR government, which regulates exploration and mining activities. The PBCA is located in the central northern Lao PDR (Fig. 1.1) and is owned by Phu Bia Mining Ltd, a local subsidiary Company of Pan Australian Resources Ltd. The entire PBCA has a total mineral resource of 1.3 Mt Cu, 3.1 M oz Au and 20.1 M oz Ag (<http://www.panaust.com.au>). The SMD is in the central Lao PDR (Fig. 1.1), and it is operated by Lane Xane Minerals Ltd, a local subsidiary Company of Oxiana Ltd. The SMD mineral resource is estimated to be a total of 4.8 M oz Au and 1.9 Mt Cu (Smith et al., 2005; <http://www.ozminerals.com.>).

The Long Chieng Track (LCT) and Ban Houayxai (BHX) deposits studied in this research are two prospective satellite deposits adjacent to the Phu Kham deposit in the southern part of the PBCA (Figs. 1.1 and 1.2). At present, sufficient resources of gold and copper have been delineated in the PBCA to make it economically viable. The Phu Kham deposit hosts the main resource containing a total mineral resource of 192 Mt at 0.62 % Cu and 0.24 g/t Au (<http://www.panaust.com.au>). Ore resources of the LCT and BHX deposits are currently estimated to be 3.66 Mt at 0.9 g/t Au (Pan Australian Resources Annual Report 2003–04) and 36 Mt at 1.2 g/t Au and 7.7 g/t Ag (<http://www.panaust.com.au>), respectively. At the Phu Kham deposit, mining started in mid-2007, whereas the LCT and BHX deposits are currently under development.

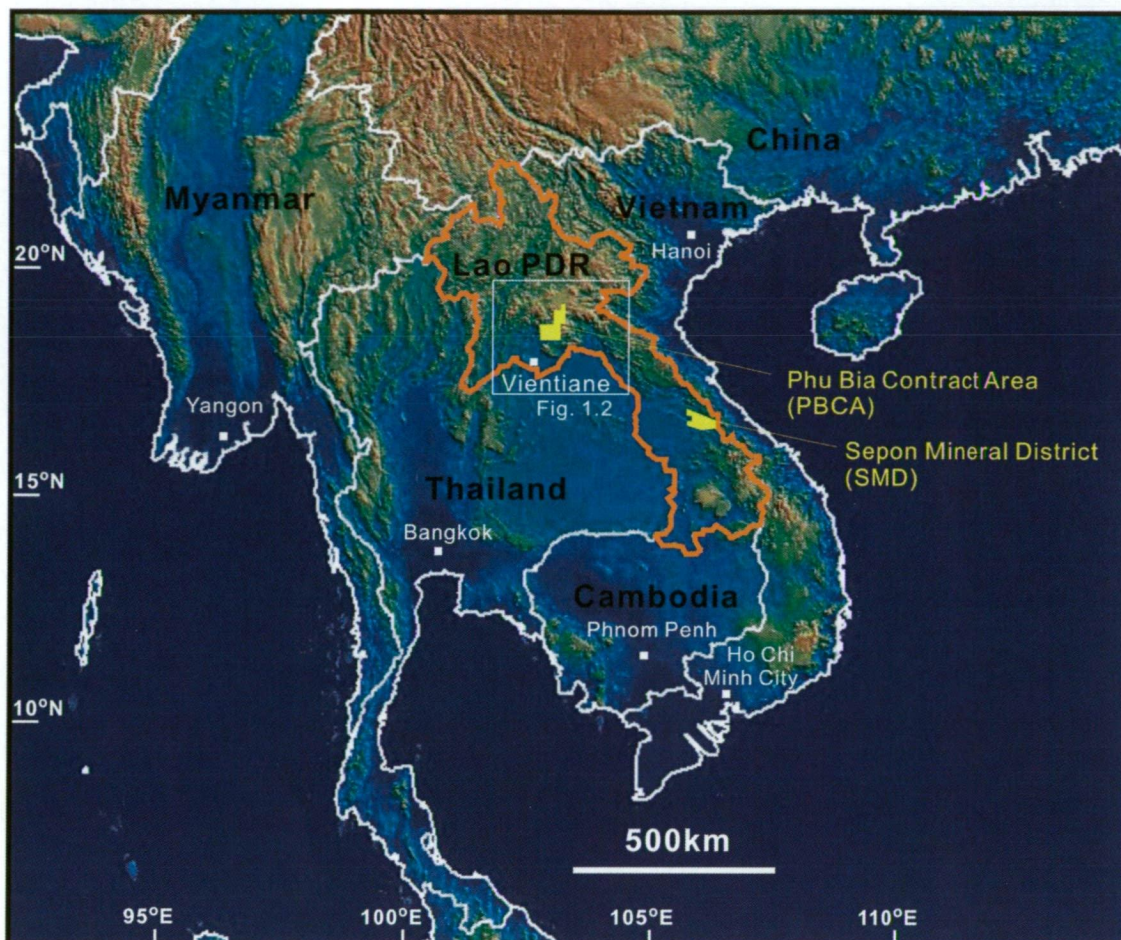


Fig. 1.1. Location of Lao PDR in mainland SE Asia, including Phu Bia Contract Area (PBCA) and Sepon Mineral District (SMD).

1.2. Location, access and geographical backgrounds

The LCT and BHX deposits are located in the southern part of the PBCA, which is located approximately 100 km north of Vientiane, the capital city of Lao PDR (Fig. 1.2). The PBCA covers 2,637 km², which is equivalent to 1.1 % of the Territory of Lao PDR (<http://www.panaust.com.au>). The BHX deposit is located 20 km east of Vang Vieng, one of the most popular tourist cities in Lao PDR; the LCT deposit is located 25 km east of the BHX and the Phu Kham deposit is located 4 km southeast of the LCT deposit (Fig. 1.2).

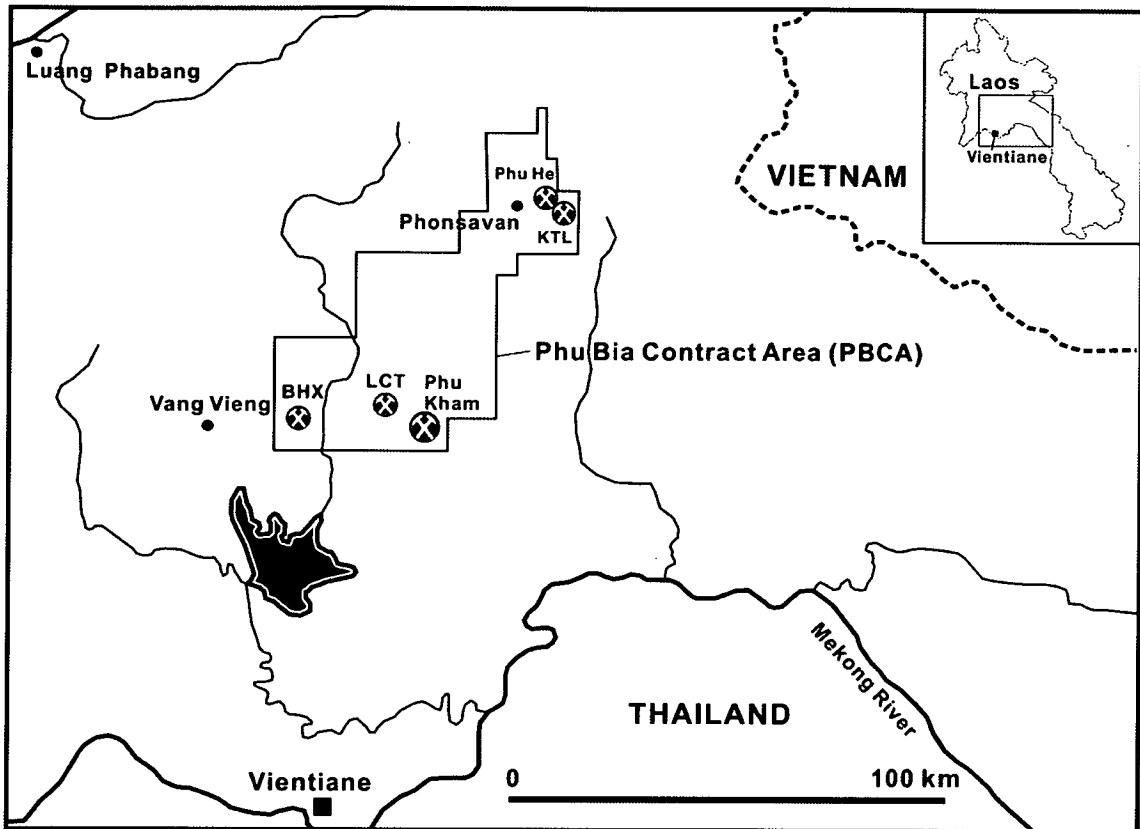


Fig. 1.2. Location of the deposits in the Phu Bia Contract Area (PBCA) in northern Lao PDR, including Phu Kham, Ban Houayxai (BHX), Long Chieng Track (LCT), Phu He and Khamthonglai (KTL) deposits.

The physiographic setting of the PBCA is characterised by mountainous topography including well-developed karst landscape, ranging from 300 to 1,500 m above sea level (Fig. 1.3A). The entire PBCA is commonly covered by dense forests (including the BHX and LCT deposit areas) (Figs. 1.3B and C), with occasional exposures of maroon red coloured rock/soil.

Access to the camp site in the southern part of the PBCA is available from Vientiane via highway 13A, then, near Vang Vieng, along rugged unshealed roads. At least five hours are required to reach the camp sites from Vientiane. Practically, the traveling time to get to the campsite is highly depended on weather and road traffic conditions, and the number of cars using the ferry to cross a local river (Fig. 1.3D).

The climate of Lao PDR is characterised by a typical monsoonal weather patterns, with two distinct wet (November–April) and dry (May–October) seasons. The annual temperature in Vientiane is 31°C, with daily temperature ranging between 22–40°C in the hottest month (April) and 15–28°C in the coolest month (January).

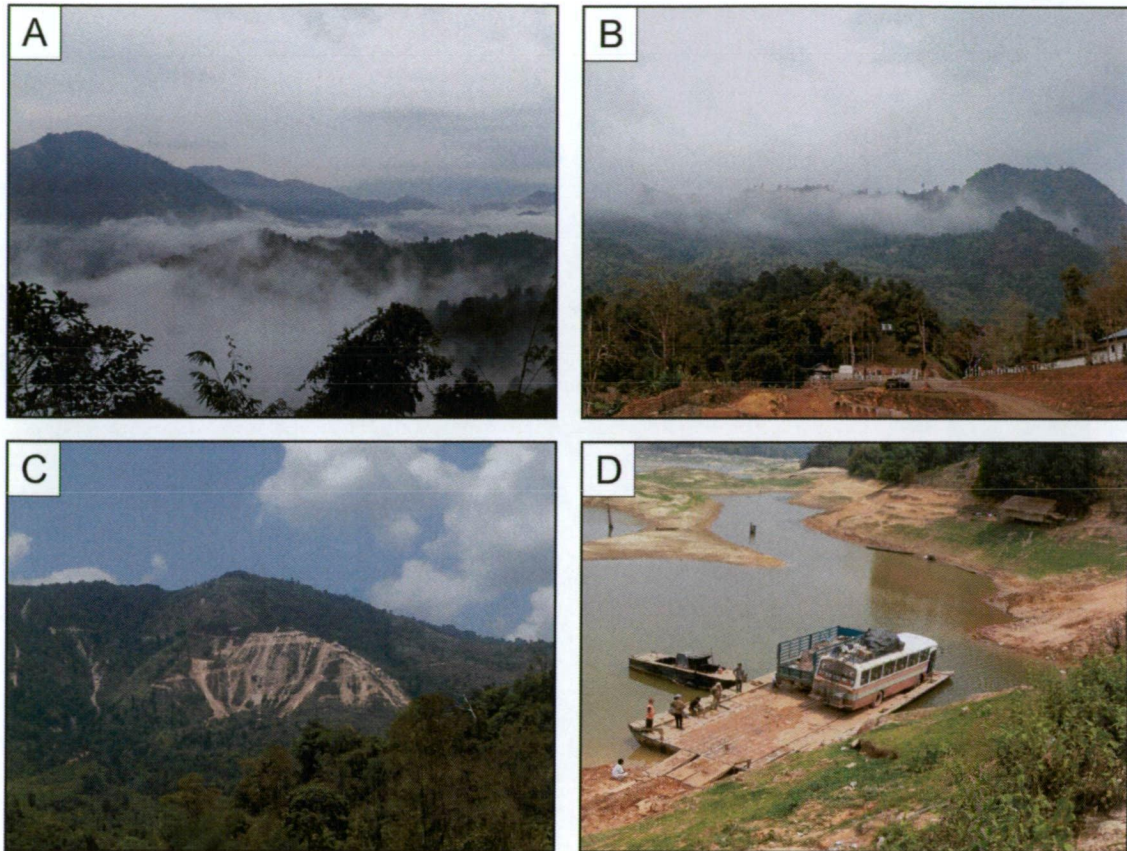


Fig. 1.3. Views in and around the Phu Bia Contract Area in northern Lao PDR.

- A) Typical mountainous landscape of the Phu Bia Contract Area.
- B) View of Ban Houayxai (BHX) deposit from Ban Houayxai campsite, looking west.
- C) View of Long Chieng Track (LCT) deposit from Phu Kham campsite, looking west.
- D) View of car ferry used to cross a local river for access to the deposits in southern section of the Phu Bia Contract Area.

1.3. Previous mining activity, exploration and geological studies

Mining activity in Lao PDR in the last few centuries has been undertaken by conventional panning techniques, focusing mostly on gold and copper (JOGMEC, 2005). This activity was most likely conducted within the PBCA and probably gave rise to the name ‘Phu Kham’ which literally means ‘Mountain of Gold’ in the local language. At present, panning is still the most common mining method for small-scale mining in Lao PDR. Modern exploration and mining techniques have been introduced to Lao PDR in the last few decades by foreign mineral companies.

The LCT and BHX deposits were initially discovered in the 1996–97 by Phu Bia Mining Ltd (Tate, 2003; Tate, 2004), originally owned by Pan Australian Resources Ltd (80%) and Newmont South East Asia Pty Ltd (20%). This discovery was a result of using systematic exploration

techniques involving regional drainage soil and rock-chip samplings and followed up by diamond drill hole testing. 6700 m of drilling was undertaken at LCT, including 27 diamond and 49 reverse circulation (RC) holes. 5700 m was undertaken at BHX, including 11 diamond and 79 RC holes.

Prior to this study, very little research has been undertaken on the LCT and BHX deposits. The limited results can be acquired from several internal company reports (e.g., Mason, 1997; Tate, 2003; Tate, 2004) and from recent ARC Linkage reports (e.g., Khin Zaw et al., 2007a; Khin Zaw and Meffre, 2007). The study by Mason (1997) documented the petrography of lithological units in the LCT deposit area. Tate (2003, 2004) reported briefly on the geology and ore mineralisation characteristics at the LCT and BHX deposits. Khin Zaw et al. (2007a) and Khin Zaw and Meffre (2007) focused mostly on the regional geology along the entire Loei Fold Belt on the basis of geochemical, geochronological and deposit-scale studies including preliminary laboratory work on the LCT and BHX deposits. However, no detailed studies on the geology and mineralisation characteristics of the deposits have been undertaken. As a part of this study, several preliminary results have been recently published by the author (i.e., Khin Zaw et al., 2007a; Manaka et al., 2007a; Manaka et al., 2007b).

1.4. Aims of this study

The aim of this study is to establish ore genesis models for the LCT and BHX deposits and to help further exploration in and around the PBCA in northern Lao PDR. The objectives of the study to be addressed are:

1. Document the detailed deposit-scale geology at the LCT and BHX deposits
2. Establish paragenetic relations of ore and gangue minerals and describe mineral chemistry of ore and the associated minerals at the LCT and BHX deposits
3. Investigate the geochemical characteristics of ore-forming fluids at the LCT and BHX deposits
4. Integrate the above results and develop ore deposit models to understand the nature and origin of ore formation and to apply the model to target the high-grade part of the mineralised system.

1.5. Methodology

The methods used to achieve the aims of this study include both field and laboratory components.

Field work methods

Field work in the LCT and BHX deposits was conducted during two visits in the dry season from late March to late April in 2006 and middle February to middle March 2007. The field work was specifically focused on:

1. Detailed surface mapping of lithological units from outcrops in the LCT and BHX deposit areas
2. Detailed logging of selected diamond drill and rock chip holes at the LCT and BHX deposits
3. Collection of samples from outcrop and diamond drill holes for detailed laboratory analyses.

During the field work, the author logged and sampled a total of 2400m of diamond drill cores from 23 drill holes at LCT and a total of 3100m of diamond drill cores from 17 drill holes at BHX. All the studied rock samples from LCT and BHX are listed in Appendix I.

Laboratory work methods

All the laboratory work presented below was conducted at the University of Tasmania, except for oxygen and hydrogen isotope analyses which were submitted to Queensland University of Queensland. The following laboratory work was undertaken:

1. Petrographic studies to establish a basic geological and lithological framework and determine the paragenesis of mineralisation and alteration at the LCT and BHX deposits
2. XRF whole rock geochemistry analysis of unaltered and the least altered host rocks to obtain major, trace and rare earth element (REE) geochemical characteristics
3. CAMECA electron microprobe analysis to determine the chemical composition of gold- and silver-bearing minerals and the associated sulphide minerals
4. LA-ICPMS analysis on zircon and pyrite to obtain geochronological and geochemical information respectively
5. PIMA analysis on altered host rocks to determine alteration mineralogy
6. Fluid inclusion analysis on quartz and dolomite of veins from main mineralisation stages to understand the formation of ore-bearing fluids
7. Stable isotopic analysis of oxygen, hydrogen and sulphur to determine the source of ore-forming fluids
8. Lead isotopic analysis to determine the source of metals.

CHAPTER 2 TECTONICS AND METALLOGENY OF THE INDOCHINA TERRANE

2.1. Introduction

In recent years, many attempts have been made to define a relationship between the metallogenesis and tectonic development of the mainland SE Asia region (e.g., Fan, 2000; Gatinsky, 2005; Khin Zaw et al., 2007a; Khin Zaw and Meffre, 2007). However, the relationship is still poorly understood as mainland SE Asia comprises several microcontinents and has a complex geology.

Mainland SE Asia consists of three major terranes (also regarded as microcontinents or crustal blocks) including the Indochina, South China and Shan-Thai Terranes (Fig. 2.1) (e.g., Metcalfe, 1988). Three major fold belts are recognised in the mainland SE Asia including the Sukhothai Fold Belt (SFB), the Loei Fold Belt (LFB) and the Truongson Fold Belt (TFB) (Fig. 2.1). Each of these fold belts is geologically characterised by the emplacement of a number of volcano-plutonic rocks (e.g., Khin Zaw et al., 2007a; Khin Zaw and Meffre, 2007; Khositantont et al., 2008). The SFB and LFB are thought to be related to westward and eastward subductions of oceanic crust respectively, and may have been formed during the collision of the Shan-Thai and Indochina Terranes (e.g., Bunopas, 1981; Srichan et al., 2006). The TFB is believed to be related to subduction/collision of the South China and Indochina Terranes during the Palaeozoic (e.g., Hutchison, 1989).

A variety of ore deposits of various commodities (i.e., lead, zinc, copper, gold, silver, iron, tin, tungsten, coal and other industrial minerals) and different mineralisation styles (i.e., epithermal, skarn, porphyry and sediment-hosted) are recognised in mainland SE Asia, (e.g., Fan, 2000; Gatinsky, 2005; Khin Zaw et al., 2007a). The occurrence of the deposits is mostly confined to either the SFB, LFB or TFB, and thus an intimate relationship between the tectonic processes and a number of ore formation along the SFB, LFB and TFB is considered (e.g., Khin Zaw et al., 2007a; Khin Zaw and Meffre, 2007; Khositantont et al., 2007).

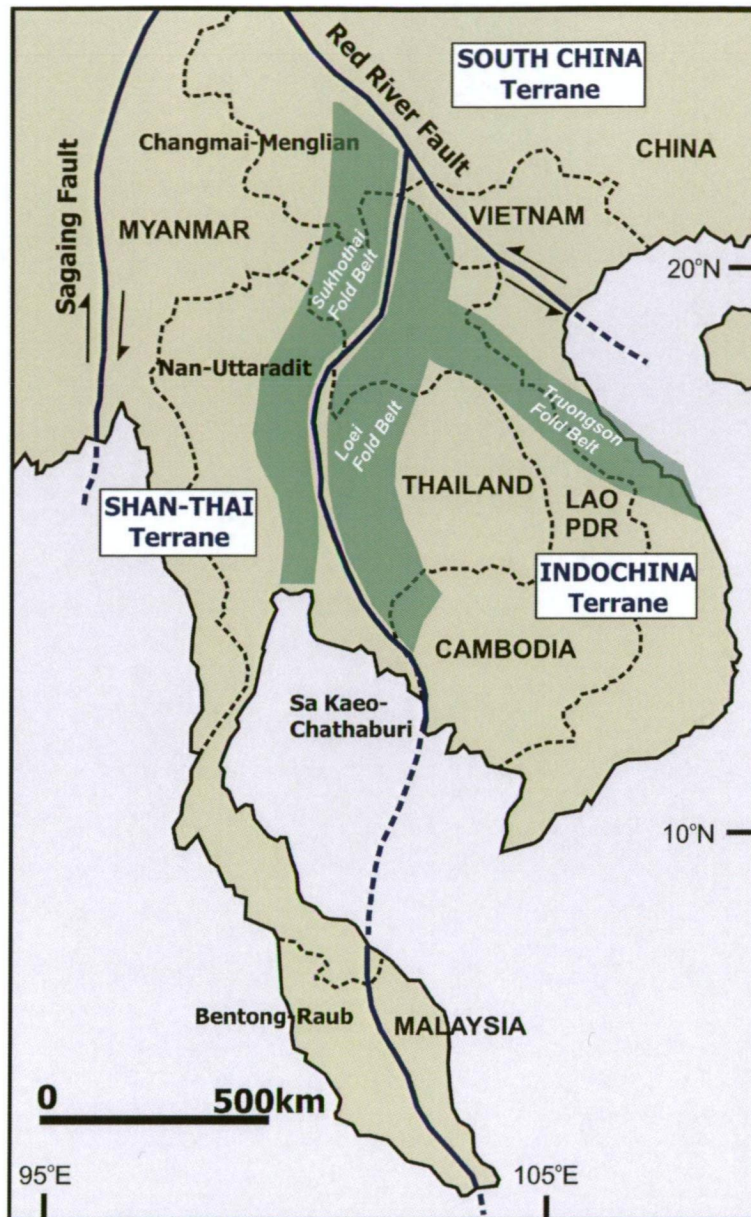


Fig. 2.1. Tectonic setting of mainland SE Asia (modified after Hada et al., 1999; Singharajwarapan and Berry, 2000). Note that the three major terranes including South China, Shan-Thai and Indochina Terranes are separated by the dextral Sagaing Fault, sinistral Red River Fault and Changmai-Menglian, Nan-Uttaradit, Sa Kaeo-Chathaburi and Bentong-Raub ophiolitic suture zones

This chapter aims at discussing the regional geological background based on literatures, before focusing on the deposit-scale geology of the LCT and BHX deposits. It includes the geological and tectonic development of mainland SE Asia and the metallogenic relations in the LFB and TFB. Several known deposits occurring along the LFB and TFB are also briefly reviewed.

2.2. Tectonic evolution of mainland SE Asia

The terranes consisting of mainland SE Asia (i.e., Indochina, South China and Shan-Thai Terranes) have a similar tectonic history as Gondwana-derived allochthonous terranes, and they are thought to have been developed by four main geological events involving rifting, drifting, amalgamation and post-amalgamation events (e.g., Metcalfe, 1988). This tectonic framework was generally accepted in the early 1990s; studies since that time mainly focus on these geological events, although there are still many controversies. The rifting, drifting, amalgamation and post-amalgamation events of the terranes are reviewed in this section.

2.2.1. Rifting

The Indochina Terrane is generally interpreted to have rifted from the Gondwanaland in the Middle-Late Palaeozoic, along with the Shan-Thai and South China Terranes, and to have started drifting northwards. This is supported by palaeomagnetic and palaeo-faunal data (e.g., Sengor and Hsu, 1984; Metcalfe, 1988). However, the timing of the rifting event from Gondwanaland is still widely debated. Metcalfe (1999) indicated that the rifting of the Indochina and South China Terranes from Gondwanaland occurred in the Devonian, and that the Shan-Thai Terrane rifted in the Carboniferous-Early Permian (Figs. 2.2A, B and C). A number of other scenarios have also been proposed, especially for the South China and Indochina Terranes, and some studies suggest that their rifting commenced as early as the Ordovician or Silurian (e.g., Hutchison, 1989; Charusiri et al., 2002). As a result, these controversies led to poor constraints for the metallogeny of these Gondwanaland-derived terranes, in association with the rifting event.

2.2.2. Drifting

The Indochina and South China Terranes separated from the margin of Gondwanaland by the Late Devonian, before the Shan-Thai Terrane, and subsequently drifted northwards, with the opening of the Palaeo-Tethys ocean (Metcalfe, 1999) (Fig. 2.2A). The drifting of these terranes is believed to have commenced by the Early Carboniferous, as there is no faunal or floral similarity or other connections in the Early Permian geological data between these terranes and Gondwanaland (Metcalfe, 1999). The Shan-Thai Terrane was welded to Gondwanaland until the Permian. It was rifted as a part of the Cimmerian continent and then drifted rapidly away in a northward direction (Metcalfe, 1999) (Figs. 2.2B and C). This temporal constraint on the Shan-Thai Terrane is also demonstrated by Hutchison (1989); it has Lower Permian diamictites, cool water Carboniferous-Permian faunas of high latitude indicators and the Upper Permian platform facies limestone of low latitude indicators. On this basis, it is known that the rapid northward

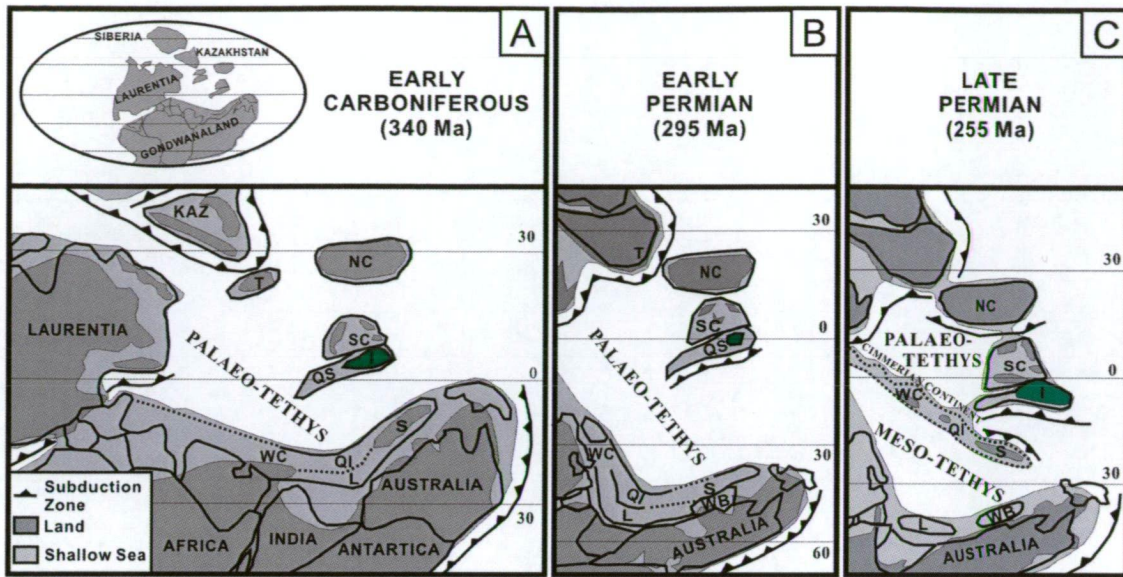


Fig. 2.2. Reconstruction maps of the Gondwanaland-derived terranes from Early Carboniferous to Late Permian (modified after Metcalfe, 1999). Note that Indochina Terrane is marked by green colour. I=Indochina, WB=West Burma, S=Shan-Thai (Sibumasu), L=Lhasa, QS=Qamdo-Simao, Q=Qiangtang, NC=North China, SC=South China, T=Tarim, KAZ=Kazakhstan.

drifting of the Shan-Thai Terrane from a high latitude in the southern hemisphere to a low latitude must have occurred throughout the Permian. During this northwards drifting, the Meso-Tethys ocean was formed between the Cimmerian continent and Gondwanaland (Metcalfe 1999) (Fig. 2.2C).

2.2.3. Amalgamation

The amalgamation of the Indochina, South China and Shan-Thai Terranes is considered to have occurred during the Late Palaeozoic to Early Mesozoic. It is believed that the Indochina Terrane was initially collided with the South China Terrane and subsequently with the Shan-Thai Terrane, along with the formation of the TFB and LFB along the north to northeast margin and western margin of the Indochina Terrane, respectively.

The amalgamation of the Indochina and South China Terranes is known to have commenced along the Song Ma (Red River) Fault in North Vietnam (e.g., Metcalfe, 1999; Hutchison, 1989). This is commonly interpreted by many authors, as the occurrence of ophiolitic rocks along the fault is reported (e.g., Hutchison, 1989). However, the timing is poorly constrained in previous studies as variable ages such as Carboniferous (Metcalfe, 1999) to Triassic (Sengor and Hsu, 1984; Lepvrier et al., 1997) have been suggested.

The amalgamation of the Indochina and Shan-Thai Terranes has also been widely debated for its timing and formation of the suture zones. Various possible timing for this amalgamation have been suggested, such as Carboniferous-Permian (Hutchison, 1989), Triassic (Sengor et al., 1988; Metcalfe, 1988; 1996) and Triassic-Cretaceous (Aduley-Charles, 1983). In addition, several candidates for the boundary between the Indochina and Shan-Thai Terranes have been postulated involving the Nan-Uttaradit/Sa Kaeo-Chanthaburi suture in Thailand and the Betong-Raub suture in Malaysia (e.g., Hutchison, 1989; Hada et al., 1999; Metcalfe, 1999) and somewhere in the further west such as Mae-Yuang (Mae Sariang-Mae Hong Son) Fault (Hisada et al., 2004).

2.2.4. Post-amalgamation

During and after the major terrane assembly in the region, a number of important extensional episodes occurred, causing subsidence within the Indochina, South China and Shan-Thai Terranes (e.g., Hall, 2002). The most notable geological event during this time was the indentation of Indochina Terrane from the continental Asia, resulting from the collision of the Indian Craton into Eurasia (Hutchison, 1989). The Indochina Terrane was consequently extruded to the southeast from the Asian continent, bordered with the dextral Saging Fault in Myanmar and sinistral Red River Fault in South China and Vietnam, and with the opening of the South China Sea in the north and the Gulf of Thailand in the south (Hall, 2002).

2.3. Metallogeny of Indochina Terrane

Mineral occurrences in the Indochina Terrane are mostly confined to the LFB and TFB, which are recognised as the largest endowments of economic metal deposits in mainland SE Asia (Fig. 2.3). However, detailed tectonic and metallogenic studies have not been conducted on this region. Consequently this has led to poorly-constrained knowledge on the metallogeny of the Indochina Terrane. On the basis of limited literatures, the metallogeny of the LFB and TFB is briefly reviewed herein.

2.3.1. Loei Fold Belt (LFB)

The LFB trends north to south and extends from the coast of the Gulf of Thailand in the south through central Thailand, north into the northern Lao PDR (Figs. 2.1 and 2.3). The geology of the LFB is generally characterised by an abundance of Permian-Triassic volcano-plutonic rocks which are interpreted to have been formed by eastward subduction of the Palaeo-Tethys oceanic crust underneath the Indochina Terrane during the Indosinian Orogeny (Bunopas, 1981). A number of economic ore deposits have been discovered along the LFB, closely associated with the occurrence of the Late Palaeozoic to Triassic volcano-plutonic rocks (e.g., Khin Zaw et al., 2007a; Khin Zaw and Meffre, 2007). The deposits occurring in the LFB are characterised by diverse types of ore deposits such as epithermal and porphyry-related skarn (Khin Zaw et al., 2007a; Khin Zaw and Meffre, 2007).

The Chatree deposit, located in central Thailand, is currently known as the largest gold-silver epithermal deposit in the LFB (Fig. 2.3). The Chatree deposit consists of 12 pits/prospects including a total resource of 74.6 Mt at 1.6 g/t Au and 13 g/t Ag, and several other prospects are also currently recognised in the adjacent area explored by Kingsgate Consolidated Ltd (<http://www.kingsgate.com.au>). The geology of the Chatree area comprises Late Permian to Early Triassic volcanic and volcanoclastic rocks which are basaltic to andesitic in composition, with minor sedimentary rocks (Salam et al., 2007a, b). The epithermal gold-silver mineralisation occurs as veins/veinlets and these are preferentially hosted within the volcanic and volcanoclastic rocks (Dedenczuk, 1998; Greener, 1999; Kromkhun, 2005; Salam et al., 2007a, b). The alteration associated with the main mineralisation stage is spatially well-defined by phyllic and propylitic alterations in the proximal vein/veinlets and silicification in the distal wall rock (Salam et al., 2007a, b). In addition, regional structures trending N-S to NNW-SSE, which overlap the elongated trends of orebodies are detected through the deposit area, and thus a combination of

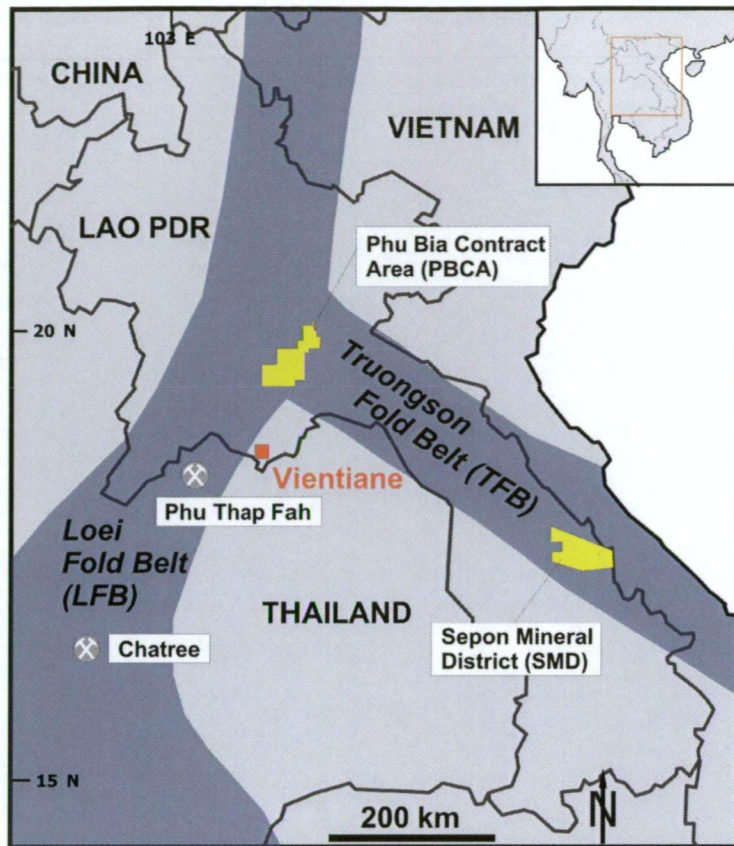


Fig. 2.3. Location of Phu Bia Contract Area (PBCA) and Sepon Mineral District (SMD) in Lao PDR and Chatree and Phu Thap Fah deposits in Thailand, with distribution of Loei and Truongson Fold Belts in mainland SE Asia.

structure and lithology is considered to be a significant contribution for the economic gold-silver mineralisation at Chatree (Salam et al., 2007a, b).

The Phu Thap Fah gold deposit is also an important currently operating mineralised skarn system, occurring in the LFB of the northeastern part of Thailand (Fig. 2.3). The host rocks of Phu Thap Fah consist of a Permian sedimentary sequence including crystalline limestone and siltstone intruded by Triassic granodiorite and microdiorite dykes (Khin Zaw et al., 2006, 2007b). The skarn mineralisation at Phu Thap Fah is characterised by an andraditic garnet-clinopyroxene prograde stage, followed by a retrograde gold-bearing stage consisting of amphiboles, epidote, chlorite, carbonate and quartz assemblage (Khin Zaw et al., 2006, 2007b). Gold occurring as electrum, gold-bismuth and gold bismuth-telluride association, is mostly confined to the massive pyrrhotite and pyrite retrograde zone (Khin Zaw et al., 2006, 2007b). The deposit contains an indicated and measured reserve of 40,700 tonnes at 3.54 g/t Au and 747,000 tonnes at 7.97 g/t Au (Khin Zaw et al., 2007b).

2.3.2. Truongson Fold Belt (TFB)

The TFB is mainly distributed within the Territory of Lao PDR. It trends NW-SE and continues to the central area of Vietnam (Fig. 2.3). Compared to the LFB, fewer metallogenic studies have been undertaken on the TFB because of the remote location, unsafe condition, thick forest cover and abundant unexploded bombs. These factors have resulted in poor knowledge of the metallogeny of the TFB. However, the Sepon Mineral District (SMD) in southern Lao PDR, which is the largest economic mineralised system occurring along the TFB, has been well-studied since its discovery in 1993 (Cromie et al., 2004a, b, 2007; Smith et al., 2005).

The SMD includes seven gold and two copper deposits/prospects. The geology of the SMD consists mostly of an Upper Palaeozoic volcano-sedimentary sequence that is dominated by continental fluvial and shallow to deep marine sedimentary rocks of Devonian to Carboniferous age, and Khorat Basin intra-continental sedimentary rocks in Jurassic to Cretaceous age, which unconformably overlay the TFB sequence in the adjacent area of the SMD (Cromie et al., 2004a, b, 2007). Disseminated gold at the SMD occurs within decalcified and silicified calcareous shale and mudstone associated with fine-grained pyrite, and thus the mineralisation characteristics of the SMD lead to its classification as a Carlin-style gold deposit (Cromie et al., 2004a, b, 2007). The intrusions of rhyodacite porphyry dykes are thought to be closely related to the genesis of the Carlin-style mineralisation at the SMD. Other mineralisation styles are also recognised in the SMD including quartz stockwork porphyry molybdenum, copper-gold skarn and copper-gold carbonate replacement (Cromie et al., 2004a, b, 2007). The SMD contains a total mineral resource of 4.8 M oz Au and 1.9 Mt Cu metals (Smith et al., 2005; <http://www.ozminerals.com>).

2.4. Phu Bia Contract Area

The PBCA is a highly prospective area as it is located at the confluence of the LFB and TFB in the northern Lao PDR (Tate, 2005) (Fig. 2.3). The PBCA is currently owned by PanAust Ltd and consists of five deposits and several prospects, which are located either in the northern or southern half sections (<http://www.panaust.com.au>). The deposits include Phu Kham, LCT and BHX in the southern section, and the Khamthonglai (KTL) and Phu He in the northern section of the PBCA (Figs. 1.2 and 2.3). The general geological characteristics of these deposits are summarised in Table 2.1, and are reviewed below.

2.4.1. Southern section of the Phu Bia Contract Area

The southern section of the PBCA includes Phu Kham, LCT and BHX deposits (Fig. 1.2). The Phu Kham deposit is currently the largest deposit in the PBCA and has the largest copper and gold resources, whereas the LCT and BHX deposits of this research project are relatively small-scale deposits hosting economic gold and silver (Table 2.1).

The Phu Kham deposit forms porphyry-related skarn copper-gold mineralisation, mainly hosted in the Late Palaeozoic volcanoclastics and limestone units that are intruded by the earliest Permian intermediate intrusive rocks (Tate, 2005; Khin Zaw et al., 2007a; Kamvong, 2007a, b). The porphyry-related skarn mineralisation system is spatially associated with the emplacement of the intermediate intrusive rocks (Tate, 2005). Kamvong (2007a, b) suggests that the intrusive rocks at the Phu Kham deposit show adakitic features, indicating that magma was generated by partial melting of the oceanic slab in the subduction zone. Alteration is mainly characterised by a sericitic alteration strongly overprinting the host rocks including volcanoclastics, limestone and intermediate intrusive rocks (Tate, 2005). At least three deformational events have been recorded during the post-mineralisation period, reflecting a thrusting of host rock sequence and the later N-S trending steeply dipping vertical faults (Tate, 2005). The Phu Kham deposit contains a total mineral resource of 192 Mt at 0.62 % Cu and 0.24 g/t Au (Table 2.1).

Table 2.1. Geological characteristics of different Cu-Au deposits in the Phu Bia Contract Area (PBCA), northern Lao PDR (Location of the deposits referred to Figs. 1.2 and 2.3).

Deposit	Location	Host rock & age	Mineralisation-related Intrusion & age	Mineralisation style	Ore mineralogy	Alteration type	Resource	Reference
Phu Kham	18.883N, 102.908E	Volcaniclastics with interbedded limestone; Carboniferous-Permian	Crowded feldspar porphyry & quartz eye porphyry (Late Carboniferous-Early Permian)	Porphyry-related skarn & high sulphidation system in hangingwall zone	Chalcopyrite, pyrite, magnetite, bornite, tetrahedrite, galena, enargite, gold	Phyllic, potassic and skarn	192 Mt @ 0.62 % Cu, 0.24 g/t Au & economic Ag	Kamvong (2007a, b); http://www.panaust.com.au
Ban Houayxai (BHX)	18.927N, 102.687E	Volcanic and sedimentary rocks; Early Permian	Aphyric mafic dyke (?); Unknown age	Low-sulphidation epithermal	Pyrite, arsenopyrite, galena, sphalerite, chalcopyrite, electrum, native silver, stephanite	Phyllic, propylitic & potassic	36 Mt @ 1.2 g/t Au & 7.7 g/t Ag	This study; http://www.panaust.com.au
Long Chieng Track (LCT)	18.937N, 102.884E	Sedimentary rocks; Carboniferous, and intrusive rocks; Early Permian	Feldspar-phyric dacite; Early Permian	Low-sulphidation epithermal	Pyrite, sphalerite, galena, chalcopyrite, electrum, native gold	Phyllic, propylitic & potassic	3.66 Mt @ 0.9 g/t Au	This study; http://www.panaust.com.au
Khamthonglai (KTL)	21.535N, 103.175E	Calcareous sedimentary rocks, volcanic and volcaniclastics; Unknown ages	Dioritic-tonalitic porphyry; Unknown age	Porphyry	Pyrite, chalcopyrite, bornite, sphalerite and pyrrhotite	Phyllic, skarn, potassic & propylitic	N/A	Peterson, (2005); http://www.panaust.com.au
Phu He	21.600N, 103.130E	Tuffs and volcanic rocks; Unknown ages	Rhyolitic quartz porphyry (Unknown age)	Low-sulphidation epithermal/mesothermal	Pyrite, galena, sphalerite and chalcopyrite	Propylitic & phyllic	N/A	Tate (2006); http://www.panaust.com.au

2.4.2. Northern section of the Phu Bia Contract Area

The northern section of the PBCA includes the KTL and Phu He deposits, both of which are located approximately 50 km northeast of the Phu Kham deposit (Fig. 1.2).

The KTL deposit, previously called French Copper Mine due to the presence of old French copper workings, was rediscovered by stream sediment sampling and subsequent extensive soil and rock chip sampling programs. Further diamond drilling intersected significant copper and gold content, and these results suggest a highly promising mineralised system. The geology of the KTL deposit area consists mainly of stratified calcareous and volcanoclastic sedimentary rocks intruded by dioritic to tonalitic dykes (Petterson, 2005). The copper-gold mineralisation develops as a stockwork vein system within the intrusive rocks, and the associated skarn, disseminated and supergene style mineralisations are also formed around the stockwork vein system (Petterson, 2005). Ore minerals include pyrite, pyrrhotite, chalcopyrite, bornite, sphalerite and galena, and these assemblages are closely associated with sericite-quartz-pyrite (phyllic) alteration within the intrusions, indicating that the KTL deposit is probably a porphyry copper-gold system (Petterson, 2005).

The Phu He deposit was initially discovered by a regional stream sediment sampling program resulting in the detection of high gold anomalies in the area. This promising result was subsequently tested by soil sampling, trenching, geological mapping and geophysical surveys, and followed up by diamond drilling that intersected high grade gold (Tate, 2006). The gold mineralisation is formed as either high-grade shoots controlled by shear structures or low grade stockwork veins (Tate, 2006). The wall rock in the proximity of the veins/shoots is dominantly altered by weak to moderate propylitic and strong phyllic alteration (Tate, 2006). On the basis of these geological characteristics, the Phu He deposit is highly likely to be an epithermal style mineralisation system (Tate, 2006).

CHAPTER 3 LOCAL GEOLOGY

3.1. Introduction

This chapter describes the results of field work that investigated the deposit-scale geology of the Long Chieng Track (LCT) and Ban Houayxai (BHX) deposits. Geochronological and geochemical studies on the major rock units of the deposits were also undertaken and are presented herein, incorporating data from the nearby Phu Kham deposit from Kamvong (2006; 2007a, b), Khin Zaw and Meffre (2007) and Khin Zaw et al. (2007a). The implications of the results for the southern Phu Bia Contract Area (PBCA) and the adjacent area are also discussed.

3.2. Local geology of the LCT and BHX deposits

3.2.1. Introduction

Until now, geological information about the LCT and BHX deposits was limited to preliminary reports by consultant geologists (e.g., Mason, 1997; Tate, 2003, 2004). These reports were undertaken before this and reviewed in this study. They provided basic geological background information about the deposits, including descriptions of lithological units, surface geological maps and schematic cross-sections. Fieldwork by the author was subsequently undertaken involving detailed geological surface mapping, drill hole logging and sampling. Based on fieldwork and detailed petrographic and microscopic studies, the geological framework of the two deposits was re-evaluated by the author. The new geological maps and cross-sections of the LCT and BHX deposits are shown (Figs. 3.1, 3.2, 3.3 and 3.4). New geological stratigraphic columns for LCT and BHX are also presented in Fig. 3.5.

3.2.2. Sedimentary units at LCT

Sedimentary units at the LCT deposit include carbonaceous limestone, alternating beds of sandstone and siltstone, polymictic sedimentary breccia and tuffaceous sandstone, in ascending order (Fig. 3.5). These units mostly dip at a shallow angle to the east with local open folds, and are locally overlain by volcanoclastic breccia.

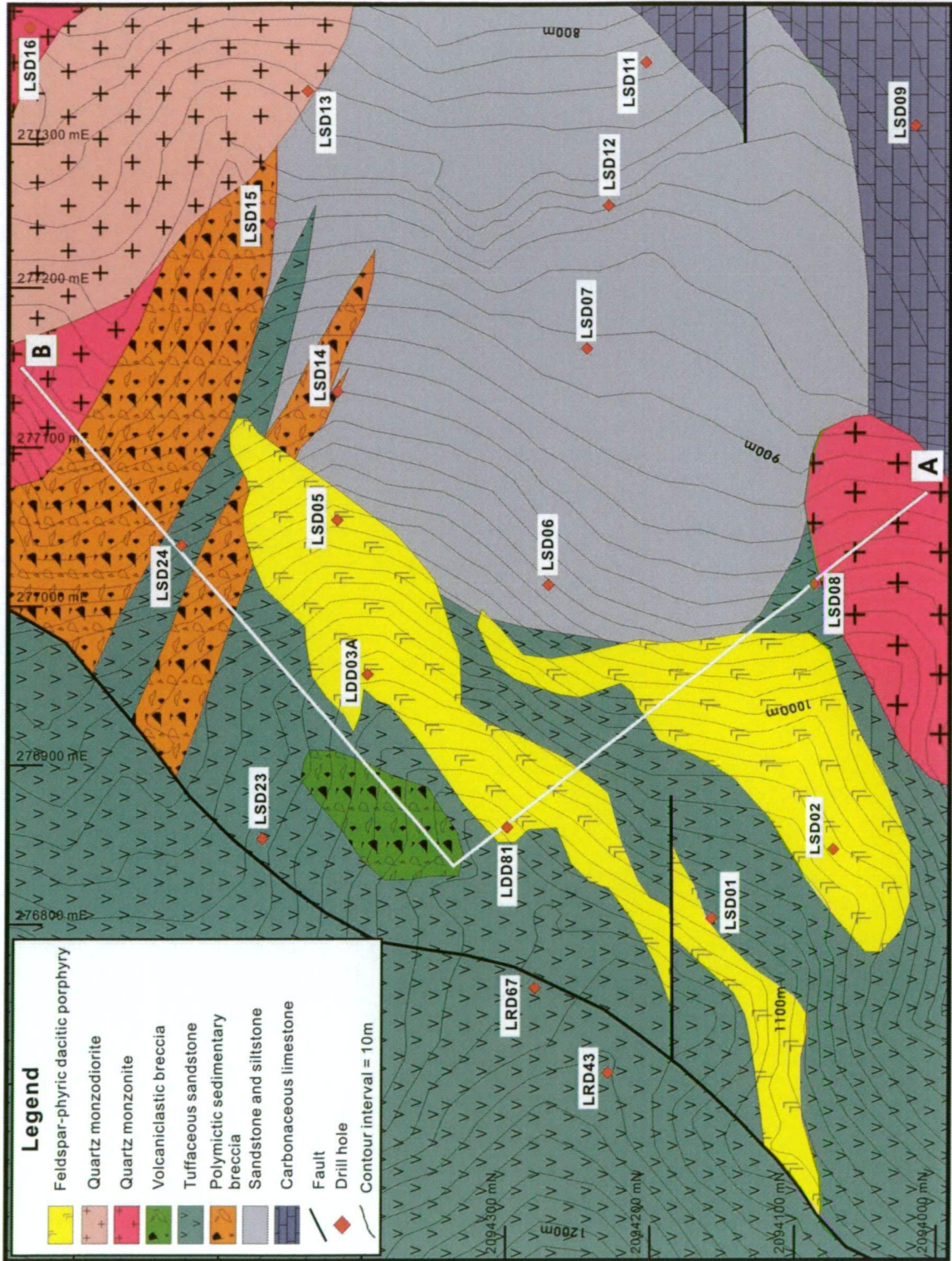


Fig. 3.1. Geological map of the LCT deposit (data after Tate 2003, and surface mapping and drill hole logging by the author).

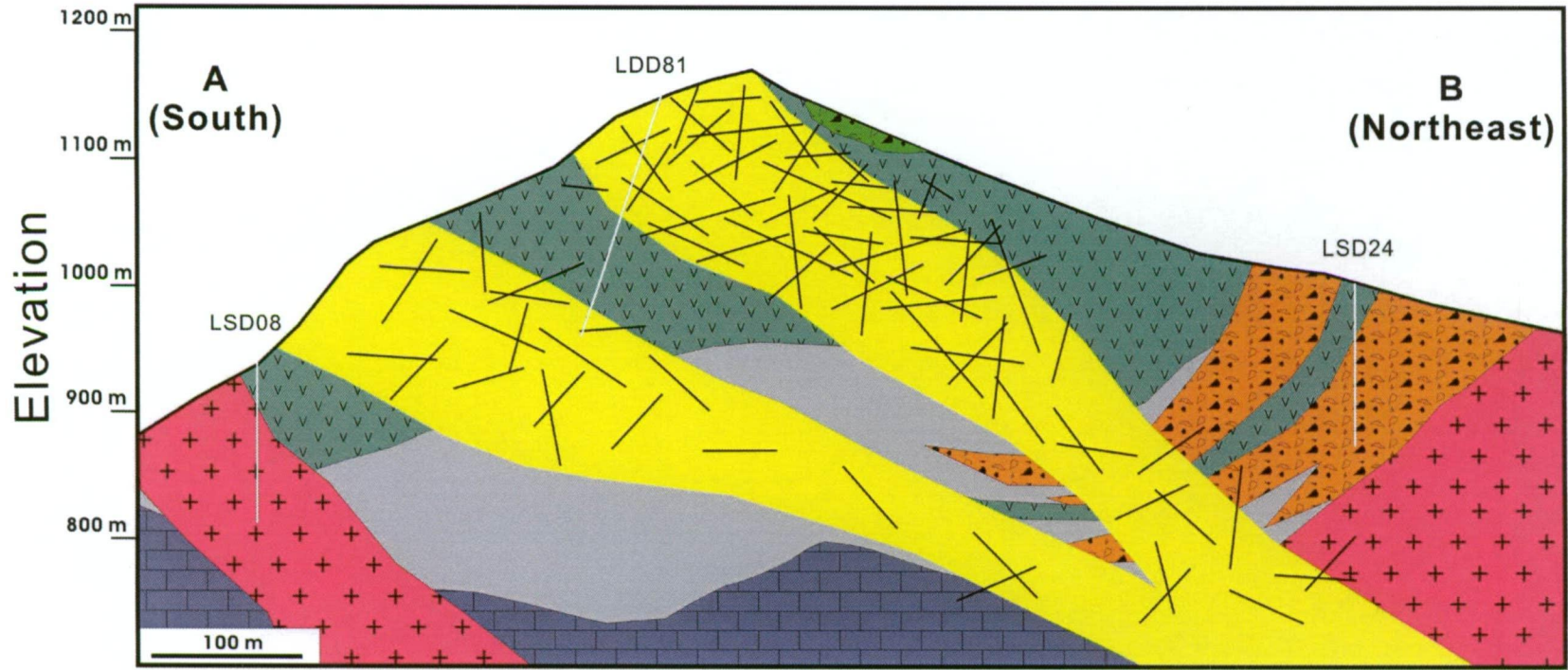


Fig. 3.2. Interpreted geological cross-section of the LCT deposit along white traverse line in Fig. 3.1, with spatial distribution of stockwork veins (black lines). Refer Fig. 3.1 for legend.

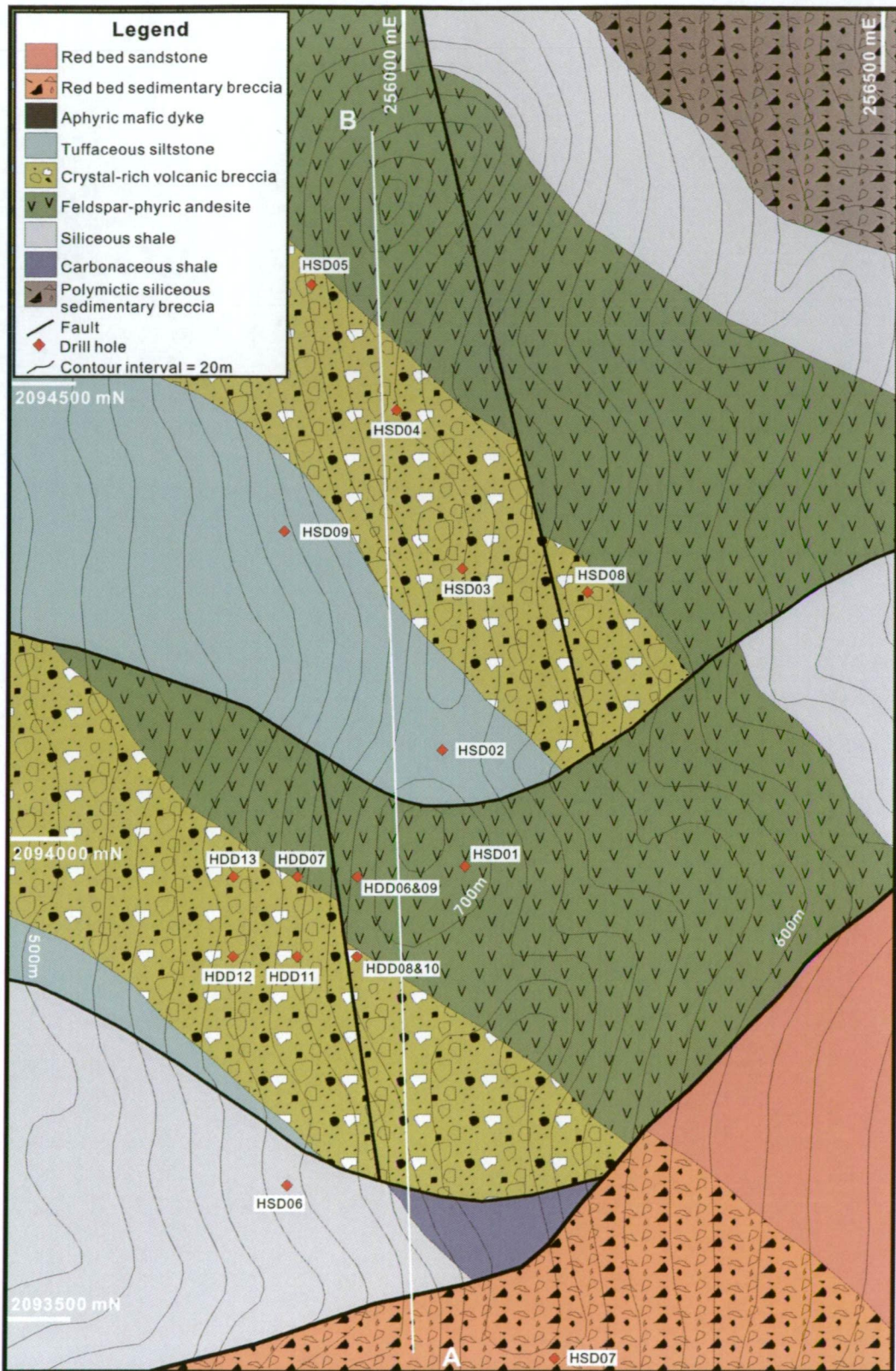


Fig. 3.3. Geological map of the BHX deposit (based on surface mapping and drill hole logging by the author). Note that the aphyric mafic dyke is not outcropped on surface.

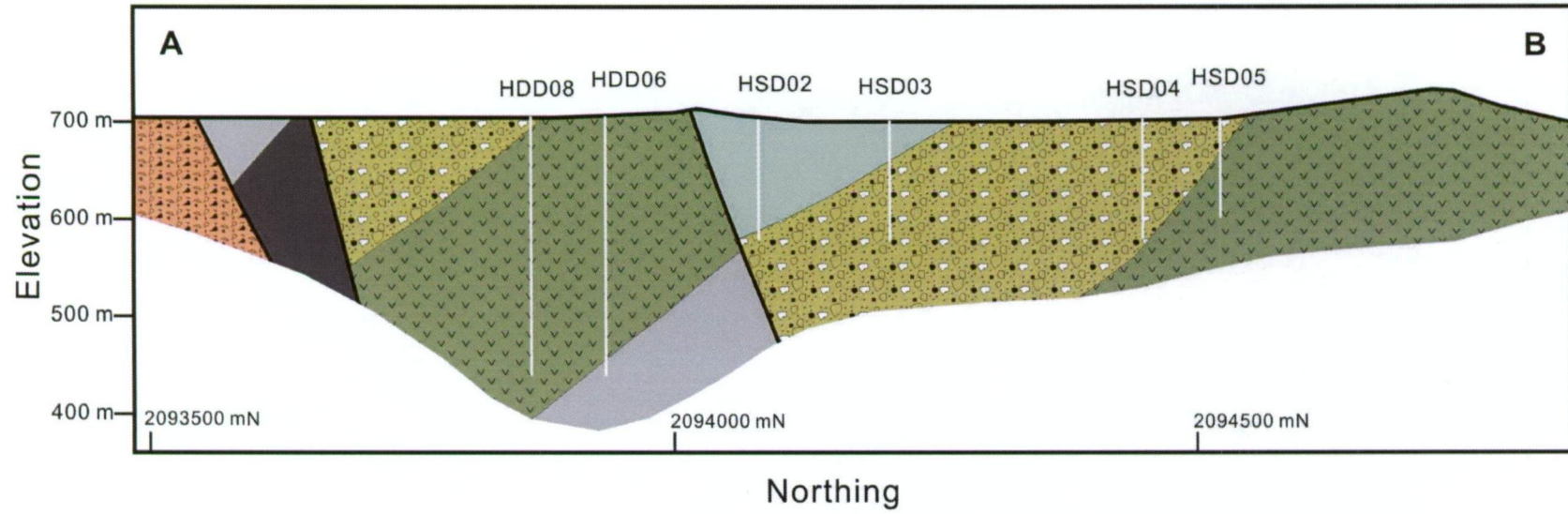


Fig. 3.4. Interpreted geological N-S cross-section of the BHX deposit along white traverse line in Fig. 3.3. Refer to Fig. 3.3 for legend.

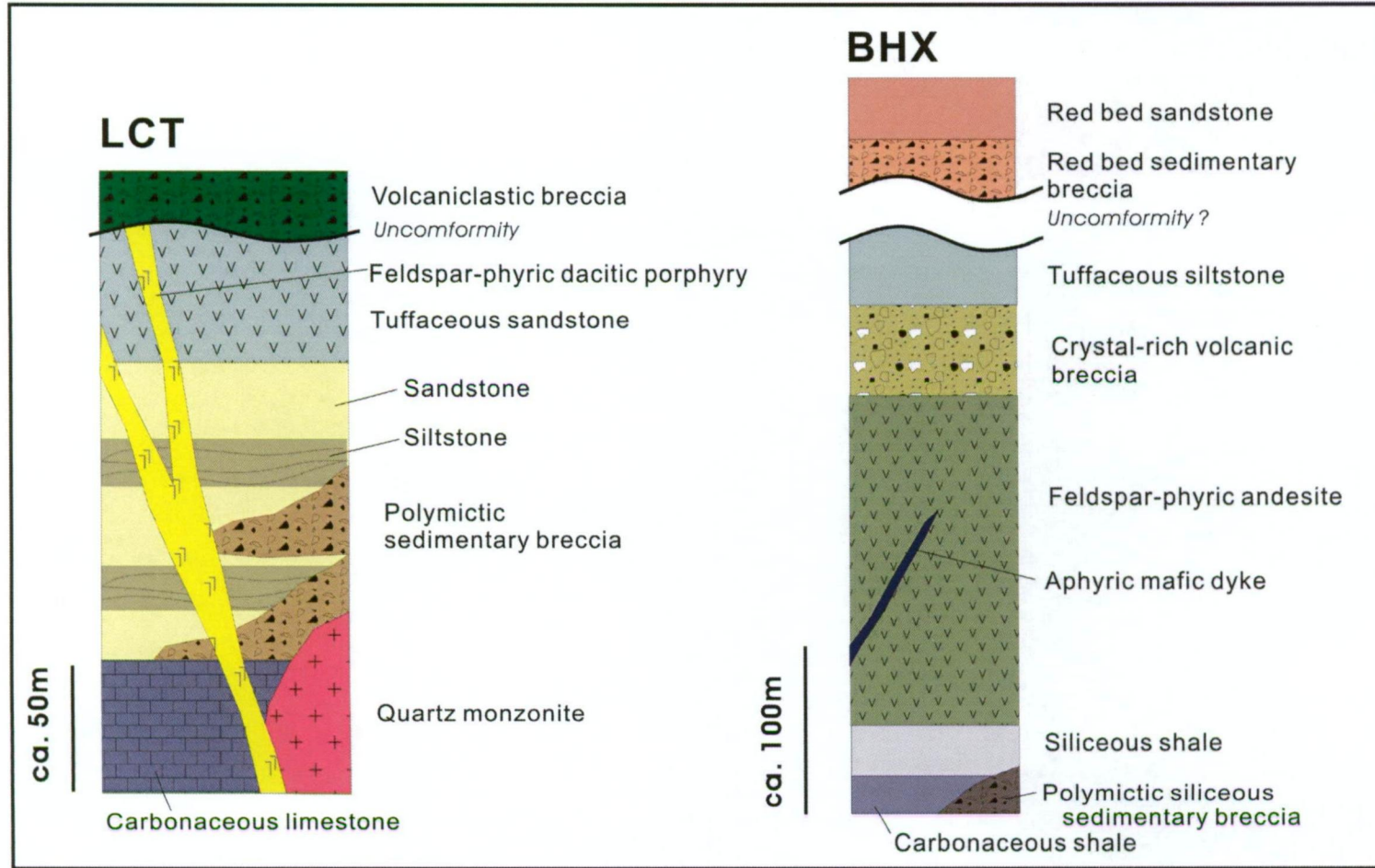


Fig. 3.5. Interpreted geological stratigraphy of the LCT (left) and BHX (right) deposits.

Carbonaceous limestone: Carbonaceous limestone occurs at the lowermost part of the sedimentary sequence of the LCT deposit. There is no outcrop of this unit in the LCT deposit area, but it is identified where it is intersected by several diamond drill holes in the eastern part of the deposit area, such as LSD09 and LSD11 (Fig. 3.1). An occurrence of Lower Carboniferous rugose coral index fossils from this limestone unit is reported by Mason (1997). The thickness of this unit is estimated to exceed several tens of metres. This unit is commonly altered to marble which may be due to contact metamorphic affect associated with intrusive activity. A fresh hand specimen sample of this unit has a dark grey, fine-grained in texture (Fig. 3.6A), which may represents presence of carbonaceous materials.

Alternating beds of sandstone and siltstone: Alternating beds of sandstone and siltstone occur in the middle part of the sedimentary sequence at the LCT deposit, above the carbonaceous limestone unit. The sandstone and siltstone occur as layers from 1 to several tens of centimetres thick. The lower part of this unit is dominated by siltstone, whereas the upper part is sandstone-dominated. In a hand specimen, the siltstone is dark grey and consists of carbonaceous materials, whereas the sandstone involves abundant discrete feldspar crystals (Fig. 3.6B).

Polymictic sedimentary breccia: Polymictic sedimentary breccia occurs locally in the northern section of the deposit area (Fig. 3.1). This unit forms in lenses within the alternating beds of the sandstone and siltstone unit. A hand specimen sample of this unit shows a clast-supported texture (clasts are up to 80–90 vol. %) and comprises polymictic clasts such as carbonaceous, chloritic or siliceous fragments (Fig. 3.6C). Most of these clasts are angular or sub-rounded, averaging 2–3 cm (up to 10 cm) in size. The matrix of this unit is commonly cemented by fine-grained carbonate minerals.

Tuffaceous sandstone: This unit occurs at the uppermost part of the sedimentary sequence at LCT, and is widely distributed in the central and western parts of the deposit area (Fig. 3.1). In the central deposit area, this unit is well-exposed and shows a strongly-foliated texture. A hand specimen sample of this unit shows its pale green in colour and fine-grained texture (Fig. 3.6D). Lithic carbonaceous fragments, commonly 1 to 3 cm in size, are occasionally present in this unit. This unit hosts the gold-bearing veins in the proximal part of the feldspar-phyric dacitic porphyry intrusive unit, and commonly the rock is strongly altered by quartz-sericite-chlorite-pyrite mineral assemblages.

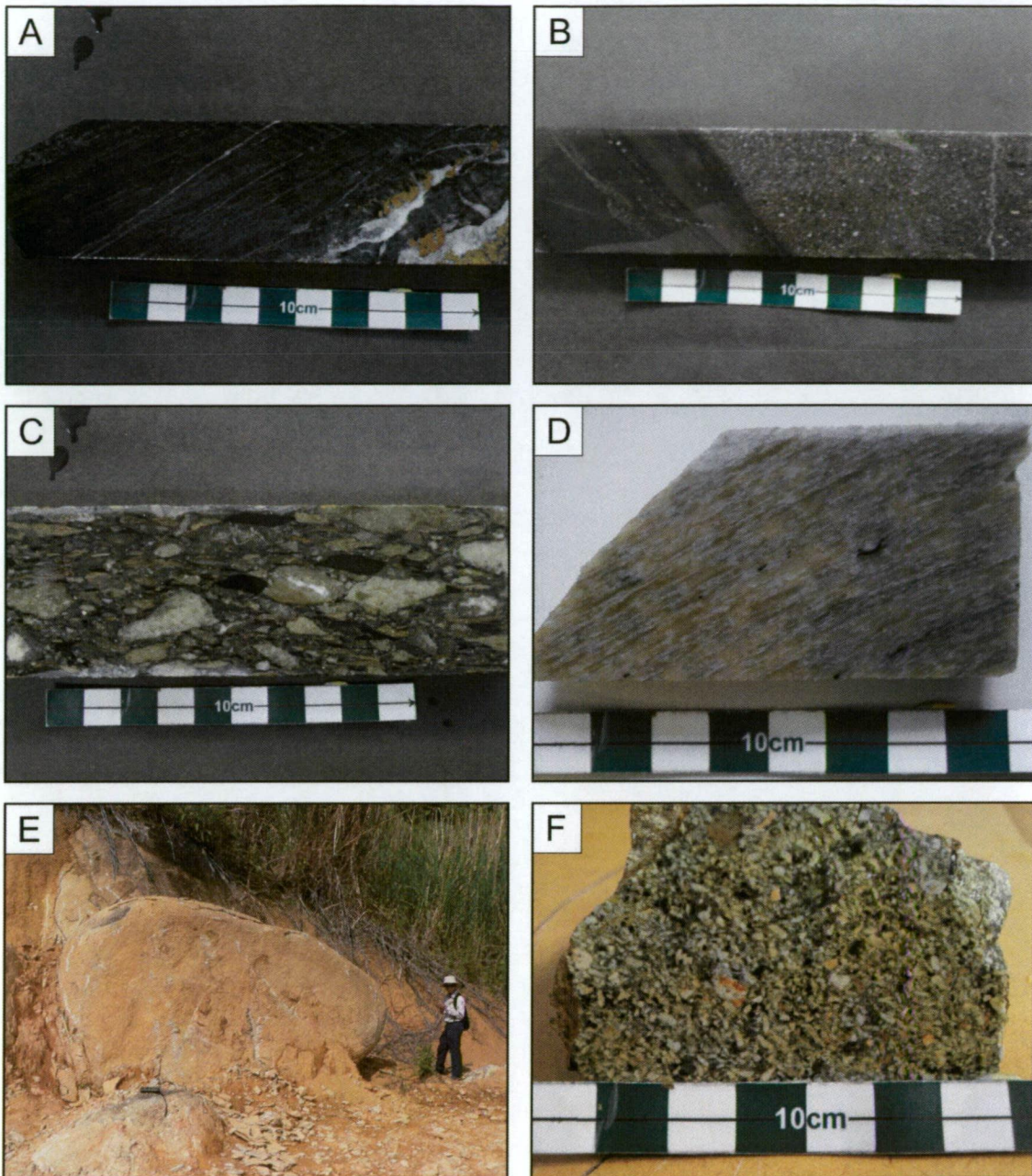


Fig. 3.6. Photographs of representative hand specimen samples of sedimentary units at the LCT deposit.

- A) A hand specimen sample of carbonaceous limestone consisting of dark grey coloured content with comb quartz-base metal sulphide vein. Sample No. LSD09@88.0m.
- B) A hand specimen sample of alternating beds of sandstone and siltstone. Sample No. LSD07@78.0m.
- C) A hand specimen sample of polymictic sedimentary breccia. Sample No. LSD24@17.0m.
- D) A hand specimen sample of tuffaceous sandstone. Sample No. LSD08@99.3m. Note that the sample is weakly foliated.
- E) An occurrence of a volcaniclastic boulder at the central part of the deposit area.
- F) A hand specimen sample of a volcaniclastic boulder. Sample No. LCT-1.

Volcaniclastic breccia: This unit occurs locally in the central part of the deposit area and unconformably overlies the tuffaceous sandstone unit which forms the top part of the sedimentary sequence at LCT. The breccias occur mostly as rounded boulders up to 5 m in size (Fig. 3.6E). A hand specimen sample of the breccia shows polymictic crystal-rich fragments which range in size from several mm to 1 cm (Fig. 3.6F). No hydrothermal alteration has been observed in this rock unit.

3.2.3. Intrusive igneous units at LCT

Three igneous units were identified at the LCT deposit, including quartz monzonite, quartz monzodiorite and feldspar-phyric dacitic porphyry. They intrude the sedimentary units as recognised from diamond drill hole logging. The igneous units at LCT are described below:

Quartz monzonite: Quartz monzonite occurs in the southern and northeastern sections of the deposit area (Fig. 3.1). The unit in the southern section shows a clear intrusive feature, whereas the other part of this unit in the northeastern section forms a large batholith-like body. This unit is moderately affected by sericite and chlorite alteration.

The least altered hand specimen sample of the quartz monzonite shows a porphyritic texture consisting of sparsely distributed lath-shaped feldspars (20–30 vol. %) with a pale greyish fine-grained groundmass (Fig. 3.7A). The phenocrysts are mostly composed of K-feldspar as detected by staining and microscopic examination. Minor mafic minerals (10–15 vol. %) are also present in this rock, and most of them are partly to totally altered by chlorite.

In thin section, quartz monzonite samples show the presence of sparsely distributed phenocrysts consisting of K-feldspar (50–60 vol. %), plagioclase (30–40 vol. %) and quartz (up to 10 vol. %) (Fig. 3.7B). The K-feldspar and plagioclase phenocrysts normally occur as euhedral laths and are up to 5 mm (2–3 mm on average) in size. Patchy alteration of sericite is also noted and it replaces most of the feldspar phenocrysts. A trace amount of biotite (up to 5 vol. %) is also present (less than 5 mm in size), mostly replaced by chlorite and calcite. The groundmass is dominantly composed of K-feldspar and plagioclase with interstitial quartz grains, ranging from several tens to hundreds μm in size. Alteration minerals are disseminated in the groundmass including calcite, chlorite and clay minerals.

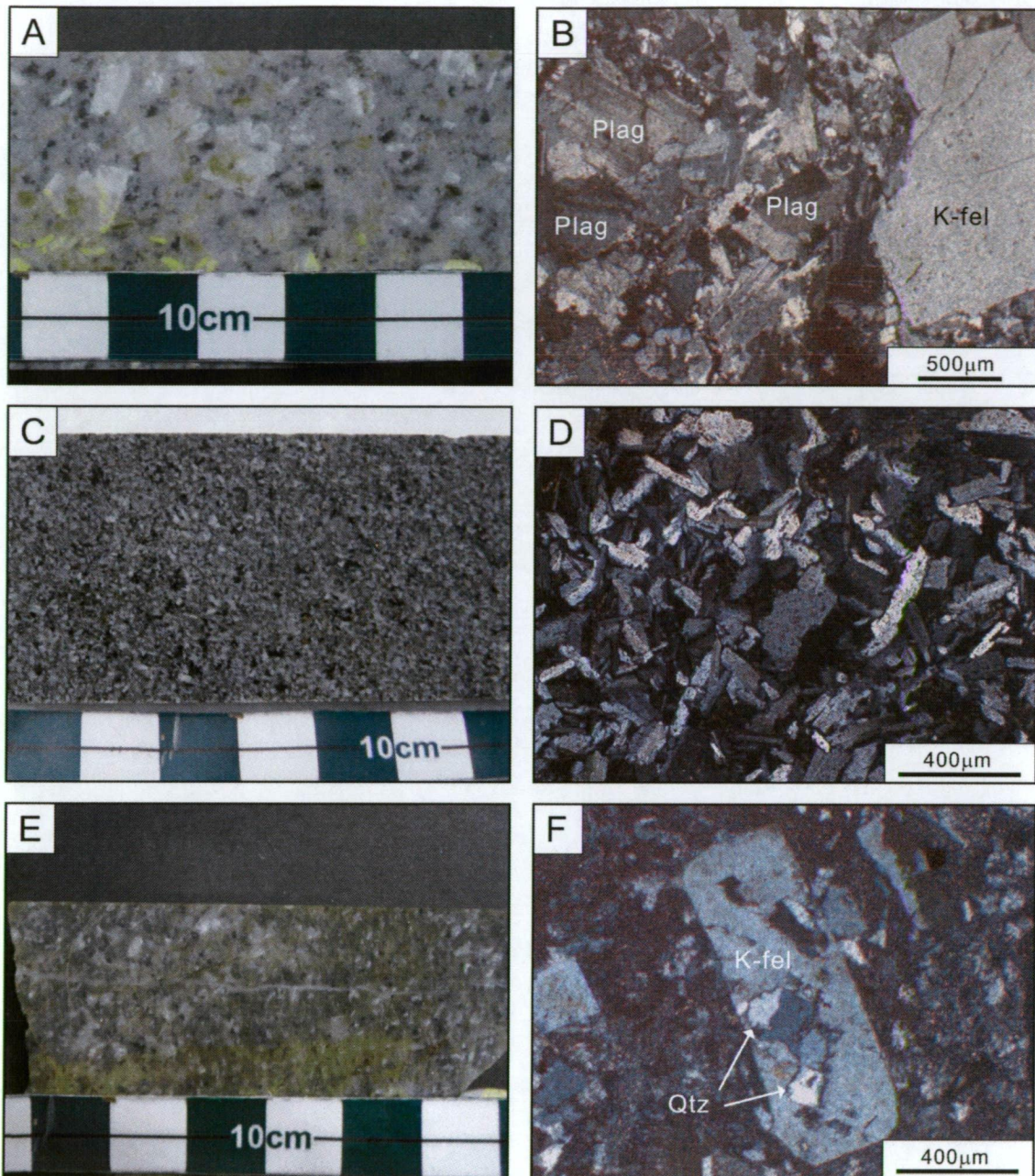


Fig. 3.7. Representative hand specimen sample and thin-section images of intrusive igneous units at the LCT deposit. Abbreviations: Plag=plagioclase, K-fel=K-feldspar, Qtz=quartz, xpl=crossed polarised light.

- A) Photograph showing a hand specimen sample of quartz monzonite. Sample No. LSD18@70.7m.
 B) Photomicrograph (xpl) showing K-feldspar and plagioclase phenocrysts in finer-grained groundmass of quartz monzonite. Sample No. LSD16@36.1m
 C) Photograph showing a hand specimen sample of quartz monzodiorite. Sample No. LSD15@99.1m.
 D) Photomicrograph (xpl) showing plagioclase-dominated interlocking crystal texture of quartz monzodiorite. Sample No. LSD15@99.1m.
 E) Photograph showing a hand specimen sample of feldspar-phyric dacitic porphyry. Sample No. LSD04@87.2m.
 F) Photomicrograph (xpl) showing a K-feldspar phenocryst in very fine-grained groundmass of feldspar-phyric dacitic porphyry, with local replacement by quartz minerals. Sample No. LSD04@87.2m.

Quartz monzodiorite: Quartz monzodiorite occurs in the northeastern section of the deposit area, where it is closely associated with the quartz monzonite. A clear contact relationship with quartz monzonite was not identified in fieldwork, but it was reported that they cross-cut each other (Tate, 2003). This unit does not outcrop, but is intersected in several diamond drill holes. A hand specimen sample shows an interlocking crystal texture consisting of less than mm sized grains (Fig. 3.7C). Composition of the grains are difficult to detect with the naked eye, except mafic minerals (up to 1 mm in size), which are patchy and disseminated (up to 20 vol. %). Euhedral, mm-sized pyrite grains (less than 10 vol. %) are also disseminated in the hand specimens.

In thin section, the phenocrysts are interlocked in texture and consist of feldspars (60 vol. %), quartz (10 vol. %) and chlorite (20 vol. %) (Fig. 3.7D). The feldspar phenocrysts normally show euhedral to tabular shape, and are mainly composed of plagioclase (80 vol. %) with minor K-feldspar (20 vol. %). Chlorite commonly replaces biotite. Pyrite is also present and is evenly disseminated throughout the sample.

Feldspar-phyric dacitic porphyry: Feldspar-phyric dacitic porphyry intrudes the sedimentary sequence at the LCT deposit area. No clear contact relationship with quartz monzonite and quartz monzodiorite was observed, and the zircon U-Pb age of this unit is distinctly younger than the ages of those units (see geochronology section). Gold-bearing stockwork veins are commonly hosted within this intrusive unit, and the rock is moderately to intensely altered.

The least altered hand specimen sample of this unit has a porphyritic texture with milky coloured, uneven-sized phenocrysts (30–40 vol. %) in a greenish coloured fine-grained groundmass (Fig. 3.7E). The phenocrysts range from less than 0.5mm up to 5 mm in size and are evenly distributed in the groundmass. Mafic minerals are also present (up to 10 vol. %) and are uniformly disseminated in the sample. Alteration minerals are visible in the hand specimen samples and include sericite and chlorite which selectively replace primary feldspar and mafic minerals, respectively.

In thin section, the phenocrysts comprise K-feldspar (70–80 vol. %) and quartz (10–20 vol. %). Minor mafic minerals are also present (up to 10 vol. %). These phenocrysts are evenly distributed throughout the sample. Euhedral to subhedral K-feldspar phenocrysts commonly occur as single crystals, ranging from 0.5 up to 2 mm in size (Fig. 3.7F). Minor primary quartz phenocrysts may also be present, although they are normally hard to distinguish from secondary alteration-related quartz. Mafic minerals, most of which show the distinctive euhedral hexagonal outline typical of

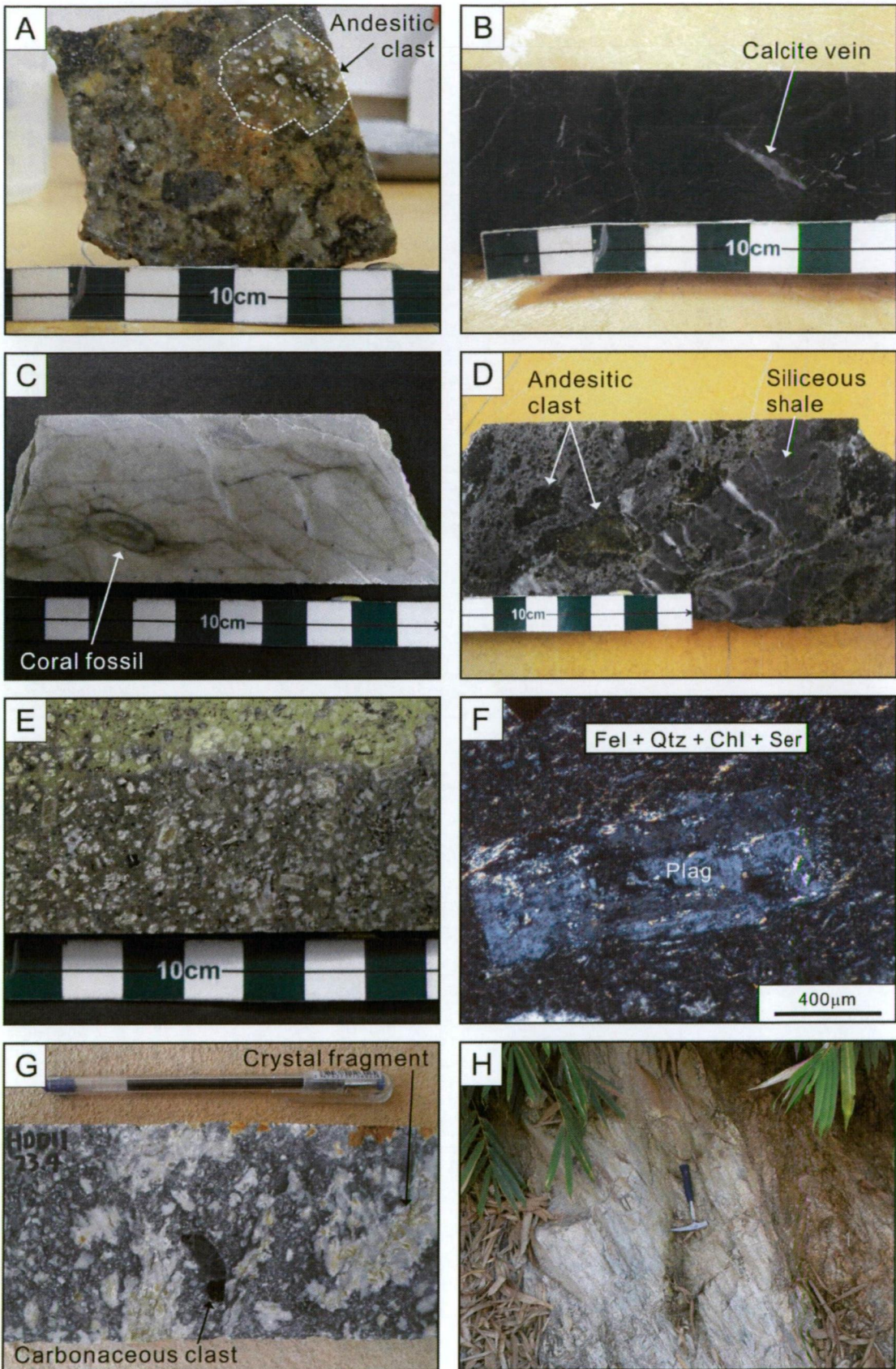
hornblende, are largely replaced by chlorite with minor fine-grained quartz clusters. The groundmass is dominantly composed of fine-grained minerals including K-feldspar, quartz, sericite, illite and chlorite, which are likely to have resulted from hydrothermal alteration. K-feldspar, quartz and chlorite are commonly present, whereas sericite and illite only occur locally. A trace amount of pyrite showing euhedral shapes is also sparsely distributed throughout the groundmass.

3.2.4. Volcano-sedimentary units at BHX

The main host sequence at the BHX deposit consists of volcano-sedimentary units including polymictic siliceous sedimentary breccia, carbonaceous shale, siliceous shale, feldspar-phyric andesite, crystal-rich volcanic breccia and tuffaceous siltstone in ascending order (Fig. 3.5). These units are generally well-layered and show a NW–SE strike with steep (probably 50°–70°) southwesterly dip throughout the deposit area. The sequence is strongly deformed and discontinuous in the deposit area due to offsets along faults. This sequence is intruded by an aphyric mafic dyke in the central part and has contact with younger red bed sedimentary units in the southeastern part of the deposit area. The lithological units at BHX are described below:

Polymictic siliceous sedimentary breccia: The polymictic siliceous sedimentary breccia locally outcrops in the northeastern part of the deposit (Fig. 3.3). In the field, the geological relationship of the breccia with other lithological units was not observed. However, this unit is interpreted to be the lowermost part of the volcano-sedimentary sequence, as interpolated from the NW–SE strike and southwesterly dip of the entire sequence throughout the deposit area. This unit is normally strongly silicified and consolidated. The least altered hand specimen sample in outcrop shows polymictic clasts with a siliceous fine-grained matrix (Fig. 3.8A). The clasts are normally angular and less than 5cm in size, and comprise altered andesitic, carbonaceous and siliceous clasts. The thickness and the distribution of this unit are poorly constrained due to limited exposure and lack of drill holes intersecting these rocks.

Carbonaceous shale: Carbonaceous shale is locally intersected in the diamond drill holes in the southern part of the deposit area. This unit has no observed contact relationship with polymictic siliceous sedimentary breccia, but shows a clear contact relationship with overlying siliceous shale in a drill core. A hand specimen sample is dark coloured, carbonaceous and very fine-grained (Fig. 3.8B) with unmineralised calcite veins in several-cm width. The thickness of this unit is estimated to be several tens of metres.



Geological setting and mineralisation characteristics of the Long Chieng Track and Ban Houayxai deposits, Lao PDR

Fig. 3.8. Representative samples of volcano-sedimentary sequence units at BHX deposit. Abbreviations: Fel=feldspar, Qtz=quartz, Chl=chlorite, Ser=sericite, Plag=plagioclase, xpl=cross polarised light.

- A) Photograph showing a hand specimen sample of polymictic siliceous sedimentary breccia including andesitic clast. Sample No. BHX-1.
- B) Photograph showing a hand specimen sample of carbonaceous shale. Sample No. HSD06@93.6m.
- C) Photograph showing a hand specimen sample of siliceous shale involving coral fossil. Sample No. HSD06@81.2m.
- D) Photograph showing a hand specimen sample of peperitic contact relationship between feldspar-phyric andesite and shale. Sample No. HDD07@290.0m.
- E) Photograph showing a hand specimen sample of feldspar-phyric andesite. Sample No. HSD01@63.8m. Note that yellow colour by staining of K-feldspar at the upper part of the sample.
- F) Photomicrograph (xpl) showing textural feature of feldspar-phyric andesite. Sample No. HSD01@63.8m.
- G) Photograph showing a hand specimen sample of crystal-rich volcanic breccia. Sample No. HDD11@73.4m.
- H) Photograph showing an outcrop of tuffaceous siltstone unit in the central area of the BHX deposit.

Siliceous shale: This unit underlies the feldspar-phyric andesite and overlies the carbonaceous shale. It is generally grayish in colour and contains occasional coral fossils (not dated) (Fig. 3.8C). This unit is locally intersected by diamond drill holes in the central and the southern part of the deposit area. It is strongly silicified and several tens of metres thick.

Feldspar-phyric andesite: This unit occurs in the central part of the volcano-sedimentary sequence in the middle section of the deposit area. The unit is strongly altered and contains mineralised and non-mineralised veins. This unit shows a peperitic contact relationship with the siliceous shale at the bottom. The contact consists of blocky clasts of this unit which are hosted in the top of the siliceous shale (Fig. 3.8D). This unit is estimated to be more than 200 m thick in the central part of the deposit area.

The least altered hand specimen of this unit shows a porphyritic texture consisting of lath-shaped feldspar phenocrysts (30–40 vol. %) with dark green coloured, fine-grained groundmass (Fig. 3.8E). The feldspar phenocrysts are on average 2–3 mm across, and may be up to 5 mm across. The phenocrysts are partly to totally replaced by alteration minerals such as sericite. Quartz and mafic minerals, commonly <1 mm in size, are also present (10–15 vol. % and 5–10 vol. % respectively), and they are evenly distributed in the sample.

In thin section, phenocrysts (50–60 vol. %) range from less than 0.5 up to 5 mm in size (1–2 mm on average). The phenocrysts are mostly composed of euhedral plagioclase (60–70 vol. %), partially replaced by patchy sericite (Fig. 3.8F). Mafic mineral phenocrysts commonly have a hexagonal shape (probably after hornblende), and are totally replaced by chlorite. The

groundmass consists of fine-grained feldspar, quartz, chlorite and sericite assemblages. Fine-grained (<50 μm in size) euhedral pyrite crystals are also sparsely and ubiquitously distributed in the groundmass.

Crystal-rich volcanic breccia: In drill core, this unit conformably overlies the feldspar-phyric andesite, and dominantly occurs in the central and northern parts of the deposit area. This unit is frequently intercalated with several cm-thick, fine-grained carbonaceous layers.

This unit commonly includes abundant crystal fragments consisting of feldspar and quartz phenocrysts and minor carbonaceous and siliceous clasts in a coarse-grained sandy matrix (Fig. 3.8G). The fragments and clasts range from mm up to >10 cm in size, with angular to sub-angular shapes. The matrix is dominantly composed of fine-grained crystal fragments of mm size.

Tuffaceous siltstone: This unit occurs at the uppermost part of the volcano-sedimentary sequence at BHX, and is locally exposed in the central deposit area. In outcrop this unit is distinctly pale-green in colour with a fine-grained matrix, and is normally unconsolidated (Fig. 3.8H). Foliation texture is strongly developed in this unit showing a generally E–W trend with a steep northerly dip.

3.2.5. Intrusive unit at BHX

Aphyric mafic dyke: This unit is locally intersected in diamond drill holes and normally has a width of several cm (up to 10 cm). The rock has an aphyric texture with a dark green, fine-grained matrix (Fig. 3.9A). The dyke appears to have been emplaced later than the Stage 1 mineralisation as this dyke cross-cuts the Stage 1 vein (Fig. 3.9A). It was probably formed during the periods of Stages 2 and 3 mineralisation veins as both the dyke and veins trend N–S with a vertical to sub-vertical westerly dip, which is similar to the Stages 2 and 3 mineralised vein geometry (see Chapter 4 in details).

In thin section, this unit displays a fine-grained aphyric texture with rare phenocrysts (< 5 vol. %). The phenocrysts are <0.5 mm in size and intensely altered to sericite (Fig. 3.9B). The groundmass is mostly composed of very fine-grained minerals which are difficult to identify even under a microscope.

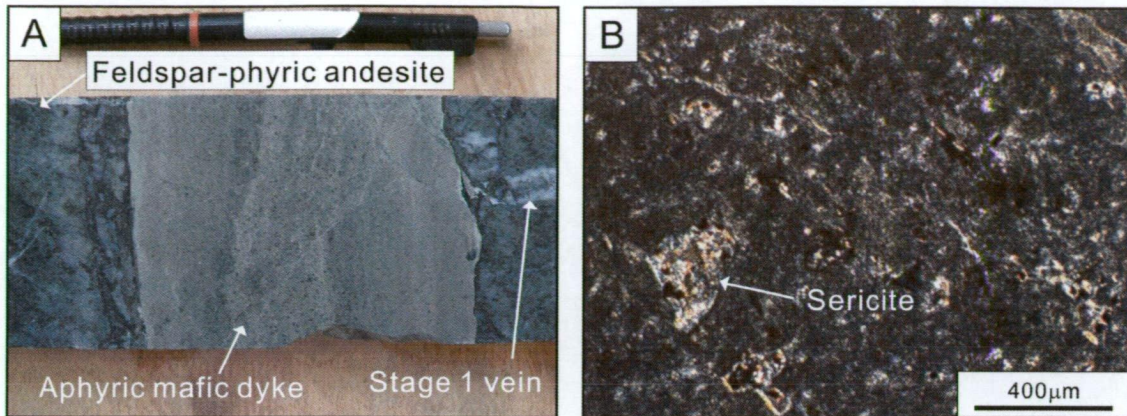


Fig. 3.9. Representative sample of aphyric mafic dyke unit at the BHX deposit. Abbreviations: xpl=cross polarised light.

- A) Photograph showing a hand specimen sample of aphyric mafic dyke, intruding feldspar-phyric andesite and cross-cutting a Stage 1 mineralised vein. Sample No. HDD13@47.5m.
- B) Photomicrograph (xpl) showing a textural feature of the aphyric mafic dyke. Sample No. HDD13@47.5m.

3.2.6. Red bed units at BHX

The red bed units at BHX consist of sedimentary breccia and sandstone units which are distributed in the southeastern part of the deposit area, where they are structurally separated from the main volcano-sedimentary sequence by a large NE–SW trending fault. The formation of these units is interpreted to be later than the volcano-sedimentary sequence, as determined by detrital zircon ages (see Chapter 3.3 in details). The thickness of these two units is poorly constrained.

Red bed sandstone: Red bed sandstone consists of maroon to red-coloured, well-sorted, fine-grained clasts (Fig. 3.10A). It commonly has many layers of tens of centimetres thick, and it mostly strikes NW–SE with a moderate (40–60°) northeasterly dip. This unit predominantly occurs in the southeastern section of the deposit. Tate (2004) suggests that this red bed sandstone at BHX is comparable to the red bed unit at the Phu Kahm in terms of its occurrence, lithology and texture.

Red bed sedimentary breccia: The red bed sedimentary breccia occurs as a well-consolidated unit and comprises angular-shaped polymictic clasts with dark green and maroon red-coloured, fine-grained matrix (Fig. 3.10B). The clasts are poorly sorted ranging from mm to cm (up to 5 cm) in size, and include carbonaceous, siliceous and sericitised rock fragments. Although no contact relationship with other units was observed, this unit is interpreted to have been overlain by the red bed sandstone unit as inferred from the dip and strike of the red bed sandstone.

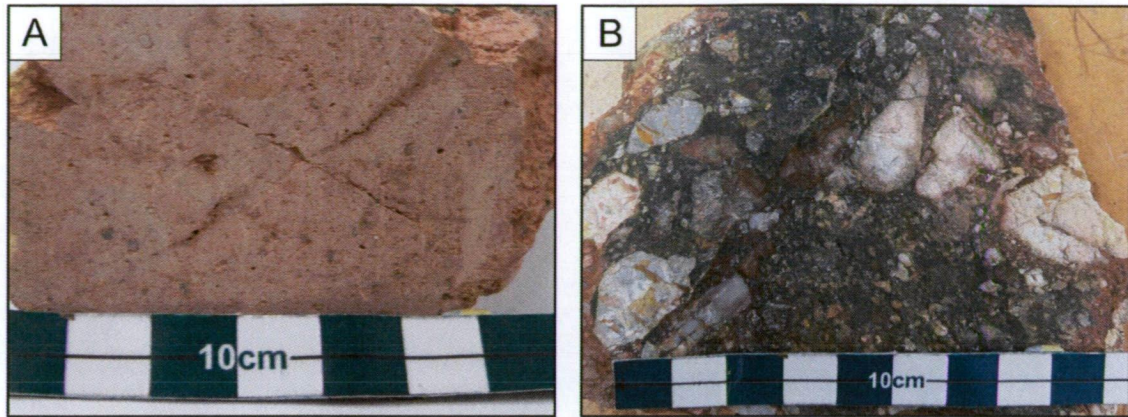


Fig. 3.10. Representative samples of red bed units at the BHX deposit.

A) Photograph showing a hand specimen sample of red bed sandstone. Sample No. BHX-2.

B) Photograph showing a hand specimen sample of red bed sedimentary breccia. Sample No. BHX-3.

3.3. Geochronology

3.3.1. Introduction

A U-Pb zircon geochronological study was conducted on the major igneous and selected sedimentary units of the LCT and BHX deposits, using Laser Ablation Inductively Coupled Plasma Mass Spectrometry (LA-ICPMS) at CODES laboratory, University of Tasmania. The study aimed to constrain the age of the main lithological units at the LCT and BHX deposits. Few geochronological studies on the deposits have been previously carried out, such as an index fossil from the limestone at LCT and a K-Ar dating on K-feldspar mineral at BHX (Table 3.1).

Table 3.1. Summary of previous geochronological data of LCT and BHX deposits, Lao PDR.

Deposit	Dated rock unit/mineral	Sample No.	Age (Ma)	Remark and Reference
LCT	Carboniferous Limestone	LSD09@69.1m	Lower Carboniferous (360–320 Ma)	An index rugose coral fossil in limestone, the lowermost unit of sedimentary sequence (Mason, 1997)
BHX	K-feldspar	HSD04@74.0m	41.9±1.8 (Eocene)	K-Ar age (Khin Zaw et al., 2007a)

3.3.2. Analytical methods

For this study, zircon crystals were separated from six lithological units including feldspar-phyric dacitic porphyry and quartz monzonite units of the LCT deposit and feldspar-phyric andesite, red bed sandstone and red bed sedimentary breccia units of the BHX deposit. Zircon crystals were

physically separated by crushing, milling and panning followed by picking out zircon crystals under the microscope. The separated zircon crystals were mounted in epoxy-resin disks, and were polished until they were exposed on the surface.

Prior to LA-ICPMS analysis, the zircon crystals were examined with a microscope and cathodoluminescence images were acquired on some samples to characterise the zircon crystals. The shape of zircon crystals offers important clues as to the origin of the crystals (Corfu et al., 2003). For example, igneous zircons tend to be euhedral with regular zoning in cathodoluminescence images. Sedimentary zircons tend to be rounded, particularly if they are much older than the formation of the sedimentary units where they are found as may have been recycled from earlier sedimentary rocks. Metamorphic zircons tend to occur as thin rounded overgrowths on older sedimentary or igneous cores. Most of the zircon crystals separated for this study are of igneous origin as shown by well-developed internal crystal-growth zoning in the crystals (Fig. 3.11A). Even the detrital zircons separated from the sedimentary units (i.e., red bed sandstone and red bed sedimentary breccia) show strong igneous features with rare rounded crystals.

Subsequently, LA-ICPMS U-Pb zircon analysis (Kosler and Sylvester, 2003) was conducted using U and Pb isotopic composition on each of the zircon crystals separated from the samples. They were ablated in a He atmosphere in a custom-made chamber at 5 Hz and 30 microns. The primary standard, the Temora standard zircons (Black et al., 2003) were analysed four times for every one hour, and additional secondary standard zircons ranging from 2.6–1063 Ma in age were analysed to check the precision and accuracy of the results. For a more detailed description of the analytical method, see Meffre et al. (2007).

3.3.3. Geochronological results

The results of this study are presented in Table 3.2, and all the data for measured individual zircon crystals are listed in Appendix II. Tera-Wasserburg U-Pb zircon concordia plots from the selected samples such as feldspar-phyric dacitic porphyry of the LCT deposit and feldspar-phyric andesite and red bed sandstone units of the BHX deposit are shown in Figs 3.11B, C and D. Some of them give near-concordant ages, whereas the others give discordant ages which are due to Pb-loss from high U crystals or due to contamination of the analyses by non radiogenic Pb (common lead). However, most of the data provide meaningful results (Figs. 3.11B, C and D).

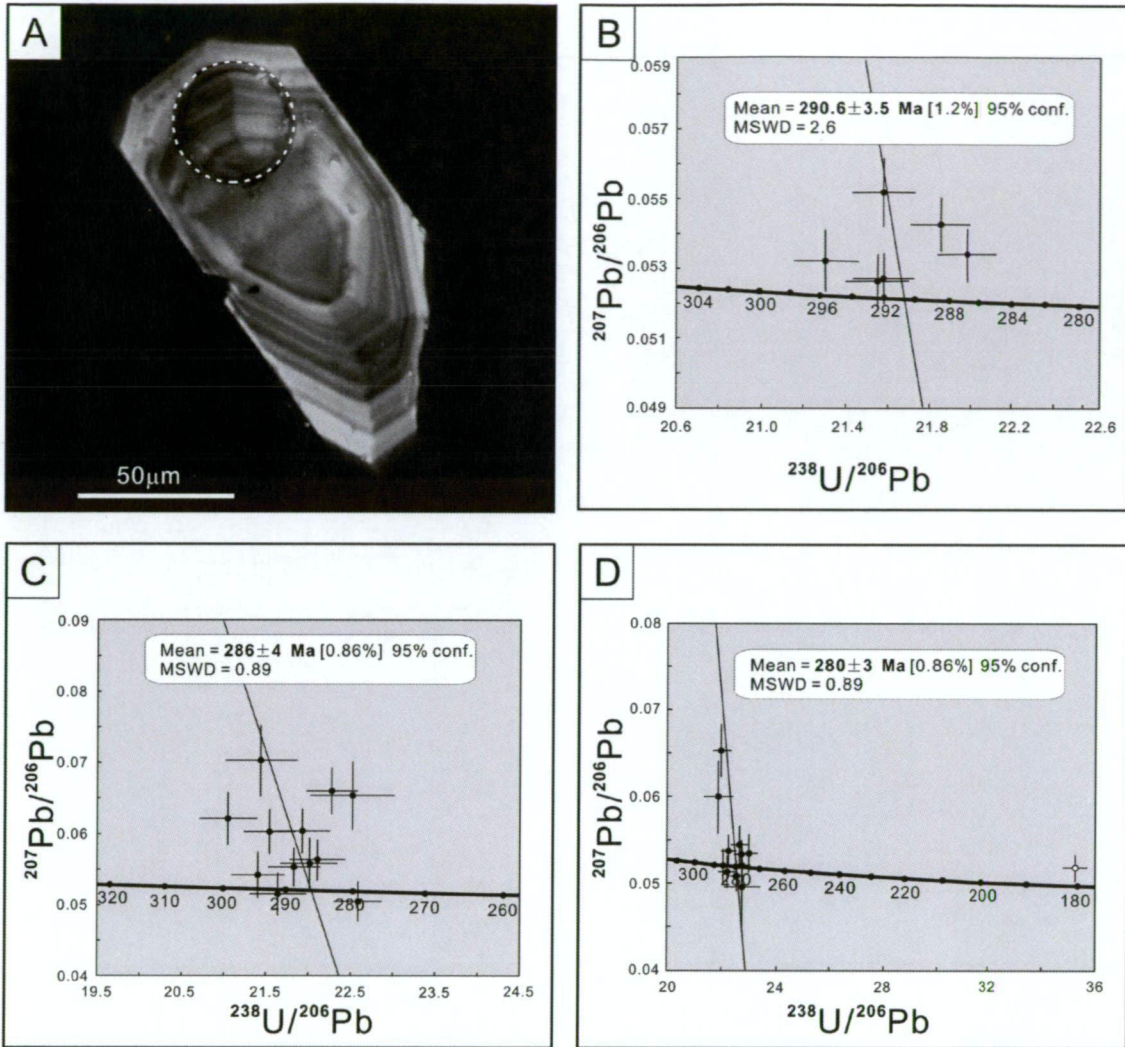


Fig. 3.11. Representatives of zircon cathodoluminescence image and zircon concordia diagrams of the selected rock units from the LCT and BHX deposits.

- A) Cathodoluminescence image showing a zircon grain with ablated hole. Sample No. BHX-2.
 B) U-Pb zircon concordia plot for feldspar-phyric dacitic porphyry of the LCT deposit. Sample No. LSD09.
 C) U-Pb zircon concordia plot for feldspar-phyric andesite of the BHX deposit. Sample No. HSD01@63.8m.
 D) U-Pb zircon concordia plot for red bed sandstone of the BHX deposit. Sample No. BHX-2.

3.3.4. Geological interpretation

The geochronological results of LCT and BHX, together with available data from the nearby Phu Kahm deposit, constrain the timing of geological events including magmatism and sedimentation at the Phu Bia Contract Area (PBCA) in the south. The igneous and detrital zircon ages of these deposits together with available index rugose coral fossil age data are summarised in Fig. 3.12. On this basis, the magmatism in the area is constrained to the Latest Carboniferous to Early

Permian, and the formation of sedimentary depositions can also be roughly estimated (Fig. 3.12). These chronological data are further discussed in the discussion section.

Table 3.2. LA-ICPMS U-Pb zircon ages of major igneous and sedimentary units from the LCT and BHX deposits, Lao PDR.

Deposit	Rock Type	Sample No.	Age (Ma)	Remark
LCT	Quartz monzonite	ACH066	292±3	
LCT	Feldspar-phyric dacitic porphyry	LSD09	290.6±3.5	
BHX	Feldspar-phyric andesite	HSD01@63.8m	286±4	
BHX	Crystal-rich volcanic breccia	HSD04@51.9m	283±4	Detrital, youngest age is 279±4 Ma
BHX	Red bed sedimentary breccia	HSD07@96.6m	260±7	Detrital, youngest age is 257±6 Ma
BHX	Red bed sandstone	BHX-2	280±3	Detrital, youngest age is 274±4 Ma

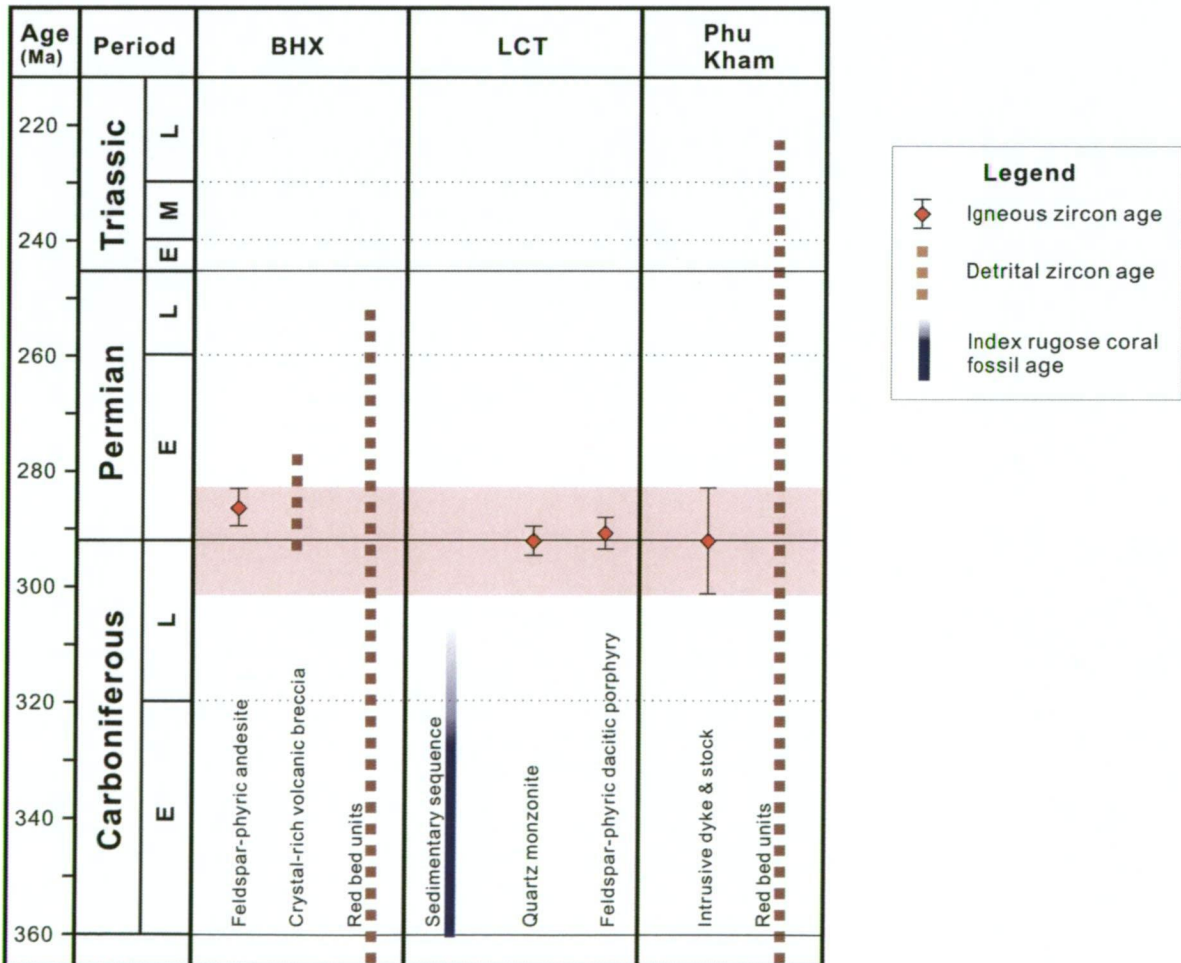


Fig. 3.12. Summary of geochronological data of the BHX, LCT and Phu Kham deposits (Phu Kham data after Khin Zaw et al., 2007a). Note that magmatism is well-constrained into Latest-Carboniferous to Early-Permian (pink coloured). E=Early, M=Middle, L=Late.

3.4. Whole rock geochemistry

3.4.1. Introduction

Whole rock geochemical compositions of igneous rocks from the LCT and BHX deposits were analysed to determine the geochemical signature of the rock units. Prior to this study, no geochemical study has been carried out at the both deposits, although some detailed geochemical studies on intrusive rocks at the Phu Kham deposit have been conducted by Kamvong (2006, 2007a, b). Geochemical data of 31 rock samples from the Phu Kham deposit reported by Kamvong (2006), are incorporated in this study and discussed together in the following section.

3.4.2. Analytical methods

A total of 24 samples, including 14 and 10 samples from the LCT and BHX deposits respectively, were analysed for major (Si, Ti, Al, Fe, Mn, Mg, Ca, Na, K and P) and trace (Rb, Sr, Ba, Sc, V, Cr, Ni, Zn, Y, Zr, Nb and Pb) elements using the X-ray Fluorescence (XRF) at CODES, the University of Tasmania, with the help of Phil Robinson. The detailed analytical technique is outlined by Norrish and Chappell (1977) and Norman et al. (2003). Rare earth elements (REE: La, Ce, Pr, Nd, Sm, Eu, Gd, Tb, Dy, Ho, Er, Tm, Yb and Lu) of 12 of these samples were also analysed using the solution ICP-MS technique at the University of Tasmania. The detailed analytical method for the solution ICP-MS technique is described by Yu et al. (2000). To obtain reliable results, samples for the analyses were carefully selected from the least altered hand specimen samples. They were initially crushed using a jaw crusher to make rock fragments several centimetres in size and were subsequently ground using a tungsten carbide rig mill to produce rock powder.

3.4.3. Geochemical results

The whole rock geochemical data obtained in this study are listed in Tables 3.3 and 3.4 for LCT and BHX, respectively.

3.4.3.1. Major elements

Bivariate diagrams for selected major elements vs SiO_2 are shown in Fig. 3.13. There are linear trends of increasing SiO_2 with decreasing TiO_2 , Fe_2O_3 , Al_2O_3 , MgO and P_2O_5 , suggesting igneous fractional crystallisation processes. However, CaO , K_2O and Na_2O show a poor correlation with SiO_2 , and this may be explained by element mobility during hydrothermal alteration. The major elements of the Phu Kham granitoids also show consistent trends similar to the LCT and BHX data.

Table 3.3. Major (wt. %), trace (ppm) and rare earth (ppm) elements geochemistry of the igneous rocks from the LCT deposit. Abbreviation: QMN=quartz monzonite.

Deposit	LCT	LCT	LCT	LCT	LCT	LCT	LCT
Sample No.	227272mE	LSD08@ 76.9m	LSD08@ 83.7m	LSD15@ 97.3m	LSD16@ 99.2m	LSD16@ 101.0m	LSD16@ 107.1m
Rock Type	QMN	QMN	QMN	QMN	QMN	QMN	QMN
SiO ₂	66.24	67.33	65.29	70.26	65.33	65.42	66.06
TiO ₂	0.71	0.26	0.22	0.17	0.3	0.27	0.25
Al ₂ O ₃	17.61	15.64	13.30	15.05	16.08	15.60	15.72
Fe ₂ O ₃	2.85	3.35	6.01	2.65	3.75	3.43	3.37
MnO	0.02	0.05	0.04	0.05	0.03	0.03	0.04
MgO	1.99	0.83	0.55	0.81	1.07	0.82	0.89
CaO	0.46	1.38	1.64	0.72	2.04	2.34	1.47
Na ₂ O	3.59	6.00	6.44	7.70	4.56	4.57	4.61
K ₂ O	2.27	1.67	0.79	0.35	5.22	5.08	5.47
P ₂ O ₅	0.18	0.10	0.10	0.06	0.12	0.10	0.11
BaO	0.02	0.02	0.01				
PbO	0.00	0.00	0.01				
ZnO	0.00	0.00	0.00				
LOI	2.88	3.21	4.99	1.74	1.26	2.08	1.67
Total	98.83	99.85	99.41	99.56	99.75	99.74	99.67
S	0.4	1.90	4.64	0.99	<0.01	0.01	0.01
Y	15	24	27	28	24	25	23
U	7	15	9	16	13	15	15
Rb	129	76	34	12	175	160	181
Th	30	50	39	54	46	50	47
Pb	10	13	47	10	15	16	13
As	51	1236	80	20	7	10	5
Bi	<2	2	5	<2	<2	<2	<2
Zn	26	31	23	38	23	37	35
Cu	6	22	355	27	13	6	25
Ni	2	3	3	1	5	4	4
Sn	10	4	3				
Nb	24	20	12	22	18	19	19
Zr	277	329	247	317	291	316	308
Sr	116	139	148	165	446	381	242
Cr	1	3	3	75	64	54	61
Ba	220	155	79	41	632	568	609
Sc	21	6	4	5	8	7	6
V	134	39	32	17	49	36	39
La	<2	56	34	45	53	73	129
Ce	7	92	66	92	88	118	162
Nd	4	36	25	35	33	38	43
La	3	60.6	36.9				
Ce	7.40	113.8	69.9				
Pr	1.03	12.12	7.82				
Nd	4.66	42.3	28.3				
Sm	1.20	7.14	5.30				
Eu	0.19	0.85	0.59				
Gd	1.52	5.31	4.69				
Tb	0.30	0.80	0.82				
Dy	2.13	4.65	4.98				
Ho	0.49	0.94	0.99				
Er	1.55	2.79	3.00				
Tm	0.25	0.43	0.46				
Yb	1.77	2.91	3.00				
Lu	0.30	0.45	0.45				

Table 3.3. (Continued.). Major (wt. %), trace (ppm) and rare earth (ppm) elements geochemistry of the igneous rocks of the LCT deposit. Abbreviation: FDP=feldspar-phyrlic dacitic porphyry.

Deposit	LCT	LCT	LCT	LCT	LCT	LCT	LCT
Sample No.	LSD04@ 87.2m	LDD03A@ 65.1m	LDD81@ 81.5m	LDD81@ 67.7m	LDD81@ 58.5m	LRD67@ 64.0m	LSD09@ 50.0m
Rock Type	FDP	FDP	FDP	FDP	FDP	FDP	FDP
SiO ₂	68.82	71.50	75.92	75.48	72.57	74.17	70.31
TiO ₂	0.18	0.17	0.16	0.16	0.17	0.17	0.28
Al ₂ O ₃	14.57	13.00	12.52	12.51	14.32	12.84	12.81
Fe ₂ O ₃	2.23	1.98	0.23	0.59	0.42	1.19	4.08
MnO	0.02	0.01	<0.01	<0.01	<0.01	0.01	0.04
MgO	0.39	0.14	0.15	0.14	0.19	0.24	0.85
CaO	0.06	<0.01	<0.01	<0.01	<0.01	<0.01	0.39
Na ₂ O	0.17	0.08	0.15	0.16	0.17	0.22	6.15
K ₂ O	11.47	9.72	9.87	10.1	10.98	10.18	0.55
P ₂ O ₅	0.08	0.05	0.07	0.06	0.07	0.05	0.09
BaO	0.38	0.45	0.32	0.32	0.37	0.33	
PbO	0.02	0.38	0.09	0.08	0.10	0.10	
ZnO	0.01	0.18	0.00	0.00	0.00	0.01	
LOI	1.36	1.87	0.61	0.61	0.85	0.94	
Total	99.77	99.50	100.09	100.20	100.20	100.46	99.54
S	1.08	1.34	0.01	<0.01	<0.01	0.11	2.15
Y	12	8	10	9	10	7	<1.5
U	3	3	4	4	4	4	18
Rb	260	219	215	220	235	232	106
Th	13	16	12	13	14	13	102
Pb	192	3500	850	696	928	954	5
As	21	177	22	17	17	309	74
Bi	<2	<2	<2	<2	<2	<2	5
Zn	93	1440	17	22	19	115	66
Cu	12	96	6	8	8	7	30
Ni	3	2	2	3	2	2	53
Sn	<2	<2	<2	<2	<2	<2	18
Nb	6	7	6	6	6	6	8
Zr	137	139	126	127	145	136	6
Sr	61	41	41	47	54	64	24
Cr	1	<1	<1	<1	<1	<1	24
Ba	3304	3907	3020	3032	3415	2833	24
Sc	2	<2	<2	2	2	1	23
V	46	16	11	12	16	17	<2
La	19	19	20	23	23	18	60
Ce	38	Pb interferes	39	42	46	38	29
Nd	11	16	13	14	15	12	4
La			20.1		23.0	19.1	
Ce			35.0		40.3	32.9	
Pr			3.57		4.04	3.32	
Nd			12.2		13.5	11.2	
Sm			1.94		2.12	1.57	
Eu			0.70		0.65	0.50	
Gd			1.52		1.66	1.21	
Tb			0.22		0.24	0.18	
Dy			1.37		1.49	1.06	
Ho			0.30		0.31	0.22	
Er			0.98		1.04	0.74	
Tm			0.16		0.17	0.12	
Yb			1.18		1.22	0.93	
Lu			0.20		0.21	0.16	

Table 3.4. Major (wt. %), trace (ppm) and rare earth (ppm) elements geochemistry of the igneous rocks from the BHX deposit. Abbreviation: FPA=feldspar-phyric andesite.

Deposit	BHX	BHX	BHX	BHX	BHX	BHX	BHX
Sample No.	HSD01@ 60.7m	HSD01@ 69.7m	HSD01@ 84.6m	HDD06@ 285.8m	HDD08@ 280.7m	HDD09@ 249.4m	HDD13@ 110.2m
Rock Type	FPA	FPA	FPA	FPA	FPA	FPA	FPA
SiO ₂	59.37	57.65		57.71	58.40	58.92	57.64
TiO ₂	0.67	0.69		0.63	0.51	0.71	0.68
Al ₂ O ₃	18.29	17.98		17.52	16.01	18.06	17.66
Fe ₂ O ₃	7.7	7.61		7.29	5.51	6.25	7.47
MnO	0.1	0.24		0.15	0.34	0.09	0.13
MgO	2.43	2.63		2.93	2.58	2.19	2.93
CaO	0.33	1.99		0.9	4.03	0.62	1.22
Na ₂ O	1.78	1.44		1.74	1.22	0.20	1.51
K ₂ O	5	4.53		6.87	5.27	8.64	6.32
P ₂ O ₅	0.22	0.22		0.21	0.16	0.21	0.22
BaO	0.08	0.06					
PbO	0.00	0.00					
ZnO	0.02	0.02					
LOI	3.51	4.98		3.95	5.77	3.96	3.72
Total	99.50	100.04		99.90	99.79	99.85	99.51
S	0.5	0.07		0.83	0.07	1.48	0.42
Y	22	22		20	20	19	20
U	3	2		3	3	4	2
Rb	231	236		307	252	351	265
Th	9	9		10	11	10	8
Pb	36	4		7	11	33	11
As	40	5		43	6	47	17
Bi	<2	<2		<2	<2	<2	<2
Zn	185	170		98	59	84	100
Cu	19	30		34	22	21	22
Ni	4	5		6	5	6	4
Sn	3	<2					
Nb	6	5		6	6	8	6
Zr	143	136		138	127	151	136
Sr	48	153		116	199	103	147
Cr	7	6		26	34	33	26
Ba	687	528		642	496	722	26
Sc	20	21		20	16	24	20
V	156	158		135	121	171	172
La	28	20		20	22	25	20
Ce	54	44		37	39	46	40
Nd	24	17		19	17	21	21
La	26.0	19.1	22.9				
Ce	51.1	38.9	46.0				
Pr	6.06	4.65	5.44				
Nd	24.0	18.7	22.0				
Sm	4.75	4.03	4.60				
Eu	1.17	1.02	1.20				
Gd	4.33	3.92	4.23				
Tb	0.67	0.64	0.63				
Dy	4.07	3.99	3.70				
Ho	0.82	0.82	0.73				
Er	2.45	2.48	2.17				
Tm	0.38	0.37	0.32				
Yb	2.49	2.45	2.11				
Lu	0.38	0.37	0.33				

Table 3.4. (Continued). Major (wt. %), trace (ppm) and rare earth (ppm) elements geochemistry of the igneous rocks from the BHX deposit. Abbreviations: FPA=feldspar-phyric andesite.

Deposit	BHX	BHX	BHX
Sample No.	HSD05@ 68.2m	HSD08@ 97.5m	HSD09@ 56.2m
Rock Type	FPA	FPA	FPA
SiO ₂	56.38	48.10	63.57
TiO ₂	0.62	0.79	0.47
Al ₂ O ₃	16.59	18.55	15.86
Fe ₂ O ₃	7.14	11.80	3.6
MnO	0.14	0.29	0.16
MgO	3.37	3.38	2.07
CaO	2.48	3.39	2.1
Na ₂ O	1.55	0.19	4.81
K ₂ O	5.39	4.74	3.75
P ₂ O ₅	0.2	0.25	0.15
BaO	0.06	0.06	0.10
PbO	0.00	0.00	0.00
ZnO	0.01	0.04	0.01
LOI	5.37	7.84	2.85
Total	99.31	99.43	99.50
S	0.68	2.84	<0.01
Y	18	23	20
U	2	2	5
Rb	246	227	132
Th	8	6	17
Pb	7	40	5
As	21	151	1
Bi	<2	<2	<2
Zn	104	310	67
Cu	32	88	16
Ni	5	13	4
Sn	<2	<2	3
Nb	4	4	8
Zr	128	117	194
Sr	143	251	423
Cr	5	30	5
Ba	556	541	901
Sc	20	35	14
V	148	264	75
La	20	23	31
Ce	37	41	59
Nd	15	22	25
La		23.2	
Ce		47.1	
Pr		5.79	
Nd		23.8	
Sm		5.20	
Eu		1.37	
Gd		5.04	
Tb		0.77	
Dy		4.62	
Ho		0.89	
Er		2.62	
Tm		0.37	
Yb		2.45	
Lu		0.38	

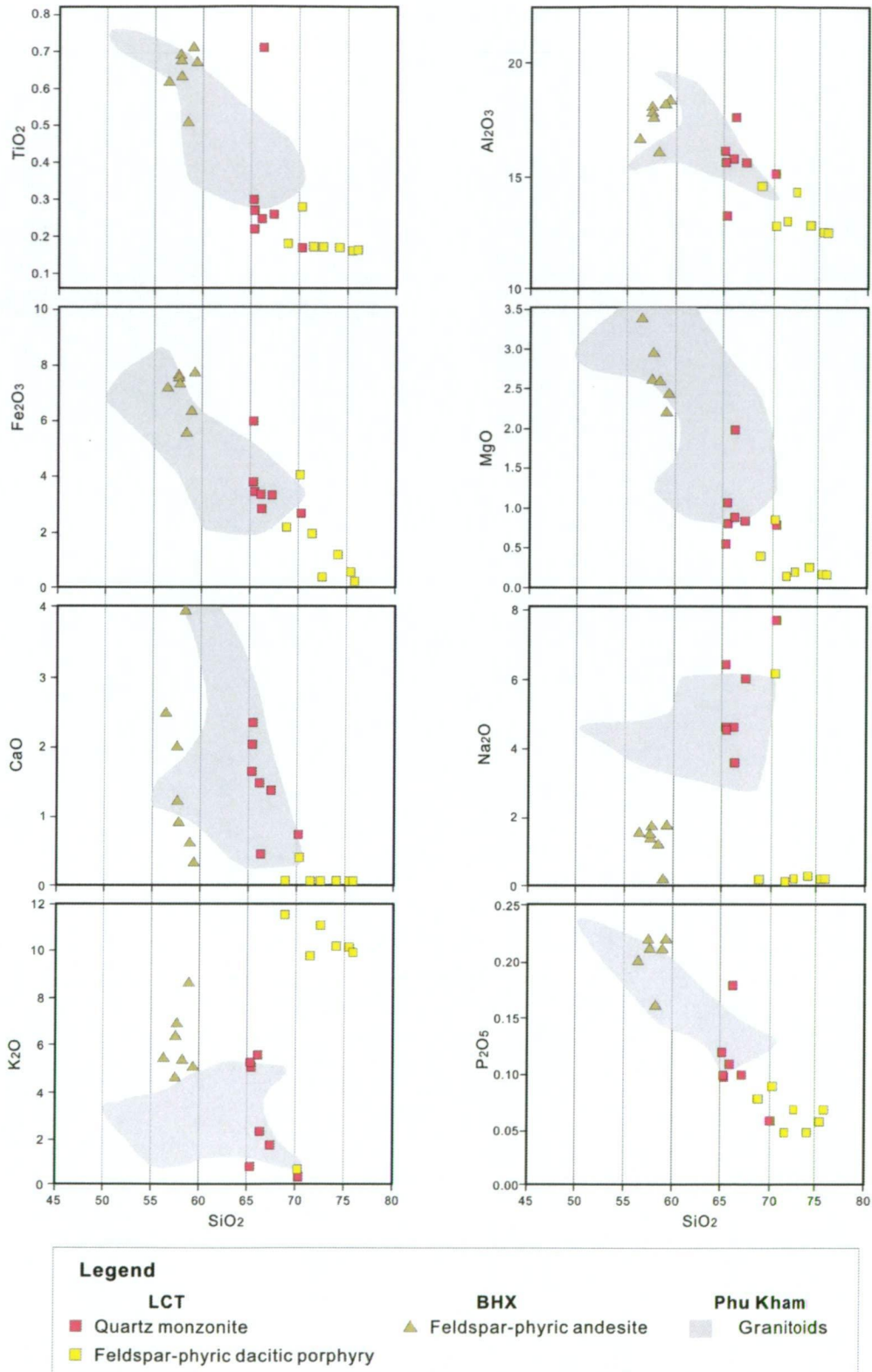


Fig. 3.13. Major element (wt. %) vs SiO₂ (wt. %) bivariate diagrams for major igneous units of the LCT and BHX deposits, with incorporated data of Phu Kham granitoids (grey coloured area) from Kamvong (2006).

3.4.3.2. Trace elements

Bivariate diagrams for selected trace elements vs SiO₂ are shown in Fig. 3.14. The data show linear trends of increasing SiO₂ with decreasing V and Sc, which may indicate the igneous fractional crystallisation processes. The Phu Kham data also display similar trends in V and Sc elements. Importantly, high field strength elements (HFSE) of quartz monzonite at LCT such as Zr, Nb and Y are consistently enriched. This could reflect the removal of HFSE phase through the crystallisation of sphene and zircon, as indicated by Hutton (1950) that Nb, La and Y are significantly contained in sphene.

3.4.3.3. REE

Chondrite-normalised REE patterns of major igneous units at the LCT and BHX deposits including quartz monzonite, feldspar-phyric dacitic porphyry and feldspar-phyric andesite, are illustrated in Figs. 3.15A, B and C, respectively. Normalisation values from Sun and McDonough (1989) were used. The REE patterns of the studied rocks are generally characterised by enrichment in light rare earth elements (LREE) and depletion in heavy rare earth elements (HREE) which are normally regarded as a characteristic of subduction zone magmatism (Wilson, 1989). This steeply dipping trend from LREE to HREE is also recognised in the Phu Kham REE patterns. The REE patterns of quartz monzonite are highly fractionated as shown in the flat to steep dipping patterns with distinctive negative Eu anomaly ($La_N/Yb_N=1.2-13.8$), although this signature is not detected in the Phu Kham granitoid REE patterns (Fig. 3.15A). The distinct negative Eu anomaly is normally related to the fractional crystallisation processes of feldspar and indicates that this was formed in the later stages of magma evolution (e.g., Rollinson, 1993).

The REE patterns of the feldspar-phyric dacitic porphyry at LCT and the feldspar-phyric andesite at BHX show enriched LREE and are flat in Middle REE (MREE) to HREE, with moderate dips from LREE to HREE, represented by $La_N/Yb_N=11.3-13.7$ and $La_N/Yb_N=5.1-7.1$, respectively (Figs. 3.15B and C). There is a negligible Eu anomaly in the REE patterns of the two units. These characteristics of REE patterns are typical of calc-alkaline to high-K alkaline basaltic rocks in the island-arc environment (Wilson, 1989). Although the feldspar-phyric rocks show similar geochemical characteristics at both the LCT and BHX deposits, they differ slightly in detail with the LCT rocks being much more evolved but much more depleted in middle REE and Y. This could be a result of extensive fractionation of REE-rich minerals in the LCT magmas (hornblende and apatite) or it could be an original characteristic of the magmatic source related to retention of

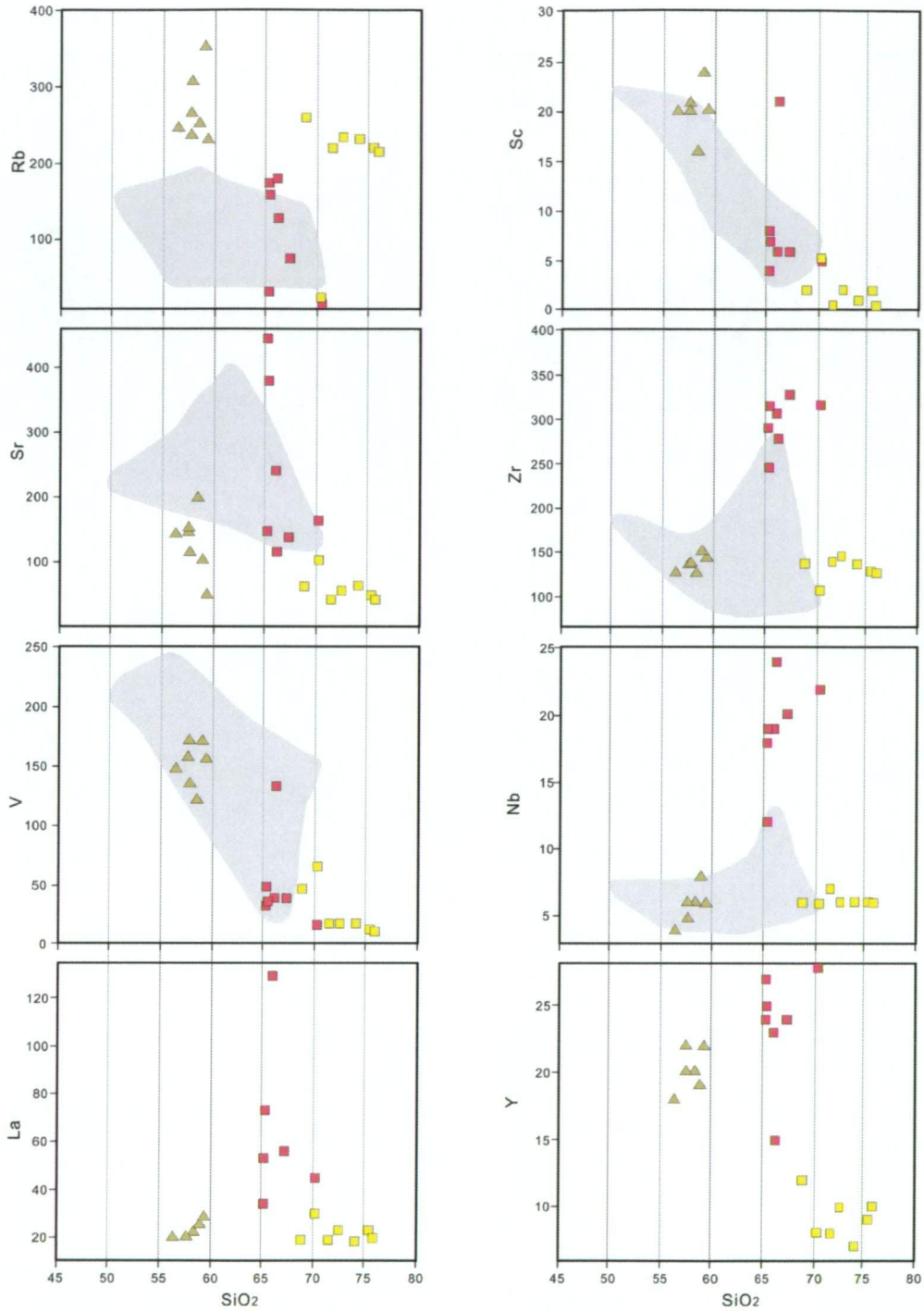


Fig. 3.14. Trace element (ppm) vs SiO₂ (wt. %) bivariate diagrams for major igneous units of the LCT and BHX deposits, with incorporated data of Phu Kham granitoids (grey coloured area) from Kamvong (2006) except La and Y elements. Refer to Fig. 3. 13 for legend.

heavy and middle REE during partial melting. Similar features in less evolved rocks have been documented as an adakitic component in the nearby Phu Kham granitoids (Kamvong, 2007a, b).

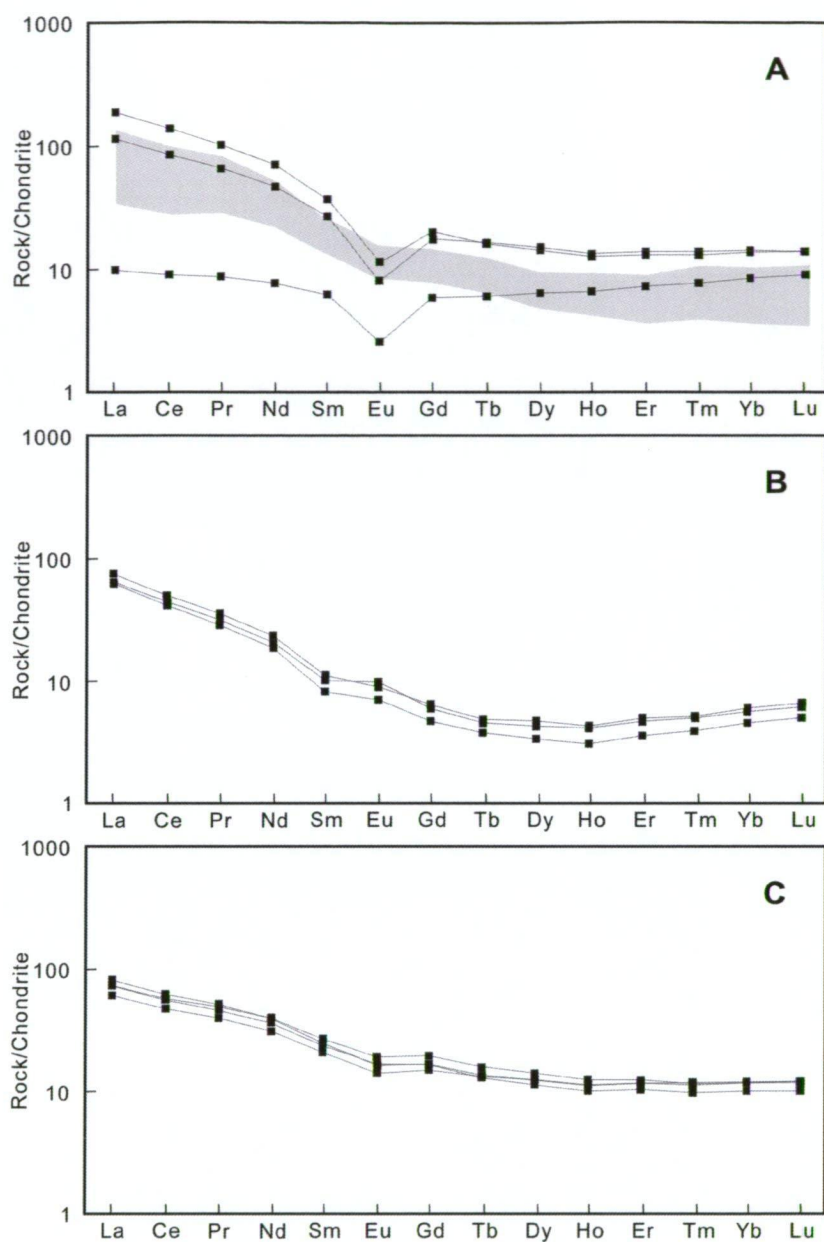


Fig. 3.15. Chondrite-normalised REE patterns of major igneous rock units of the LCT and BHX deposits.
 A) REE patterns of LCT quartz monzonite with Phu Kham granitoids ranges (grey coloured area) from Kamvong (2006).
 B) REE patterns of LCT feldspar-phyric dacitic porphyry.
 C) REE patterns of BHX feldspar-phyric andesite.

3.4.3.4. *Geochemical classification*

Whole rock chemical composition of the major igneous rock units at LCT and BHX were plotted on tectonic discrimination diagrams to investigate the likely tectonic setting of magmatism in the region. On an AFM ternary diagram by Irvine and Bargar (1971; Fig. 3.16A), all the samples from the LCT and BHX deposits as well as the Phu Kham granitoids data are classified into calc-alkaline series (except one LCT quartz monzonite). The LCT igneous rock suites have very high alkali contents, probably related to alteration. Discrimination diagrams using less mobile elements such as the Nb/Y vs Zr/TiO₂ of Winchester and Floyd (1977; Fig. 3.16B) and the Zr/TiO₂ vs SiO₂ of Maniar and Piccoli (1989; Fig. 3.16C), illustrate that the LCT igneous suites are scattered mostly in the rhyolite and rhyodacite/dacite fields, whereas the BHX igneous samples plot within the andesite field. These geochemical classifications are mostly comparable to the result of petrography using hand specimen and thin section samples as described in Chapter 3.2.

On the Ti, Zr and Y diagrams of Pearce and Cann (1973; Fig. 3.17A) and Pearce and Gale (1977) (Fig. 3.17B), the feldspar-phyric andesite samples of BHX are plotted within the calc-alkaline and plate margin basalt fields, respectively. On the discrimination diagram by Pearce et al. (1984), the quartz monzonite from LCT and the Phu Kham granitoids plot in the volcanic-arc field, and the feldspar-phyric dacitic porphyry samples are plotted in the syn-collisional field (Fig 3.17C).

3.5. Discussion and Summary

3.5.1. Discussion

Based on the obtained field, chemical and chronological data from the LCT and BHX deposits, the tectonic history of the area will be discussed to assess whether the magmatism in the Phu Bia Contract Area (PBCA) was part of an arc stretching southwards into the Loei Fold Belt (LFB) of Thailand or southeastwards into the Truongson Fold Belt (TFB) of southern Lao PDR and central Vietnam. The sedimentary history of the area will also be discussed.

Is the magmatism part of the Loei Fold Belt or Truongson Fold Belt?

The PBCA is interpreted to have occurred at the confluence of the LFB and TFB (e.g., Tate, 2005). A previous study has shown that the main episode of magmatism along the LFB is the Late Permian to Latest Triassic (245–200 Ma) (Khin Zaw et al., 2007a). This contrasts with the Late Carboniferous to Early Permian age (310–280 Ma) of magmatism in the PBCA reported in this study and in previous studies (Kamvong, 2006, 2007a, b). The age for the PBCA is very

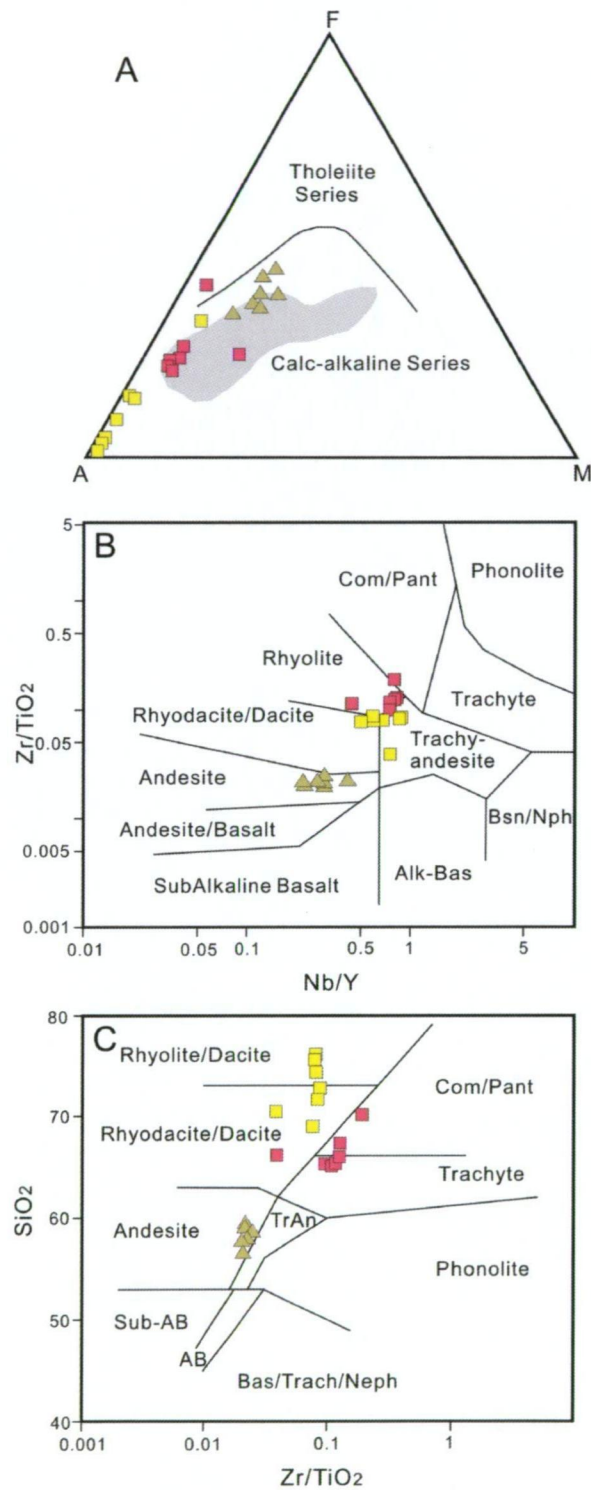


Fig. 3.16. Geochemical discrimination diagrams for the igneous units of the LCT and BHX deposits. Refer to Fig. 3.13 for legend.

- A) AFM ternary diagram (after Irvine and Bargar, 1971), with incorporated data of the Phu Kham granitoids (grey coloured area) from Kamvong (2006). A=Na₂O+K₂O, F=total FeO, M=MgO.
 B) Nb/Y vs Zr/TiO₂ classification diagram (after Winchester and Floyd, 1977).
 C) Zr/TiO₂ vs SiO₂ classification diagram (after Maniar and Piccoli, 1989).

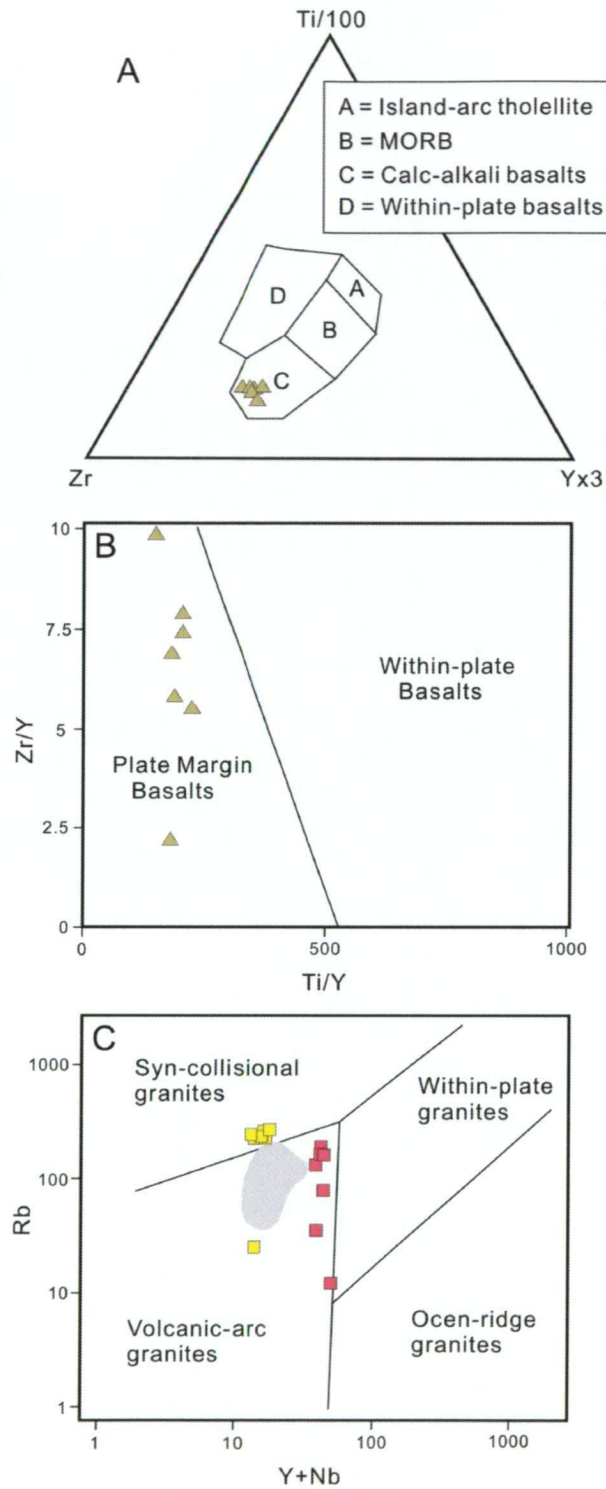


Fig. 3.17. Tectonic discrimination diagrams for igneous units of the LCT and BHX deposits. Refer to Fig. 3.13 for legend.

- A) Ti-Zr-Y discrimination diagram for basaltic rocks (after Pearce and Cann, 1973).
- B) Ti/Y vs Zr/Y discrimination diagram for basaltic rocks (after Pearce and Gale, 1977).
- C) Y+Nb vs Rb discrimination diagram for felsic rocks (after Pearce et al., 1984), with incorporated data of the Phu Kham granitoids (grey coloured area) from Kamvong (2006).

close to the age of magmatic rocks in the Sepon Mineral District of the TFB (approximately 300 Ma) (Cromie et al., 2007), and slightly older than the ages of Early Permian (270–260 Ma) high P/T metamorphic rocks occurring along the Song Ma Suture in Vietnam (Nakano et al., 2004; Osanai et al., 2004, 2007). It is therefore likely that the magmatism of the PBCA is a part of the TFB, as also suggested by Khin Zaw et al. (2007a).

Sedimentary history in PBCA South

The oldest rocks in the region are Silurian felsic volcanics, granitoids, volcanoclastic rocks and chert which outcrop in the Loei area (e.g., Intasopa, 1993). These rocks are probably present at depth beneath the LCT and BHX deposit area, and outcrop 4 km southeast of the LCT deposit (immediately west of Phu Kham) (Khin Zaw et al., 2007a). Based on comparisons with rocks further southwest between Vang Vieng and Loei, it is likely that the Silurian basement in the area is overlain by a thick Early Carboniferous sequence of marine quartz-rich sandstone and siltstone capped by Carboniferous limestone (Fountaine and Workman, 1978; Hutchison, 1989; Khin Zaw et al., 2007a).

The stratigraphy at LCT outlined as part of this study shows that the Early Carboniferous limestone is overlain by a marine turbiditic volcanoclastic rock sequence which coarsens upwards from fine-grained siltstone-dominated turbidites to coarse volcanoclastic breccias. The exposed rocks at the BHX and Phu Kham deposits only preserve the Early Permian part of the sequence. The Late Permian and Triassic volcanic and volcanoclastic rocks which characterise the LFB appear to be missing in this area. Previous studies on the metamorphic rocks of Vietnam suggest that the Late Permian and Early Triassic may have been a period of uplift and metamorphism in the area (e.g., Owada et al., 2007). In the PBCA South, the latest thick, preserved unit is likely to be the basal part of the Khorat Group red beds. The Khorat Group is mostly of Mesozoic age and was deposited throughout Thailand and central and southern Lao PDR (e.g., Bunopas, 1983). The detrital zircon geochronology presented in this study suggests that they were formed later than Late Permian and Late Triassic in the BHX and Phu Kham areas respectively.

3.5.2. Summary

The geology of the LCT and BHX deposits, and the interpreted geology of the PBCA South area are summarised below:

LCT

The geology of the LCT deposit consists of an Early Carboniferous sedimentary sequence intruded by Early Permian porphyritic rocks including quartz monzonite, quartz monzodiorite and feldspar-phyric dacitic porphyry. The igneous units at LCT are geochemically classified as calc-alkaline series, resulting from a syn-collisional to volcanic-arc setting.

BHX

The BHX deposit is hosted in a thick Early Permian volcano-sedimentary sequence which includes a massive calc-alkaline andesite formed at the plate-margin in tectonic environment. The sequence is locally intruded by an aphyric mafic dyke and has a faulted contact with younger red bed sedimentary rocks in the southeastern part of the deposit area.

PBCA South

The geology of the PBCA South area is dominantly composed of an Early Carboniferous to Early Permian volcano-sedimentary sequence. The sequence is intruded by Late Carboniferous to Early Permian porphyritic rocks as identified at LCT, whereas the Early Permian sequence is intercalated with andesite at BHX. The formation of the igneous rock units at the PBCA South is chronologically constrained to approximately 30 Ma, from Latest Carboniferous to Early Permian (310–280 Ma), with formation in a volcanic-arc environment. The geological characteristics of the magmatism during the Early Permian could be explained by the subduction of an ocean basin attached to the South China Terrane beneath the Indochina Terrane. The formation of red bed sedimentary rocks, extensively distributed in the PBCA South area, was probably formed in the Late Triassic onwards.

CHAPTER 4 MINERALISATION CHARACTERISTICS

4.1. Introduction

This chapter documents the mineralisation characteristics of the LCT and BHX deposits, focusing on the nature of mineralisation including vein texture, mineralogy and the paragenetic relationships. Additionally, the chemical-compositional variations of the electrum and the sphalerite in the syn-mineralisation stages were analysed, and the obtained data are compiled and discussed in the last section.

4.2. Analytical methods

4.2.1. Mineralisation and ore mineral description

The mineralisation characteristics of the LCT and BHX deposits are initially documented using the data obtained during field work including drill hole logging and surface mapping. Additional microscopic examination of the samples and the Portable Infrared Mineral Analyser (PIMA) and Scanning Electron Microscope (SEM) examinations were followed up to help in identifying unknown alteration minerals in hand specimens. The K-feldspar staining technique was also used to detect the occurrence of adularia. To back up the alteration mineral assemblages identified using the above mentioned techniques, X-ray diffraction (XRD) analyses on selected samples of typical alteration facies were undertaken at Mineral Resources of Tasmania with the help of Ralph Bottrill. The detailed XRD results are listed in Appendix III.

4.2.2. Gold fineness and FeS variation in sphalerite

For these studies, the CAMECA SX-50 microprobe equipment at Central Science Laboratory (CSL), University of Tasmania was used for the measurement. A total of five grains (spots) of three samples from LCT and twenty-two grains (spots) of ten samples from BHX were analysed to measure the gold fineness of electrum and calculated using a formula of $(Au/(Au + Ag) \times 1000)$. Some known/unknown gold- and silver-bearing minerals were also identified during this work.

A total of forty-two and thirty-five grains (spots) of seven samples from LCT and fourteen samples from BHX respectively were analysed using the microprobe, to determine the FeS

content of sphalerite. Zn, S and Fe elements were mainly focused for this study and were measured from all of the samples.

4.3. Mineralisation

In the following sections, mineralogy, texture, paragenesis and mineralisation characteristics of the LCT and BHX deposits are described in details.

4.3.1. LCT observation, drill hole logging, macroscopic and microscopic investigation

Tate (2003) firstly identified alteration facies and reported a paragenetic relationship of the vein system at the LCT deposit. However, his work does not provide adequate information for a comprehensive understanding of the mineralisation system at LCT, as veins of his main stage mineralisation (equivalent to Stage 2 veins in this study) were only documented in his report. Mineralisation of the LCT deposit is mineralogically and paragenetically divided into five stages (Fig. 4.1). The five mineralisation stages at LCT recognised in this study include:

Stage 1: Quartz + chlorite + sulphides + calcite + sericite + illite

Stage 2: Quartz + sulphides + adularia + sericite + illite ± electrum ± native gold

Stage 3: Sulphides + sericite + illite + calcite ± quartz

Stage 4: Calcite + quartz ± chlorite ± illite ± pyrite

Stage 5: Kaolinite + halloysite ± alunite

Stage 1: Quartz + chlorite + sulphides + calcite + sericite + illite

Stage 1 occurred during early hydrothermal brecciation at LCT and consists of quartz, sulphides, chlorite, calcite, sericite and illite. The hydrothermal breccia facies commonly show a jigsaw-fit texture consisting of feldspar-phyric dacitic porphyry, quartz monzonite and quartz monzodiorite clasts. The matrix is normally composed of a fine-grained, dark-coloured component (Fig. 4.2A), and also locally includes aggregated sulphides (Fig. 4.2B). In thin section, the matrix mainly consists of quartz and chlorite, and also includes minor sericite and illite and traces of calcite and pyrite. The sulphide-enriched matrix is predominantly composed of pyrite with a trace of sphalerite, galena, chalcopyrite and arsenopyrite (Figs. 4.2C and D). Some sericite and illite are also filled in the sulphide-enriched matrix. Although variable sulphides are present in this stage, no gold-bearing mineral (i.e., electrum) is found. The occurrence of this stage hydrothermal

Stage		1	2	3	4	5
Mineralogy		(Pre-)	(Syn-)	(Post-)	(Post-)	(Supergene)
ORE	Pyrite			Major		
	Sphalerite			Major		
	Galena			Major		
	Chalcopyrite			Major		
	Arsenopyrite			Major		
	Electrum			Major		
	Native gold			Major		
GANGUE	Quartz		Major			
	Chlorite		Major			
	Calcite				Major	
	Adularia		Major			
	Sericite		Major			
	Illite		Major			
	Kaolinite					Major
	Halloysite					Major
	Alunite					Major

Relative mineral abundance

Major **█** Minor **▬** Trace **⋯**

Fig. 4.1. Summary of mineralisation and paragenesis of the LCT deposit, Lao PDR.

breccia is confined to the northern part of the deposit area, where the rocks of the sedimentary sequence have contact with intrusive units such as quartz monzonite and/or quartz monzodiorite. This hydrothermal breccia stage is clearly cross-cut by the Stage 2 vein as evidenced by diamond drill hole logging, and this clearly shows that this mineralisation stage occurred prior to the main gold-bearing mineralisation (Stage 2) at the LCT deposit (Fig. 4.2B).

Stage 2: Quartz + sulphides + adularia + sericite + illite ± electrum ± native gold

The Stage 2 mineralisation at LCT is characterised by a quartz-sulphide vein system. This stage mineral assemblage occurs as vein infill and the associated alteration is developed in the wall rock. The veins of this stage show various textures including stockwork (Fig. 4.3A), crystalline (Fig. 4.3B) and crustiform (Fig. 4.3C) veins. The stockwork veins, mainly occurring in the central

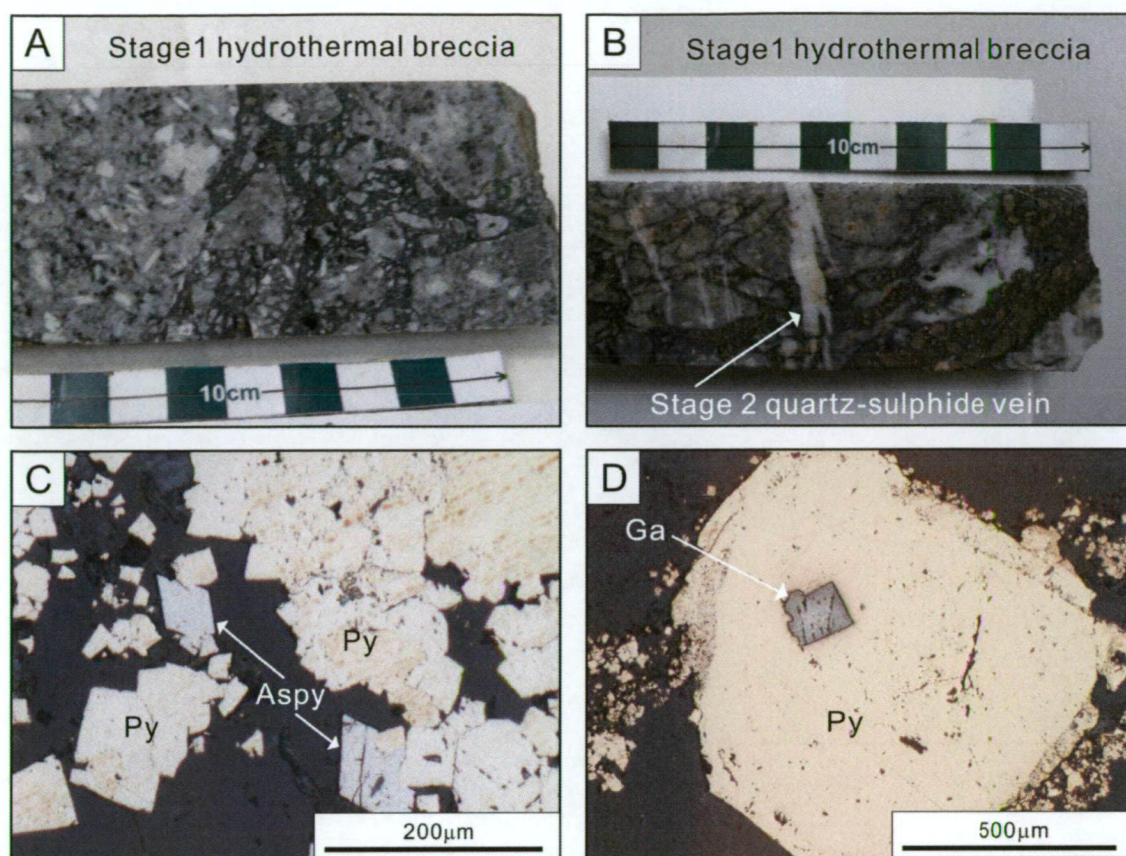


Fig. 4.2. Photographs showing Stage 1 mineralisation facies of the LCT deposit. Abbreviations: Py=pyrite, Aspy=arsenopyrite, Ga=galena, rl=reflected light.

- A) Hydrothermal breccia facies. Sample No. LSD13@35.2m.
 B) Hydrothermal breccia facies involving sulphide-rich matrix. Note that Stage 1 hydrothermal breccia is cross-cut by Stage 2 quartz-sulphide vein. Sample No. LSD24@86.0m.
 C) Sulphide assemblages in the sulphide-rich matrix of Stage 1 hydrothermal breccia. Sample No. LSD24@86.0m (rl).
 D) Sulphide-rich matrix of Stage 1 hydrothermal breccia. Note euhedral to subhedral pyrite grain with a galena inclusion. Sample No. LSD24@86.0m (rl).

deposit area, are the most common vein texture at LCT, and these veins are confined to the shallower part of the system. In contrary, the crystalline and crustiform veins, which are rare at LCT, occur mostly in the eastern part of the deposit area and are confined to the deeper part of the system. The occurrence of the Stage 2 veins may also be lithologically controlled as they are preferentially hosted in the feldspar-pyritic dacitic porphyry and tuffaceous sandstone units (Fig. 3.1).

The Stage 2 mineralisation includes quartz, pyrite, chalcopyrite, arsenopyrite, sphalerite, galena, electrum, sericite and illite mineral assemblage as observed by microscopic examination.

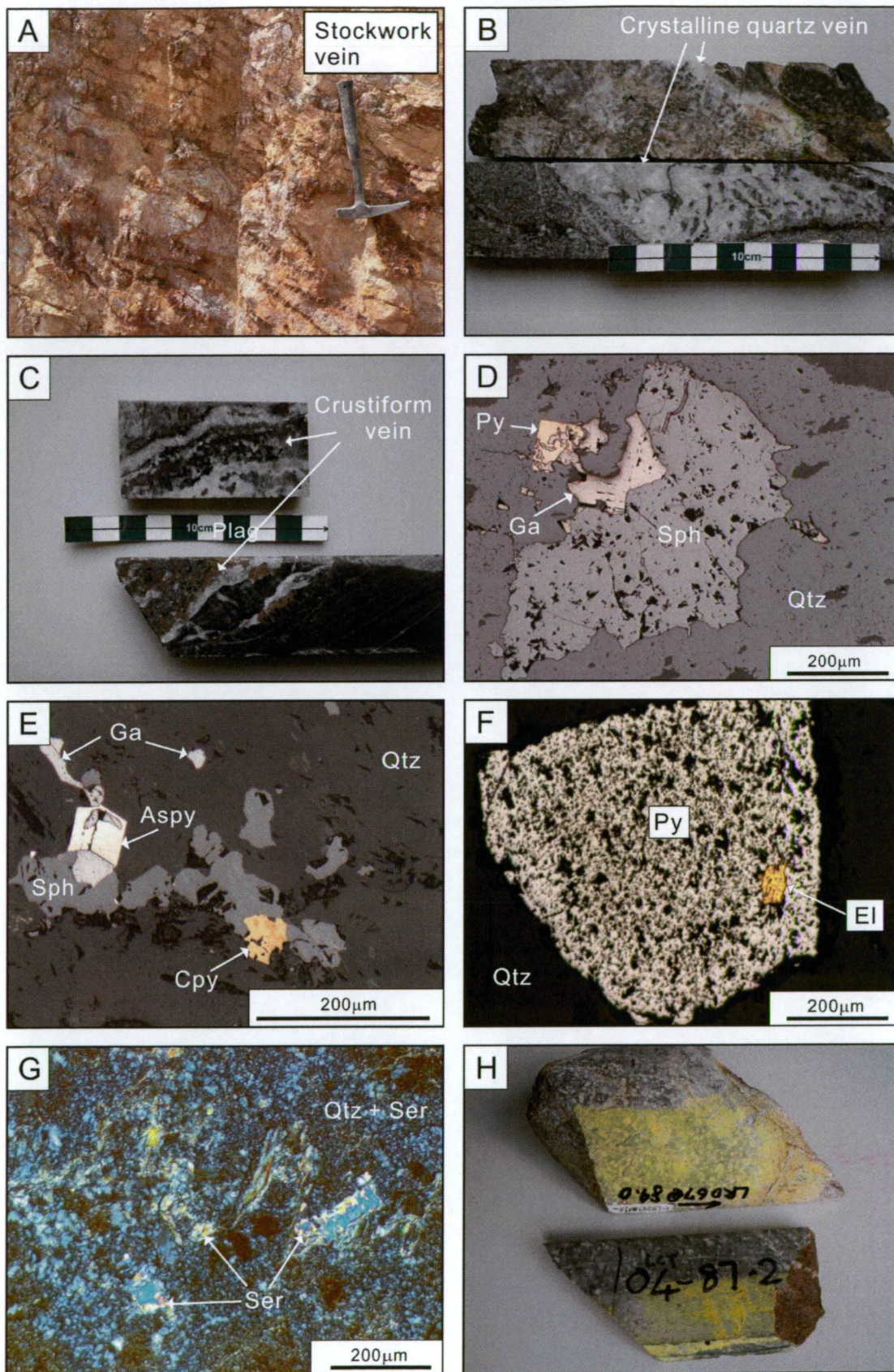


Fig. 4.3. Textural features of Stage 2 mineralisation facies of the LCT deposit. Abbreviations: Py=pyrite, Cpy=chalcopyrite, Ga=galena, Sph=sphalerite, Qtz=quartz, Aspy=arsenopyrite, El=electrum, Ser=sericite, WR=wall rock, rl=reflected light, xpl=cross polarised light.

- A) Photograph showing Stage 2 stockwork veins on outcrop in the central part of the deposit area. Vein margins are stained by iron-oxides, showing brown colour.
- B) Photograph showing Stage 2 crystalline quartz veins mainly consisting of quartz. Sample No. LSD05@90.8m (top) and LSD13@96.6m (bottom).
- C) Photograph showing Stage 2 crustiform veins, dominantly consisting of base metal sulphides. Sample No. LRD67@50.0m (top) and LSD09@88.0m (bottom).
- D) Photomicrograph (rl) showing sulphide mineral assemblage of Stage 2 including pyrite, galena and sphalerite. Sample No. LDD03A@75.0m.
- E) Photomicrograph (rl) showing sulphide mineral assemblage of stage 2 including chalcopyrite, galena, sphalerite and arsenopyrite. Sample No. LSD14@88.1m.
- F) Photomicrograph (rl) showing electrum occurrence as an inclusion of vein-hosted pyrite. Sample No. LSD05@90.8m.
- G) Photomicrograph (xpl) showing an example of Stage 2 alteration mineral assemblages in the wall rock, consisting of major quartz and minor sericite. Sample No. LRD67@50.0m.
- H) Photograph showing stained (yellow) adularia in hand specimen samples. Sample No. LRD67@89.0m (top) and LSD04@87.2m (bottom).

Additional microprobe analysis of the electrum revealed that some can be compositionally classified as native gold (see Chapter 4.5 in details). Normally, the sulphides such as pyrite, chalcopyrite, arsenopyrite, sphalerite and galena are closely associated (Figs. 4.3D and E), and their occurrence is limited to vein infill. The occurrence of electrum is detected as inclusions of vein-located pyrite (Fig. 4.3F). It is noted that the sulphides in stockwork veins are commonly composed of pyrite, whereas those in crystalline and crustiform veins are enriched in chalcopyrite, arsenopyrite, sphalerite and galena. The alteration associated with veins of this stage is extensively developed throughout the deposit area, consisting dominantly of quartz, sericite, illite and minor pyrite and chlorite. In thin section, the proximal part of the wall rock to the vein is intensely altered by abundant sericite and minor quartz and illite assemblages, whereas the distal part of the wall rock to the vein is pervasively altered by major chlorite with minor sericite (Fig. 4.3G). Adularia is also involved both in the proximal and distal parts of the wall rock to the veins (Fig. 4.3H), which was confirmed by a staining technique and XRD analysis (see Appendix III; LSD04@87.2m). A trace amount of euhedral pyrite, associated with the alteration mineral assemblage of this stage, is also present in the wall rock.

Stage 3: Sulphides + sericite + illite + calcite ± quartz

Stage 3 mineralisation occurs both as vein and breccia infill, and the associated alteration is developed in the vein selvage. In a hand specimen sample, the vein and breccia infill is mostly composed of an aggregate of fine-grained sulphides and the selvage is strongly sericitised (Fig. 4.4A). This Stage 3 mineralisation is rare at LCT and is locally formed throughout the deposit

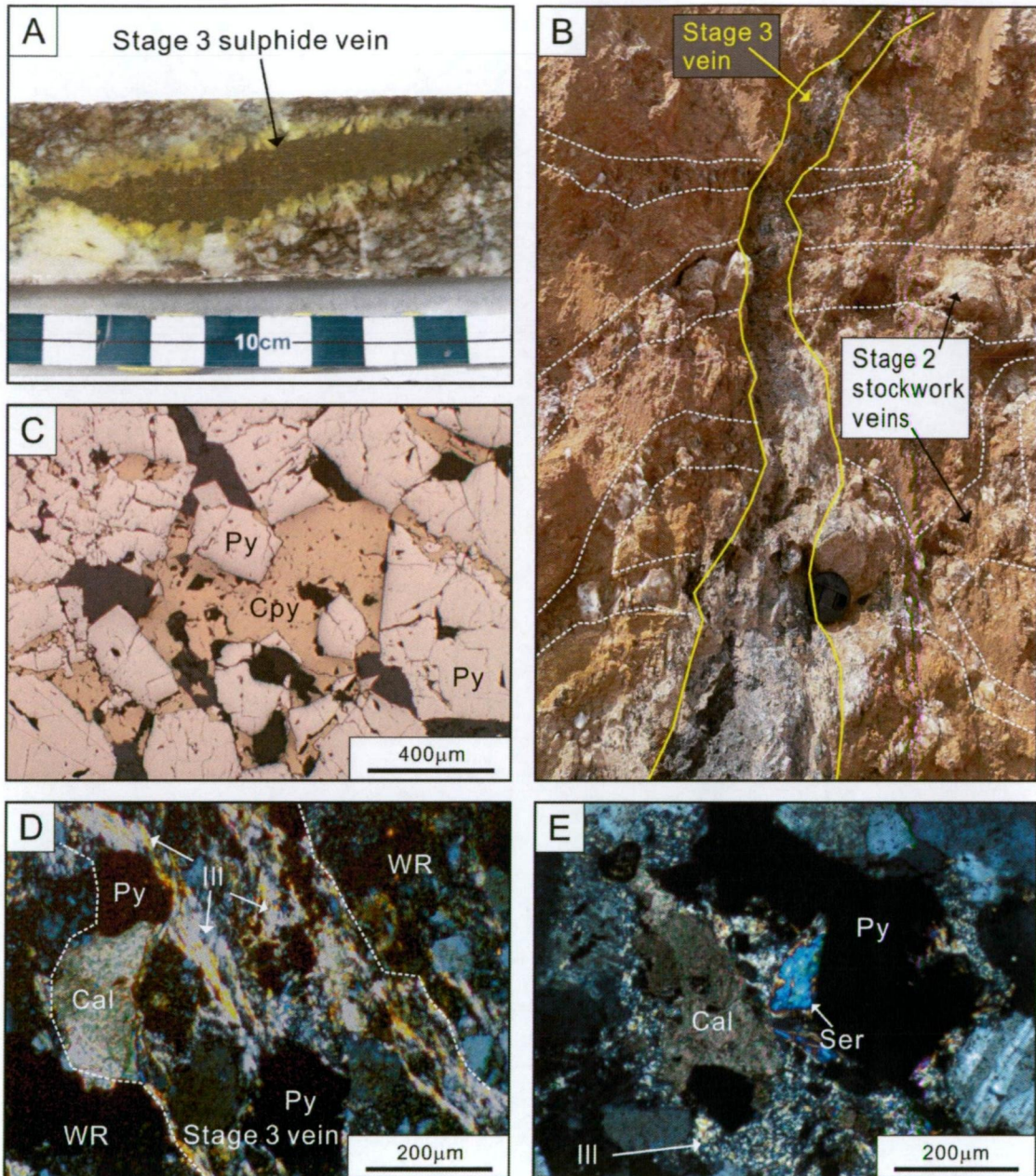


Fig. 4.4. Textural features of Stage 3 mineralisation facies of the LCT deposit. Abbreviations: Py=pyrite, Cpy=chalcopyrite, Cal=calcite, Ill=illite, WR=wall rock, Ser=sericite, rl=reflected light, xpl=cross polarised light.

- A) Photograph showing an example of Stage 3 sulphide vein in a diamond drill core. Sample No. LSD08@79.5m.
- B) Photograph showing Stage 3 sulphide vein cross-cutting stage 2 stockwork veins on the outcrop in the central part of the deposit area.
- C) Photomicrograph (rl) showing infill of Stage 3 sulphide vein. Pyrite is dominated with minor chalcopyrite infill. Sample No. LSD08@83.4m.
- D) Photomicrograph (xpl) showing an example of Stage 3 alteration minerals infilling. Sample No. LSD08@83.4m.
- E) Photomicrograph (xpl) showing an example of Stage 3 alteration mineral assemblages in the proximal part of the wall rock of the vein. Sample No. LSD08@83.4m.

area, as only identified in few diamond drill holes and outcrops. A clear cross-cutting relationship with the Stage 2 stockwork veins observed in outcrop in the central part of the deposit area (Fig. 4.4B), indicates that this stage mineralisation was formed later than the Stage 2 main mineralisation at LCT. In polished thin section, the veins of this stage consist of abundant euhedral to subhedral pyrite with minor chalcopyrite infilling the interstitial pyrite grains (Fig. 4.4C). Alteration minerals such as illite and calcite are present in the vein, together with the pyrite (Fig. 4.4D), or the alteration is limited to the vein selvage consisting of sericite, illite and calcite, and is particularly developed in the proximity of the wall rock (Fig. 4.4E).

Stage 4: Calcite + quartz ± chlorite ± illite ± pyrite

Stage 4 mineralisation is locally developed in the southern and northern sections of the deposit area. A clear cross-cutting relationship with a Stage 3 sulphide vein can be identified in a hand specimen sample (Fig. 4.5A). This stage is mostly composed of alteration minerals including major calcite, minor quartz and a trace amount of chlorite and illite. This mineral assemblage normally occurs as vein infill in the wall rock of siltstone, sandstone, polymictic sedimentary breccia and tuffaceous sandstone. Veins of this stage are commonly white in colour and less than 5 cm in width, and are favorably hosted in the sedimentary units. In thin section, the vein infill consists of abundant calcite and minor amounts of quartz and chlorite, and the veins normally have a sharp contact with the wall rock in which a weak and patchy alteration is developed including illite, calcite and pyrite assemblages (Fig. 4.5B). Generally, this stage of alteration is local and strongly developed in the polymictic sedimentary breccia, showing that the matrix of the clasts is completely cemented by calcite.

Stage 5: Kaolinite + halloysite ± alunite

Stage 5 mineralisation consists of abundant kaolinite, halloysite and trace of alunite. These minerals were identified by PIMA inspection as samples are intensely altered and fragile. On the surface throughout the deposit area, the mineral assemblages of this stage are commonly found and overprint all earlier mineralisation stages and alteration facies. This stage of alteration is spatially formed in the central part of the deposit area where the stockwork veins are mainly developed and it forms a blanket-like cover up to about 100 m thick, as measured from the surface. In comparison, this alteration is only a few tens of metres deep in the other parts of the deposit area.

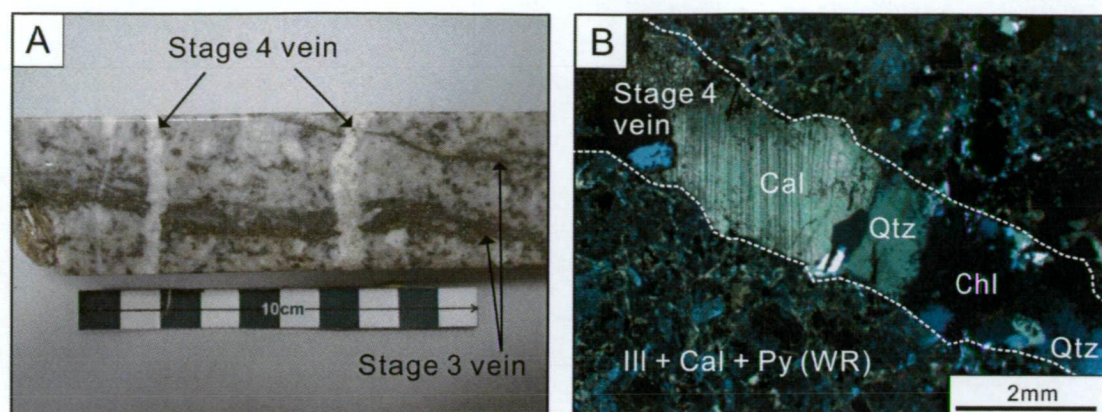


Fig. 4.5. Textural features of Stage 4 mineralisation facies of the LCT deposit. Abbreviations: Qtz=quartz, Chl=chlorite, Cal=calcite, Ill=illite, Py=pyrite, WR=wall rock, xpl=cross polarised light.

- A) Photograph showing Stage 4 calcite-dominated veins cross-cutting Stage 3 sulphide-dominated veins. Sample No. LSD08@83.4m.
- B) Photomicrograph (xpl) showing an example of Stage 4 vein infill and alteration facies in the proximal part of the wall rock. Sample No. LSD24@94.2m.

Kaolinite and halloysite are the main minerals in this stage. The clay-altered rocks are typically leached to a whitish or yellowish in colour (Fig. 4.6A). This stage of alteration completely destroyed the primary texture of the rock. Alunite is also locally developed in association with kaolinite and halloysite and mostly occurs as infill of the earlier stage vein cavities (Fig. 4.6B). This textural feature suggests that the alunite is a secondary product. These alteration mineral assemblages are commonly interpreted to have formed under extremely acidic conditions (e.g., Hedenquist et al., 1996), and the blanket-like nature of this stage of alteration near surface indicates that the clay alteration may have formed by the supergene process of percolating ground water.

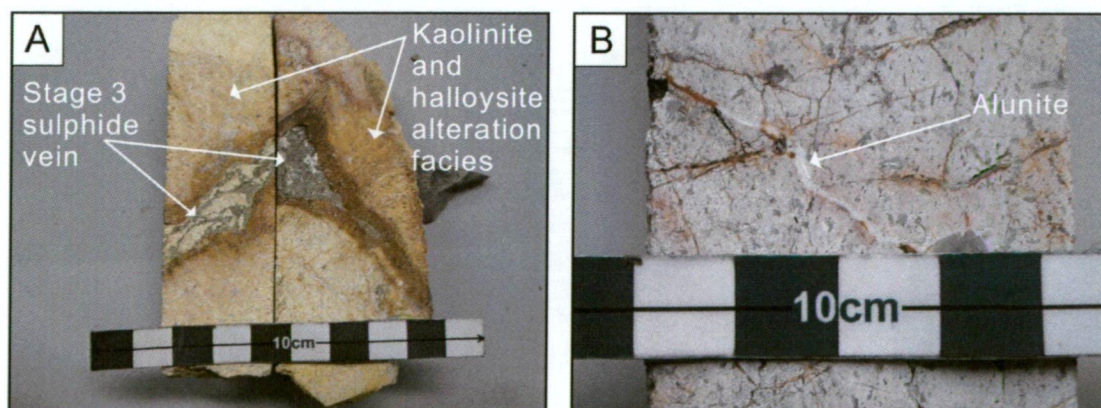


Fig. 4.6. Textural features of Stage 5 mineralisation facies of the LCT deposit.

- A) Photograph showing diamond drill cores intensely altered by kaolinite and halloysite assemblage with Stage 3 sulphide veins. Sample No. LDD81@79.6m (left) and LDD81@51.7m (right).
- B) Photograph showing alunite infilling the earlier stage vein cavity. Sample No. LSD02@16.8m.

4.3.2. BHX observation, drill hole logging, macroscopic and microscopic investigation

Tate (2004) initially studied the mineralisation at the BHX deposit on the basis of nine old diamond drill holes which were conducted during 1996–1997, and documented that the gold mineralisation occurs within both veins and the wall rocks. However, his work does not include adequate information to fully understand the mineralisation system at BHX, as there were a limited number of drill holes available at that time.

In this study, the mineralisation and paragenetic relationships of the BHX deposit were investigated on the basis of the eight recently-drilled diamond holes completed in the 2006–2007 dry season, as well as investigation of the previous nine old diamond drill holes. As the result of drill core logging and additional microscopic, PIMA and microprobe examinations, seven mineralisation stages were identified as described below:

Stage 1: Calcite + quartz + sulphides + chlorite + sericite + adularia + illite ± chalcedony ± electrum

Stage 2: Calcite + quartz + sulphides + sericite + chlorite ± native silver ± stephanite

Stage 3: Sulphides + dolomite + ankerite ± hematite ± electrum ± native silver

Stage 4: Rock flour + graphite + siderite + pyrite + chlorite ± rutile

Stage 5: Dolomite + quartz ± calcite

Stage 6: Quartz + calcite + chlorite + pyrite

Stage 7: Illite + halloysite + kaolinite

The paragenetic relationship of the BHX deposit and the mineralisation stages are illustrated in Fig. 4.7 and are described in detail from the oldest to the youngest order in the following section:

Stage 1: Calcite + quartz + sulphides + chlorite + sericite + adularia + illite ± chalcedony ± electrum

The Stage 1 mineralisation consists mainly of calcite, quartz and minor sulphides, and this mineral assemblage occurs mostly as vein infill (Fig. 4.8A). The chalcedony-dominated vein also occurs locally and is grouped in this stage (Fig. 4.8B). Veins of this stage are commonly thin (<5 cm in width) and are spatially well-developed throughout the deposit area, forming a stockwork vein system (Fig. 4.9). In addition, it is recognised that the stockwork veins are favourably developed in the feldspar-phyric andesite and crystal-rich volcanic breccia rock units.

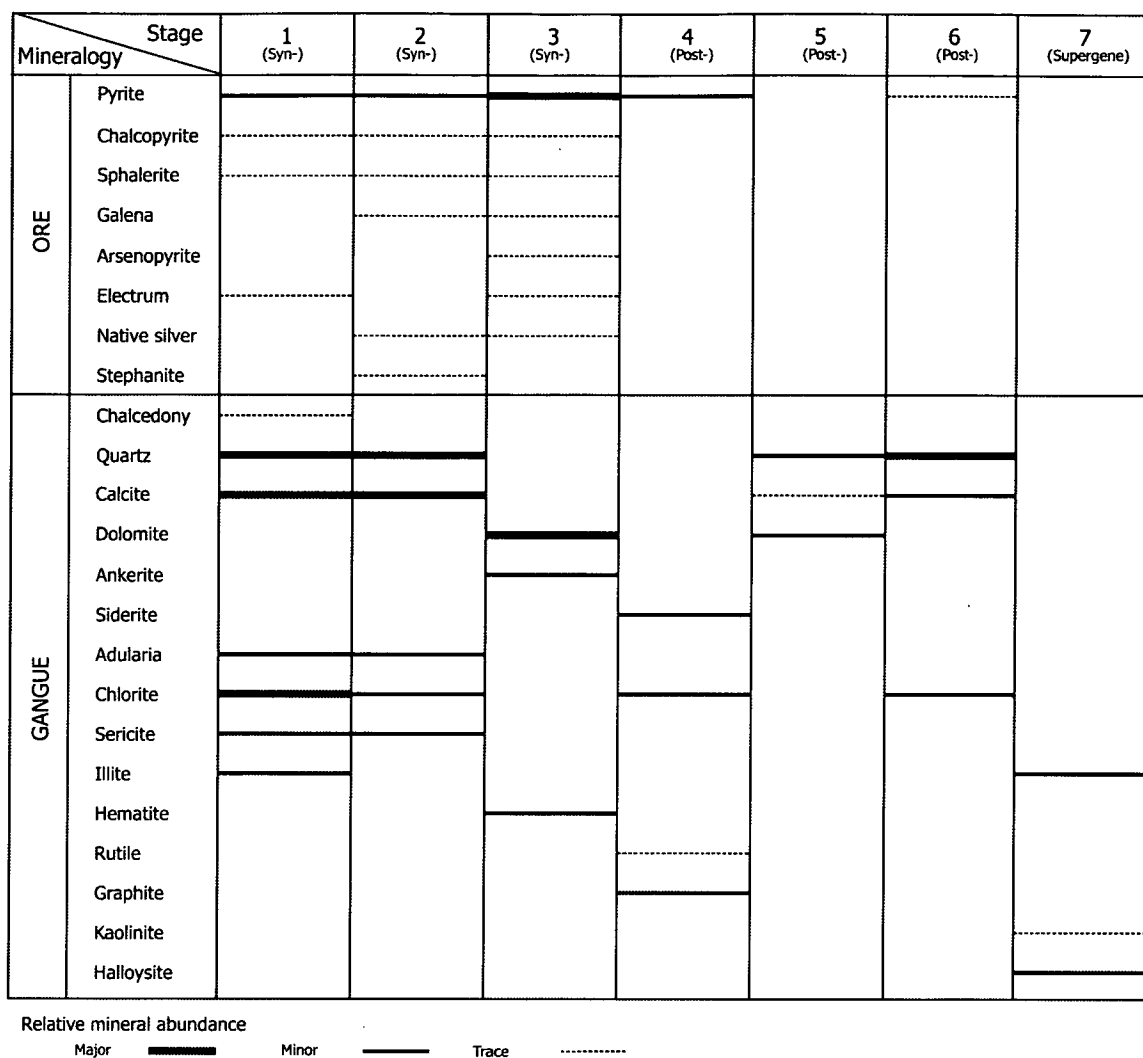


Fig. 4.7. Summary of mineralisation and paragenesis of the BHX deposit, Lao PDR.

The sulphide minerals in the vein are composed of pyrite, chalcopyrite and sphalerite, and these are closely associated with the occurrence of trace of electrum (Fig. 4.8C).

The alteration associated with this stage of mineralisation is pervasively and intensely developed in the central part of the deposit area surrounding the stockwork veins. The altered wall rock is commonly pale-green in colour and fine-grained disseminated pyrite is also present (Fig. 4.8D). In thin section, the pale-green coloured sample shows chlorite, adularia and sericite altered mineral assemblages (Fig. 4.8E). The presence of adularia was also confirmed by staining examination (Fig. 4.8F). A sample of the alteration facies from this stage (HSD01@98.4m) was analysed by XRD and the result shows a consistency with the interpreted mineral assemblages as well as the confirmation of the presence of adularia (see Appendix III; HDD09@123.9m).

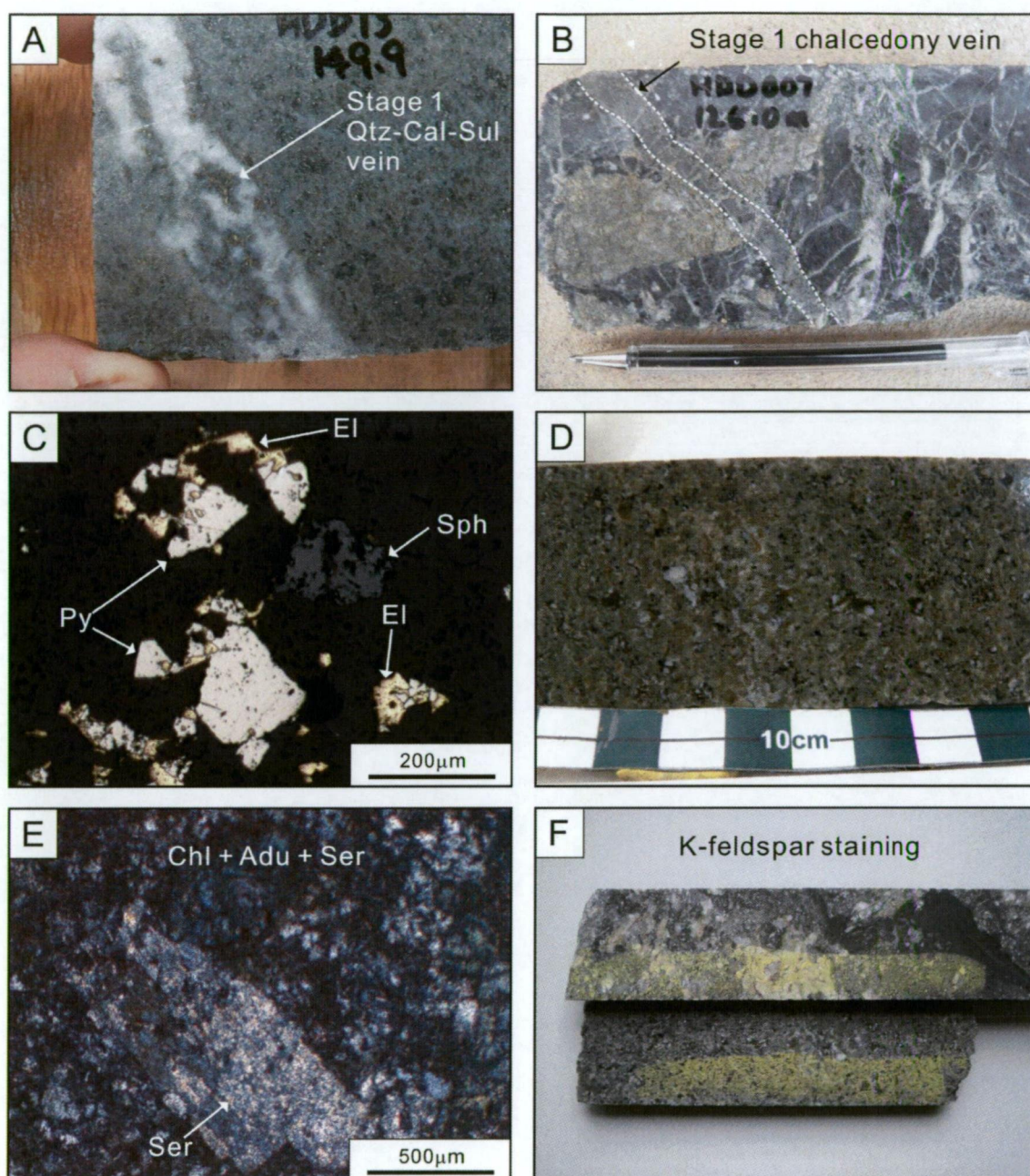


Fig. 4.8. Textural features of Stage 1 mineralisation facies of the BHX deposit. Abbreviations: Qtz=quartz, Cal=calcite, Sul=sulphide, Py=pyrite, El=electrum, Sph=sphalerite, Chl=chlorite, Adu=adularia, Ser=sericite, rl=reflected light, xpl=cross polarised light.

- A) Photograph showing Stage 1 calcite-quartz-sulphides vein facies. Sample No. HDD13@149.9m.
 B) Photograph showing Stage 1 chalcedony vein facies. Sample No. HDD07@126.0m.
 C) Photomicrograph (rl) showing ore mineral assemblages of Stage 1 vein including pyrite, sphalerite and electrum. Sample No. HDD07@126.0m
 D) Photograph showing Stage 1 alteration facies in wall rock. Sample. No. HSD01@94.8m.
 E) Photomicrograph (xpl) showing Stage 1 alteration mineral assemblage of chlorite, adularia and sericite in wall rock. Sample No. HSD01@94.8m.
 F) Photograph showing stained (yellow) adularia in hand specimen samples. Sample No. HSD04@75.2m (top) and HSD01@98.4m (bottom).

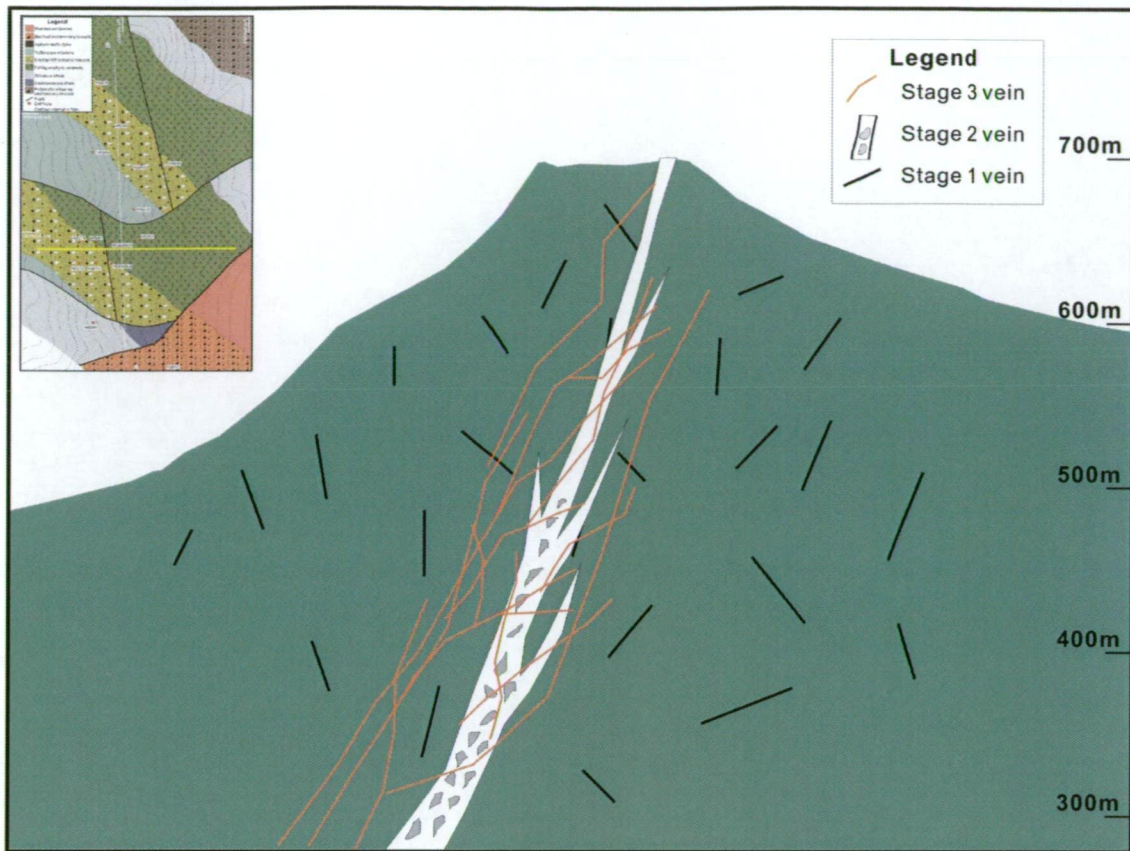


Fig. 4.9. Schematic diagram of syn-mineralisation stage vein occurrences at the BHX deposit, along E-W cross-section.

Stage 2: Calcite + quartz + sulphides + sericite + chlorite ± native silver ± stephanite

The Stage 2 mineralisation is mainly composed of calcite, quartz and sulphides, which are more or less similar to the Stage 1 mineralisation assemblage. However, the Stage 1 veins commonly form a stockwork system throughout the deposit area, whereas the Stage 2 mineral assemblage occurs as infill of massive vein and hydrothermal breccia and they are locally developed (Figs. 4.10A and B). The Stage 2 mineralisation is predominantly confined in the shear zone, which is N-S trending with a steep westerly dipping fault zone (Fig. 4.9). The sulphide minerals in the Stage 2 veins are pyrite, chalcopyrite, sphalerite and galena, and they are sparsely distributed in the vein and breccia infill. In addition, a trace amount of native silver and stephanite was detected in this stage by microprobe analysis (see Chapter 4.5 in details), intimately associated with the sulphide minerals (Figs. 4.10C and D). Alteration of this stage is weakly developed in the wall rock adjacent to the veins and breccias (less than 1m thick), replacing the wall rock with a sericite, chlorite and adularia mineral assemblage.

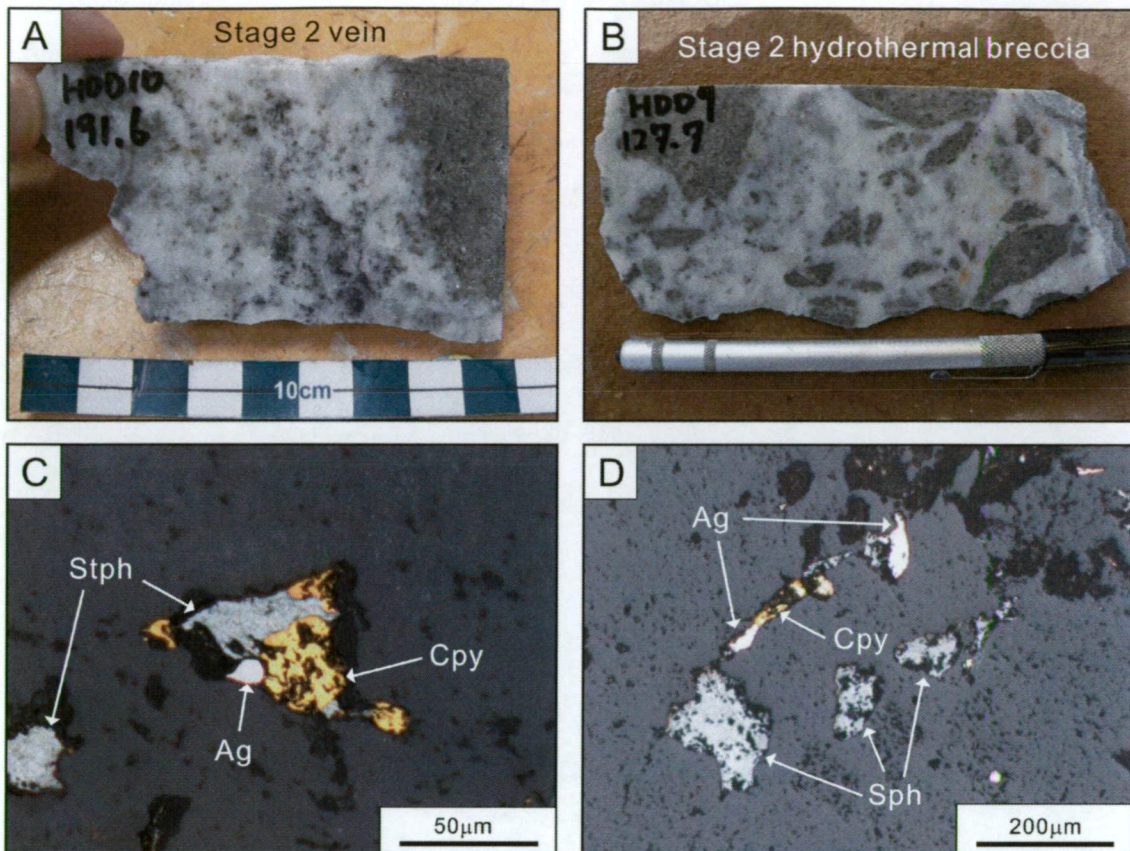


Fig. 4.10. Textural features of Stage 2 mineralisation facies of the BHX deposit. Abbreviations: Stph=stephanite, Cpy=chalcopyrite, Ag=native silver, Sph=sphalerite, rl=reflected light.

- A) Photograph showing Stage 2 calcite-quartz-sulphide vein. Sample No. HDD10@191.6m.
 B) Photograph showing Stage 2 hydrothermal breccia consisting of calcite-quartz-sulphide infill. Sample No. HDD09@127.7m.
 C) Photomicrograph (rl) showing Stage 2 ore mineral assemblage in vein. Sample No. HDD10@191.4m.
 D) Photomicrograph (rl) showing Stage 2 ore mineral assemblage in vein. Sample No. HDD10@191.4m.

Stage 3: Sulphides + dolomite + ankerite ± hematite ± electrum ± native silver

Stage 3 mineralisation occurs as veinlets infilling microfractures and commonly overlaps the Stage 2 massive veins and hydrothermal breccias (Figs. 4.11A and B). This stage of mineralisation is dominated by sulphides including pyrite, chalcopyrite, sphalerite, galena and arsenopyrite. A trace amount of electrum and native silver is also present, as identified by microprobe analysis (see Chapter 4.5 in details), closely associated with the sulphide mineral assemblage (Figs. 4.11C and D). Pale-yellowish coloured carbonate minerals of this mineralisation stage are observed in hand specimen samples and these were identified as dolomite and ankerite by SEM analysis. A trace amount of hematite occurs locally as infilling microfractures that are developed in the earlier stage veins. The aggregated pyrite infilling in the

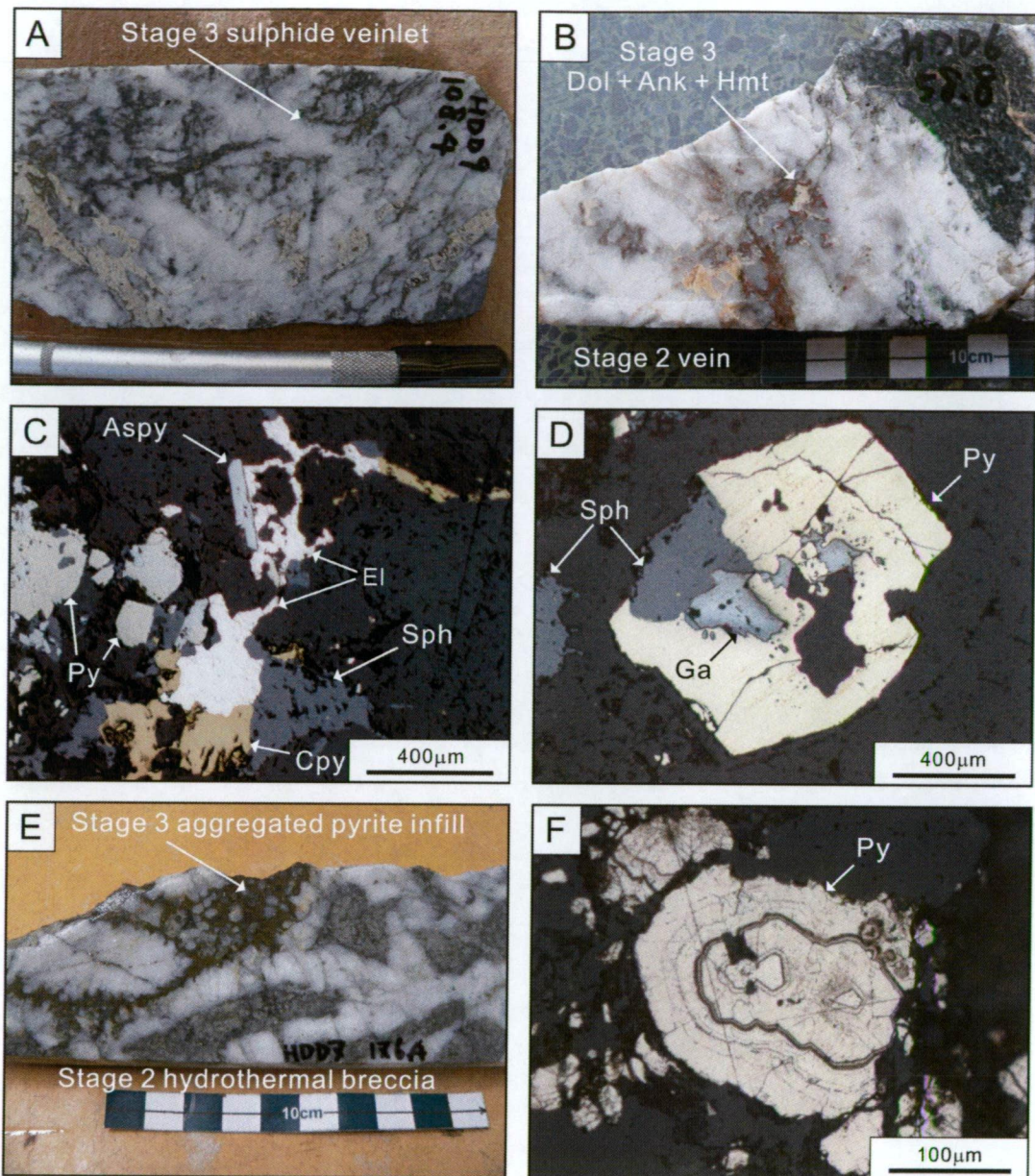


Fig. 4.11. Textural features of Stage 3 mineralisation facies of the BHX deposit. Abbreviations: Dol=dolomite, Ank=ankerite, Hmt=hematite, Aspy=arsenopyrite, Py=pyrite, El=electrum, Sph=sphalerite, Cpy=chalcopyrite, Ga=galena, rl=reflected light.

- A) Photograph showing Stage 3 sulphide and dolomite-ankerite veinlets infilling microfractures in Stage 2 massive vein. Sample No. HDDD09@108.4m.
- B) Photograph showing Stage 3 dolomite-ankerite-hematite vein infill developing in Stage 2 vein. Sample No. HDD06@58.8m.
- C) Photomicrograph (rl) showing Stage 3 sulphide mineral assemblage of veinlet. Sample No. HDD09@108.4m.
- D) Photomicrograph (rl) showing Stage 3 sulphide mineral assemblage of veinlet. Sample No. HDD09@99.2m.
- E) Photograph showing Stage 3 aggregated pyrite infilling in Stage 2 hydrothermal breccia. Sample No. HDD07@176.4m.
- F) Photomicrograph (rl) showing texture of Stage 3 aggregated pyrite infill. Sample No. HDD07@179.6m.

Stage 2 vein and hydrothermal breccia is also locally recognised (Figs. 4.11E and F). The occurrence of veinlets of this stage is spatially confined to the N-S trending shear zone with its steep westerly dipping fault (Fig. 4.9), which is similar to Stage 2. No alteration assigned to this mineralisation stage is developed in the wall rock.

Stage 4: Rock flour + graphite + siderite + pyrite + chlorite ± rutile

Stage 4 occurs as breccia in the deeper part of the deposit and as veins in the shallower part of the deposit. The breccia consists mostly of wall rock clasts and minor mineralised clasts of the earlier stages, and the matrix is composed of rock flour, graphite, siderite and pyrite, showing distinct dark coloured assemblages in hand specimen sample (Figs. 4.12A, B, C and D). The veins occurring in the shallower part of the system consist of fine-grained graphite, siderite and pyrite (Fig. 4.12E). The alteration of this stage is well-developed in the proximal part of the wall rock of the vein, showing intense replacement by siderite as an orange colour (Fig. 4.12F); this alteration commonly overprints the alteration facies of the earlier stages. However, no alteration of this stage is formed in the wall rock in the deeper part of the system. The breccias/veins of this stage also appear to be hosted by the N-S trending, steep westerly dipping shear zone, as recognised in the drill hole logging.

Stage 5: Dolomite + quartz ± calcite

The Stage 5 mineralisation occurs as vein and veinlet infill, commonly comprising a quartz, dolomite and calcite assemblage (Fig. 4.13A). These minerals are spatially distributed throughout the deposit area and are commonly observed in the most of the drill holes. The dolomite-only veinlets are also found locally. These overprint the Stage 4 breccia (Fig. 4.13B). No alteration associated with this mineralisation stage is formed in the wall rock.

Stage 6: Quartz + calcite + chlorite + pyrite

The Stage 6 mineralisation mainly comprises of quartz with a subordinate amount of chlorite and calcite. The vein cross-cutting relationships with the veins of the earlier mineralisation stages are clearly observed (Figs 4.14A and B). The mineral assemblage of this stage occurs as vein infill and the veins are spatially well-developed in the deposit area as frequently intersected in the drill holes. It is identified that the vein infill is made up of calcite, chlorite and quartz throughout this stage mineralisation period (Fig. 4.14C). The occurrence of this stage mineral assemblage is confined within the vein (Fig. 4.14D).

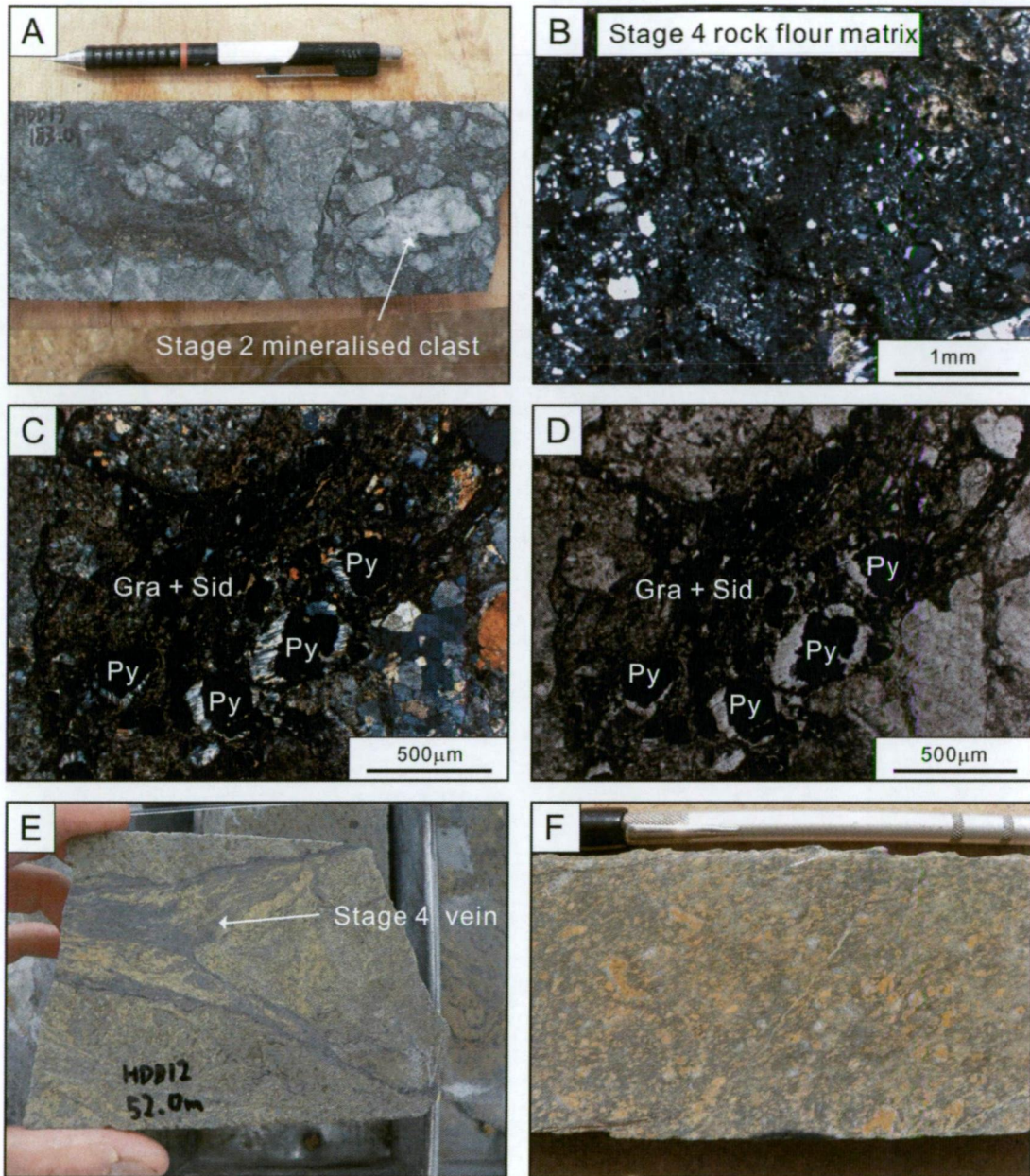


Fig. 4.12. Textural features of Stage 4 mineralisation facies of the BHX deposit. Abbreviations: Gra=graphite, Sid=siderite, Py=pyrite, xpl= cross polarised light, ppl=plane polarised light, rl=reflected light.

- A) Photograph showing Stage 4 breccia including Stage 2 mineralised clast. Sample No. HDD13@187.0m.
- B) Photomicrograph (xpl) showing Stage 4 breccia matrix consisting of rock flours. Sample No. HDD13@187.0m.
- C) Photomicrograph (xpl) showing Stage 4 breccia matrix consisting of graphite-siderite-pyrite assemblage. Sample No. HDD13@187.0m.
- D) Photomicrograph (ppl) showing Stage 4 breccia matrix consisting of graphite-siderite-pyrite assemblage. Sample No. HDD13@187.0m.
- E) Photograph showing Stage 4 vein comprising graphite-siderite. Sample No. HDD12@52.0m.
- F) Photograph showing Stage 4 siderite (orange coloured) alteration in wall rock. Sample No. HDD09@60.0m.

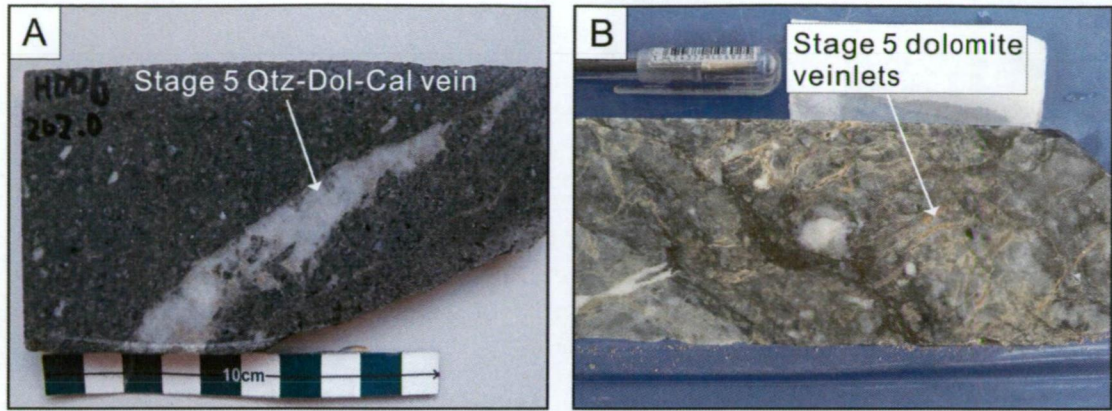


Fig. 4.13. Textural features of Stage 5 mineralisation facies of the BHX deposit. Abbreviations: Qtz=quartz, Dol=dolomite, Cal=calcite.
 A) Photograph showing Stage 5 quartz-dolomite-calcite vein. Sample No. HDD06@202.0m.
 B) Photograph showing Stage 5 dolomite veinlets overprinting Stage 4 rock flour breccia. Sample No. HDD12@60.0m.

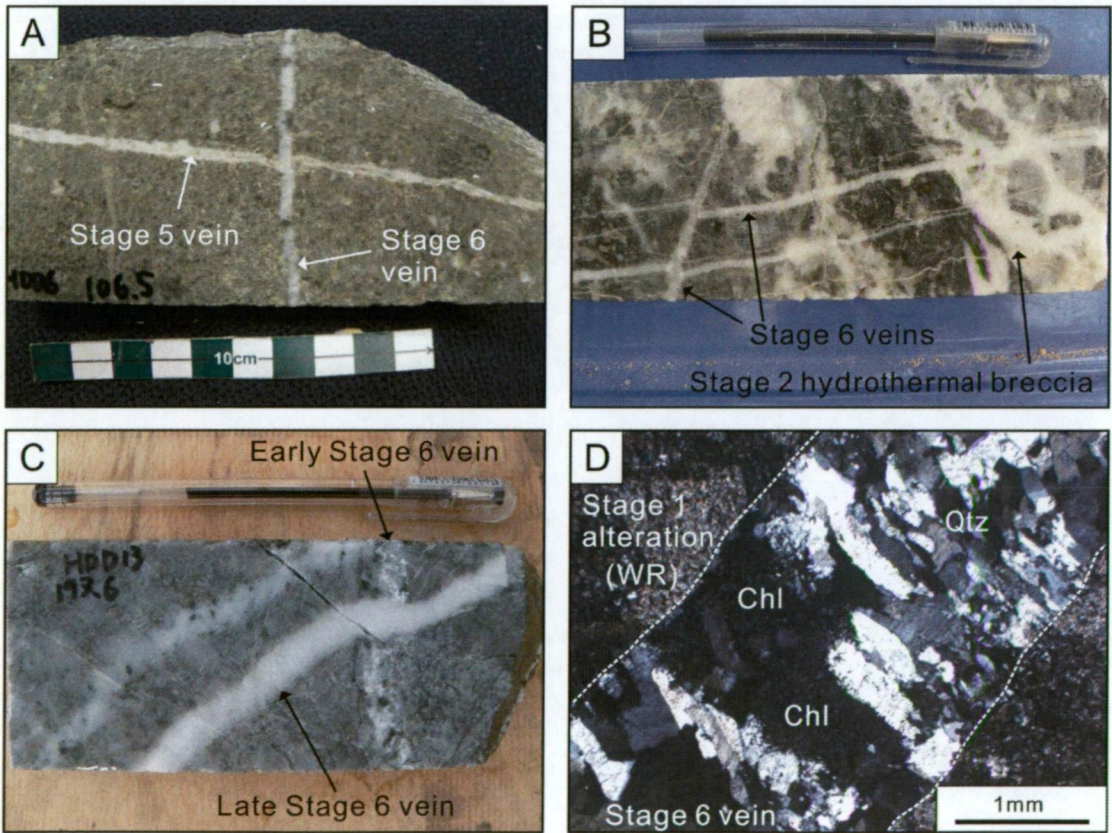


Fig. 4.14. Textural features of Stage 6 mineralisation facies of the BHX deposit. Abbreviations: Qtz=quartz, Chl=chlorite, WR=wall rock, xpl=cross polarised light.
 A) Photograph showing Stage 6 quartz-chlorite-calcite vein cross-cutting Stage 5 quartz-dolomite vein. Sample No. HDD06@106.5m.
 B) Photograph showing Stage 6 quartz-dominated veins overprinting Stage 2 hydrothermal breccia. Sample No. HDD12@58.2m.

- C) Photograph showing quartz-calcite-chlorite early Stage 6 veins cross-cutting late Stage 6 quartz-dominated vein. Sample No. HDD13@197.6m.
- D) Photomicrograph (xpl) showing Stage 6 vein infill and no alteration in the vein proximity. Sample No. HDD6@106.5m.

Stage 7: Illite + halloysite + kaolinite

This stage of mineralisation consists of illite, halloysite and kaolinite. This mineral assemblage may have occurred due to a supergene process during the latest post-mineralisation stage as its distribution is confined near surface. This stage of mineralisation is commonly recognised in outcrops and in diamond drill holes of the shallower part of the deposit.

In the field, this alteration mineral aggregates assemblage is observed on outcrops showing its intensely leached and fragile character (Fig. 4.15A). This alteration widely covers the surface in the deposit area and is typically developed along the N-S trending ridge as observed where it is exposed. The rocks in the shallower part of the diamond drill holes are also intensely altered by clay minerals such as illite, halloysite and kaolinite (Fig. 4.15B). Systematic PIMA examination of diamond drill holes in the central part of the deposit area reveals that this alteration develops up to 50 m deep from the surface.

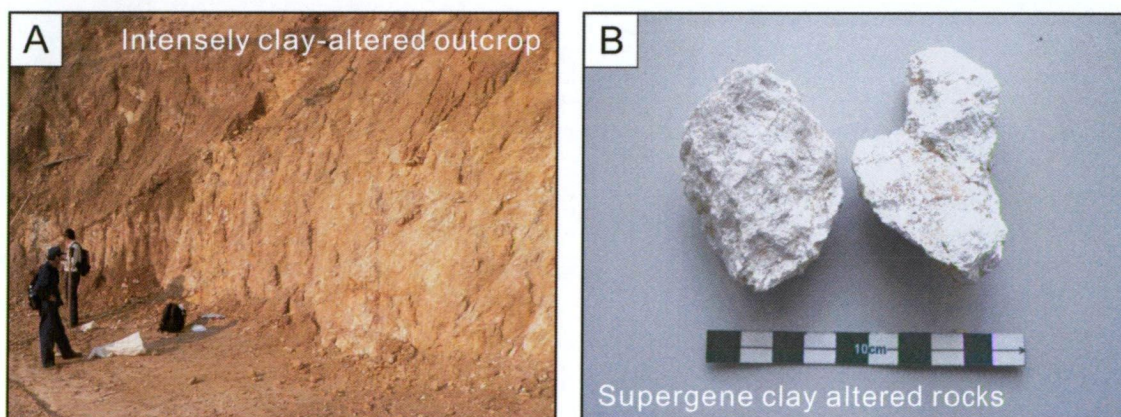


Fig. 4.15. Textural features of Stage 7 mineralisation facies of the BHX deposit.

- A) Photograph showing intense clay-altered outcrop at the central deposit area.
- B) Photograph showing intense supergene clay alteration facies. Sample No. 255974mE (both).

4.4. Ore minerals

On the basis of the mineralisation stages presented in Chapter 4.3, ore assemblages of the LCT and BHX deposits were studied under the microscope and their nature, texture and distribution are described in detail in this section:

4.4.1. LCT ore minerals

The LCT deposit contains abundant sulphide minerals including pyrite, chalcopyrite, sphalerite, galena, arsenopyrite and electrum. The occurrence of these sulphide minerals is mostly confined to pre- and syn-mineralisation stages including Stages 1 and 2 (Fig. 4.1). However, pyrite occurs throughout most of the mineralisation stages (Stages 1 to 4) and is ubiquitously present in the vein as well as the wall rock at LCT.

Pyrite

Pyrite mostly occurs within the veins and is also sparsely disseminated in the wall rock throughout the deposit area. It is commonly associated with other sulphide minerals in the veins, such as chalcopyrite, sphalerite, galena and arsenopyrite, and usually displays a euhedral to subhedral shape (Figs. 4.16A and B). In contrast, pyrite in the wall rock occurs commonly as single discrete grains. The size of pyrite grains varies from a few hundreds μm to 1 mm. The texture of vein-located pyrite uniformly shows euhedral to subhedral shape, whereas pyrite in the wall rock commonly displays a sponge core with euhedral rim texture (see Chapter 5 in details).

Chalcopyrite

Chalcopyrite is also a common sulphide mineral at LCT as found in Stages 1, 2 and 3, although the volume is not abundant as much as pyrite. It mostly occurs in veins and is sparsely distributed. In most cases, chalcopyrite is closely associated with pyrite and fills the interstitial areas of the pyrite grains (Fig. 4.16A), but it also occurs associated with other sulphides such as sphalerite, galena and arsenopyrite (Figs. 4.16C and D). The chalcopyrite grains are normally $<100 \mu\text{m}$ in size.

Sphalerite

Sphalerite mainly occurs in Stage 2, and rarely in Stage 1. The occurrence is mostly as vein infill, but it is also occasionally present in the proximal part of the host rock in stockwork veins. It has a close association with other sulphides such as pyrite, chalcopyrite, galena and arsenopyrite (Figs. 4.16B, C and D). The sphalerite grains vary in size from several hundreds μm to 5 mm.

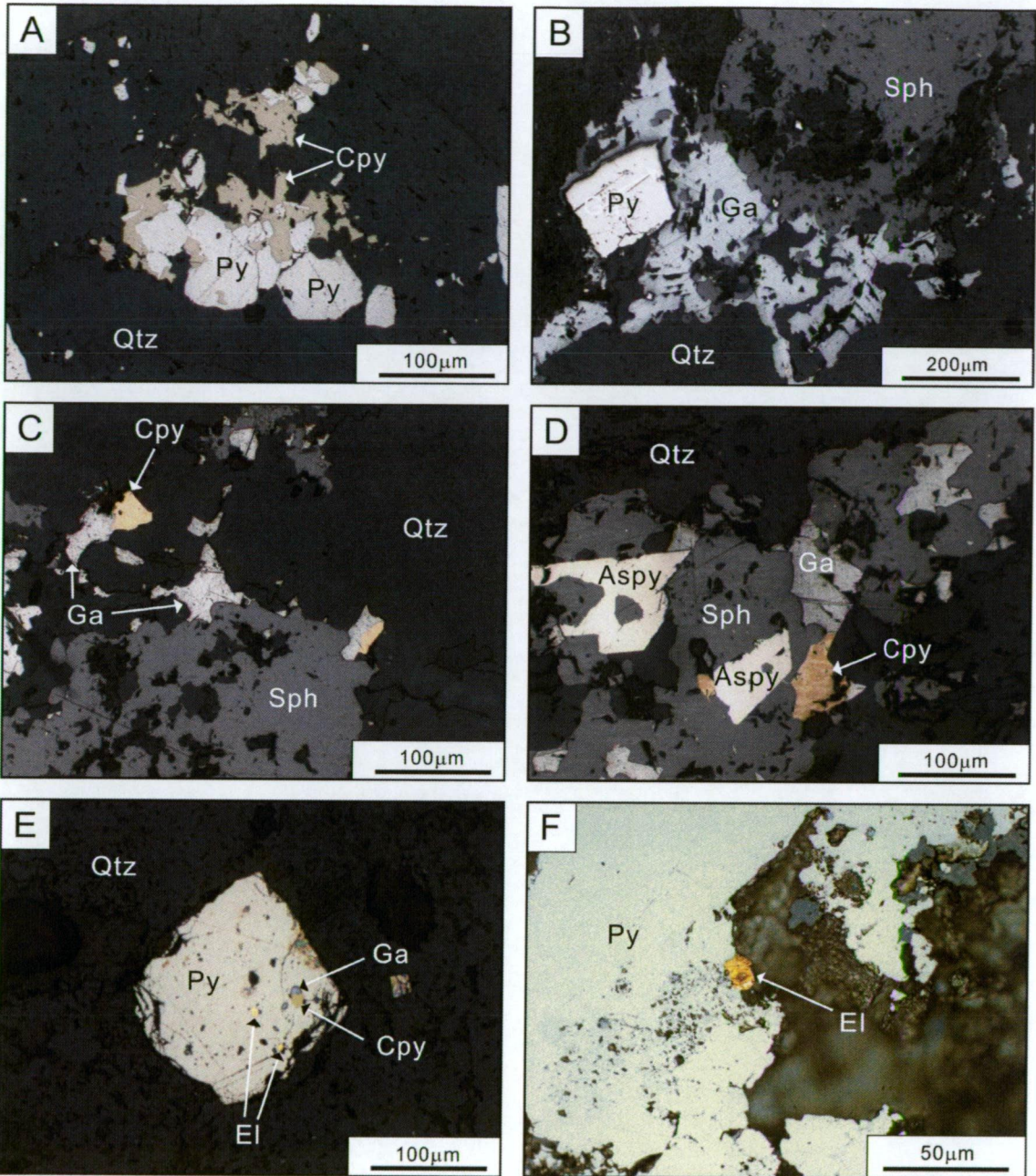


Fig. 4.16. Photomicrographs showing ore minerals of the LCT deposit (rl). Abbreviations: Py=pyrite, Cpy=chalcopyrite, Qtz=quartz, Sph=sphalerite, Ga=galena, Aspy=arsenopyrite, El=electrum, rl=reflected light.

- A) Pyrite and chalcopyrite assemblage. Sample No. LSD13@55.0m.
 B) Euhedral pyrite, galena and sphalerite assemblage. Sample No. LRD67@72.2m.
 C) Sphalerite, galena and chalcopyrite assemblage. Sample No. LSD09@88.0m.
 D) Arsenopyrite, sphalerite, galena and chalcopyrite assemblage. Sample No. LSD14@88.1m.
 E) Electrum, galena and chalcopyrite inclusions in pyrite. Sample No. LDD03A@50.7m.
 F) Free electrum grain enclosed by pyrite. Sample No. LRD67@43.0m.

Galena

Galena is rarely found at LCT, and where it does occur it is found in Stage 1 and 2 veins. The occurrence is mostly limited to the base metal-enriched veins of Stage 2, which are located in the deeper part of the stockwork veins. It is associated with pyrite, chalcopyrite, sphalerite and arsenopyrite, and shows an average grain size of 100 μm across (Figs. 4.16B, C and D).

Arsenopyrite

A minor amount of arsenopyrite occurs locally in Stages 1 and 2. It is only found in the veins and is commonly associated with pyrite, chalcopyrite, sphalerite and galena (Fig. 4.16D). It commonly shows euhedral rhombic shape, with a grain size of less than 100 μm .

Electrum and native gold

A trace amount of electrum was identified in Stage 2 veins under the microscope. It commonly occurs as an inclusion of the vein-located pyrite (Fig. 4.16E), but it is also occasionally found as free grain in the veins (Fig. 4.16F). Although electrum and native gold are mostly intimately associated with pyrite, they also occur together with other sulphides such as chalcopyrite, sphalerite, galena and arsenopyrite. The grain varies in size from <10 to 100 μm . Additional microprobe analysis on the electrum found in Stage 2 veins indicated that some can be chemically classified as native gold (see Chapter 4.5 in details).

4.4.2. BHX ore minerals

Eight ore minerals were identified in the samples from BHX, including pyrite, chalcopyrite, sphalerite, galena, arsenopyrite, electrum, native silver and stephanite. These are mostly hosted in veins and a minor amount of them is present in the wall rock. The electrum, native silver and stephanite were classified based on the chemical composition analysed by microprobe (see Chapter 4.5 in details). Each ore mineral is described below in detail:

Pyrite

Pyrite is the most abundant sulphide at BHX, as it occurs in syn- and post-mineralisation stages including Stages 1, 2, 3, 4 and 6 (Fig. 4.7). Pyrite is mostly found as disseminated and aggregated assemblages in the vein/veinlet, whereas it is also sparsely present in the wall rock. It is commonly associated with chalcopyrite, sphalerite, galena, arsenopyrite, electrum and native silver (Figs. 4.17A, B, C, D, E, F and G), and shows a size range of several hundreds μm to 2 mm.

Chalcopyrite

Chalcopyrite is frequently found in veins/veinlets of syn-mineralisation stages (i.e., Stages 1 to 3) and forms as inclusions of pyrite as well as free grains, closely associated with pyrite, sphalerite, galena, native silver and stephanite (Figs. 4.17A, B and H). A trace amount of patchy chalcopyrite is also present in the wall rock associated with pyrite and sphalerite. The chalcopyrite grains are normally less than 100 μm in size.

Sphalerite

Sphalerite is commonly found at BHX, and mostly occurs in veins/veinlets of syn-mineralisation stages (i.e., Stages 1 to 3). It is commonly associated with pyrite, chalcopyrite, galena, arsenopyrite, electrum, native silver and stephanite (Figs. 4.17A, B, F and H). A trace amount of sphalerite is also present in the wall rock, associated with pyrite and chalcopyrite. The grain size of sphalerite ranges from a few tens to 500 μm (100 μm in average).

Galena

A minor amount of galena is locally present in the veins/veinlets of Stages 2 and 3, commonly occurring as inclusions of pyrite (Figs. 4.17B and C). The occurrence is confined to the sample from the deeper part of the drill holes, which again suggests that galena occurs at the deeper part of the BHX mineralisation system. It commonly shows a size range less than 100 μm across.

Arsenopyrite

Arsenopyrite is locally present in the veinlets of Stage 3 and shows a light yellowish colour under the microscope. It is intimately associated with pyrite, electrum and sphalerite, and grains are normally several tens (<100) μm in size (Figs. 4.17D and F).

Electrum

Electrum occurs in veins/veinlets of Stages 1 and 3 forming as inclusions in pyrite as well as free grains. It is closely associated with pyrite, chalcopyrite, sphalerite, galena and arsenopyrite (Figs. 4.17D, E and F). The grain size of electrum varies from several tens of μm (<100 μm) in size in the Stage 1, and range in size from 100 to 800 μm across, with an average of 300 μm , in Stage 3.

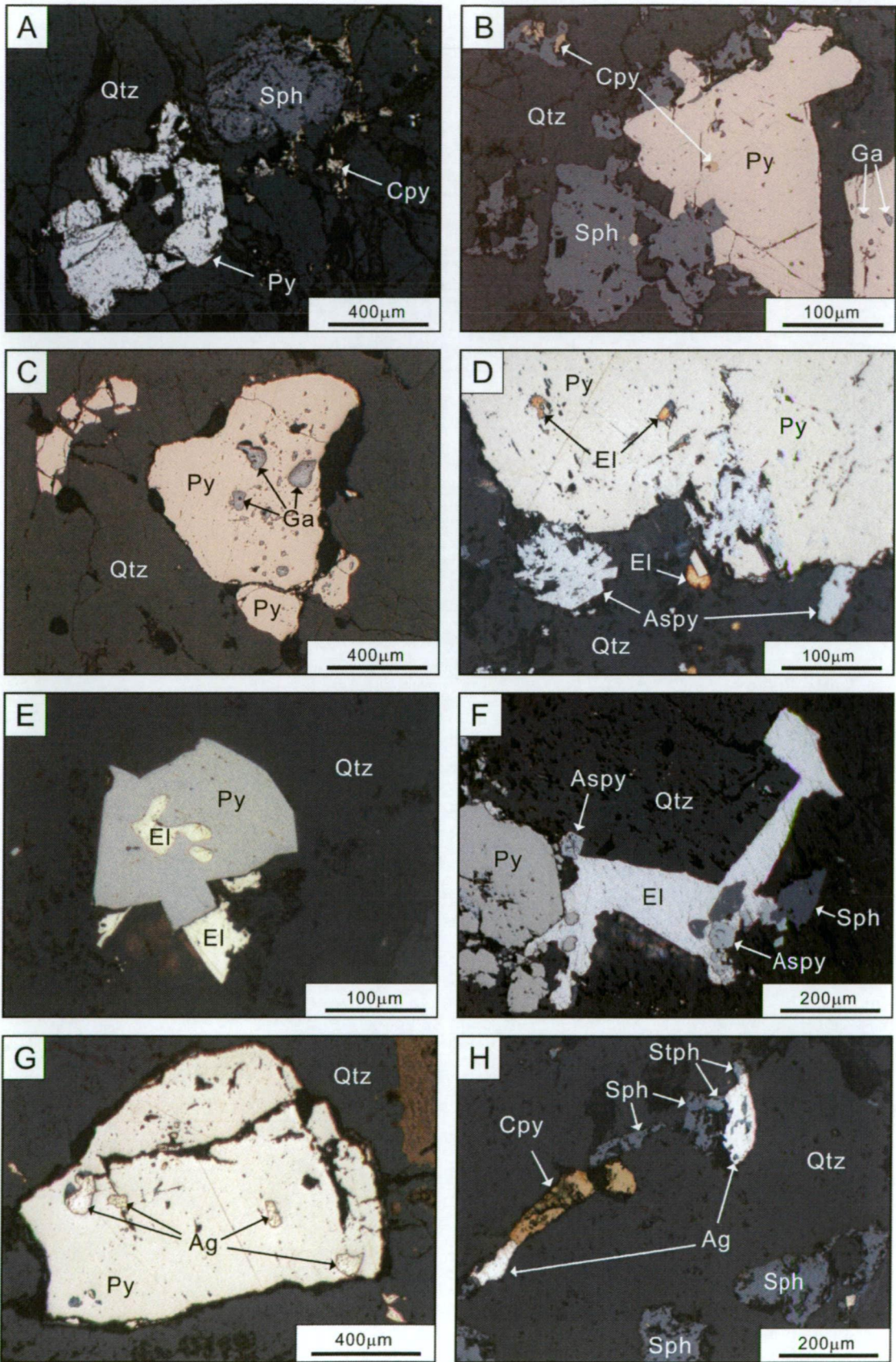


Fig. 4.17. Photographs of ore minerals of the BHX deposit (rl). Abbreviations: Py=pyrite, Cpy=chalcopyrite, Sph=sphalerite, Qtz=quartz, Ga=galena, Aspy=arsenopyrite, El=electrum, Ag=ative silver, Stph=stephanite, rl=reflected light.

- A) Pyrite, sphalerite and chalcopyrite assemblage. Sample No. HDD07@179.6m.
- B) A large pyrite crystal with sphalerite, chalcopyrite and galena. Sample No. HSD02@90.3m.
- C) Galena inclusions of pyrite. Sample No. HSD02@90.3m.
- D) Pyrite, arsenopyrite and electrum assemblage. Note electrum occurs as inclusion in pyrite as well as free grain. Sample No. HDD10@88.0m.
- E) Pyrite and electrum assemblage. Electrum occurs as inclusion of pyrite and free grain. Sample No. HDD07@126.0m.
- F) Electrum, pyrite, arsenopyrite and sphalerite assemblage. Sample No. HDD09@108.4m.
- G) Native silver inclusions in pyrite. Sample No. HDD08@74.8m.
- H) Sphalerite, chalcopyrite, native silver and stephanite assemblage. Sample No. HDD10@191.6m.

Native silver

A minor amount of native silver is present at BHX, occurring both as inclusions in pyrite and free grains in veins/veinlets of Stages 2 and 3. It is commonly associated with other sulphides such as pyrite, chalcopyrite, sphalerite and arsenopyrite (Figs. 4.17G and H). The grain size varies from 50 to 200 μm across.

Stephanite

A trace amount of stephanite (Ag_5SbS_4) was identified at BHX using microprobe analysis. The presence of stephanite is confined to the Stage 2 vein and it is closely associated with native silver, chalcopyrite and sphalerite (Fig. 4.17H). The grains are normally less than 100 μm in size and typically show a light greyish colour under the microscope.

4.5. Gold fineness

The gold fineness of electrum in a hydrothermal system has been used to classify the genetic type of the deposits and to indicate the geochemical behaviour of gold and silver transport (e.g., Huston et al., 1992). In an epithermal mineralised system, the gold fineness of electrum varies widely and this variation is believed to be affected by depositional conditions such as depth, acidity and temperature (Spycher and Reed, 1989). Thus, the gold fineness of electrum in the LCT and BHX deposits was determined and studied here to understand the geochemical characteristics of the gold and silver deposition. In addition, this analysis aimed to chemically identify unknown gold- and silver-bearing minerals.

The chemical composition of the measured gold- and silver-bearing minerals at LCT and BHX was calculated and listed in Table 4.1 and the variation of the gold fineness is presented in Fig. 4.18. The data are classified based on syn-mineralisation stages including Stage 2 at the LCT deposit and Stages 1 to 3 at the BHX deposit. The gold fineness value of the electrum from LCT shows a range of 520 to 867, indicating that some (above 800) can be compositionally classified as native gold. The range of the gold fineness values from Stages 1, 2 and 3 at BHX are 317 to 558, 0 to 167 and 0 to 267, respectively. This indicates that most of the electrum of Stage 2 and 3 can be compositionally classified as native silver. This analysis also recognised some unknown ore minerals that were found to be stephanite (Ag_5SbS_4). Moreover, it appears that the range of fineness values is distinct between the LCT and BHX deposits, indicating that LCT is enriched in gold, whereas BHX is enriched in silver.

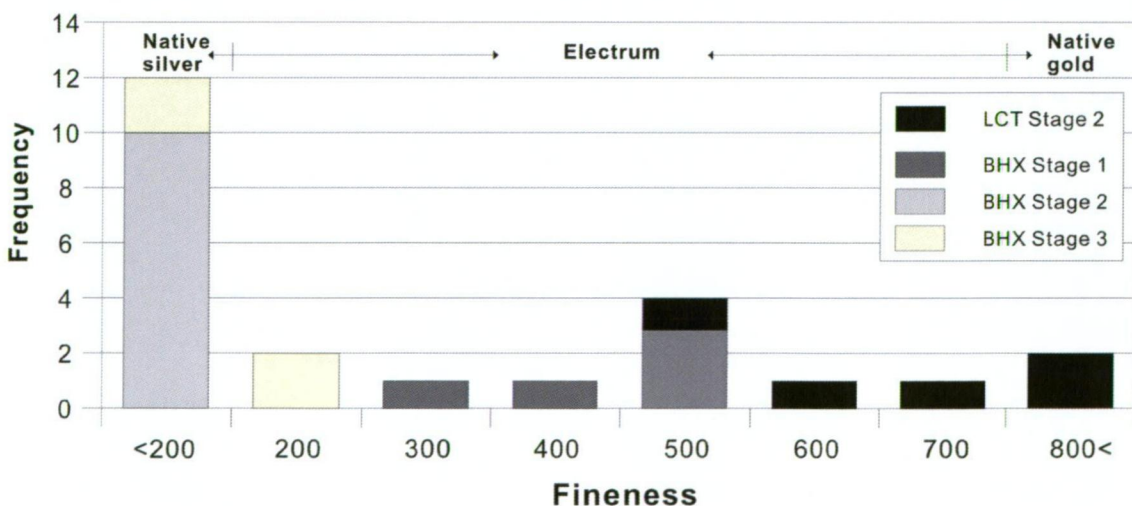


Fig. 4.18. Histogram of gold fineness values in electrum, native gold and native silver from the syn-mineralisation stages of the LCT and BHX deposits.

Table 4.1. Summary of microprobe analysis (wt%) of gold- and silver-bearing ore minerals from the LCT and BHX deposits, Lao PDR.

Sample No.	Au	Ag	S	Fe	Cu	As	Sb	Pb	Se	Zn	Te	Si	Total	Fineness	Assigned mineralisation stage	Remark
LCT																
LRD67@43.0m	73.1	26.9	0.3	1.1									101.4	731	Stage 2	
LDD03A@50.7m-A	51.2	47.2	0.2	1.6									100.2	520	Stage 2	
LDD03A@50.7m-B	60.4	39.1	0.3	1.7									101.4	607	Stage 2	
LSD05@90.8m-A	86.8	13.4	0.1	<DL									100.3	866	Stage 2	
LSD05@90.8m-B	86.8	13.3	0.2	<DL									100.3	867	Stage 2	
BHX																
HSD02@90.3m	48.3	52.5	0.3	1.3	<DL				<DL	<DL	<DL		102.3	479	Stage 1	
HDD07@126.0m-A	56.3	44.6	<DL	0.3	<DL	<DL	<DL	<DL	<DL	<DL	<DL	<DL	101.2	558	Stage 1	
HDD07@126.0m-B	55.1	44.9	<DL	0.1	<DL	<DL	<DL	<DL	<DL	<DL	<DL	<DL	100.2	551	Stage 1	
HDD07@126.0m-C	56.1	45.8	0.1	<DL	<DL	<DL	<DL	<DL	<DL	<DL	<DL	<DL	102.0	550	Stage 1	
HDD13@47.5m	31.1	66.8	0.3	1.1	<DL	<DL	<DL	<DL	<DL	<DL	<DL	<DL	99.3	317	Stage 1	
HDD06@58.8m-A	<DL	99.8	0.2	0.1	0.3	<DL	<DL	0.1	<DL	<DL	<DL	0.3	100.7	0	Stage 2	
HDD06@58.8m-B	<DL	90.2	3.0	2.9	<DL	<DL	<DL	<DL	<DL	<DL	<DL	0.4	96.4	0	Stage 2	
HDD06@58.8m-C	<DL	94.8	0.4	0.4	0.2	0.1	0.1	<DL	0.9	<DL	<DL	2.5	99.2	0	Stage 2	
HDD06@58.8m-D	0.2	71.5	10.2	1.8	2.8	<DL	8.0	<DL	2.8	<DL	3.9	0.5	101.8		Stage 2	Stephanite
HDD06@58.8m-E	<DL	70.1	13.0	0.3	10.0	<DL	8.6	<DL	<DL	<DL	<DL	0.1	102.1		Stage 2	Stephanite
HDD08@74.8m	14.6	78.8	0.1	0.1	0.1	<DL	0.1	<DL	<DL	<DL	<DL	<DL	93.8	156	Stage 2	
HDD08@228.5m	<DL	94.2	0.7	0.2	<DL	<DL	1.2	<DL	<DL	<DL	<DL	<DL	96.4	0	Stage 2	
HDD10@191.4m-A	<DL	70.6	12.6	0.1	1.2	0.1	9.2	<DL	0.1	0.1	<DL	<DL	94.0		Stage 2	Stephanite
HDD10@191.4m-B	0.1	95.0	<DL	0.1	0.1	<DL	0.5	<DL	<DL	<DL	0.1	0.1	96.0	2	Stage 2	
HDD10@191.4m-C	13.5	83.7	<DL	<DL	<DL	<DL	<DL	<DL	<DL	0.1	<DL	<DL	97.3	139	Stage 2	
HDD10@191.4m-D	11.9	85.3	<DL	<DL	0.1	<DL	0.1	<DL	<DL	0.4	0.1	<DL	97.8	122	Stage 2	
HDD11@24.8m-A	16.2	81.2	0.3	0.1	<DL	<DL	<DL	<DL	<DL	<DL	<DL	<DL	97.7	167	Stage 2	
HDD11@24.8m-B	14.8	83.2	0.2	0.1	<DL	<DL	<DL	<DL	<DL	<DL	<DL	0.1	98.4	151	Stage 2	
HDD09@108.4m-A	22.5	76.1	<DL	<DL	<DL	<DL	<DL	<DL	<DL	<DL	<DL	<DL	98.5	228	Stage 3	
HDD09@108.4m-B	<DL	94.2	0.1	0.7	<DL	<DL	<DL	<DL	<DL	0.2	<DL	<DL	95.2	0	Stage 3	
HDD10@88.0m-A	25.6	70.2	0.2	0.3	<DL	<DL	0.2	<DL	<DL	<DL	0.1	<DL	96.5	267	Stage 3	
HDD10@88.0m-B	16.5	79.1	0.3	0.3	<DL	<DL	<DL	<DL	<DL	<DL	0.1	0.1	96.4	173	Stage 3	

*<DL=under detection limit

4.6. Sphalerite geochemistry

The FeS content of sphalerite can be an indicator of the physico-chemical conditions of ore-forming fluids in the hydrothermal system. Many studies have been conducted on VHMS deposits (e.g., Hannington and Scott, 1989; Khin Zaw and Large, 1996). Some studies on the FeS content of sphalerite in epithermal deposits were also undertaken to determine the ore-forming fluid characteristics (e.g., Gemmell et al., 1988; Khin Zaw and Henderson, 1993). It has been suggested that the FeS content of sphalerite can be used as a geothermometer for metamorphosed sulphide deposits (e.g., Khin Zaw, 1991; Khin Zaw and Large, 1996). In this study, the FeS contents of sphalerite from the LCT and BHX deposits are analysed and documented, focusing on the relationships with the gold and silver grade of diamond drill core samples to understand the gold and silver mineralisation.

The measured chemical composition of sphalerite from the LCT and BHX deposits are listed in the Appendix IV. The calculated FeS mole % values are present in Table 4.2 and are displayed in Fig. 4.19. The composition of sphalerite at LCT has a range from 4.9 to 11.5 FeS mole %, whereas sphalerite at BHX has a narrowed range from 2.7 to 4.5 FeS mole % with one outlier value of 6.2 FeS mole % (Fig. 4.19). The correlations between the FeS mole % of sphalerite with gold and silver assay results of each drill core sample at LCT and BHX are shown in Figs. 4.20 and 21, although some assay results of the LCT samples are missing. A weak negative correlation between FeS mole % and silver grade was found ($R^2=-0.32$), but the correlation with gold grade is not clear.

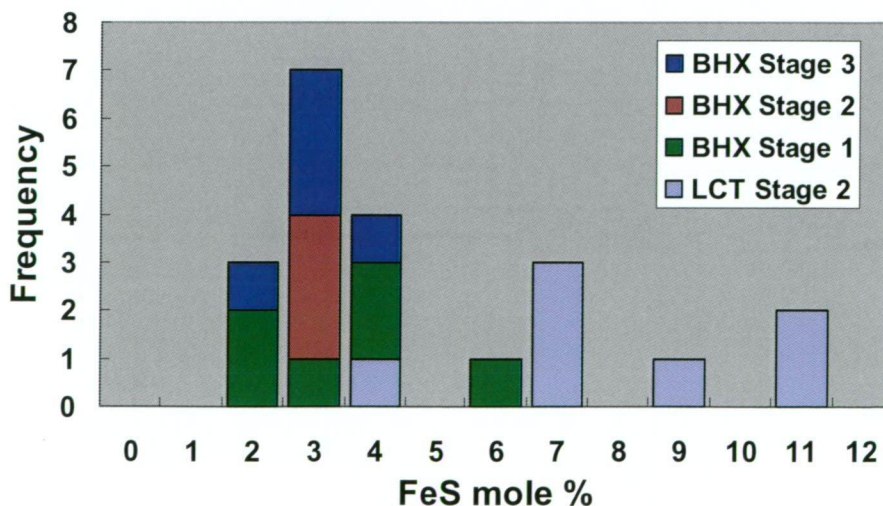


Fig. 4.19. Histogram of FeS mole % in sphalerite from the LCT and BHX deposits, Lao PDR.

Table 4.2. Summary of microprobe analysis of average FeS mole % composition in sphalerite with gold and silver grade of diamond drill core samples from the LCT and BHX deposits. n/a=not available.

Sample No.	No. of grain (spot)	FeS mole %	Au g/t	Ag g/t	Assigned stage
LCT					
LSD02@94.8m	3	11.46	0.04	0.7	Stage 2
LSD05@90.0m	4	9.72	0.74	6.4	Stage 2
LSD09@88.0m	6	4.88	n/a	n/a	Stage 2
LSD14@103.6m	5	7.30	0.07	0.9	Stage 2
LRD67@43.0m	5	7.52	n/a	n/a	Stage 2
LRD67@50.0m	4	11.98	n/a	n/a	Stage 2
LDD03A@75.0m	15	7.88	0.29	n/a	Stage 2
BHX					
HSD01@56.0m	2	3.77	0.03	4.1	Stage 1
HSD02@90.3m	7	4.40	0.06	5.0	Stage 1
HSD04@86.0m	5	2.76	0.02	1.0	Stage 1
HSD08@77.0m	4	6.19	0.10	3.1	Stage 1
HDD07@126.0m	1	2.79	71.20	55.1	Stage 1
HDD08@74.8m	3	3.38	7.23	176.0	Stage 3
HDD08@228.5m	1	3.04	0.30	19.2	Stage 2
HDD09@99.2m	2	4.17	43.50	56.8	Stage 3
HDD09@108.4m	2	2.73	56.70	771.0	Stage 3
HDD10@88.0m	1	3.80	3.20	57.7	Stage 2
HDD10@191.4m	2	3.89	3.50	51.5	Stage 2
HDD11@24.8m	2	3.20	10.20	581.0	Stage 3
HDD11@249.0m	1	3.24	0.40	12.8	Stage 3
HDD13@198.0m	2	4.52	5.20	5.7	Stage 1

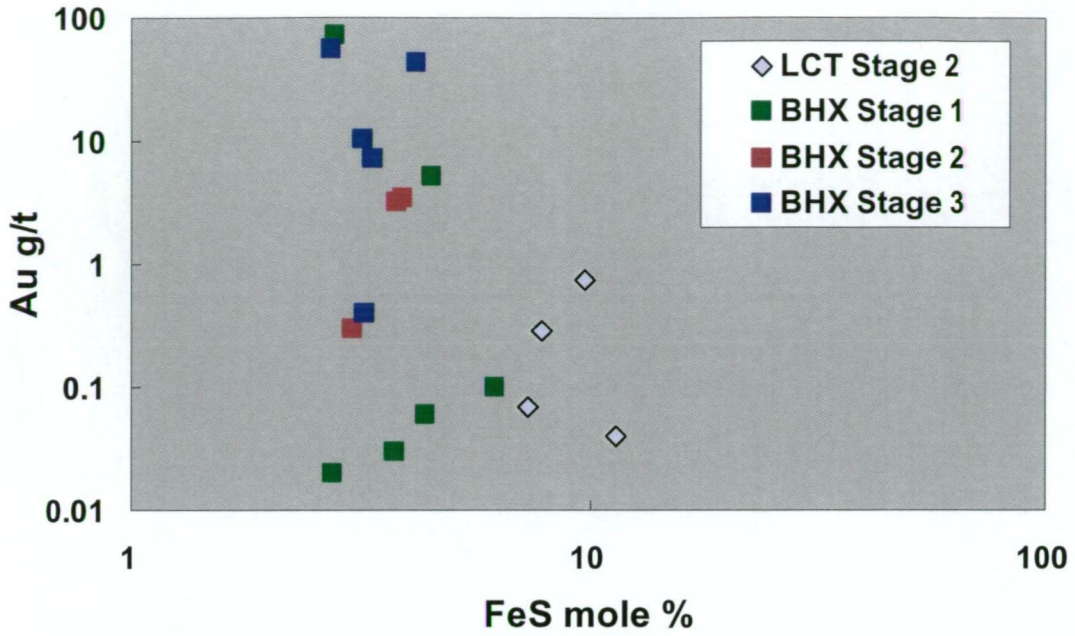


Fig. 4.20. Plot of FeS mole % in sphalerite and gold assay (g/t) of the sample from LCT and BHX deposits, Lao PDR.

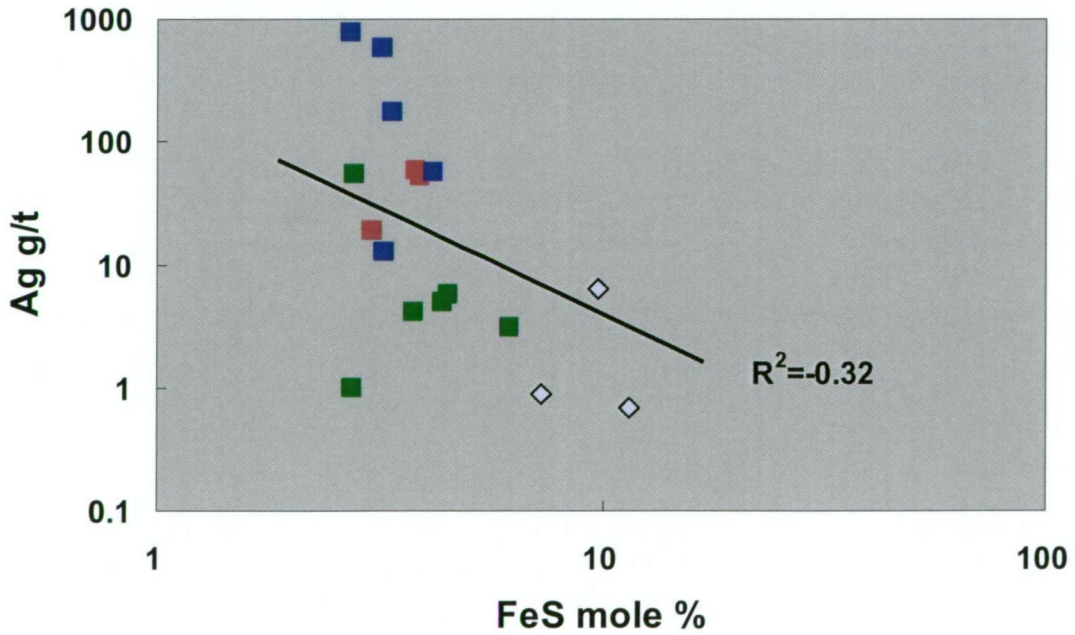


Fig. 4.21. Plot of FeS mole % in sphalerite and silver assay (g/t) of the sample from LCT and BHX deposits, Lao PDR.

4.7. Discussion

This section discusses the mineralisation characteristics of the ore-bearing stages of the LCT and BHX deposits, and the chemical compositions of ore minerals such as electrum, native silver, native gold and stephanite as well as sphalerite FeS content. In addition, these data will be discussed further with fluid inclusion data in Chapter 6.

Stage 2 mineralisation of LCT

The observed characteristics of the Stage 2 mineralisation at the LCT deposit are compatible with those collected from the Au–Ag epithermal deposits of the Hauraki goldfield in New Zealand (Christie et al., 2007). The vein textures observed in Stage 2 such as stockwork and crystalline and abundance of sulphides are typical of the deeper part (>800m depth) of the Au–Ag epithermal systems in the Hauraki goldfield. The vein infill of Stage 2 consists of a quartz and sulphide assemblage, including pyrite, chalcopyrite, sphalerite, galena, arsenopyrite, electrum and native gold: these mineral assemblages are also a main product in the Hauraki goldfield epithermal systems, except for arsenopyrite which is not reported. The alteration in the host rock at LCT is dominated by quartz, adularia, sericite, chlorite and illite assemblages, which can be correlated to the typical alteration features of the epithermal systems in the Hauraki goldfield (Christie et al., 2007).

Stage 1 mineralisation of BHX

The characteristics of the Stage 1 mineralisation at BHX are stockwork veins, very similar to the Stage 2 at LCT, and comparable to the epithermal systems of the Hauraki goldfield in terms of vein texture, mineralogy and alteration features. As well as stockwork veins, the ore minerals including pyrite, chalcopyrite, sphalerite, galena and electrum are commonly observed in the epithermal deposits of the Hauraki goldfield (Christie et al., 2007). In addition, the gangue minerals of quartz, calcite and sulphides with the associated alteration of sericite, chlorite, quartz and adularia assemblages are considered to have similar characteristics of those in the Hauraki goldfield epithermal systems.

Stage 2 mineralisation of BHX

The Stage 2 mineralisation at BHX is clearly distinct from Stage 1 of the stockwork vein system. The Stage 2 mineralisation occurs as a massive vein and brecciation, locally hosted in the shear zone of the N–S trend with a steep westerly dipping fault. The vein and breccia consists of quartz, calcite, sulphides, sericite and chlorite, and notably includes silver-enriched ore minerals such as

native silver and stephanite. It was recognised that a weak alteration zone (<1 m) associated with this mineralisation stage is developed. These characteristics can be similar to other Ag-enriched epithermal systems such as the Santo Nino deposit in Mexico, where the formation of mineralisation is strongly controlled by fault structures (Gemmell et al., 1988).

Stage 3 mineralisation of BHX

The Stage 3 mineralisation at BHX is veinlet-hosted in a N–S trending narrow shear zone with a steep westerly dipping fault, similar to Stage 2. However, the occurrence of this stage is different from Stage 2, in terms of vein texture and ore and gangue mineral assemblages, particularly marked by the sulphide and carbonate assemblage veinlets. The sulphides are pyrite, chalcopyrite, sphalerite, galena and arsenopyrite associated with silver-enriched electrum and native silver. The locally associated carbonate minerals consist of dolomite and ankerite. The presence of coarser grained electrum and native silver, up to several hundreds μm grain size, are markedly noted. The occurrence of this mineralisation stage may also be compatible to the Ag-enriched epithermal systems in Mexico, and this is further discussed with fluid inclusion data in Chapter 6.

Gold fineness

The gold fineness of electrum as well as native gold, native silver and stephanite shows a distinct distribution and variation among the syn-mineralisation stages at the LCT and BHX deposits. The Stage 2 mineralisation at LCT and Stage 1 mineralisation at BHX both have relatively high gold fineness values of electrum, while the mineralisation of Stages 2 and 3 at BHX have a relatively low gold fineness value of electrum. These results can be correlated with the electrum fineness behaviours in VHMS and epithermal systems, in which the behaviours appear to be different. Huston et al. (1992) studied gold fineness values of electrum from VHMS systems, and suggest that the fineness range can be used as a diagnostic tool for assessing hydrothermal fluids of the deposit. For example, the high fineness value of electrum is indicative of a high temperature hydrothermal system and it is commonly formed in the deeper part of the VHMS mineralised system, while the low and variable gold fineness is equivalent to the low temperature hydrothermal system, the shallower part of the VHMS system. In comparison, Spycher and Reed (1989) studied electrum behaviour in epithermal hydrothermal systems, and found that silver-dominated deposits correspond to the deeper part of the epithermal system where boiling is occurring, whereas the gold-dominated deposit is equivalent to the shallower part of the system where the gold deposition forms due to the mixing of boiling water with acid sulphate water. The

depositional conditions of gold and silver at LCT and BHX are further discussed with fluid inclusion data in Chapter 6.

Compositional variation of sphalerite

At the Santo Nino Ag-Pb-Zn epithermal deposit in Mexico, the sphalerite has a wide variation in colour as well as FeS content, and these relationships are documented by Gemmell et al. (1988) indicating that there is a positive correlation between the FeS content and colour of sphalerite (i.e., darker colour for samples with a higher FeS content). Furthermore, combined with the fluid inclusion study in which mantle-derived helium was found, it is considered that the formation of dark-coloured, high Fe content of sphalerite is responsible for the input of reduced magmatic fluids. On this basis, the dominance of darkened colour sphalerite at LCT and BHX may imply a reduced-magmatic-fluid interaction for the formation of sphalerite. However, the interaction of the reduced-magmatic-fluids at LCT and BHX may be limited to episodic as revealed by the values of FeS mole % of sphalerite. The LCT and BHX have a highest value of 11.98 and 6.19 mole % FeS content in sphalerite respectively, whereas the Santo Nino has a highest value of 20.1 mole % FeS content, indicating that the input of reduced-magmatic-fluid at LCT and BHX is much less than those of Santo Nino.

Hannington and Scott (1989) found that there are generally negative correlation trends between the FeS content of sphalerite with gold grade in VHMS deposits. However, no clear trend was noted at the LCT and BHX deposits between the FeS mole % of sphalerite and the assay data of diamond core samples, although there was a weak negative correlation with the silver grade of diamond core samples. In other epithermal deposits where this relationship was studied, similar poor relationships of the FeS content of sphalerite with gold grade were reported from the Chatree Au-Ag deposit in Thailand (Salam, 2007) and the Waitangi Au-Ag deposit in New Zealand (Khin Zaw and Henderson, 1993). This may be due to the complex mechanisms in the ore-forming fluid interacting with the wall rock including boiling, mixing and pH changes, as suggested by Khin Zaw and Henderson (1993).

4.8. Summary

The mineralisation characteristics of the LCT and BHX deposits are summarised below:

- At the LCT deposit, five mineralisation stages were identified including Stage 2 gold-bearing mineralisation, which mainly occurs as stockwork quartz-sulphide veins with the associated alteration of quartz, sericite, illite, pyrite and chlorite assemblages. The gold mainly occurs as electrum and native gold.
- At the BHX deposit, seven mineralisation stages were identified including three ore-bearing mineralisation stages; Stage 1, 2 and 3. Stage 1 occurs as stockwork veins of quartz, calcite and sulphide infill associated with electrum. The alteration of this stage consists of chlorite, sericite and adularia assemblages, developing in the wall rock throughout the deposit area. The following Stages 2 and 3 are locally occurring and are hosted in the N–S trending, steep westerly dipping fault. These stages are enriched in silver rather than gold as shown by the occurrence of native silver, stephanite and silver-rich electrum. The associated alteration of the Stage 2 is limited to the vein proximity (less than 1 m) and consists of a sericite, chlorite and adularia assemblage. No alteration is associated with Stage 3.
- The gold fineness values of electrum range from 520 to 867 and from 0 to 558 at the LCT and BHX deposits, respectively. The values at BHX are further divided on the basis of three syn-mineralisation stages, showing ranges of 317 to 558, 0 to 167 and 0 to 267 in Stages 1, 2 and 3, respectively. These results demonstrate that the electrum gold fineness values in Stage 2 of LCT and Stage 1 of BHX are moderately to highly Au-rich, whereas those in Stages 2 and 3 of BHX are Ag-rich.
- The sphalerite occurring at LCT and BHX is predominantly dark coloured, which can be responsible for the high Fe content. However, based on the Fe contents of sphalerite are relatively low compared to those of other epithermal systems, it is likely that the input of reduced magmatic fluid at LCT and BHX were episodic or minimal.

CHAPTER 5 PYRITE GEOCHEMISTRY

5.1. Introduction

Pyrite is a common and abundant sulphide mineral in hydrothermal ore deposits. The trace element geochemistry of pyrites can be used to understand the source of fluids and metals and as vectors in mineral exploration (e.g., Wood and Large, 2007; Large et al., in press; Meffre et al., in press). In this study, pyrite crystals which are commonly and abundantly present at the LCT and BHX deposits, were analysed for their trace element composition to investigate the geochemical behavior of pyrite in the mineralised systems.

The primary objectives of this study are (1) to document the trace element geochemical signature of pyrite from different syn-mineralisation stages of the LCT and BHX deposits, (2) to determine the residence of gold and the associated elements in the pyrite of the LCT and BHX hydrothermal systems and (3) to use the trace element data as indicators and discriminators for characterising similar mineralised systems.

5.2. Analytical methods

Preparation

A total of twenty-one polished mounted samples, including six samples from LCT and fifteen samples from BHX, were selected to study the pyrite trace element geochemistry using the LA-ICPMS technique developed at CODES, University of Tasmania (see Large et al., in press). Prior to the analysis, all the samples were etched with nitric acid to clarify the internal texture of pyrites. This etching was conducted by placing a few drops of nitric acid (70% HNO₃) on the surface of the polished mounts and by subsequent rinsing with water after 20 seconds. In most cases, pyrite did not show any internal texture, but some from the BHX samples show a distinct textural variation.

Analysis

Spot and line analyses were used for this study. The spot analysis was dominantly conducted on the homogeneous pyrite, and line analysis was performed focusing particularly on the pyrite with distinct internal textures. For spot analysis, the targeted pyrite samples were pre-ablated with the

laser to remove surface contamination (1 Hz pulse for 5 s), followed by analysis of the gas background (30 s) and analysis of the pyrite (70 s). The samples were normally ablated with a laser beam size of either 15 or 30 μm in diameter with 10 Hz pulse rate. For lines across the surface of the samples, the laser was set to 8 μm in diameter with 10 Hz pulse rate without pre-ablation. Instrumental mass bias and machine drift were monitored by analysing 4 spots of an in-house Fe, Li, B glass standard every hour.

Data reduction and interpretation

The measured data were compiled and the concentrations were calculated using Microsoft Excel. The data were firstly plotted as a line graph of contents versus time, and the integration times for the background and signal were selected for each analysis. This was straightforward for the analysis of standards which give a flat signal after an initial setting period of about 10 seconds. To calculate the signal intensity, the counts were averaged over the selected interval and the average background counts subtracted. Analyses of pyrite grains selected from LCT and BHX were generally more complex than standards and require careful interpretation of time charts and the selection of integration intervals, as they commonly include inclusions of some other minerals. Interpretations tend to be element dependent, based on the chemistry of the sulphide and knowledge of associated minerals in the sample.

Once integration intervals have been selected for each analysis, the data were compiled in an Excel spreadsheet, where the counts are corrected for instrument drift and converted to concentration (ppm). To be able to quantify an analysis the concentration of one element, the initial standard, needed to be known. For most sulphides, stoichiometric concentrations for Fe and Cu were assumed. The drift was calculated by comparing the average counts-per-second, normalised to the intensity of the internal standard, of the two standards run at the beginning and end of a set of analyses. The unknowns were then corrected using a linear regression. The average counts-per-seconds of the standard analyses were used to calculate ppm. The detection limits (DL) is herein defined as the lowest concentration that can be confidently measured above the background. The DL varies with spot size, being larger for small spots since there are less counts per ppm.

5.3. Pyrite morphology and occurrence

On the basis of microscopic studies, three types of pyrite texture were identified, including (1) homogeneous (Fig. 5.1A); (2) multiple overgrowth (Figs. 5.1B and C); and (3) spongy core with

euohedral rim (Fig. 5.1D). The homogeneous texture dominantly occurs in the both vein and wall rock pyrite samples of LCT and BHX, whereas the presence of the multiple overgrowth texture is limited to the pyrite in the Stage 3 vein at BHX. The spongy core with euohedral rim texture occurs in wall rock samples at LCT and BHX, but is the most common in the distal part of the ore zones.

5.4. Result

A total of 26 elements including Ti, Cr, Mn, Fe, Co, Ni, Cu, Zn, As, Se, Zr, Mo, Ag, Cd, Sn, Sb, Te, Ba, La, W, Au, Tl, Pb, Bi, Th and U were measured for the pyrite grains from LCT and BHX. All the measured data are listed in Appendix V. Of the elements analysed Ti, Mn, Co, Ni, Cu, Zn, As, Zr, Ag, Sb, Ba, Au, Tl, Pb and Bi are commonly above detection limit and they have a wide range of values (Fig. 5.2). Many of the elements measured are present in small mineral inclusions (5 micron or less) within the pyrite crystal or crystal aggregate. Only a few elements are present as solid solution within the pyrite structure (e.g., As and low level Au). The chalcophile elements (e.g., Zn, Pb, Cu, Mo, Bi, Sb, W) are generally concentrated within mineral inclusions which crystallised close to the time of pyrite growth. The least mobile lithophile elements (Ti, Al, Zr, Cr) tend to occur in various resistant phases which existed prior to pyrite growth (e.g., zircon, rutile) and were included within the pyrite (see Large et al., in press for further discussion).

LCT pyrite

The pyrite at LCT has trace element concentrations ranging from below the detection limit to close to 1 % and each grain shows a large variation (up to 3–4 orders of magnitude) (Figs. 5.2A and B). Some elements such as Cu, As and Pb are present at high concentration (>100 ppm) in both the Stage 2 vein pyrite and wall rock pyrite. Au concentration varies between 3 ppm with maximum values up to 200 ppm, with only a little enrichment in the veins compared to the wall rock (Fig. 5.2.A).

BHX pyrite

The trace element concentrations in the pyrite at BHX also have a wide range from 0.01 ppm to more than a thousand ppm (Figs. 5.2C, D and E). Pyrites in the Stage 1 veins are enriched in Cu, As and Pb (>100 ppm), similar to the Stage 2 vein pyrite from LCT. However, unlike LCT, As, Ag and Au are significantly enriched compared to the values in the wall rock pyrite (Fig. 5.2C). Pyrite from the Stage 3 vein have high concentrations of the chalcophile element compared to both the wall rock and Stage 1 veins (>100 ppm) (Fig. 5.2D and E).

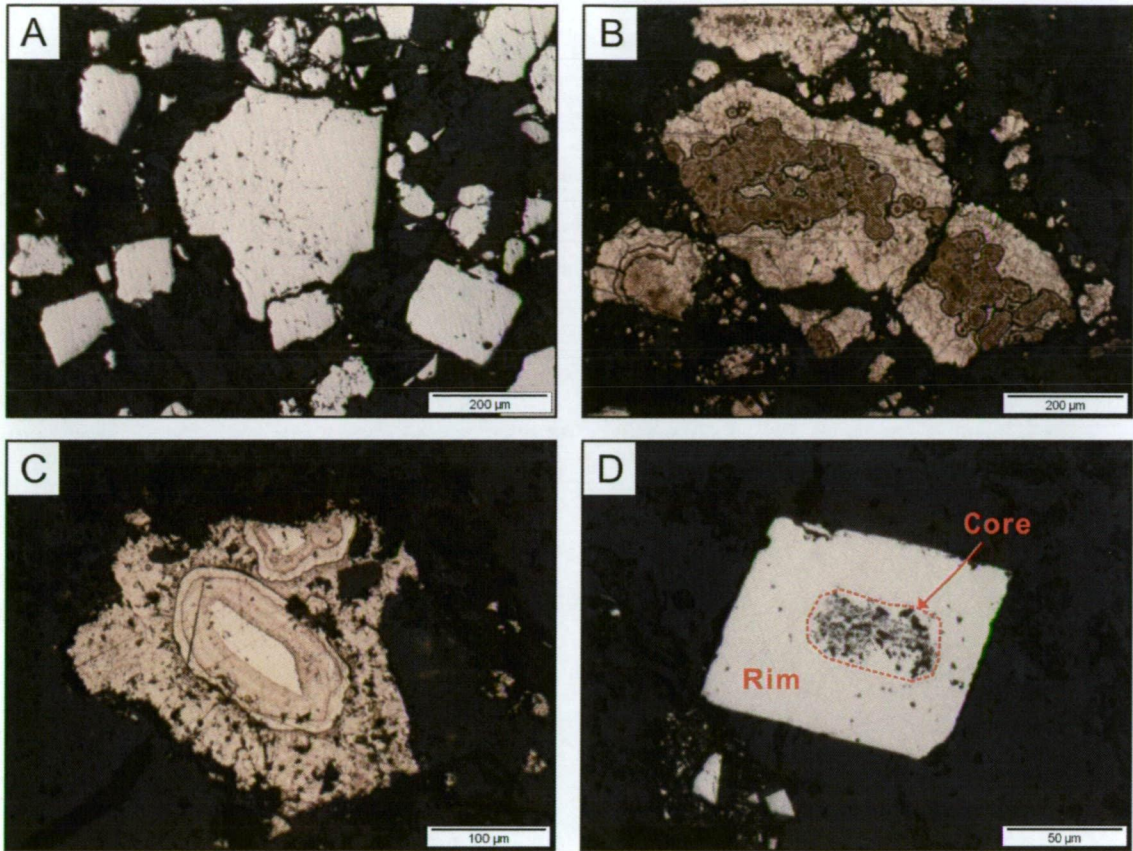


Fig. 5.1. Examples of different pyrite textures in the LCT and BHX deposits. Abbreviations: rl=reflected light.

- A) Photomicrograph (rl) showing homogeneous texture. Sample No. HDD07@71.4m.
- B) Photomicrograph (rl) showing multiple overgrowth texture. Sample No. HDD07@179.6m.
- C) Photomicrograph (rl) showing multiple overgrowth texture. Sample No. HDD11@249.6m.
- D) Photomicrograph (rl) showing spongy core with euhedral rim texture. Sample No. HSD04@57.9m.

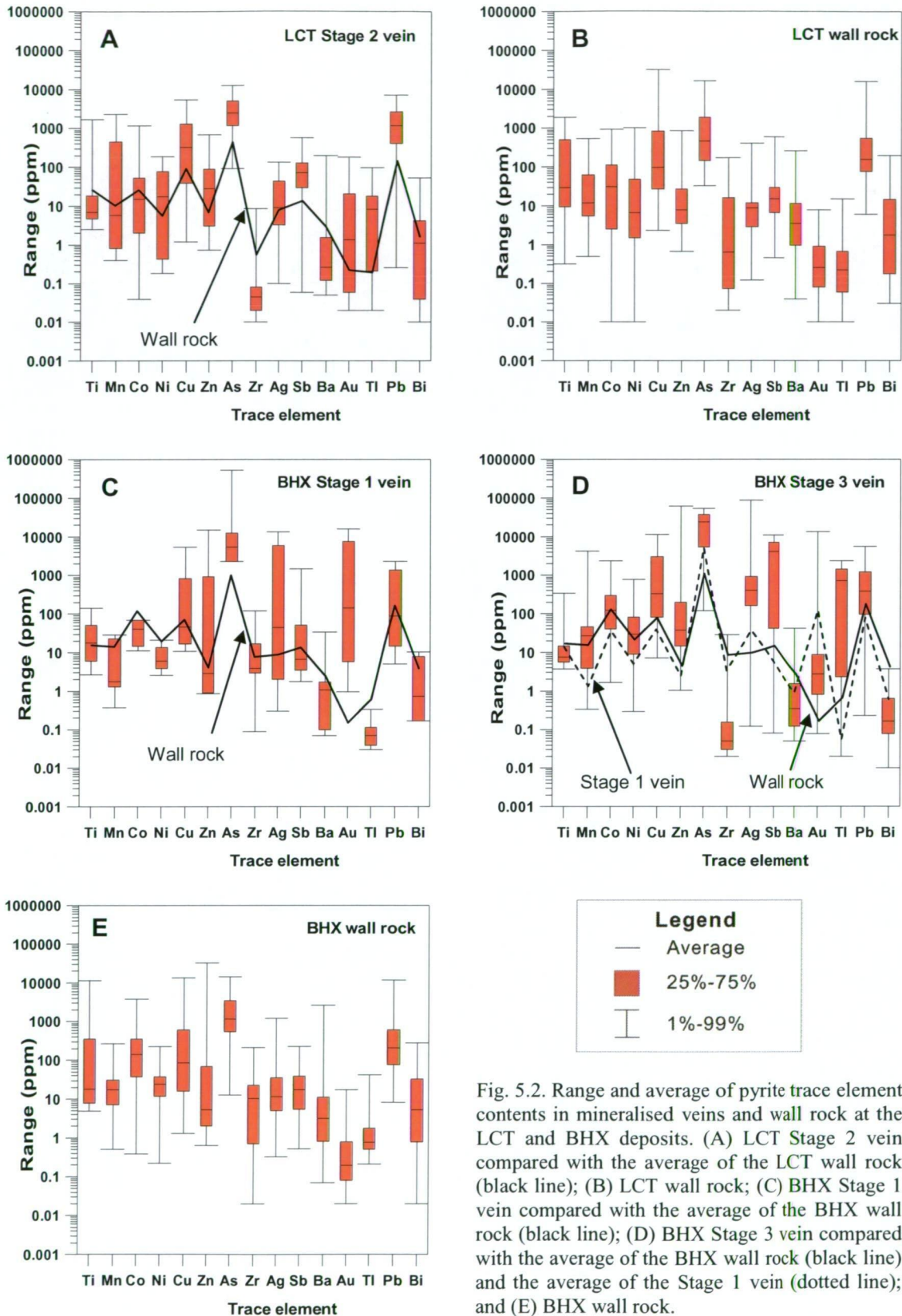


Fig. 5.2. Range and average of pyrite trace element contents in mineralised veins and wall rock at the LCT and BHX deposits. (A) LCT Stage 2 vein compared with the average of the LCT wall rock (black line); (B) LCT wall rock; (C) BHX Stage 1 vein compared with the average of the BHX wall rock (black line); (D) BHX Stage 3 vein compared with the average of the BHX wall rock (black line) and the average of the Stage 1 vein (dotted line); and (E) BHX wall rock.

5.4.1. Au and Ag concentration in pyrite

A wide range of Au and Ag is concentrated in the pyrites from the LCT and BHX deposits, having a values in the <0.1 to 10000–<100000 ppm range and 0.1–<1 to 10000–<100000 ppm range, respectively (Figs. 5.3 and 4). In the pyrite at LCT and BHX, Ag is more enriched than Au as the measured Au values have a mode in the <0.1 to 1–<10 ppm range, whereas the Ag values are mostly plotted in a range from 1–<10 to 100–<1000 ppm (Figs. 5.3 and 4). However, it is demonstrated that the very high concentrations of Au (> few hundreds ppm) and the associated Ag occur as inclusion of pyrite (see Fig. 5.10. in details).

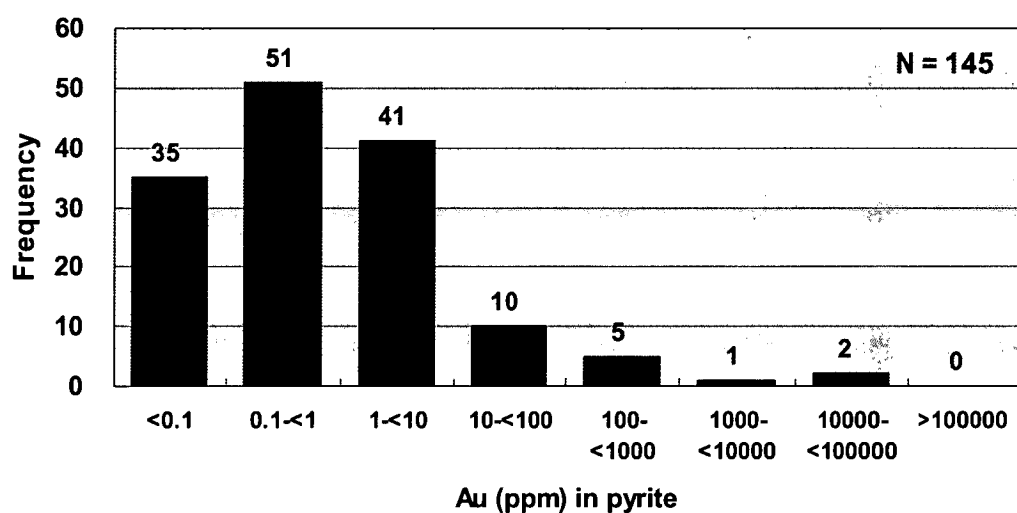


Fig. 5.3. Histogram of Au concentration in the pyrite from the LCT and BHX deposits, Lao PDR.

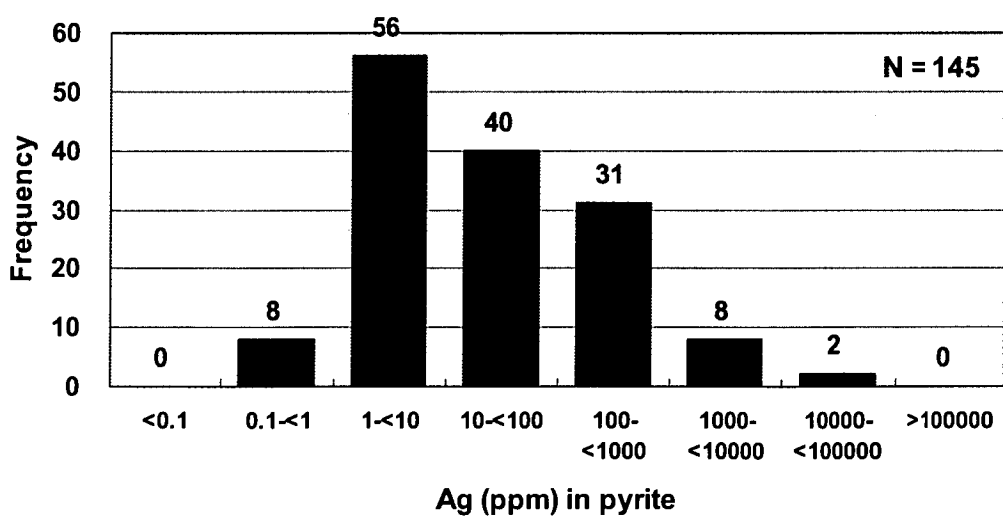
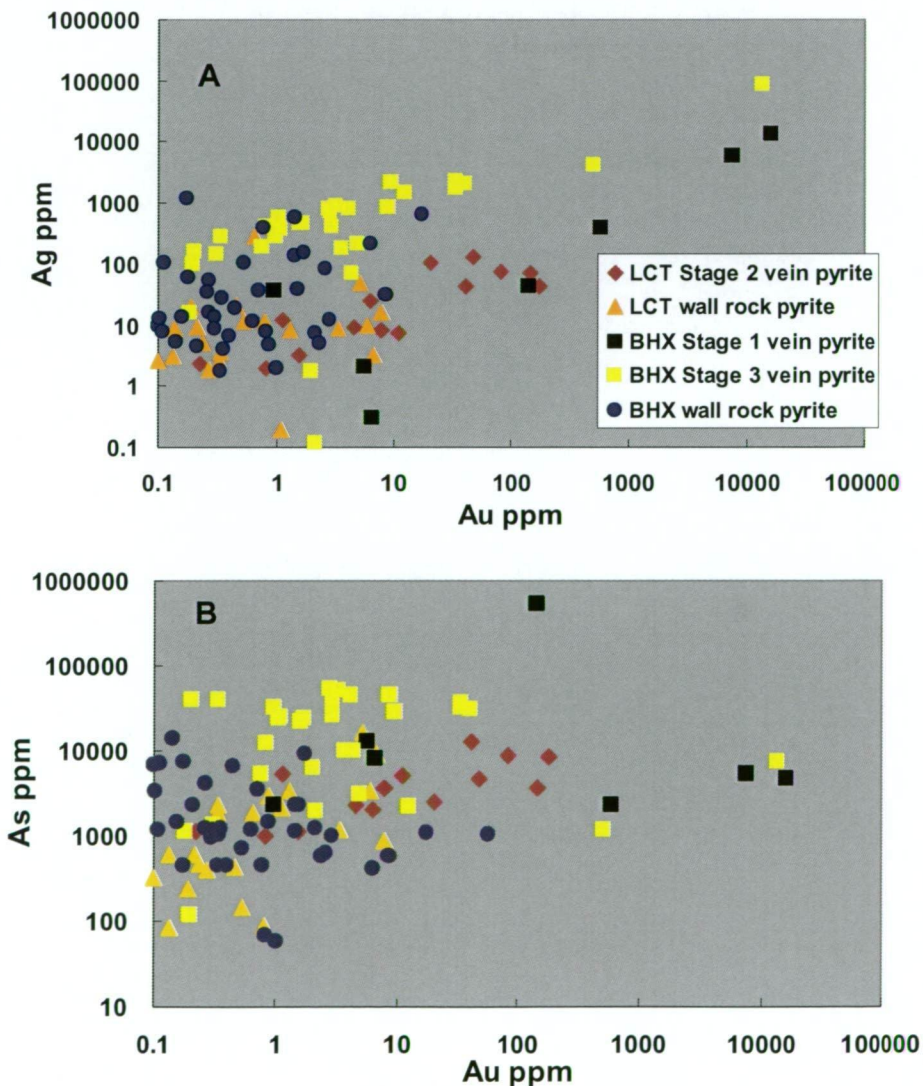
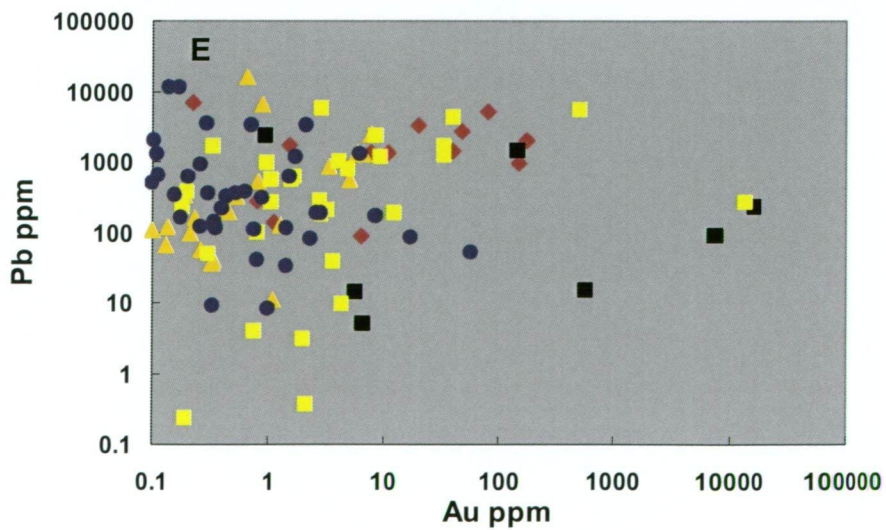
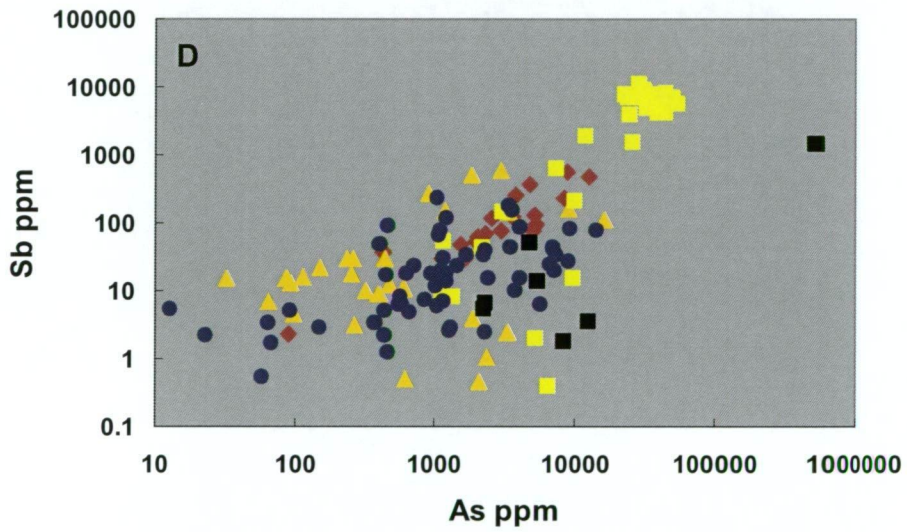
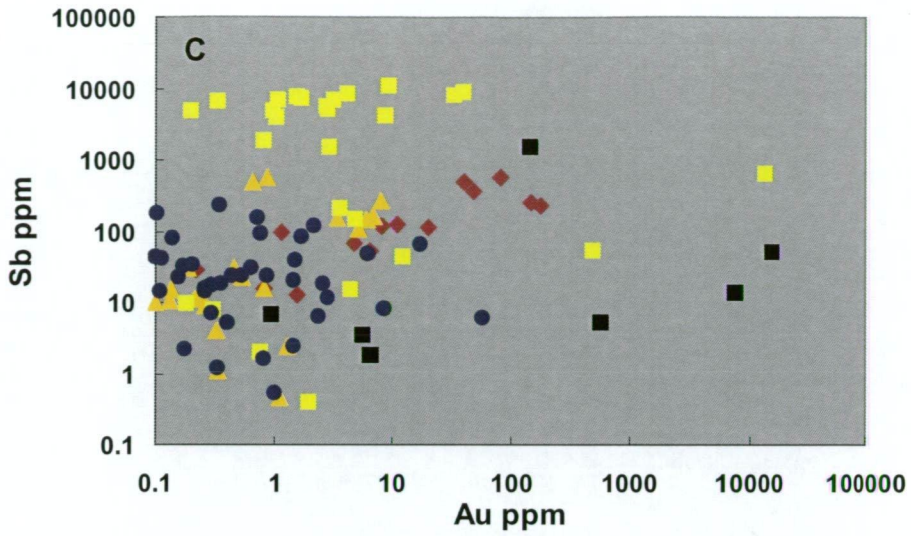


Fig. 5.4. Histogram of Ag concentration in the pyrite from the LCT and BHX deposits, Lao PDR.

5.4.2. Correlation of elements

Analysis of the trace element content of the LCT and BHX pyrites was undertaken by plotting a series of bi-variate diagrams focusing mostly on the relationship between various trace elements and Au. The strong positive trend between Au and Ag in vein pyrite shows that these two elements were enriched by similar processes (Fig. 5.5A) (this is further examined in the Discussion section). Similar positive trends can be recognised in plots of As and Sb versus Au (Figs. 5.5B and C). As and Sb are strongly correlated in the pyrite (Fig. 5.5D), but other elements such as Pb, Cu and Zn show different patterns of enrichment in the association with Au (Figs. 5.5E, F and G). In addition, the Se and Co elements are herein displayed (Fig. 5.5H) to present the variation of the elements, rather than examine the correlation (see Discussion section for details).





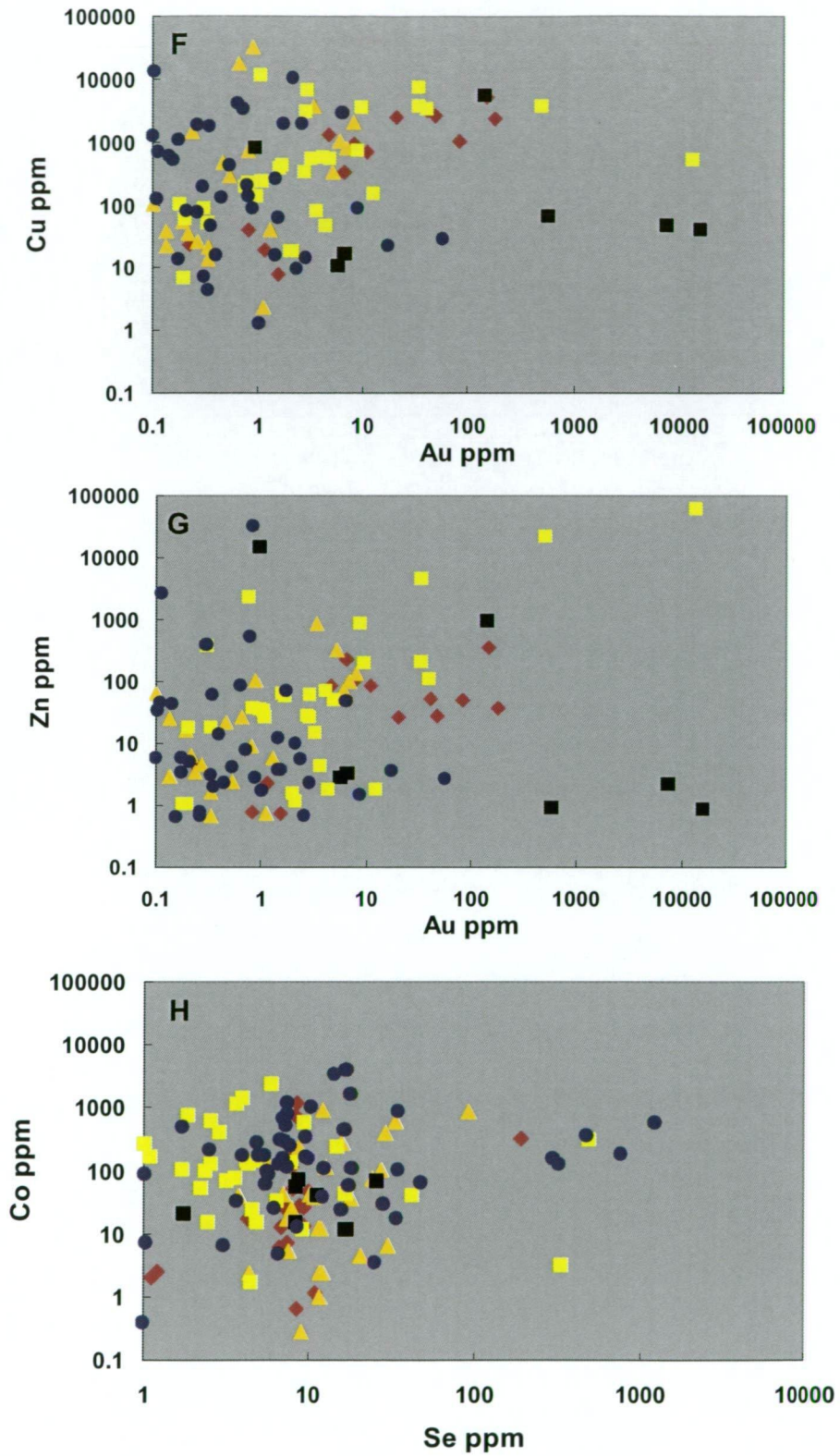


Fig. 5.5. Bi-plots of the selected elements in pyrites from the LCT and BHX deposits. (A) Ag-Au; (B) As-Au; (C) Sb-Au; (D) Sb-As; (E) Pb-Au; (F) Cu-Au; (G) Zn-Au ; (H) Co-Se.

5.4.3. Trace element variation in different textural types of pyrite

Line analyses were also performed on selected pyrite samples which have a distinct internal texture. Described below are the results for two representative textures including pyrite with multiple overgrowth and spongy core with euhedral rim textures. Each texture has a significant difference in trace element concentrations.

Three line scans on the pyrite with multiple overgrowth texture were undertaken and the results show a distinct variation in the concentration of Au and the associated elements in different growth zones (Figs. 5.6A and B and 5.7). In the pyrite in Fig. 5.5A, which has a distinct core and rim in the texture, Au is highly concentrated in the core and other elements such as As, Sb, Co, Cu, Ag, Pb and Tl are also closely associated with the Au concentration. In the pyrite with three distinct overgrowth zones in the texture (Fig 5.6B), Au is mostly enriched in the middle part of the growth zone, with close associations with some elements such as As, Ag, Cu, Pb, Co, Sb and Tl. The line analysis on the pyrite with four distinct overgrowth zones in the texture, reveals that Co, Cu, As, Ag, Sb, Tl and Pb are highly concentrated in all of the overgrowth zones except in the core (Fig. 5.7). In particular, Au and the associated elements such as Pb, Co, Ag, Cu are distinctly concentrated in the outer-middle texture. On this basis, it is indicated that Au is unevenly concentrated in different growth zones of the pyrite texture, with close associations of particular elements such as As, Ag, Cu, Pb Co, Sb and Tl, although their association is not always consistent.

The line analysis on the pyrite with a spongy core with euhedral rim texture in the wall rock reveals that trace elements in the texture have a low concentration in comparison with those of pyrites with the multiple overgrowth texture. The result shows that some elements such as Co, As, Pb and Bi are locally enriched in the transitional zone of spongy core and euhedral rim, but most of the measured elements including Ti, Co, Cu, As, Ag, Sb, Au, Pb and Bi in the core and the rim are depleted (Fig. 5.8).

5.4.4. Trace element variation in the mineralised veins and the wall rock

To simply compare between the mineralised and the wall rock pyrites of the LCT and BHX deposits, the average values of the measured elements in each unit were used. At LCT, the Stage 2 vein pyrite has higher Au and Tl contents than those in the wall rock pyrite (Fig. 5.9A). Similarly the Stage 1 vein pyrite at BHX is enriched in Au, Ag and As compared to those in the wall rock pyrite (Fig. 5.9B). The Stage 3 vein pyrite at BHX is strongly enriched in Au, Tl, Sb,

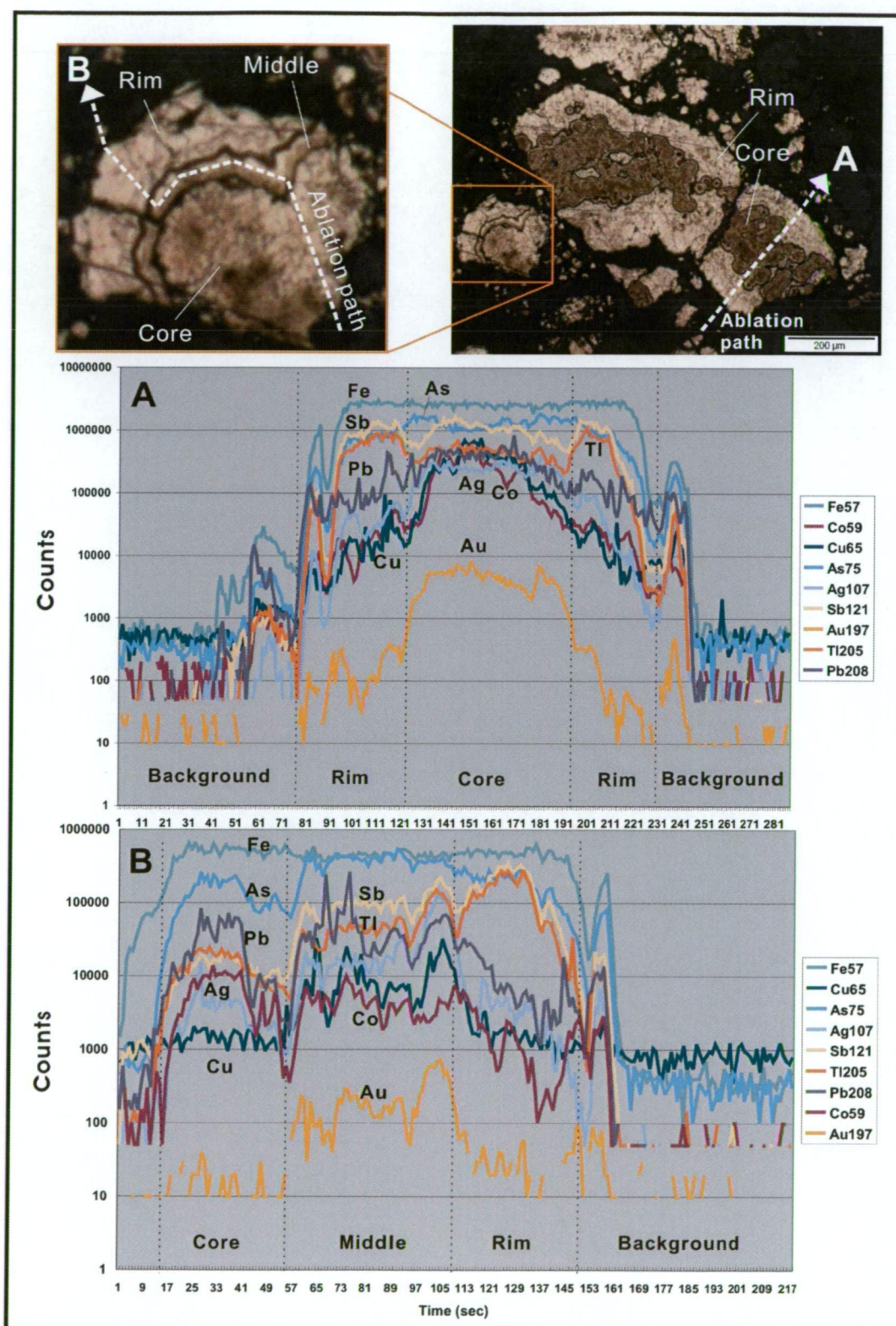


Fig. 5.6. Time chart of the selected LA-ICPMS line analyses of pyrite with multiple overgrowth zone texture from the BHX deposit, showing enrichment of Fe, Cu, As, Ag, Sb, Tl, Pb, Co and Au. Sample No. HDD07@179.6m.

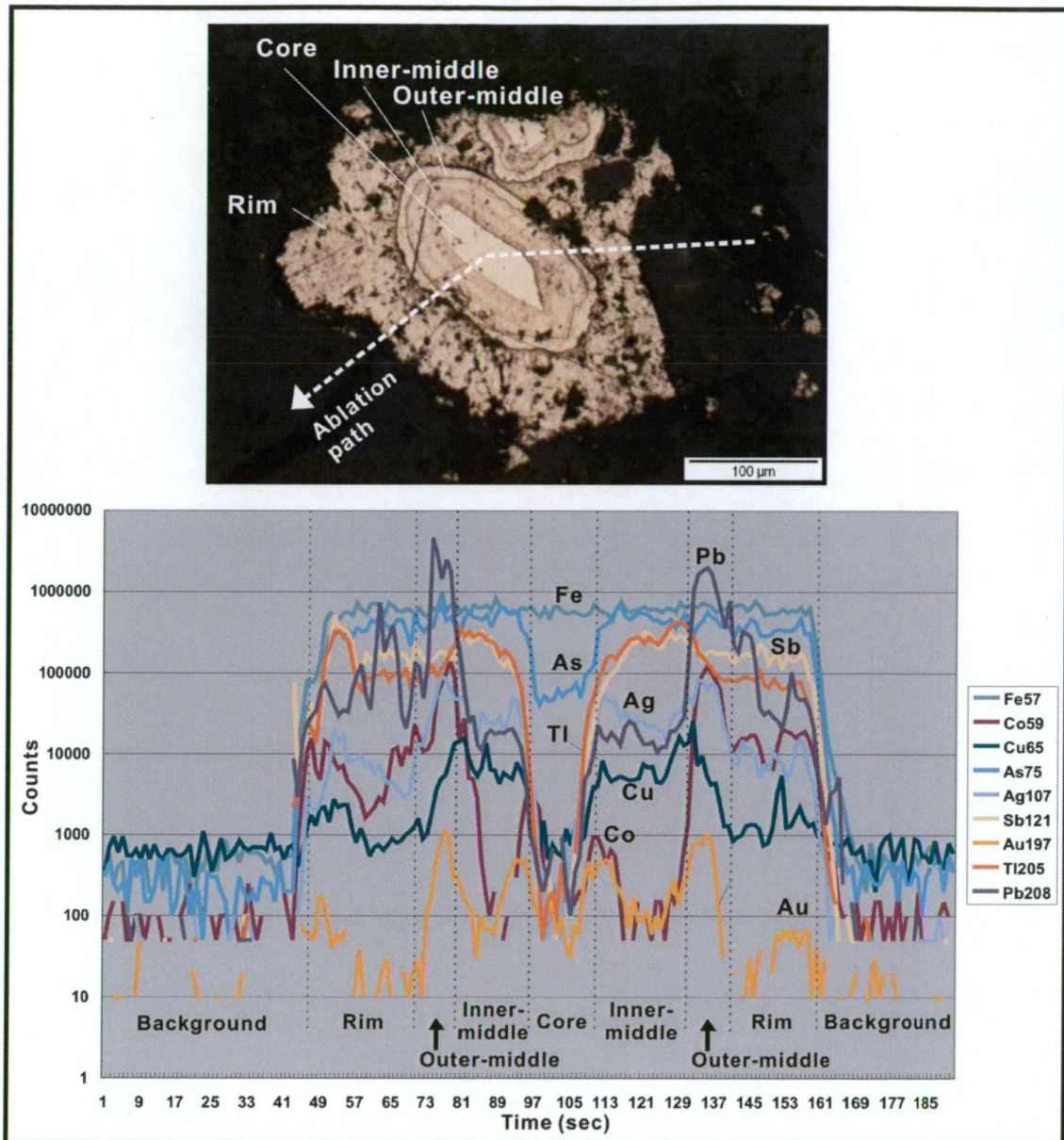


Fig. 5.7. Time chart of the selected LA-ICPMS line analysis of the pyrite with multiple growth zone texture from the BHX deposit, showing enrichment of Fe, Co, Cu, As, Ag, Sb, Au, Tl and Pb. Sample No. HDD11@249.6m.

Ag and As compared to those in the wall rock pyrite (Fig. 5.9C). Comparison between the Stage 1 vein and the Stage 3 vein at BHX shows that the two stages have similar pyrite trace element contents with the exception of Tl which is strongly enriched in the Stage 3 vein (Fig. 5.9D).

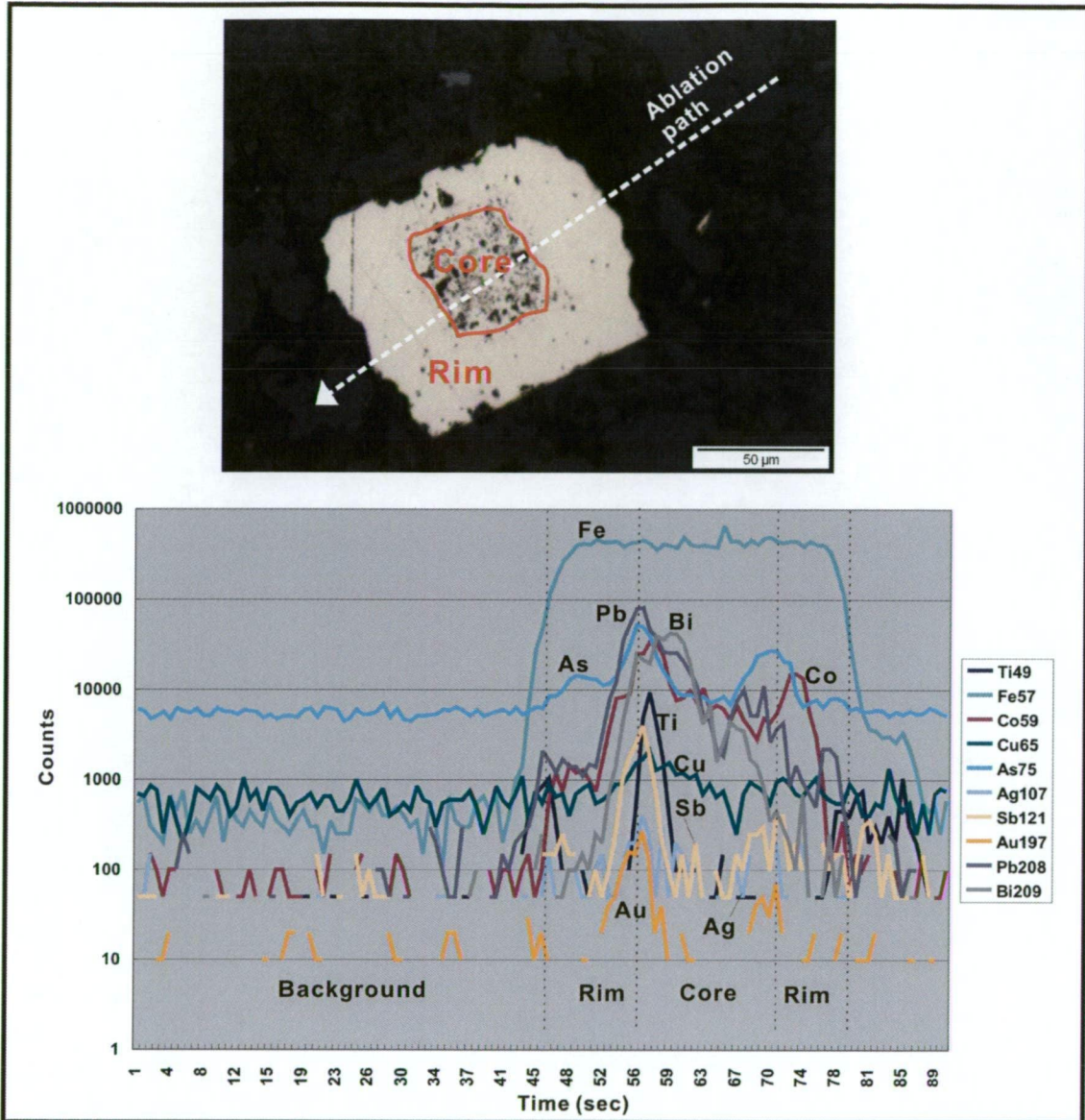
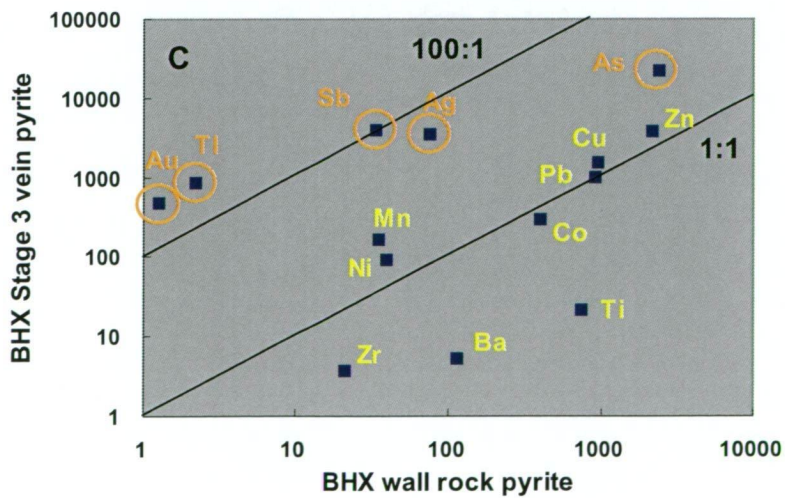
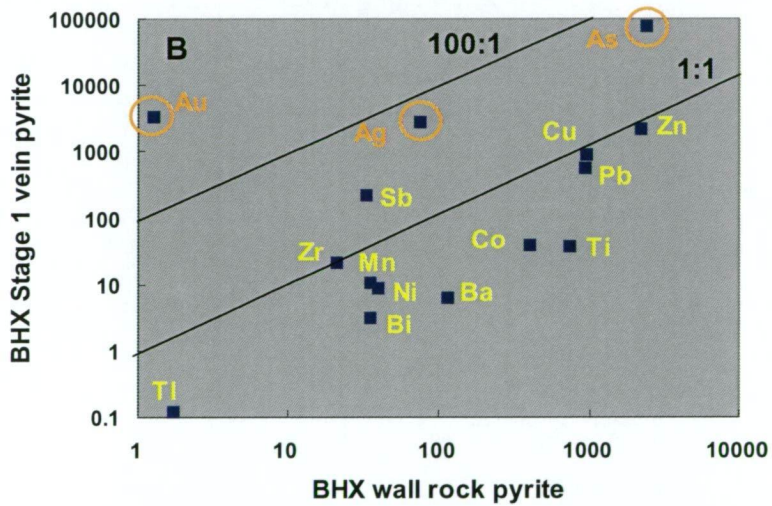
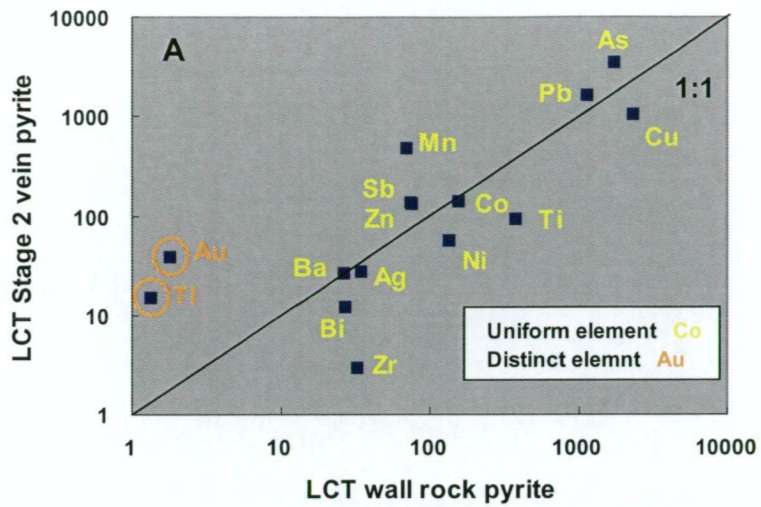


Fig. 5.8. Time chart of the selected LA-ICPMS line analyses of wall rock pyrite with spongy core and euhedral rim texture from the BHX deposit, showing enrichment of Ti, Fe, Co, Cu, As, Ag, Sb, Au, Pb and Bi. Sample No. HSD04@57.9m.



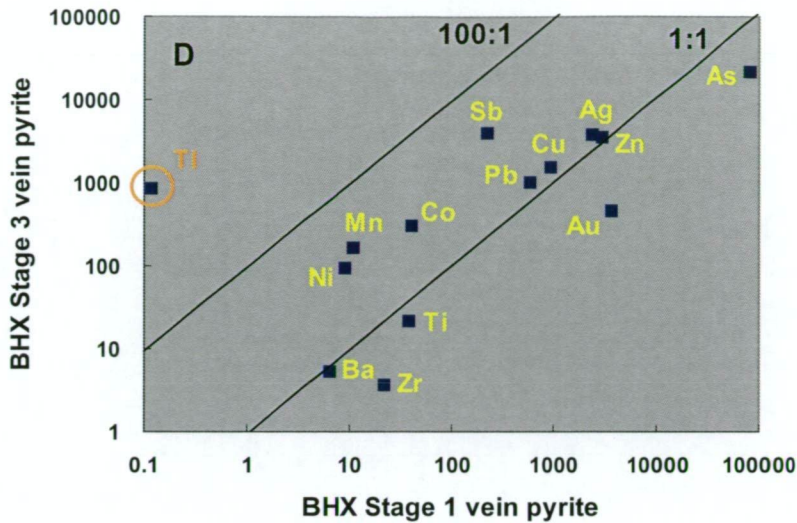


Fig. 5.9. Comparison of average values of trace elements in pyrite from the LCT and BHX deposits. (A) Stage 2 vein vs wall rock at LCT; (B) Stage 1 vein vs wall rock at BHX; (C) Stage 3 vein vs wall rock at BHX; (D) Stage 1 vein vs Stage 3 vein at BHX.

5.5. Discussion

The analyses of trace elements in the pyrite from the LCT and BHX deposits provide several important constraints on the origin of Au mineralisation at the deposits. They are discussed below:

5.5.1. As contribution to Au concentration in pyrite

The detailed relationship between As and Au has been investigated in Au-mineralised systems, particularly sedimentary-hosted Au deposits (e.g., Reich et al., 2005; Large et al., in press), revealing that As strongly controls the amount of Au available to be incorporated in the pyrite structure. In Carlin-type Au deposits, arsenian pyrite is known to be an economically important host for Au as it includes gold as nanoparticles in the pyrite crystals (e.g., Cook and Chryssoulis, 1990). At higher Au to As ratios, Au tends to form as larger inclusions of electrum, as it can no longer be incorporated within the pyrite structure.

At the LCT and BHX deposits, the pyrite we studied displays a wide range of variation in both As and Au with the contents of the two elements being correlated in many of the pyrite types (Figs. 5.5B, 5.6 and 5.7). Most of the analyses from this study plot below the Au saturation line of Reich et al. (2005), with the exception of a few of the Stage 1 and the Stage 3 vein pyrites at BHX (Fig. 5.10). This result indicates that a large amount of Au at the LCT and BHX deposits is hosted

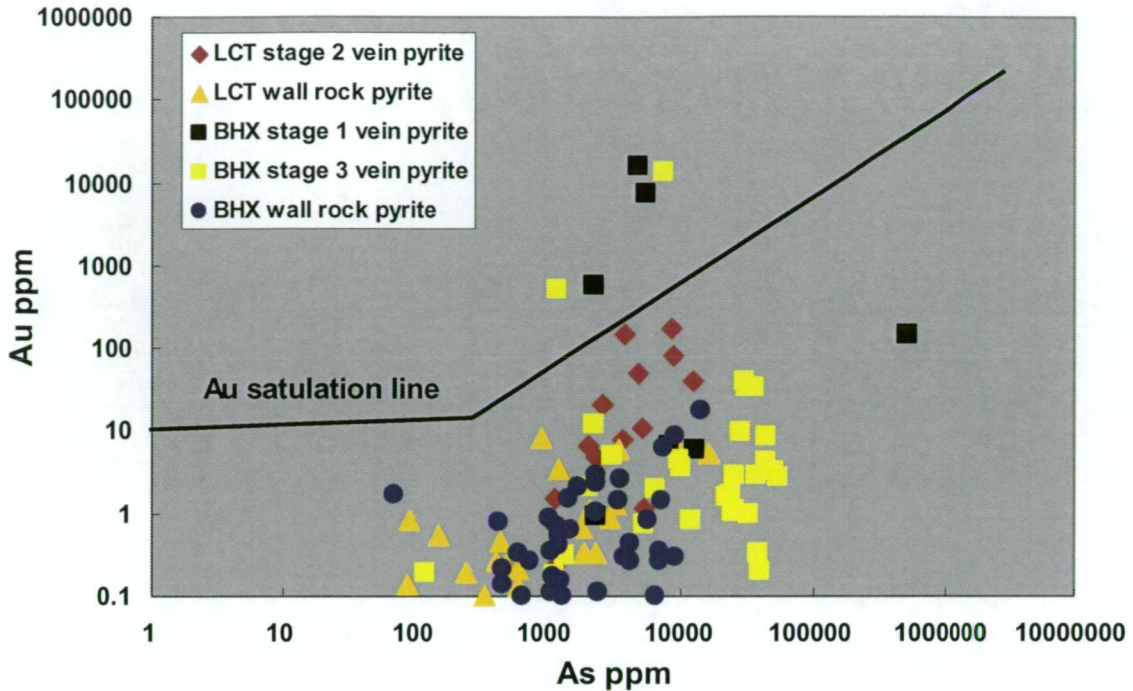


Fig. 5.10. Au-As plot of pyrite geochemistry at the LCT and BHX deposits. The Au saturation line is after Reich et al. (2005).

in pyrite as nanoparticles (below the line), with a small amount of Au occurring as inclusions of free gold.

5.5.2. Au/Ag ratio in pyrite

Au and Ag contents are strongly correlated in the pyrites and the associated inclusions but each type of pyrite shows different positive trends in Fig. 5.5A. Those are further considered herein. The Au and Ag correlation developed from Fig. 5.5A is displayed in Fig. 5.11, focusing on pyrites analysed with >10 ppm Au. The figure shows that the mineralisation stages of each deposit have a characteristic Au/Ag ratio (Fig. 5.11), with a low ratio for the BHX Stage 3, a high ratio for the BHX Stage 1 and an intermediate ratio for the LCT Stage 2. This implies that the mineralisation stages can be discriminated using the Au/Ag ratio in the pyrite and the associated inclusions. Comparison of Au/Ag ratio in the pyrite and inclusion with the Au and Ag assay in drill core reveals that the data between the assay and the pyrites and the associated inclusions are similar in the BHX deposit (Table 5.1) but different for the LCT deposit. This may be due to the presence of other Ag bearing phases (such as galena) in the LCT core that was analysed for Ag.

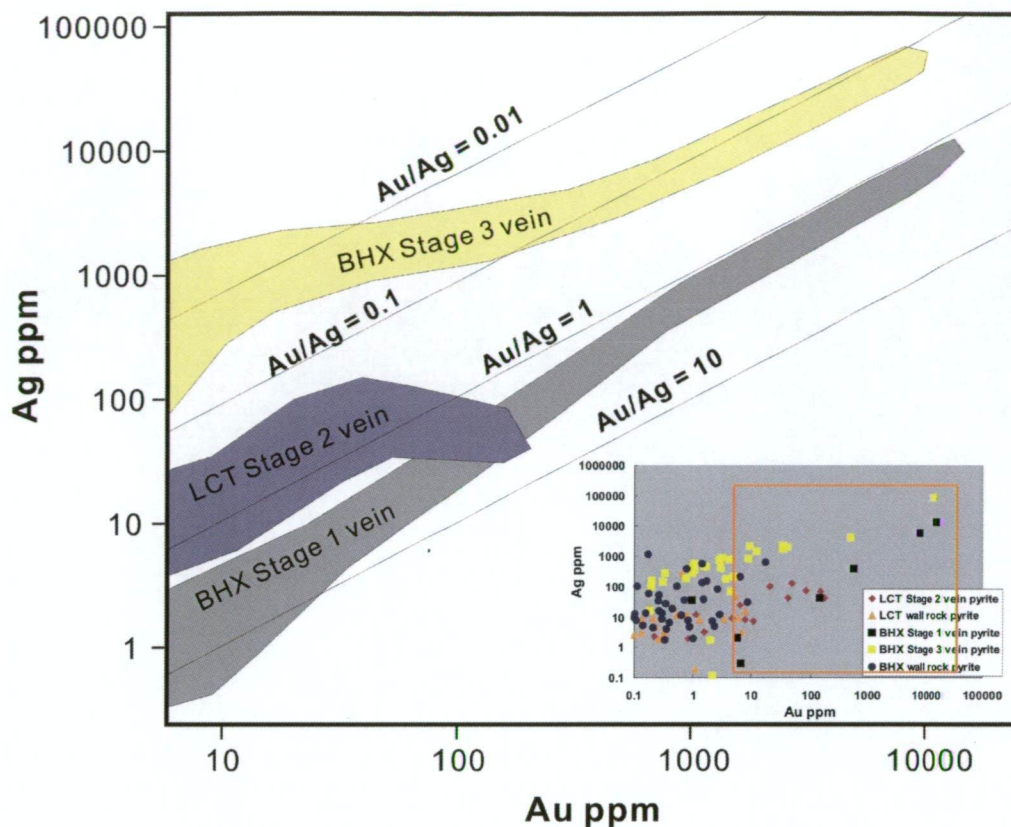


Fig. 5.11. Au-Ag correlation in the pyrite and the associated inclusions from Stage 2 vein at LCT and from Stages 1 and 3 veins at BHx developed from Fig. 5.5A, with lines in different Au/Ag ratios.

Table. 5.1. Au and Ag core assay data with Au/Ag ratio of the samples analysed for pyrite trace element geochemistry. n/a=not available.

Mineralisation stage	Sample No.	Au core assay (g/t)	Ag core assay (g/t)	Au/Ag ratio	Au/Ag ratio in pyrite
LCT					
Stage 2	LSD05@96.6m	0.32	3.6	0.09	0.2-3
	LSD09@88.0m	n/a	n/a	n/a	
	LDD81@78.0m	0.8	n/a	n/a	
BHX					
Stage 1	HDD07@126.0m	71.2	55.1	1.29	1-10
Stage 3	HDD07@179.6m	0.68	17.2	0.04	0.005-0.1
	HDD09@108.3m	49.5	771	0.06	
	HDD11@249.6m	0.42	12.8	0.03	

5.5.3. Origin of pyrite

The origin of pyrite in hydrothermal mineralised systems, particularly whether magmatic-hydrothermal contributions, has been examined using some elements such as Co and Se of VHMS systems (e.g., Huston et al., 1995). Huston et al. (1995) found that pyrites of Cu-rich VHMS deposits which are commonly formed by high temperature (300-350 °C) due to a significant magmatic water input have high Se concentration (20-200 ppm), whereas those of Cu-poor VHMS deposits which are mainly formed by sea water circulation have low Se concentration (<5 ppm). At LCT and BHX, Se concentrations in pyrite vary from several to more than 1000ppm, with a population of 1 to 30 ppm (Fig. 5.5H). In the field between 20 to 200 ppm which is considered to be of magmatic source, there are scattered several plots of both vein and wall rock pyrites. This may suggest that pyrites at LCT and BHX are dominantly irresponsible for the magmatic hydrothermal fluids, although few of them can be of magmatic hydrothermal origin. Thus, based on the pyrite trace element geochemistry, the LCT and BHX mineralised systems have a minimal contribution of magmatic water.

5.6. Summary

- Au is commonly hosted in the pyrite of the LCT and BHX deposits and it has a wide range in concentration from <0.1 ppm to several hundreds ppm. The very high concentrations of Au (>few hundreds ppm) represent inclusions.
- Au in the pyrite has positive correlations with As and Ag, and is partially correlated with Pb, Cu, Co, Sb and Tl in the LCT and BHX deposits.
- The different textures identified under the microscope were found to have different trace element contents. In particular, the different growth zones in pyrite textures found in Stage 3 at BHX show distinct differences in trace element concentration.
- The pyrite in the Stage 2 vein at LCT has an anomalous concentration of Au and Tl compared to those in the wall rock pyrite. At BHX, Au, Ag and As contents of the Stage 1 vein pyrite and Au, Ag, As, Sb and Tl in the Stage 3 vein pyrite are enriched compared with those in the wall rock. On this basis, the enrichment of these elements can discriminate different syn-mineralisation stages at LCT and BHX.
- The strong correlation of Au/Ag ratios between the drill core assay data and the pyrite and associated inclusion geochemistry was found in the BHX deposit. The low Au/Ag ratio in the Stage 3 vein pyrite and the associated inclusion discriminates this stage from those of the Stage 1 vein at BHX.
- The pyrite geochemistry reveals that there is a minimal contribution of magmatic source water, for responsible with the ore formations at LCT and BHX. Other fluid sources such as meteoric water and sea water have to be considered.

CHAPTER 6 FLUID INCLUSION STUDY

6.1. Introduction

A fluid inclusion study was undertaken to characterise the ore-forming fluids of the LCT and BHX deposits. A fluid inclusion study provides two significant aspects of fluid conditions, involving fluid temperatures and salinity by heating/freezing experiments, and these fluid characteristics help to deduce the physico-chemical environment of the ore-forming processes and the nature of mineralising fluids (e.g., Roedder, 1984; Shepherd et al., 1985; Bodnar, 2007).

6.2. Analytical methods

Two main analytical methods were applied in this study, including microthermometry and Laser Raman Spectrometry to investigate the fluid characteristics of the LCT and BHX deposits. The microthermometric measurements were made to determine the homogenisation temperature and salinity of fluid inclusions, whereas the Laser Raman Spectrometry was applied particularly to estimate the gas composition of the fluid inclusions.

A Linkham TH600 heating/freezing stage was used for microthermometric analysis of fluid inclusions at CODES, University of Tasmania. The general method and procedure for heating/freezing experiments are reported elsewhere (e.g., Roedder, 1984). The precision of the temperature measurements is better than $\pm 1^\circ\text{C}$ for heating and $\pm 0.3^\circ\text{C}$ for freezing. Accuracy of the measurements was insured by calibration against the triple point of CO_2 (-56.6°C), the freezing point of water (0.0°C), the critical point of water (374.1°C) and synthetic fluid inclusions. In estimating salinity data of fluid inclusions, freezing point depressions were measured and the equation of Bodnar (1993) was used.

The Laser Raman spectrometric analysis was conducted at Geoscience Australia in Canberra using a Dilor[®] SuperLabram spectrometer equipped with a hologenic notch filter, 600 and 1800 g/mm gratings, and a liquid- N_2 -cooled, 2000×450 pixel CCD detector. The inclusions were illuminated with 514.5 nm laser excitation from a Spectra Physics Model 2017 argon ion laser, using 5 nW powers on the samples, and a single 30 seconds accumulation. The focused laser spot on the samples was $\sim 1 \mu\text{m}$ in diameter. Wavenumbers are accurate to $\pm 1 \text{ cm}^{-1}$ as determined by

plasma and neon emission lines. For the analysis of CO₂, O₂, N₂, H₂S and CH₄ in the vapour phase, spectra were recorded from 1000 to 3800 cm⁻¹ using a single 20 seconds integration time per spectrum. Raman detection limits are estimated to be ~0.1 mol. % for CO₂, O₂ and N₂, and 0.03 mol. % for H₂S and CH₄, and errors in the calculated gas ratios are generally <1 mol. %.

6.3. Inclusion petrography

Fluid inclusion petrography was initially conducted before the freezing/heating and Laser Raman Spectroscopic experiments, using a microscope on the doubly polished fluid inclusion chips from the LCT and BHX deposits. This petrography aimed to distinguish fluid inclusion types such as primary, pseudo-secondary and secondary as defined by Roedder (1984). Primary fluid inclusions provide information about syn-mineralisation fluid characteristics, whereas secondary fluid inclusions do not include significant information about ore deposition although they may involve post-mineralisation fluid conditions. In this study, workable fluid inclusions in the sample from the syn-mineralisation stages of the LCT and BHX deposits were identified and measured. The petrographic characteristics of the fluid inclusions are shown in Fig. 6.1.

Three types of fluid inclusions were found in the samples from the LCT and BHX deposits. They include:

Type I: Primary two-phase liquid and vapour inclusions. These inclusions have high liquid/vapour ratios and homogenised into liquid phase (L-V → L) (Fig. 6.1A).

Type II: Primary two-phase liquid and vapour inclusions. These inclusions have low liquid/vapour ratios and homogenised into liquid phase (V-L → L) (Fig 6.1B).

Type III: Secondary two-phase liquid-rich inclusions. These inclusions tend to be aligned along healed crystal fractures (Fig. 6.1C).

In this study, only the primary Type I and II inclusions were analysed. The size of the primary fluid inclusions range from <5µm to 30µm (10µm in average) (Figs. 6.1A and B). Most of the Type III secondary inclusions are small (<5µm) and cross-cut the grain boundaries (Fig. 6.1C). The characteristics of the primary fluid inclusions from individual mineralisation stages at LCT and BHX are as follows:

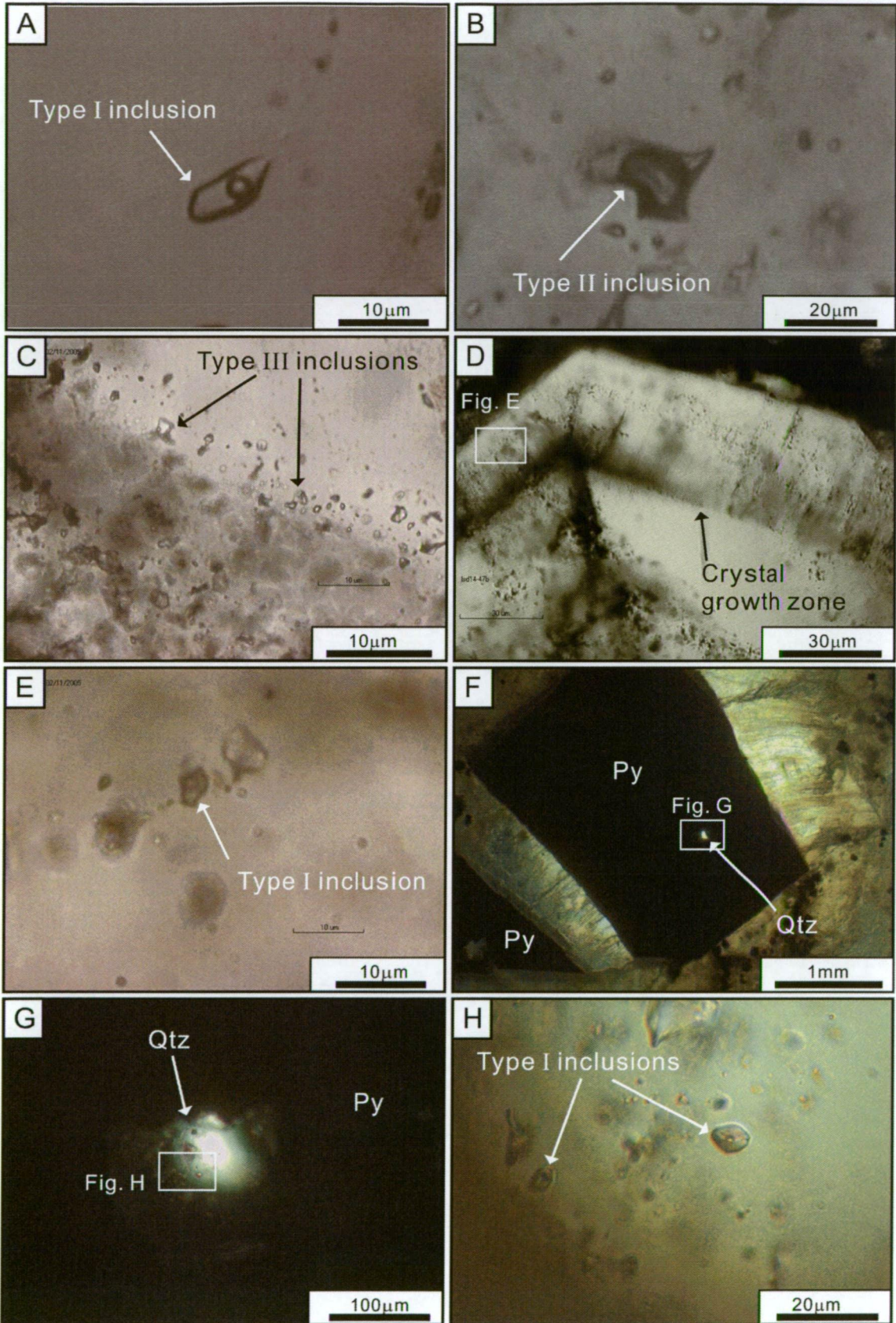


Fig. 6.1. Photomicrographs showing fluid inclusion characteristics of the LCT and BHX deposits. Abbreviations: Py=Pyrite, Qtz=quartz, ppl=plane polarised light.

- A) Type I fluid inclusion. Sample No. HDD12@142.0m (ppl).
- B) Type II fluid inclusion. Sample No. HDD12@142.0m (ppl).
- C) Type III fluid inclusions. Sample No. LSD14@47.8m (ppl).
- D) A crystal growth zone texture in quartz. Sample No. LSD14@47.8m (ppl).
- E) Type I primary fluid inclusion locked along crystal growth zone in quartz. Sample No. LSD14@47.8m (ppl).
- F) Quartz inclusion in pyrite crystal. Sample No. HSD08@68.8m (ppl).
- G) Fluid inclusion-bearing quartz locked in pyrite. Sample No. HSD08@68.8m (ppl).
- H) Type I primary fluid inclusion in pyrite-locked quartz. Sample No. HSD08@68.8m (ppl).

Type I primary fluid inclusions are located along the growth zone of crystalline quartz in the Stage 2 vein of LCT (Figs. 6.1D and E). The Stage 1 vein of BHX is strongly fractured and secondary or pseudo-secondary fluid inclusions are abundant in the quartz of this stage vein, however, detailed petrographic studies indicate that Type I primary fluid inclusions are preserved in quartz crystals locked within the euhedral pyrite in this stage (Figs. 6.1F, G and H). It appears that the brittle and massive nature of the pyrite protected the deformation and recrystallisation of the primary fluid inclusions in quartz hosted in the pyrite. The primary Type I and II fluid inclusions were identified in the crystalline quartz of the Stage 2 vein of BHX, and those located in the growth zones were measured. A few workable Type I fluid inclusions in dolomite of the Stage 3 veinlets at BHX were also observed and measured. Most of the fluid inclusions in the dolomite appear to have been stretched and leaked, and yielded a variable homogenization temperatures – they were discarded in this study.

6.4. Microthermometric results

The summarised microthermometric data of fluid inclusions from the syn-mineralisation stage veins at the LCT and BHX deposits are listed in Table 6.1, including homogenisation temperature, freezing point depressing temperature and the calculated salinity values. The detailed microthermometric results are presented in Appendix VI. The results of measured data in each of the syn-mineralisation stages at LCT and BHX are described in details below.

LCT Stage 2: Homogenisation temperatures were measured from a total of twenty-five fluid inclusions in quartz and the data are graphically presented in Fig. 6.2A. The results show a homogenisation temperature range from 175.0 to 207.0°C (n=25) with a mode of 180 to 200°C (n=16) (Fig. 6.2A). The obtained salinity values have a range from 1.7 to 8.3 wt. % NaCl equiv. (n=20) with a mode at 4 to 5 wt. % NaCl equiv. (Fig. 6.3A).

Table. 6.1. Summary of fluid inclusion microthermometric data of syn-mineralisation stages at the LCT and BHX deposits, Lao PDR.

Stage (Sample No.)	Host mineral	Inclusion type	Homogenisation temperature range (°C)	Freezing point depression range (°C)	Salinity range (NaCl wt.% equiv.)
LCT					
Stage 2	Quartz	I	175.2 - 206.7	-1.0 to -5.3	1.7 - 8.3
BHX					
Stage 1	Quartz	I	188.1 - 213.9	-1.7 to -3.9	2.9 - 6.3
Stage 2	Quartz	I, II	245.8 - 413.1	-2.9 to -9.1	4.8 - 12.9
Stage 3	Dolomite	I	238.7 - 315.8	-1.6 to -4.9	2.7 - 7.7

BHX Stage 1: A total of thirteen fluid inclusions in quartz from the BHX Stage 1 vein were measured by heating analysis and the collected homogenisation temperatures show a range between 188.0 and 214.0°C (n=13). These data are plotted in Fig. 6.2B. The salinity values in the fluid inclusions have values from 2.9 to 6.3 wt. % NaCl equiv. (n=11) with a mode of 3 - 4 wt. % NaCl equiv. (Fig. 6.3B).

BHX Stage 2: In this stage, the crystalline quartz samples consist of two types of primary fluid inclusions (Types I and II) in quartz, and the homogenisation temperatures of the fluid inclusions have a wide range from 246.0 to 413.0°C (n=23), with a mode of 340-360°C (Fig. 6.2C). The salinity values in this stage fluid inclusions range from 4.8 to 12.9 wt. % NaCl equiv. (n=20) with a mode of 6-8 wt. % NaCl equiv. (Fig. 6.3C).

BHX Stage 3: The fluid inclusion data from dolomite in the Stage 3 mineralisation at BHX display a wide range of homogenisation temperatures from 239.0 to 316.0°C (n=10) (Fig. 6.2D). The salinity data have a range of 2.7 to 7.7 wt. % NaCl equiv. (n=17), with a mode of 5-7 wt. % NaCl equiv. (Fig. 6.3D).

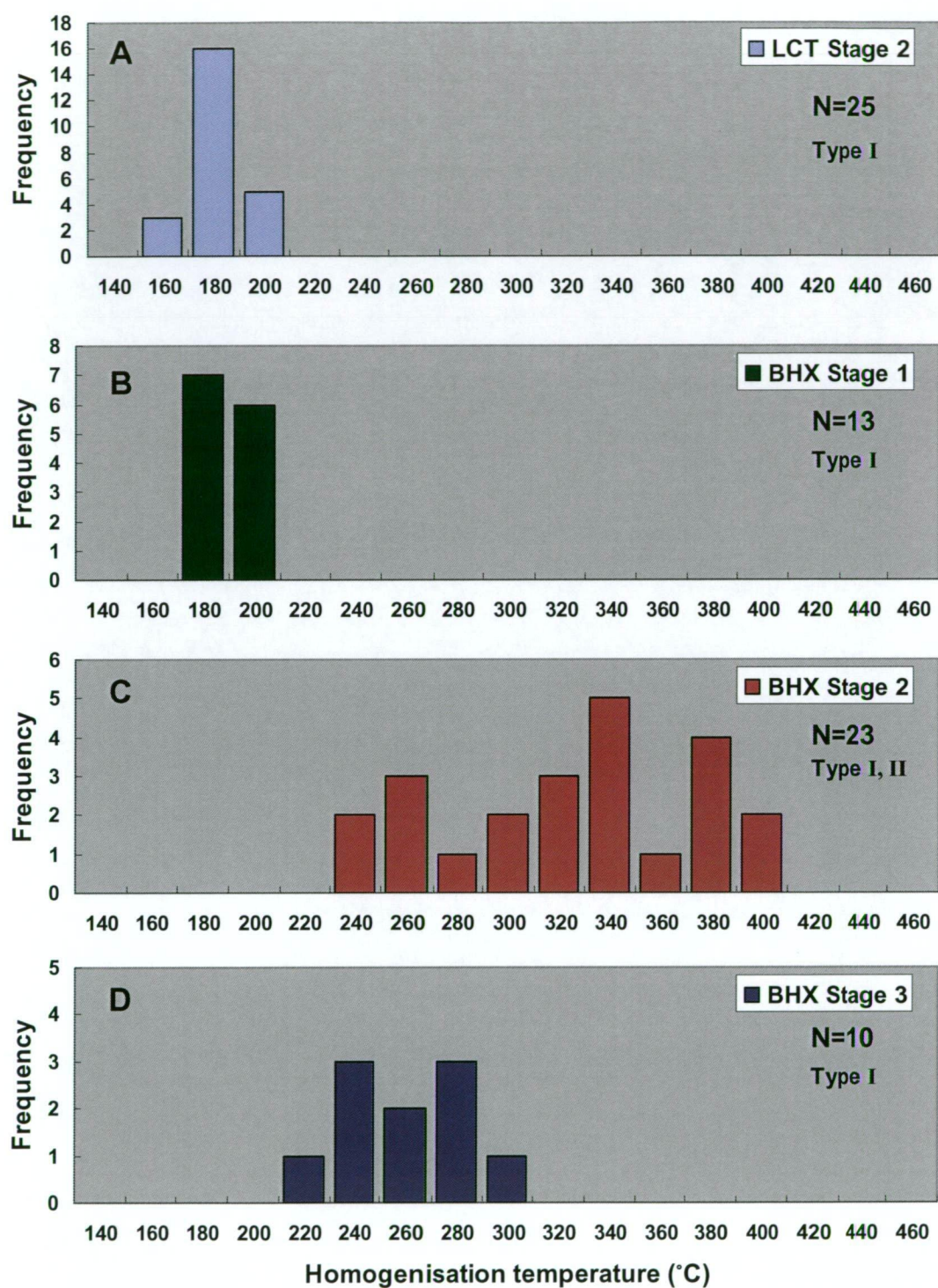


Fig. 6.2. Histograms of homogenisation temperatures of fluid inclusions in syn-mineralisation stages at the LCT and BHX deposits. (A) LCT Stage 2; (B) BHX Stage 1; (C) BHX Stage 2; (D) BHX Stage 3.

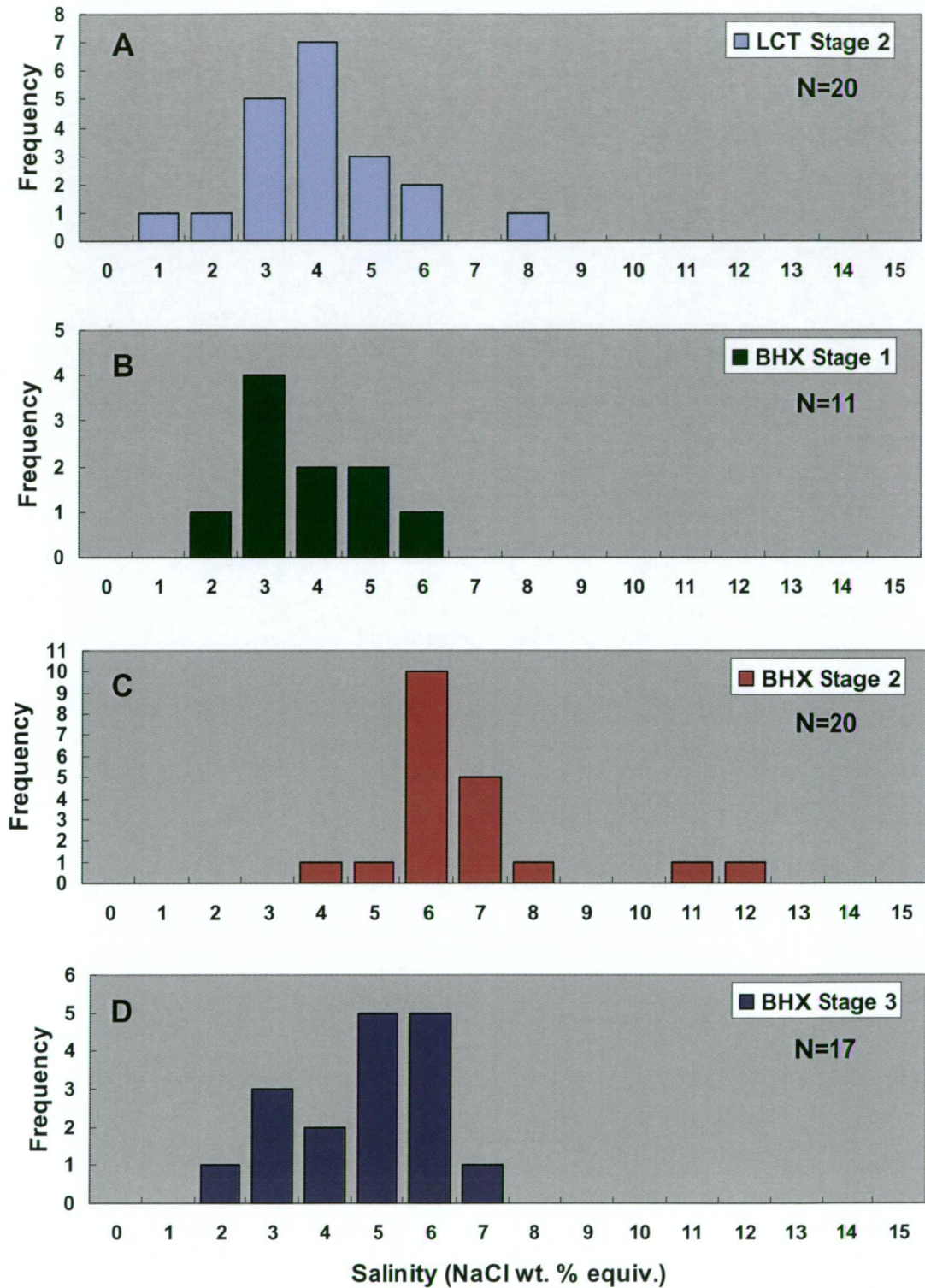


Fig. 6.3. Histograms of salinity data from fluid inclusions in syn-mineralisation stages at the LCT and BHX deposits. (A) LCT Stage 2; (B) BHX Stage 1; (C) BHX Stage 2; (D) BHX Stage 3.

6.5. Laser Raman Spectrometric data

Laser Raman spectrometric analysis was conducted on the three selected samples including two samples from the Stage 2 vein of LCT and one sample from the Stage 1 vein of BHX, to measure gas composition trapped in fluid inclusions. Although gases were identified in the two LCT samples, no gas was found in the BHX sample. The results of gas compositions are numerically presented in Table 6.2, and an example of Raman spectral profile having CO₂-CH₄ gas composition is shown in Fig. 6.4.

Gas composition: The results of the Laser Raman spectrometry analysis of the fluid inclusions from the LCT Stage 2 vein samples show that the gas phase is dominantly composed of CO₂, commonly with a minor amount of CH₄. One fluid inclusion (LDD03A@75.0m-inclusion1) consists of 100 mole % CO₂. CH₄ gas is also present in the sample of LSD13@55.0m, up to 34 mole %. A trace amount (4 mole %) of N₂ gas is also detected in one fluid inclusion sample (LSD13@55.0m-inclusion5).

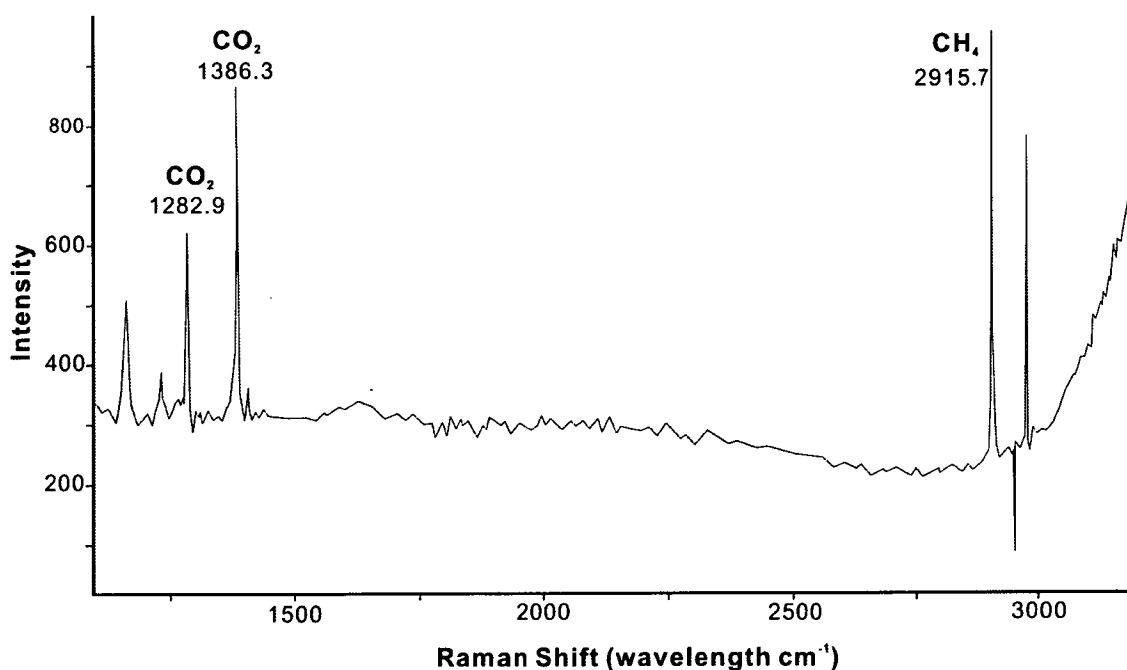


Fig. 6.4. An example of Laser Raman spectral profile of CO₂ and CH₄ gas compositions in fluid inclusion from the Stage 2 mineralisation of the LCT deposit. Sample No. LSD13@55.0m-inclusion2.

Table. 6.2. Summary of Laser Raman spectrometric data of fluid inclusions from the LCT deposit, Lao PDR.

Sample No.	CO ₂ (mole %)	N ₂ (mole %)	H ₂ S (mole %)	C ₃ H ₈ (mole %)	CH ₄ (mole %)	C ₂ H ₆ (mole %)	NH ₃ (mole %)	H ₂ (mole %)	Composition
LCT									
LDD03A@75.0m-inclusion1	100	0	0	0	0	0	0	0	CO ₂
LSD13@55.0m-inclusion1	83	0	0	0	17	0	0	0	CO ₂ -CH ₄
LSD13@55.0m-inclusion2	79	0	0	0	21	0	0	0	CO ₂ -CH ₄
LSD13@55.0m-inclusion3	66	0	0	0	34	0	0	0	CO ₂ -CH ₄
LSD13@55.0m-inclusion4	96	0	0	0	4	0	0	0	CO ₂ -CH ₄
LSD13@55.0m-inclusion5	62	4	0	0	34	0	0	0	CO ₂ -CH ₄ -N ₂

6.6. Discussion

The collected fluid inclusion data of the LCT and BHX deposits show a distinct variation of homogenisation temperatures and salinity values in different mineralisation stages. On this basis, the fluid processes and the estimated depth of the fluid trap are examined. The nature of the detected gas compositions of the fluid inclusions are also discussed below.

Homogenisation temperature: On the basis of the measured homogenisation temperature ranges, two distinct groups are recognised including; (1) low and narrow temperature range of the Stage 2 of LCT and the Stage 1 of BHX, and (2) high and wide temperature range of the Stages 2 and 3 of BHX.

The homogenisation temperature range of the Stage 2 of LCT and Stage 1 of BHX are comparable to those in the Au-rich low-sulphidation deposits of the Hauraki goldfield in New Zealand, which has a general range of 180 to 250°C (Christie et al., 2007). It is also comparable to the homogenisation temperature range in the low-sulphidation epithermal model of Buchanan (1981), in which the fluid temperature has a range from 150 to 250°C in the main part of the epithermal system.

In contrast, the homogenisation temperatures of Stages 2 and 3 of BHX have a wider and higher temperature range compared to those in Stage 2 of LCT and Stage 1 of BHX, and they are similar to Ag-rich epithermal systems. For example, the Ag-rich Martha epithermal deposit, which has the lowest Au/Ag ratio (0.16) among all the epithermal systems in Hauraki goldfield of New

Zealand, shows a range from 190 to 295°C (Christie et al., 2007). Wide homogenisation temperature ranges are also observed in the Ag-rich epithermal systems in Mexico. For instance, the San Francisco del Oro deposit has a range of 163 to 385°C (Grant and Ruiz, 1988; Albinson et al., 2001) and a temperature range of 180 to 388°C is also recorded at the Real de Angeles deposit (Pearson et al., 1988; Albinson et al., 2001). These wide and high homogenisation temperature ranges are likely to be favourable to form an Ag-rich system, as suggested in the Mexican epithermal systems by comparing Au-rich and Ag-rich systems (Albinson et al., 2001).

Salinity: Stage 2 of LCT, and Stages 1 and 3 of BXH have similar salinity ranges from 1.7 to 8.3 wt. % NaCl equiv., 2.9 to 6.3 wt. % NaCl equiv., and 2.7 to 7.7 wt. % NaCl equiv., respectively. These salinity ranges can be compared to those in low-sulphidation epithermal systems in the Hauraki goldfield, which have a range from 0 to 6.1 wt. % NaCl equiv. (Christie et al., 2007).

In comparison, Stage 2 of BHX has a wider and higher salinity value of 4.8 to 13.0 wt. % NaCl equiv. which is distinct from the other stages at LCT and BHX. This wide range is comparable to the Mexican Ag-rich epithermal deposits which have as high as 23 wt. % NaCl equiv. (Albinson et al., 2001). Moreover, the importance of high salinity in an Ag-rich epithermal system is also noted by Simmons (1991), revealing that high salinity fluids are intimately associated with silver transport at the Fresnillo silver epithermal system in Mexico. Seward and Barnes (1997) also advocate that chloride complexes play a significant role in silver transport in epithermal silver deposits. This is consistent with the high salinity data in the BHX Stage 2, and this may be responsible for the Ag-rich nature of the structurally-hosted vein systems at BHX.

Fluid processes: The plot of individual inclusion data of homogenisation temperature and salinity value can be used to constrain the fluid evolution and processes such as fluid mixing, boiling, cooling or dilution (Shepherd et al., 1985). Compared with the fluid evolution trends developed by Shepherd et al. (1985), two fluid evolutionary trends were observed at the LCT and BHX deposits including (1) isothermal mixing trend in the Stage 2 of LCT and Stage 1 of BHX (Figs. 6.5A and B), and (2) fluid dilution trend in the Stages 2 and 3 of BHX (Figs. 6.5C and D). On this basis, it is likely that the Au-rich stockwork veins (LCT Stage 2 and BHX Stage 1) and the Ag-rich structurally-hosted veins (BHX Stages 2 and 3) may have been formed due to the different fluid processes. Cooke (1992) suggested that fluid mixing typically occurs in epithermal

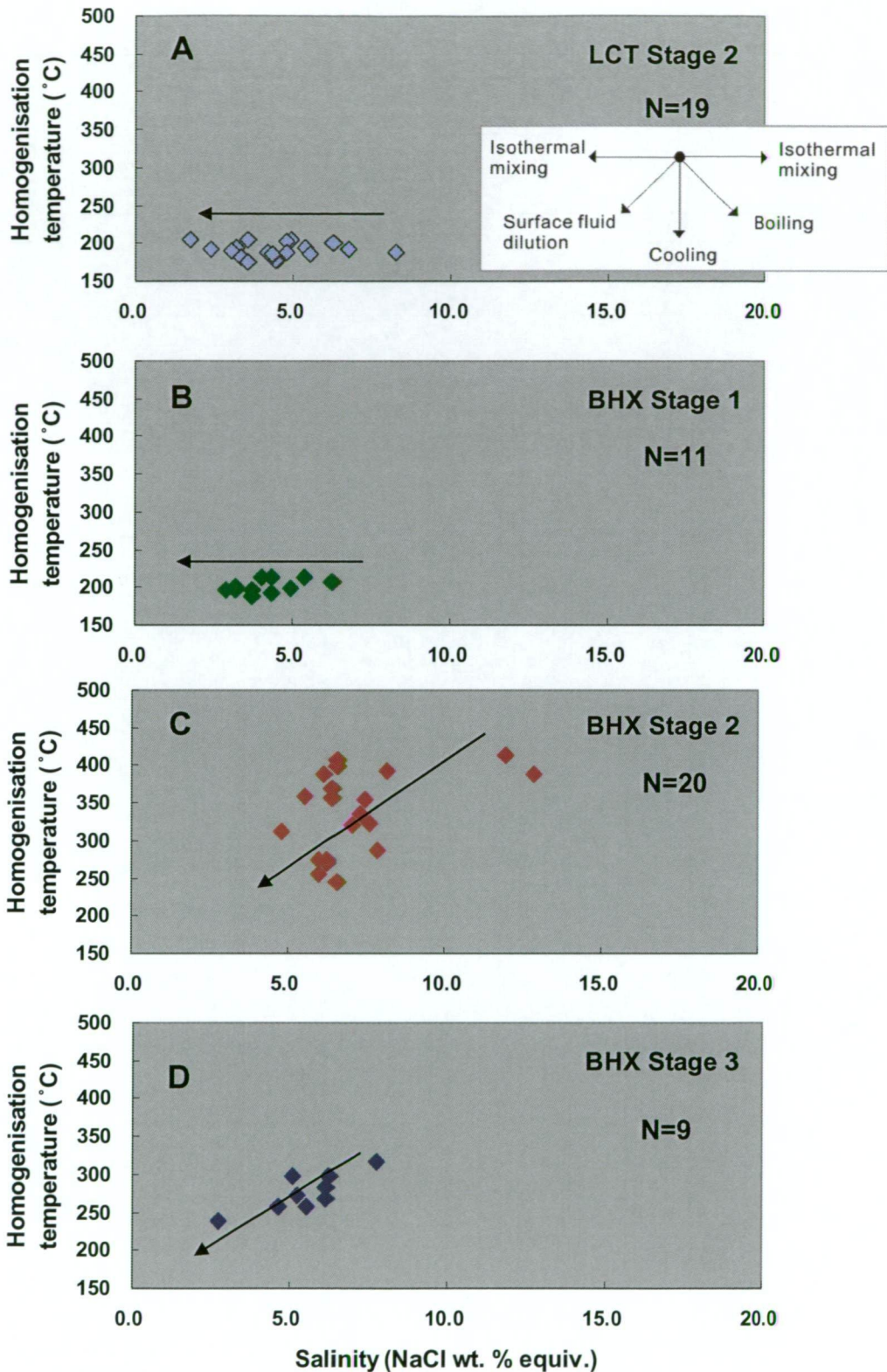


Fig. 6.5. Plots of salinity vs homogenisation temperatures from fluid inclusions in syn-mineralisation stages at the LCT and BHX deposits. (A) LCT Stage 2; (B) BHX Stage 1; (C) BHX Stage 2; (D) BHX Stage 3. Inset in Fig. 7.4A indicates possible fluid processes as defined by Shepherd et al. (1985).

systems, and this is consistent with the fluid process in the Au-rich stockwork veins of LCT Stage 2 and BHX Stage 1. In contrast, the dilution trends recognised in the BHX Stages 2 and 3 probably indicate the presence of two fluids of different temperatures and salinities; one with higher temperature (probably of magmatic origin) and salinity and one with lower temperature and salinity (meteoric origin).

Gas composition: The Laser Raman spectrometric analysis of the fluid inclusion gases in the Stage 2 vein quartz crystals at LCT revealed that the gases are mostly CO₂ with minor CH₄, although the presence of CO₂ gas in the fluid inclusions was not recorded by the microthermometry. In the low-sulphidation epithermal systems of the Hauraki goldfield in New Zealand, the CO₂ content in fluid inclusions is generally low (<0.1 mole %) (Christie et al., 2007). In comparison, the LCT ore fluids contain significant CO₂ content. The abundance of CO₂ gas in the LCT fluid inclusions invokes several other origins and associated gold mineralised styles including Carlin-type (e.g., Hofstra and Cline, 2000) and orogenic type (e.g., Groves et al., 1998) systems of metamorphic origin, and intrusion-related (e.g., Lang and Baker, 2001) or formation in the deeper part of an epithermal environment (e.g., Simmons et al., 2007). Accordingly, the source of CO₂ at LCT is most likely to be a magmatic origin, as there is no alternative origin is recognised. The presence of crystalline quartz and the lack of typical crustiform, colloform vein textures and abundant sulphides at LCT may also collaborate with the deeper part of an epithermal system or a transitional epithermal to mesothermal environment.

The involvement of a minor amount of CH₄ in the studied fluid inclusions at LCT may indicate that CH₄ is contributed from a crustal fluid source, as there is little CH₄ in volcanic gases and the CH₄ in fluids is commonly suggested to be an indicator of a crustal source of volatiles (Giggenbach, 1997). Norman et al. (1997) also suggest that CH₄ gas in fluid inclusions is mainly derived from organic materials in sedimentary and meta-sedimentary rocks. At LCT, the carbonaceous limestone is found at the lowermost part of the host rock sequence (see Chapter 2 for details), thus the CH₄ in the fluid inclusions is considered to have derived from interaction between ore fluids and the carbonaceous limestone.

6.7. Summary

The results of the fluid inclusion study of the syn-mineralisation stages at the LCT and BHX deposits are summarised below.

- Homogenisation temperatures of the primary fluid inclusions in Stage 2 of LCT show a range from 175.0 to 207.0°C, and those in Stages 1, 2 and 3 of BHX have values of 188.0 to 214.0°C, 246.0 to 413.0°C and 239.0 to 316.0°C, respectively.
- Salinity values of the primary fluid inclusions in Stage 2 of LCT range from 1.7 to 8.3 wt. % NaCl equiv., and those in Stages 1, 2 and 3 at BHX range from 2.9 to 6.3 wt. % NaCl equiv., 4.8 to 12.9 wt. % NaCl equiv. and 2.7 to 7.7 wt. % NaCl equiv., respectively.
- Different fluid processes are identified between the stockwork veins (LCT Stage 2 and BHX Stage 1) and the structurally-hosted veins (BHX Stages 2 and 3). The stockwork veins show isothermal mixing, whereas the structurally-hosted veins have a fluid dilution trend.
- The Laser Raman spectrometric analysis of gases in the primary fluid inclusions of Stage 2 at LCT shows that CO₂ is dominantly involved with a minor amount of CH₄. The CO₂ was probably derived from a magmatic source and CH₄ originated from a crustal source.

CHAPTER 7 SULPHUR, OXYGEN AND HYDROGEN ISOTOPES

7.1. Introduction

In recent years, sulphur, oxygen and hydrogen isotope studies have been undertaken to understand the source of ore fluids and the physico-chemical environment of ore deposition (e.g., Sheppard, 1986; Rollinson, 1993; Huston, 1999). In this study, the stable isotopes were studied to characterise the nature and origin of the syn-mineralisation fluids at the LCT and BHX deposits. The stable δS^{34} analyses of sulphides including pyrite, sphalerite, galena and chalcopyrite provide the source of sulphur in the hydrothermal systems at LCT and BHX. The oxygen and hydrogen stable isotopes were used to constrain the extent of mixing of the ore-forming fluids at LCT and BHX. The combined isotopic data characterise the isotopic behaviour and signatures of the LCT and BHX deposits in relation to the origin and chemical environments of the ore formation.

7.2. Analytical methods

7.2.1. Sulphur isotope

Twenty-six sulphide samples from LCT were selected for this study and the sulphides were drilled out from each sample and analysed using conventional techniques, whereas twenty-four samples from BHX were analysed using either conventional or laser ablation techniques. All the sulphides analysed for this study were obtained from vein samples.

Conventional technique: Visible sulphide minerals in the hand specimen samples were manually drilled out using a dentist's drill to obtain powdered (>5 mg) sulphide samples at CODES, University of Tasmania. The powdered samples were subsequently submitted to the Central Science Laboratory (CSL), University of Tasmania, and the isotopic compositions were measured using the $^{34}S/^{32}S$ sulphides combustion method, operated by Mrs. Christine Cook. The detailed analytical method of this combustion technique is explained by Robinson and Kusakabe (1975).

Laser technique: Polished thin sections with 150 μm thickness were prepared for the laser analysis using a VG Micromass SIRA Series II mass spectrometer at CSL, University of Tasmania. The samples were ablated in an oxygenated environment, and SO_2 gas was generated and separated from other gas using freezing and heating taps. Subsequently, δS^{34} value in the obtained SO_2 gas was analysed using the known standards of galena from Broken Hill and Rosebery. The detailed analytical technique is described by Huston (1995).

7.2.2. Oxygen and hydrogen isotopes

A total of twenty-three samples including eleven samples from LCT and twelve samples from BHX were selected for the oxygen isotope analysis. In this study, only samples from stockwork veins from LCT and BHX were investigated. All the eleven LCT samples were obtained from the Stage 2 stockwork quartz vein samples, whereas the twelve BHX samples consist of eight from the Stage 1 stockwork vein samples and the rest of the four from the sericitised wall rock samples. A total of six samples including three vein samples from each deposit were selected for the hydrogen isotope analysis. The selected samples were crushed using a jaw crusher and only pure quartz fragments were obtained to avoid contamination. These prepared samples were subsequently submitted to the University of Queensland and they were analysed with the aid of Dr. Sue Golding.

The measurement of the oxygen and hydrogen isotopes on the submitted samples was conducted using a Micromass 602E mass spectrometer, which obtains the isotopic composition from the gas in the samples. The measured isotopic data are shown in per mil relative to Vienna Standard Mean Ocean Water (SMOW). Analytical precisions are ± 0.2 per mil (1σ) and ± 3 per mil (1σ) for the oxygen and hydrogen isotope analyses, respectively. The measured isotopic values were normalised against an international standard through repeat analyses of NSB 28 (+9.6 per mil $\delta^{18}\text{O}$) and NSB 30 (-65 per mil δD).

The measured oxygen isotope results were calculated using a formula of Zheng (1993), to account for quartz fractionation factors. For this calculation, a website calculator (<http://www.ggl.ulaval.ca/cgi-bin/isotope/generisotope.cgi>) was used based on the modeling temperature of 200°C, which is a reasonable temperature as recorded from a fluid inclusion study for the stockwork vein system (see Chapter 6 for details).

7.3. Sulphur isotope data

Table 7.1 summarises the sulphur isotope data for fifty samples from the LCT and BHX deposits including sample number, analysed sulphide mineral, related mineralisation stages and measured δS^{34} value. The histograms of the measured δS^{34} values (‰) of LCT and BHX are shown in Fig. 6.1. The δS^{34} value at LCT has a range between -16.49 and 2.74 ‰, with a high mode of -5.85 and -0.39 ‰ for the syn-mineralisation stage (i.e., Stage 2) (Fig. 7.1A). The δS^{34} values of the LCT Stage 1 (unmineralised stage) pyrite have a range between -2.61 and 2.67 ‰, whereas the δS^{34} values of the LCT Stage 3 (unmineralised stage) pyrite have a wide range of values from -16.49 to 2.74 ‰ (Fig. 7.1A). At BHX, the δS^{34} values of the measured samples range widely from -26.79 to 3.31 ‰ (Fig. 7.1B). The collected δS^{34} values of the pyrites from Stages 1 and 2 have ranges from -8.23 to 3.31 ‰ and -1.85 to -1.01 ‰ respectively, whereas the δS^{34} values of the Stage 3 pyrite vary widely from -26.79 to 0.92 ‰.

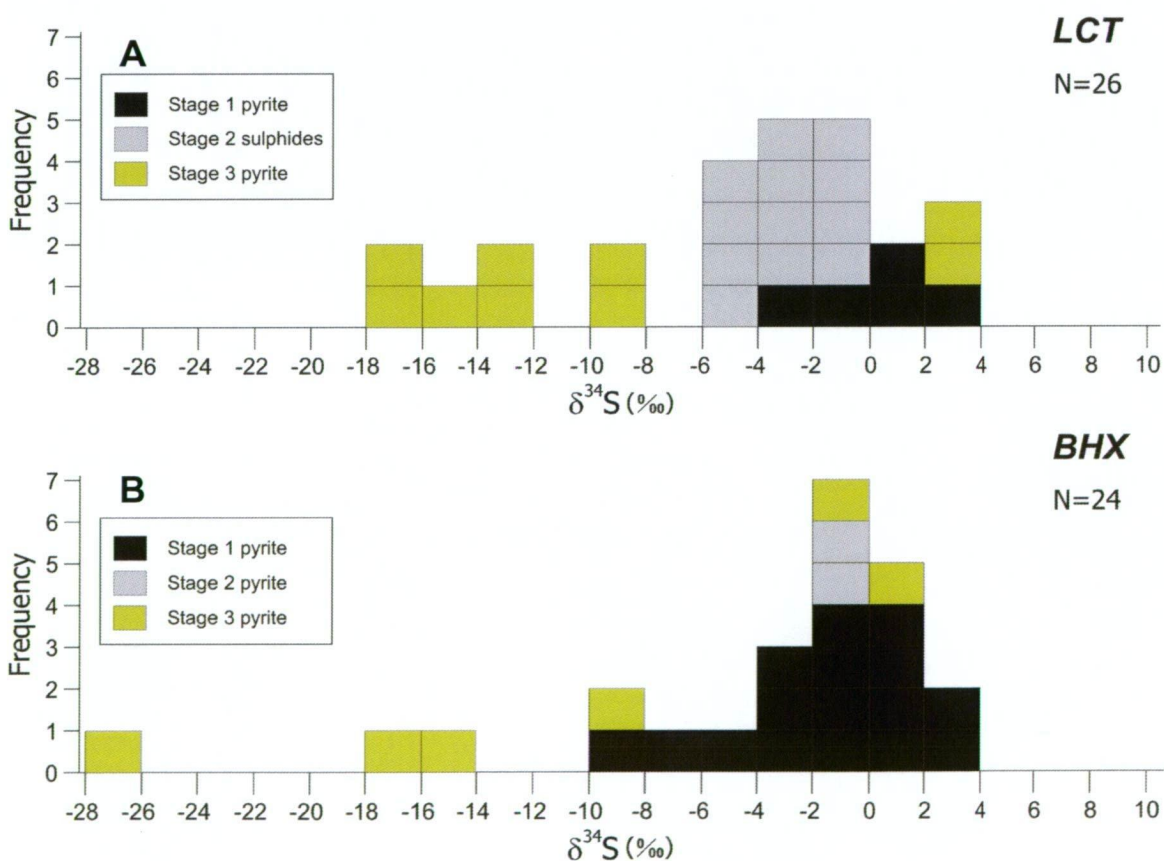


Fig. 7.1. Histograms of δS^{34} values for sulphides at the (A) LCT and (B) BHX deposits, Lao PDR.

Table 7.1. Summary of $\delta^{34}\text{S}$ isotope data of the LCT and BHX deposits, Lao PDR.

Deposit/ sample No.	Analytical method	Measured sulphide	$\delta^{34}\text{S}$ (‰)	Mineralisation stage
LCT				
LDD03A@75.0m	conventional	pyrite	-12.34	Stage 3
LSD05@98.2m	conventional	sphalerite	-2.59	Stage 2
LSD05@98.6m	conventional	pyrite	-2.30	Stage 2
LSD09@88.0m-a	conventional	sphalerite	-2.46	Stage 2
LSD09@88.0m-b	conventional	sphalerite	-1.47	Stage 2
LSD11@88.7m	conventional	pyrite	-0.18	Stage 1
LSD13@15.3m	conventional	pyrite	1.27	Stage 1
LSD15@96.6m	conventional	sphalerite	-0.39	Stage 2
LDD81@51.7m	conventional	pyrite	-9.98	Stage 3
LDD81@63.6m	conventional	pyrite	-5.65	Stage 2
LDD81@79.6m	conventional	pyrite	-13.57	Stage 3
LDD81@126.6m	conventional	pyrite	-9.01	Stage 3
LSD13@55.0m-a	conventional	chalcopyrite	-1.99	Stage 2
LSD13@55.0m-b	conventional	pyrite	-2.09	Stage 2
LSD14@47.8m	conventional	pyrite	0.02	Stage 1
LSD05@80.3m	conventional	sphalerite	-0.61	Stage 2
LSD08@79.5m	conventional	pyrite	2.45	Stage 3
LSD08@83.7m	conventional	pyrite	2.74	Stage 3
LSD14@88.1m	conventional	pyrite	2.67	Stage 1
LSD24@69.6m	conventional	pyrite	-15.00	Stage 3
LSD24@79.0m	conventional	pyrite	-16.49	Stage 3
LSD24@86.0m	conventional	pyrite	-16.44	Stage 3
LSD24@99.2m	conventional	pyrite	-2.61	Stage 1
LRD67@43.0m	conventional	galena	-5.84	Stage 2
LRD67@47.3m	conventional	sphalerite	-4.65	Stage 2
LRD67@50.0m	conventional	sphalerite	-4.72	Stage 2
BHX				
HDD07@179.6m	conventional	pyrite	-14.03	Stage 3
HDD07@179.7m	conventional	pyrite	-16.10	Stage 3
HDD07@197.0m	conventional	pyrite	-26.79	Stage 3
HDD08@228.5m	conventional	pyrite	-9.22	Stage 3
HDD09@94.3m	conventional	pyrite	-1.85	Stage 2
HDD09@99.0m	conventional	pyrite	-0.34	Stage 3
HDD09@108.3m	conventional	pyrite	-1.01	Stage 2
HDD11@44.8m	conventional	pyrite	0.92	Stage 3
HSD01@56.0m-a	laser	pyrite	-1.06	Stage 1
HSD01@56.0m-b	laser	pyrite	-1.94	Stage 1
HSD01@56.0m-c	laser	pyrite	-1.95	Stage 1
HSD01@56.0m-d	laser	pyrite	-8.23	Stage 1
HSD01@56.0m-e	laser	pyrite	-4.15	Stage 1
HSD01@56.0m-f	laser	pyrite	-2.00	Stage 1
HSD01@56.0m-g	laser	pyrite	-6.51	Stage 1
HSD04@55.9m	laser	pyrite	1.67	Stage 1
HSD04@57.9m-a	laser	pyrite	3.31	Stage 1
HSD04@57.9m-b	laser	pyrite	1.65	Stage 1
HSD04@75.3m-a	laser	pyrite	-0.28	Stage 1
HSD04@75.3m-b	laser	pyrite	1.52	Stage 1
BH-1	conventional	pyrite	-3.09	Stage 1
HSD01@56.0m-h	conventional	pyrite	-3.15	Stage 1
HSD03@86.4m	conventional	pyrite	0.81	Stage 1
HSD08@97.5m	conventional	pyrite	2.73	Stage 1

7.4. Oxygen and hydrogen isotope data

Oxygen and hydrogen stable isotope data were collected from the syn-mineralisation stage vein and the associated wall rock samples of LCT and BHX, and the results are summarised in Table 7.2. The measured oxygen isotopic compositions of the LCT samples have a range from 10.6 to 15.9 ‰, and those of the BHX samples show a range from 11.9 to 18.9 ‰. The calculated oxygen isotopic composition data of the LCT and BHX samples at 200°C modeling temperature which was obtained from the fluid inclusion study, have a range from -1.0 to 4.3 ‰ and 0.3 to 7.3 ‰ respectively. The hydrogen isotope data show values from -79 to -55 ‰ and -79 to -60 ‰ in the LCT and BHX samples, respectively. The measured oxygen and hydrogen isotope data are graphically displayed in Figs 7.2 and 7.3, respectively.

Table 7.2. Oxygen and hydrogen isotope data with calculated oxygen data at the LCT and BHX deposits, Lao PDR. ND = not detected.

Deposit/ Sample No.	Measured $\delta^{18}\text{O}$ (‰)	Calculated* $\delta^{18}\text{O}$ (‰)	Measured δD (‰)	Assigned stage/wall rock
LCT				
LSD02@50.0m	12.9	1.3	-79	Stage 2 quartz vein
LSD03@27.0m	14	2.4		Stage 2 quartz vein
LSD04@61.9m	12.7	1.1		Stage 2 quartz vein
LSD05@90.0m	10.6	-1.0	ND	Stage 2 quartz vein
LSD08@79.5m	10.7	-0.9		Stage 2 quartz vein
LSD13@55.0m	15.9	4.3		Stage 2 quartz vein
LSD15@96.6m	12.4	0.8	-55	Stage 2 quartz vein
LSD24@76.2m	13.3	1.7	ND	Stage 2 quartz vein
LRD67@50.0m	13.3	1.7	ND	Stage 2 quartz vein
LDD81@129.2m	11.9	0.3	-61	Stage 2 quartz vein
LRD83@140.4m	15.7	4.1		Stage 2 quartz vein
BHX				
HSD01@82.0m	15.2	3.6		Stage 1 quartz vein
HSD02@59.0m	18.4	6.8		Stage 1 quartz vein
HSD03@7.8m	13.5	1.9		Stage 1 quartz vein
HSD04@96.4m	14.7	3.1		Stage 1 quartz vein
HSD05@63.3m	14.9	3.3	-68	Stage 1 quartz vein
HSD06@101.8m	17.7	6.1	-79	Stage 1 quartz vein
HSD08@66.5m	18.9	7.3	-60	Stage 1 quartz vein
HSD09@47.6m	15.3	3.7		Stage 1 quartz vein
BH-5	12	0.4		Sericitised wall rock
HSD01@82.0m	11.9	0.3		Sericitised wall rock
HDD06@76.9m	12.6	1.0		Sericitised wall rock
HDD09@12.9m	12.9	1.3		Sericitised wall rock

* The oxygen isotopic composition was calculated at 200°C using equation of Zheng (1993).

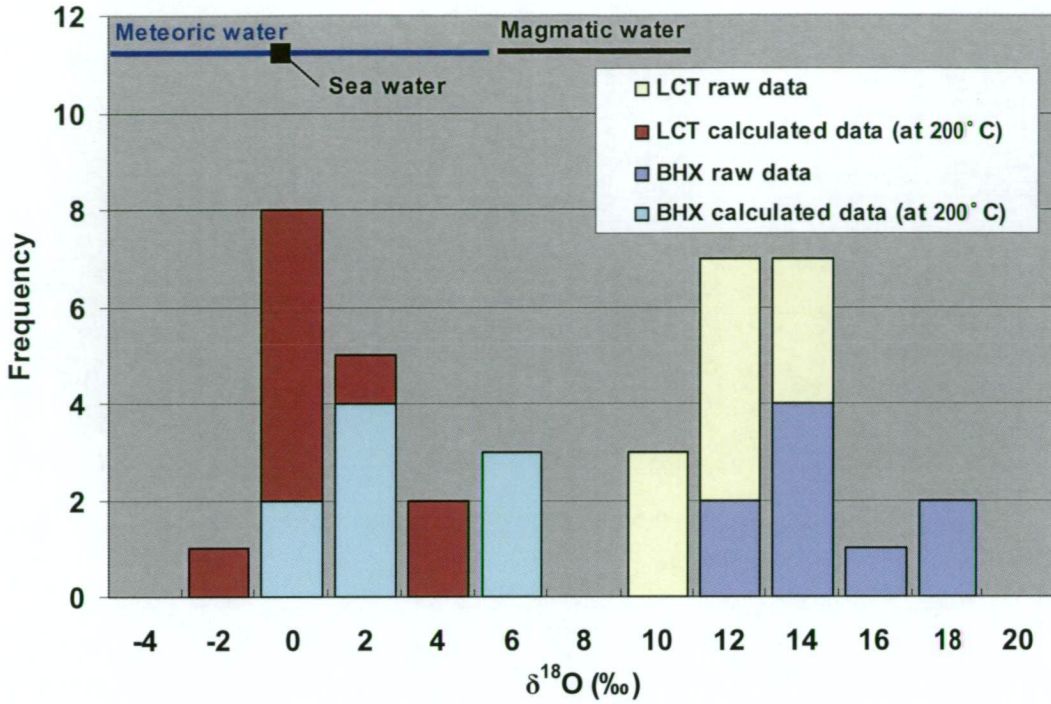


Fig. 7.2. Histogram of the calculated $\delta^{18}\text{O}$ compositions of the Stage 2 vein at LCT and Stage 1 vein and sericitised wall rock samples at BHX using quartz fractionation formula of Zheng (1993) at 200°C, with the ranges of magmatic water, meteoric water and sea water after Rollinson (1993).

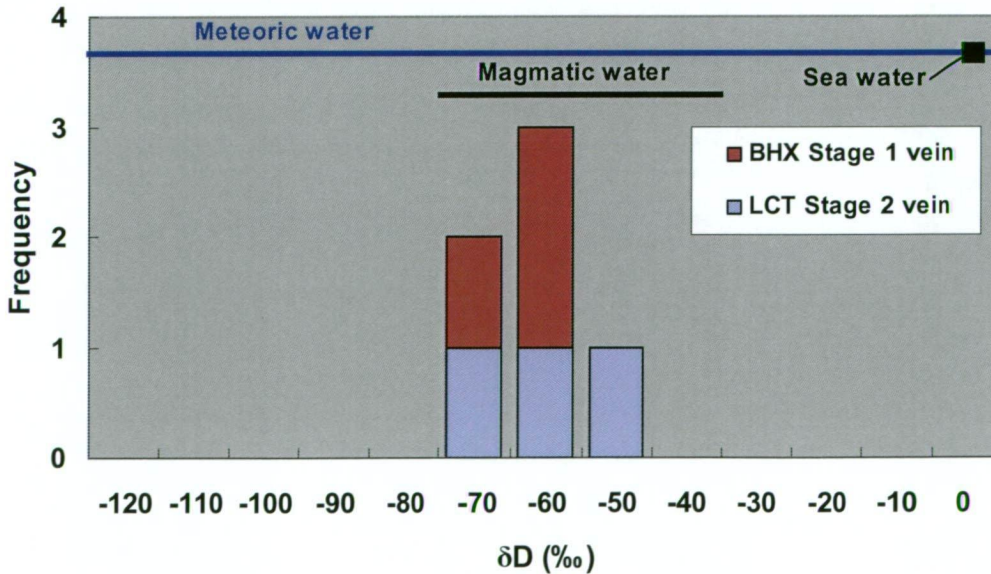


Fig. 7.3. Histogram of the measured δD compositions of the Stage 2 vein at LCT and the Stage 1 vein at BHX, with the ranges of magmatic water, meteoric water and sea water after Rollinson (1993).

7.5. Discussion

7.5.1. Source of sulphur

An igneous source is the most likely source of the sulphur for the sulphide minerals in the LCT and BHX deposits, as the δS^{34} composition of the syn-mineralisation stages at LCT and BHX are similar to the range of igneous sulphur which commonly has values of -5 to 5 per mil (Ohmoto and Rye, 1979) (Fig. 7.4). However, the δS^{34} values of pyrite from the BHX Stage 3 and the LCT Stage 3 are remarkably depleted down to -26.79 ‰ and -16.49 ‰, respectively. These depleted values are likely due to a bacteriogenic source which often reduces the δS^{34} composition of the sulphides (Rollinson, 1993) (Fig. 7.4). This interpretation is also consistent with the reported sulphur isotopic values from modern seafloor sediments which are depleted up to -41 ‰ due to biogenic processes (Kohn et al., 1998).

Meanwhile, it should be noted that the obtained δS^{34} values of sulphides from the LCT and BHX deposits are also comparable with those of VHMS deposits which have formed on the seafloor during Permian to Triassic. Large (1992) reported that the relationship of δS^{34} values of sulphides in the VHMS deposits and the δS^{34} values of sea water are consistent throughout the Phanerozoic, as the ore-forming fluids of VHMS mineralised systems are mainly derived from sea water. By comparison, the δS^{34} values of sulphides from the LCT and BHX deposits are also consistently plotted on the δS^{34} range of the Permian to Triassic VHMS systems (Fig. 7.5). Accordingly, this may indicate that sea water may have been an additional source of sulphur at LCT and BHX.

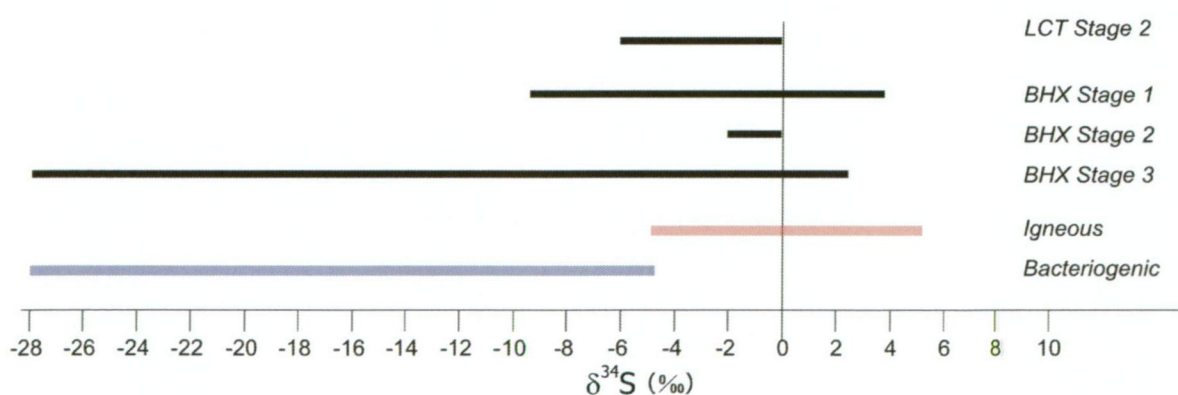


Fig. 7.4. Comparison of δS^{34} values in syn-mineralisation stages at the LCT and BHX deposits with the igneous (Ohmoto and Rye, 1979) and bacteriogenic ranges (Rollinson, 1993).

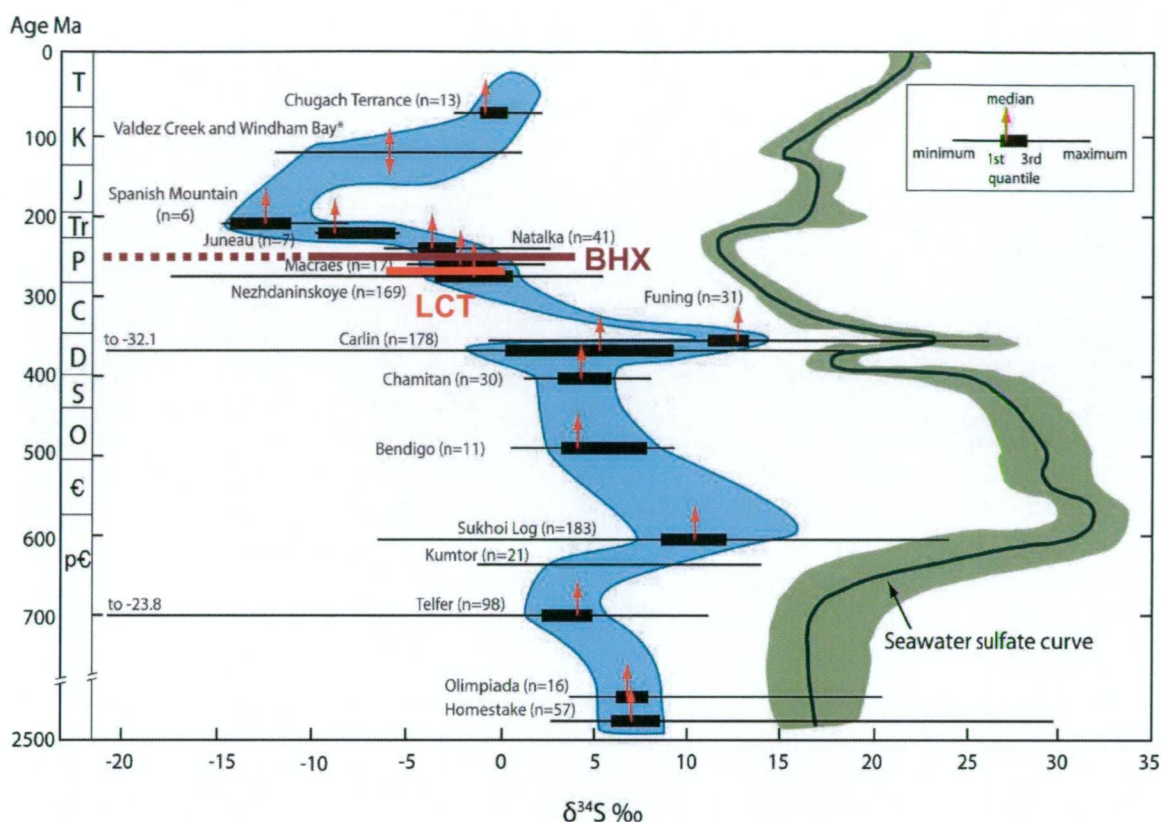


Fig. 7.5. Comparison of the S^{34} value ranges between the LCT and BHX deposits and the major VHMS deposits occurred throughout Phanerozoic time (modified after Large, 1992).

7.5.2. Source of ore-forming fluids

The oxygen and hydrogen isotope data of LCT and BHX were plotted on the bi-variate diagram, incorporated with the magmatic water field (Rollinson, 1993) and the data from several low-sulphidation deposits (Cooke and Simmons, 2000) (Fig. 7.6). On the diagram, the LCT and BHX data are plotted in the field between magmatic water and the meteoric water line. These plots are represented in Fig. 7.6 by an arrow from magmatic water field to meteoric water line, suggesting that LCT and BHX data comprise a mixing of magmatic and meteoric water. In addition, a comparison of LCT and BHX isotopic compositions with those from several low-sulphidation deposits reveals that the LCT and BHX data have similar characteristics to the McLaughlin deposit, and they are distinctly shifted magmatic values (i.e., higher oxygen isotopic composition) from the other deposits. At McLaughlin, Sherlock et al. (1995) considered that a magmatic contribution to the deposit is important and the high oxygen isotopic compositions are thought to have formed due to extremely high oxygen isotopic compositions in the host rock. In comparison, the oxygen and hydrogen isotopic compositions at LCT and BHX may indicate that the ore-

forming fluids formed due to a strong magmatic input and/or a fluid interaction with host rock. The higher salinities of fluid inclusions (Chapter 6) and sulphur isotope data corroborate with magmatic affinity.

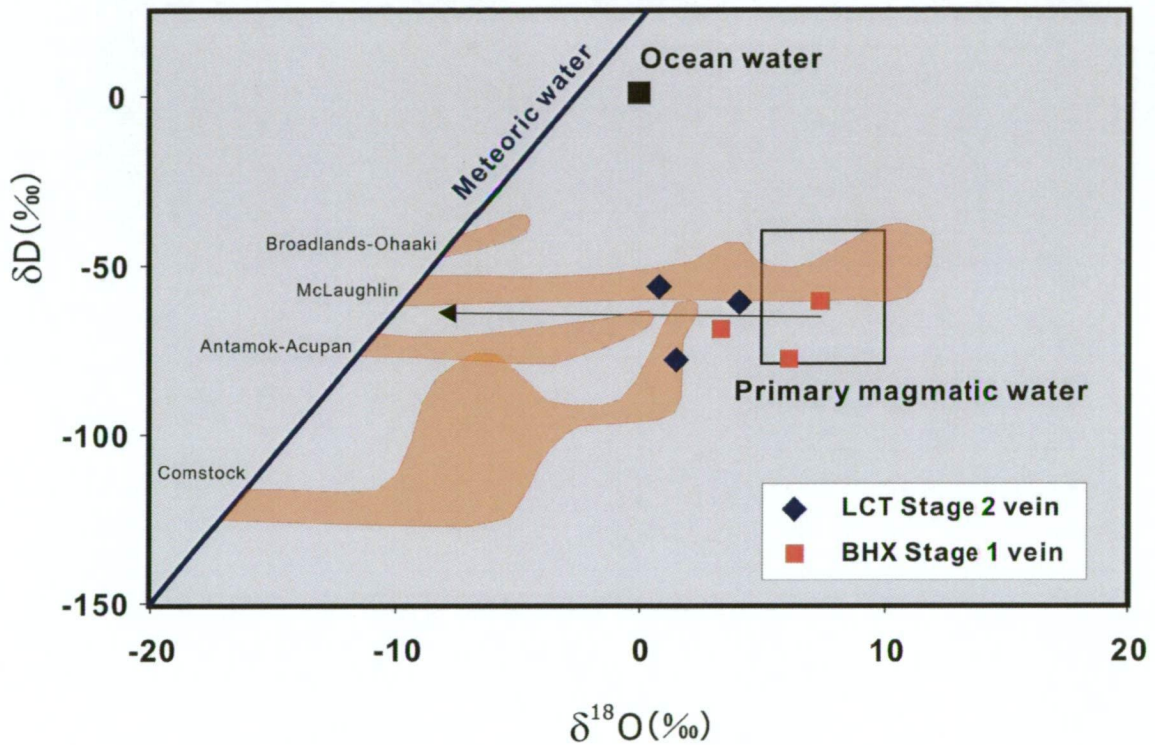


Fig. 7.6. Calculated $\delta^{18}\text{O}$ (with 200°C modeling temperature) and δD values of the ore-bearing fluids at the LCT and BHX deposits, with fields of low-sulphidation deposits (orange coloured) (Cooke and Simmons, 2000) and primary magmatic water (Sheppard, 1986), and mixing trend line (arrow).

7.6. Summary

The nature and significance of the stable isotopic compositions of the LCT and BHX deposits including sulphur, oxygen and hydrogen isotopes are summarised below.

- The sulphur isotope data obtained from Stage 2 of LCT and Stages 1, 2 and 3 of BHX have an igneous source signature, and biogenic sulphur source is also locally recognised in Stage 3 of BHX showing that is depleted as low as -26.79 ‰.
- The oxygen and hydrogen isotopic compositions from Stage 2 of LCT and Stage 1 of BHX may indicate that the ore-forming fluids are characterised by either a mixing of the magmatic and meteoric water, and/or fluid interaction with host rock.

CHAPTER 8 LEAD ISOTOPES

8.1. Introduction

The ratios of ^{204}Pb , ^{206}Pb , ^{207}Pb and ^{208}Pb in Pb-rich minerals (i.e., galena, pyrite, K-feldspar) can provide information as about the age and source of lead in ore deposits (Gulson, 1986). They can be used in this way because the lead isotopic composition of the earth is continually changing.

The lead isotopic composition in minerals and rocks is a mixture of primordial lead, which has existed on earth since it was formed (i.e., 4.57Ga ago), and lead derived from radioactive decay of U and Th (Gulson, 1986). Uranium and thorium are at the top of decay chain which proceeds through many intermediate steps before eventually ending at three different isotopes of Pb (^{206}Pb , ^{207}Pb and ^{208}Pb). One isotope of Pb (^{204}Pb) is not derived from the decay Th and U so that the $^{206}\text{Pb}/^{204}\text{Pb}$, $^{207}\text{Pb}/^{204}\text{Pb}$ and $^{208}\text{Pb}/^{204}\text{Pb}$ are continually changing through the time. As a result of this, the age of Pb-rich minerals can be estimated as they preserve lead isotopic ratios present in the rocks and fluids when they were formed. Different Pb reservoirs in the earth have different U/Pb ratio (μ) so that Pb evolution does not proceed at the same rates in different parts of the crust and the mantle.

The evolution of Pb in a reservoir is generally represented by growth curve. One of the growth curves widely used for describing the evolution of the crust as a whole is the two stage model of Stacey and Kramers (1975). A more complicated set of growth curves for different reservoirs within the earth is outlined in Zartman and Doe (1981) in their plumbotectonic model.

The lead isotopic values are unique from region to region and have been used extensively in mineral exploration (Gulson, 1986). The lead isotopic compositions were investigated to determine the age and source of metals at the LCT and BHX deposits.

8.2. Analytical methods

Three techniques including aqua regia acid digestion, HF-H₂SO₄ high pressure digestion, and LA-ICPMS methods were used in this study to investigate the lead isotopic composition of the

samples from the LCT and BHX deposits. All of the techniques described below were conducted at CODES, University of Tasmania.

Aqua regia acid digestion (Galena solution): This technique was used for samples with large galena crystals which can be easily drilled out using the dentist drill. 4 ml aqua regia (3 ml HCl, 1ml HNO₃) was added to 50 mg of powdered galena sample in 7 ml screw top Teflon Savillex vessels, and heated on a hotplate at 120°C overnight (~16 hours). They were then evaporated and uncovered on a hotplate to incipient dryness. To remove all HCl, 1ml of HNO₃ was added and evaporated to incipient dryness, and this step was repeated. The final residue was dissolved in 4 ml 50 % HNO₃ and heated at ~100°C overnight. Samples were then diluted to 100 ml (1000 times dilution) with the final solutions in an acid matrix of 2 % HNO₃. The samples were further diluted to 100,000 times, to measure the concentration of Pb, and then a final dilution was made to give ~150 ppb Pb in solution for isotope analysis. The samples were analysed on an Agilent 4500 ICP-MS within 24 hours of dilution. For more details of the technique see Townsend et al. (1988).

HF-H₂SO₄ high pressure digestion (Whole rock solution): This technique was used for the selected whole rock samples which had more than 100 ppm Pb as revealed by XRF analysis. 3ml HF and 3ml H₂SO₄ were added to 100 mg of powdered sample in 25 mL Teflon PicoTrace vessels, and heated under pressure at 180°C for 24 hours. The acid was then evaporated to incipient dryness. To remove all trace of HF and H₂SO₄, 1ml HClO₄ was added and again evaporated to incipient dryness. The final residue was dissolved in 2 ml HNO₃ and 5 ml water, and heated at ~70°C overnight. Samples were then diluted to 100 ml (1000 times dilution) with the final solutions in an acid matrix of 2 % HNO₃. Samples were analysed for Pb concentration, and then diluted (if necessary) to give ~150 ppb Pb in solution for isotope analysis. The samples were analysed on an Agilent 4500 ICP-MS within 24 hours of dilution.

LA-ICPMS technique: The LA-ICPMS technique was used to measure the lead composition of galena and pyrite minerals in BHX samples and LCT samples. This method is new and has been shown to work well on pyrite (Meffre et al., 2008). However, the method has never been used on galena prior to this study and as such the laser galena results must be regarded as potentially less accurate than results from better characterised techniques (laser pyrite and solution galena). The poor precision of the laser galena data presented in this study and a small systematic offset between solution and laser data undertaken on the same sample suggest that the laser galena technique require more development.

8.3. Lead isotope data

Table 8.1 presents the summary of the measured lead isotopic compositions including $^{206}\text{Pb}/^{204}\text{Pb}$, $^{207}\text{Pb}/^{204}\text{Pb}$ and $^{208}\text{Pb}/^{204}\text{Pb}$ values. The collected lead isotopic compositions show a small difference in measured values.

The LCT samples analysed using all of the methods including galena solution, whole rock solution and LA-ICPMS method have a consistent range of 18.14 to 18.47, 15.60 to 15.71 and 37.90 to 38.72 in the $^{206}\text{Pb}/^{204}\text{Pb}$, $^{207}\text{Pb}/^{204}\text{Pb}$ and $^{208}\text{Pb}/^{204}\text{Pb}$ ratios, respectively. The lead isotopic data of the BHX Stage 3 samples have a wide range from 17.91 to 18.97, 15.47 to 16.06 and 37.32 to 40.58, in the $^{206}\text{Pb}/^{204}\text{Pb}$, $^{207}\text{Pb}/^{204}\text{Pb}$ and $^{208}\text{Pb}/^{204}\text{Pb}$ ratios respectively. The lead isotopic compositions of the BHX whole rock samples have narrow ranges from 18.16 to 18.97, 15.71 to 15.97 and 38.98 to 39.65 in the $^{206}\text{Pb}/^{204}\text{Pb}$, $^{207}\text{Pb}/^{204}\text{Pb}$ and $^{208}\text{Pb}/^{204}\text{Pb}$ ratios, respectively.

The lead isotopic compositions plot either on or above the terrestrial lead evolution curve of Stacey and Kramers (1975) (Figs, 8.1 and 8.2). The results from the pyrite and whole rock generally plot on a trend towards more radiogenic compositions with decreasing lead contents. The LA-ICPMS results on both the LCT and the BHX data (experimental technique) plot to the left of the solution galena and LA-ICPMS pyrite data (more conventional techniques). The LCT galena was analysed on the same samples using both technique so that the small systematic offset between these two data sets suggest a small analytical problem with the LA-ICPMS galena data.

Table 8.1. Lead isotope data of the LCT and BHX deposits, Lao PDR.

Deposit/ Sample No.	$^{206}\text{Pb}/^{204}\text{Pb}$	$^{207}\text{Pb}/^{204}\text{Pb}$	$^{208}\text{Pb}/^{204}\text{Pb}$	Split method	Assigned stage/wall rock
LCT					
LSD05@80.3m	18.29 ± 0.14	15.65 ± 0.12	38.46 ± 0.12	1	Stage 2
LSD09@88.0m	18.35 ± 0.18	15.71 ± 0.19	38.60 ± 0.19	1	Stage 2
LSD09@88.0m galena	18.14 ± 0.09	15.60 ± 0.08	37.90 ± 0.20	3	Stage 2
LSD13@55.0m	18.31 ± 0.11	15.67 ± 0.11	38.49 ± 0.12	1	Stage 2
LSD15@96.6m	18.31 ± 0.17	15.64 ± 0.16	38.55 ± 0.16	1	Stage 2
LSD24@36.5m	18.47 ± 0.13	15.71 ± 0.15	38.72 ± 0.16	2	Wall rock
LDD03@75.0m	18.30 ± 0.17	15.66 ± 0.20	38.50 ± 0.20	1	Stage 2
LRD67@43.0m	18.31 ± 0.13	15.67 ± 0.12	38.54 ± 0.12	1	Stage 2
BHX					
HSD01@-60.7m	18.69 ± 0.16	15.71 ± 0.21	39.16 ± 0.16	2	Wall rock
HSD03@83.0m	18.66 ± 0.10	15.79 ± 0.11	39.13 ± 0.11	2	Wall rock
HSD04@66.6m	18.97 ± 0.28	15.97 ± 0.22	39.65 ± 0.22	2	Wall rock
HSD06@42.3m	18.72 ± 0.15	15.71 ± 0.14	39.21 ± 0.13	2	Wall rock
HSD08@97.5m	18.61 ± 0.15	15.75 ± 0.13	38.98 ± 0.16	2	Wall rock
256710mE	18.97 ± 0.19	15.84 ± 0.19	39.58 ± 0.14	2	Wall rock
HDD8@228.5m galena-1	17.91 ± 0.17	15.47 ± 0.15	37.32 ± 0.39	3	Stage 3
HDD8@228.5m galena-2	18.31 ± 0.11	15.73 ± 0.10	38.54 ± 0.26	3	Stage 3
HDD7@179.4m pyrite-core	18.86 ± 0.50	16.06 ± 0.45	40.58 ± 0.85	3	Stage 3
HDD7@179.4m pyrite-rim	18.43 ± 0.09	15.78 ± 0.08	39.24 ± 0.19	3	Stage 3

¹Split methods including; 1=galena solution, 2=whole rock solution, and 3=LA-ICPMS

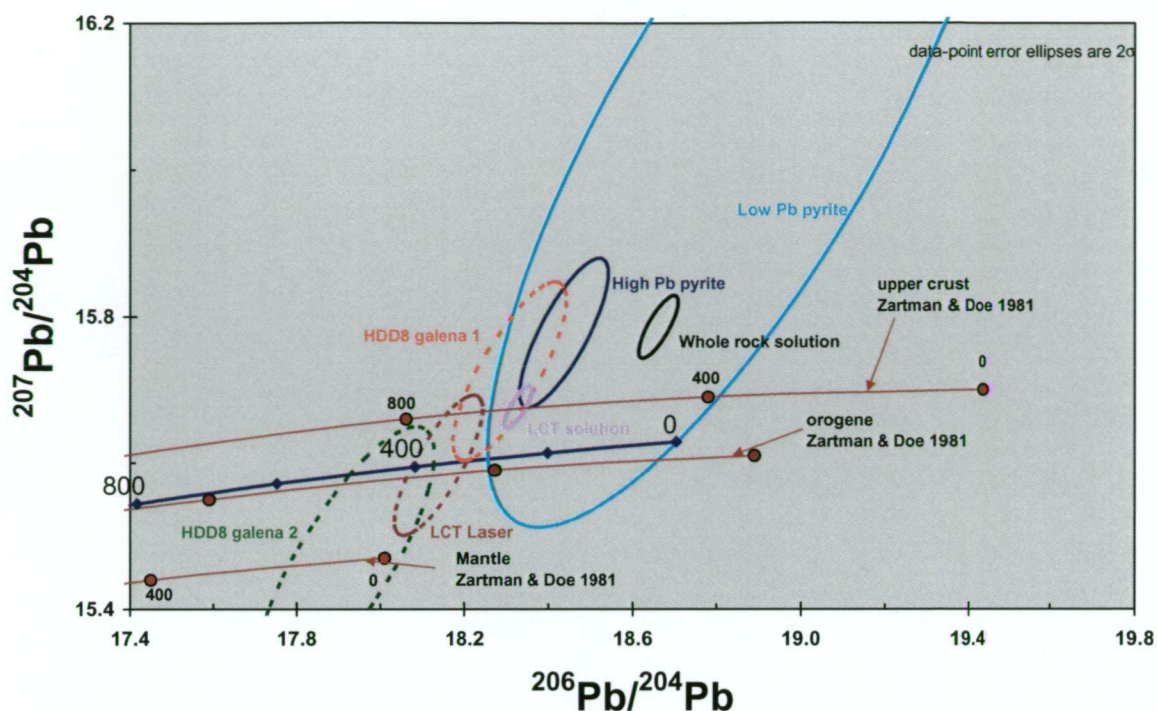


Fig. 8.1. Lead isotopic composition of $^{207}\text{Pb}/^{204}\text{Pb}$ vs $^{206}\text{Pb}/^{204}\text{Pb}$ ratios of the LCT and BHX deposits, with growth curve of Stacey and Kramers (1975) and Zartman and Doe (1981).

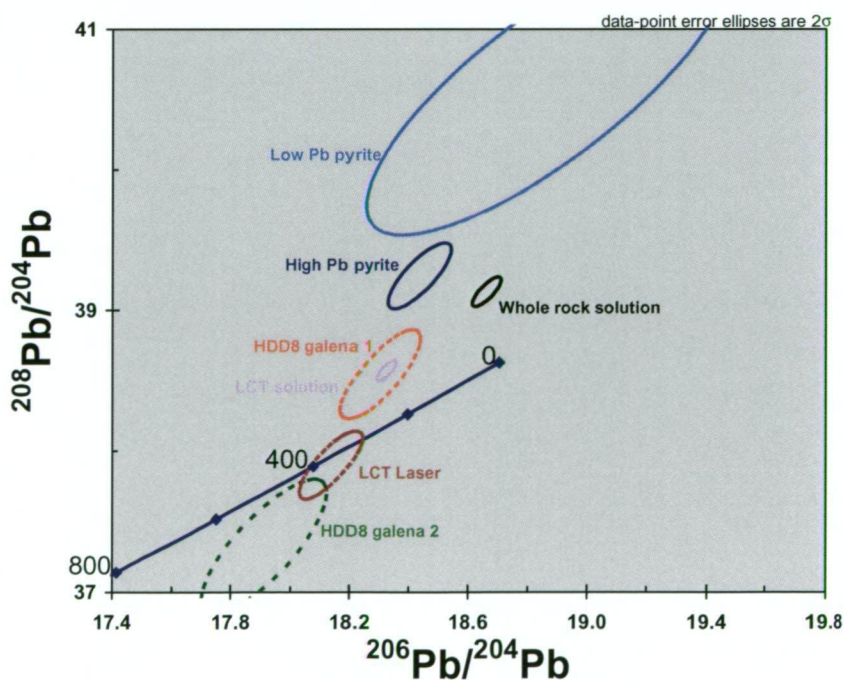


Fig. 8.2. Lead isotopic composition of $^{208}\text{Pb}/^{204}\text{Pb}$ vs $^{206}\text{Pb}/^{204}\text{Pb}$ ratios of the LCT and BHX deposits, with growth curve of Stacey and Kramers (1975).

8.4. Discussion

The lead isotopic data from the LCT and BHX deposits are discussed below.

Lead reservoir: If the experimental LA-ICPMS galena data are discounted, all of the lead isotopic data plots above the terrestrial evolution curve of Stacey and Kramers (1975) and on the upper crustal growth curve of Zartman and Doe (1981) (Fig. 8.1). If the lead was derived purely from a subduction-related magmatic source, the analyses should plot very close to the terrestrial curve, because arc magmas generally plot close to this curve (Zartman and Doe, 1981). The fact that they tend to plot slightly above this curve suggests the involvement of crustal lead.

The trend towards more radiogenic lead isotopic composition with decreasing lead contents in the pyrite and the whole rock can be explained by the addition of more radiogenic lead to the system at some time after mineralisation. This will tend to affect minerals with low lead (such as the whole rock composition) much more than the high Pb-mineral (e.g., galena). Such radiogenic lead addition in ore deposits commonly occurs in low-lead content samples, as reported by Gulson (1986).

The analyses are content with a 350-250Ma age for the early (galena) lead reservoir on both the global growth curve of Stacey and Kramers (1975) (Figs. 8.1 and 8.2). A locally constrained lead growth curve would be more appropriate than the global curves, however very little lead isotopic work has been undertaken prior to the beginning of the CODES SE Asian projects. Preliminary unpublished results from this CODES SE Asian project suggest that the local growth curve is very close to the average crustal curve of Stacey and Kramers (1975) (Figs. 8.3 and 8.4). The lead isotopic composition at both LCT and BHX is slightly more radiogenic (particularly in $^{207}\text{Pb}/^{204}\text{Pb}$) than that from pyrites from Phu Kham although this may not be significant as the error ellipses are very close to each others.

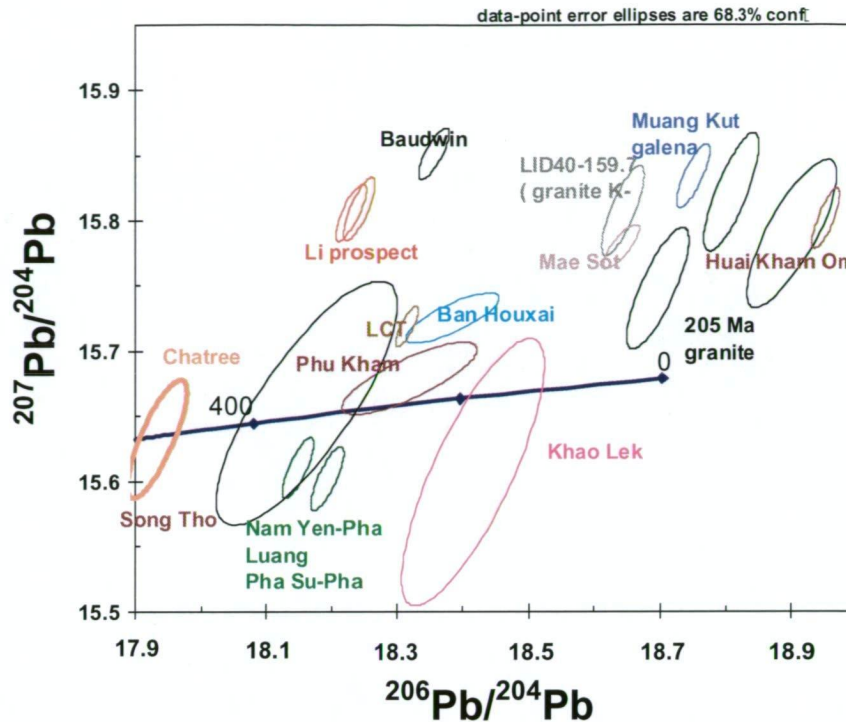


Fig. 8.3. Plots of lead isotope fields of the LCT and BHX deposits and those of other deposits and granites in mainland SE Asia with a growth curve of Stacey and Kramers (1975) (Meffre, unpublished).

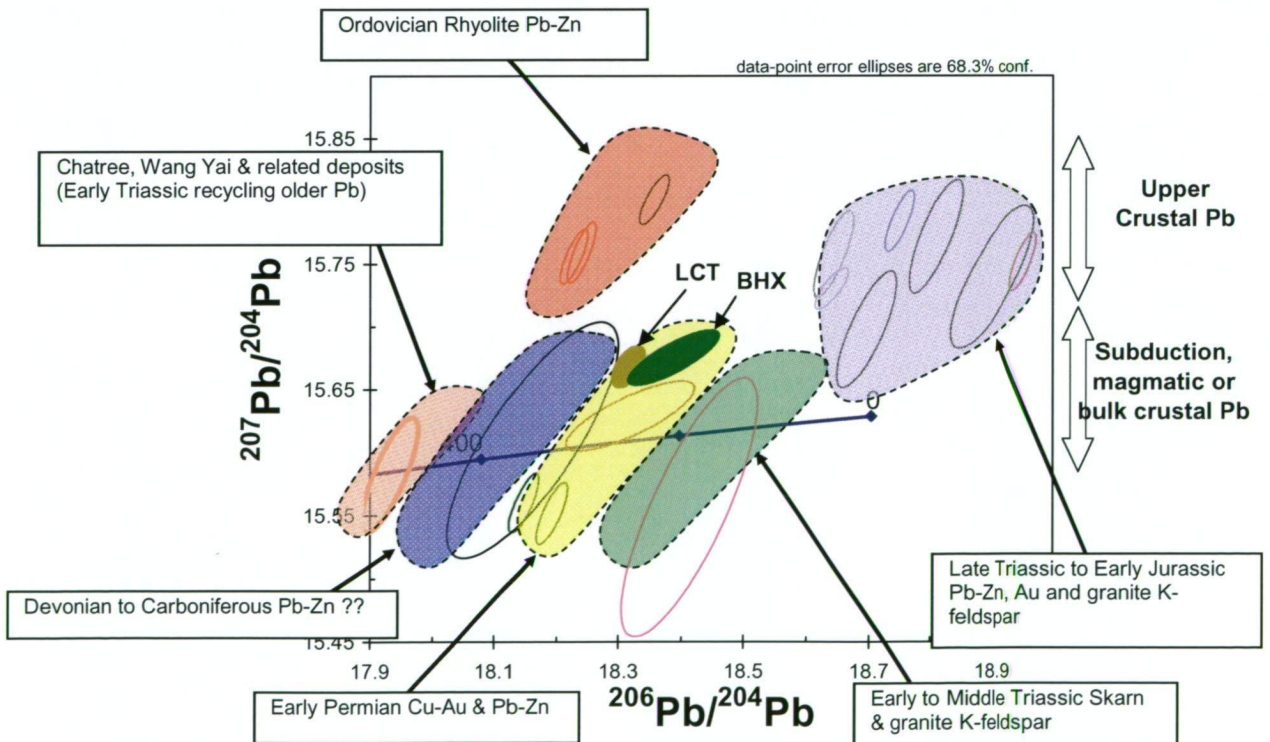


Fig. 8.4. Plots of lead isotope fields for metallogenic styles and granites of mainland SE Asia with a growth curve of Stacey and Kramers (1975) (Meffre, unpublished). Note that lead isotope fields of LCT and BHX plot in Early-Permian Cu-Au & Pb-Zn field.

8.5. Summary

The characteristics of the lead isotopic compositions obtained from the LCT and BHX deposits are summarised below.

- The lead isotope data of the LCT and BHX deposits suggest that lead was derived from an upper crustal source.
- The lead isotopic composition for the galena at LCT and pyrite at BHX is consistent with the both deposit forming around 300 Ma based on the preliminary growth curve local currently being developed from major ore deposits of mainland SE Asia.

CHAPTER 9 DISCUSSION AND CONCLUSIONS

9.1. Introduction

This chapter combines the geological and geochemical data collected in this study on the LCT and BHX deposits to further discuss their nature and origin. An attempt is made herein to compare the LCT and BHX deposits with the known epithermal deposit models and, based on these genetic models, to discuss the implications for mineral exploration in the region.

9.2. Formation of vein stages

Prior to discussion, the mineralisation occurrences of the LCT and BHX deposits are briefly summarised herein.

At LCT, five mineralisation stages were recognised including one syn-mineralisation stage (i.e., Stage 2), which occurs as stockwork veins. The mineralisation at LCT initially occurred with Stage 1 hydrothermal breccia (Fig. 9.1A), followed by the Stage 2 veins occurring preferentially in the feldspar-phyrlic dacitic porphyry unit (Fig. 9.1B). The extensive alteration associated with this stage forms throughout the deposit area and is characterised by sericite-rich proximal alteration in and around the vein, and chlorite-rich alteration in the distal part (Fig. 9.1B). The Stage 2 is followed-up by the post-mineralisation stages comprising sulphide veins, calcite veins and supergene clay alteration stages (Stages 3, 4 and 5) at LCT (Fig. 9.1C).

The BHX deposit includes seven mineralisation stages involving three early syn-mineralisation stages (i.e. Stages 1, 2 and 3). All the syn-mineralisation stages occur as either veins, breccia or veinlets. Stage 1 stockwork veins occur throughout the deposit area, whereas the occurrences of the Stage 2 vein/breccia and Stage 3 veinlets are confined to the N-S fault zone (Figs. 9.2A, B and C). The extensive sericitic and chloritic alteration formed in the host rock at BHX is associated with the Stage 1 mineralisation. Late non-mineralised stages are also identified such as Stages 4, 5, 6 and 7, which mostly comprise quartz and carbonate mineral assemblages.

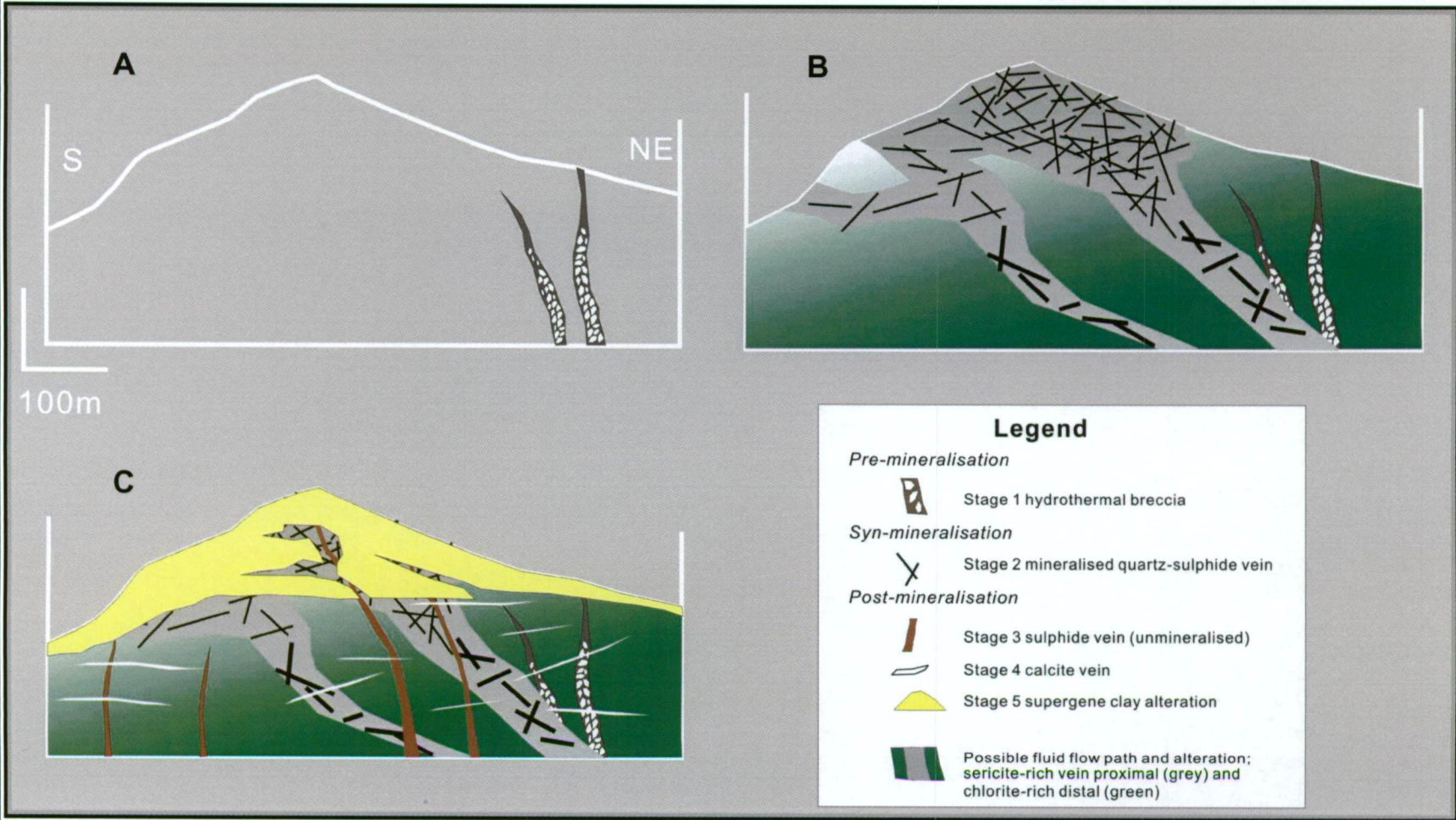


Fig. 9.1. Schematics showing mineralisation stages of the LCT deposit. (A) Pre-mineralisation Stage 1, (B) Syn-mineralisation Stage 2, and (C) Post-mineralisation Stages 3, 4 and 5.

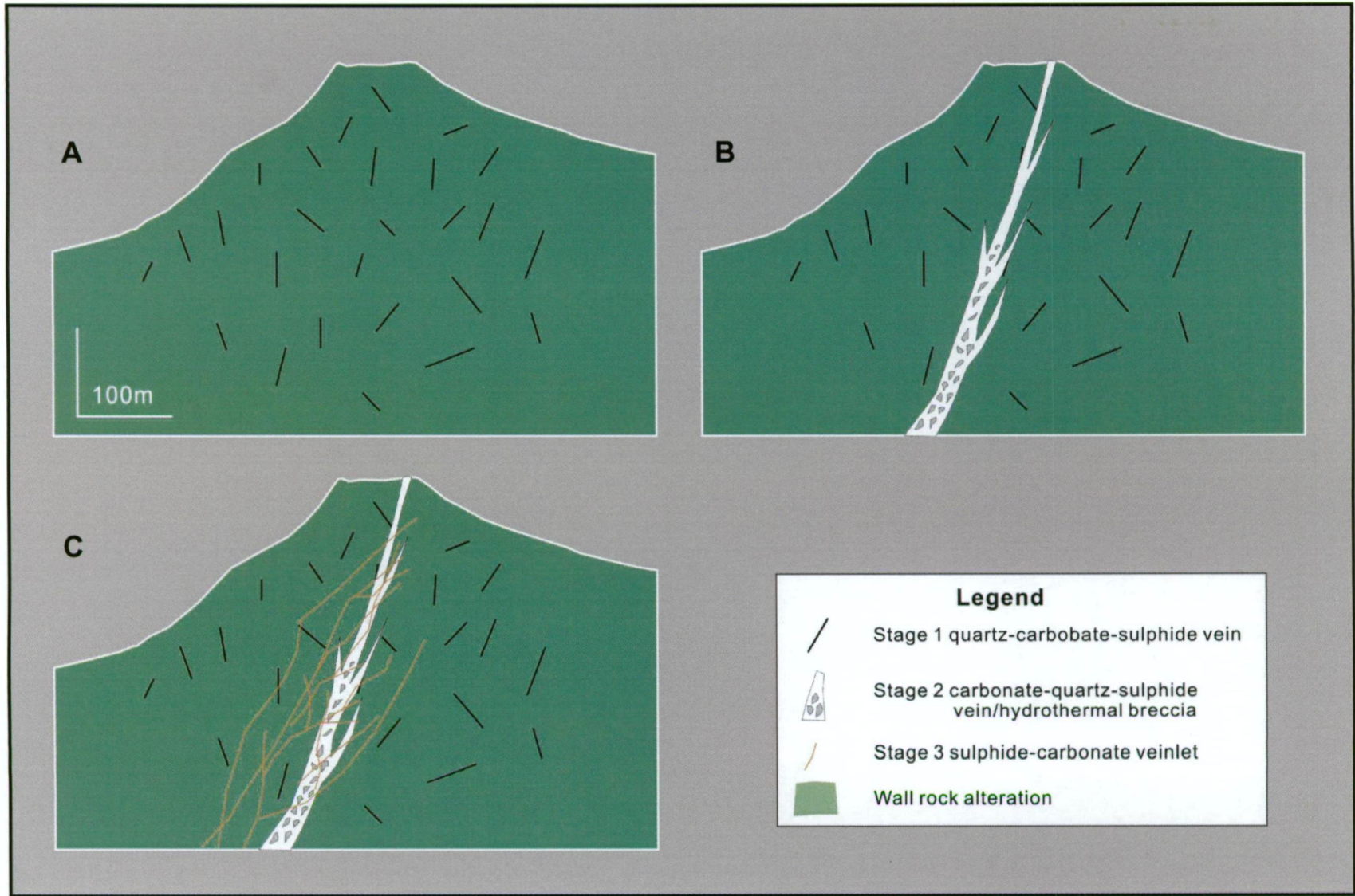


Fig. 9.2. Schematic diagram showing syn-mineralisation stages of the BXH deposit. (A) Stage 1, (B) Stage 2, and (C) Stage 3.

9.3. Origin of the LCT and BHX deposits

The geological, mineralogical, paragenetic, geochemical, isotopic and fluid inclusion data of the LCT and BHX deposits are summarised in Table 9.1. On this basis, the principal factors of the ore deposition of the deposits including source, transport and trap are discussed below for the purpose of characterising the genetic features of the LCT and BHX deposits.

Source: Different source regions can be postulated for the ore-forming fluids and metals at the LCT and BHX deposits. The ore-forming fluids may have consisted of mixed magmatic and meteoric water as revealed by Se concentration in pyrite, oxygen and hydrogen isotopic compositions and lead isotopic compositions. Se concentrations in pyrite suggest that pyrites at LCT and BHX are mostly of non-magmatic source although few data have strong magmatic feature (Chapter 5). Comparison of the oxygen and hydrogen isotopic compositions with those of the other low-sulphidation deposits also indicates that ore fluids responsible for the stockwork veins at LCT and BHX have a stronger magmatic input (Chapter 7). The sulphur isotopic data of the LCT and BHX deposits also show a strong magmatic source affinity (Chapter 7). The lead isotopic compositions of the LCT and BHX deposits display a mixed crustal source, implying lead was derived from various sources (Chapter 8).

Transport: The gold and silver in the LCT and BHX deposits may have been transported by bisulphide and chloride complexes. The relatively high salinity values of the fluid inclusions in the Ag-rich Stages 2 and 3 at BHX may indicate that the silver was dominantly transported by chloride complexes (Chapter 6). The importance of chlorite complexes for silver transport in the Ag-rich hydrothermal system is well-documented through the detailed studies on the Ag-rich epithermal deposits in Mexico (e.g., Simmons et al., 1988; Albinson et al., 2001). By contrast, the sulphide complexes may have been the main transport mechanisms in the low salinity fluids of the Au-rich stockwork veins recognised as Stage 2 at LCT and Stage 1 at BHX (Chapter 6). In the typical Au-Ag low-sulphidation epithermal systems, it is generally accepted that the gold is predominantly transported as bisulphide complexes (e.g., Huston et al., 1992; Cooke and Simmons, 2000), and on this basis the bisulphide complexes are considered to play a significant role for gold transport in the Au-rich vein systems at LCT and BHX.

Trap: The metal deposition in the LCT and BHX deposits may have occurred due to complex trap mechanisms. Buchanan (1981) suggests that boiling is the principal factor for metal precipitation

Table 9.1. Summary of the geological, mineralogical and geochemical characteristics of the LCT and BHX deposits, Lao PDR. N/D = no data.

		LCT	BHX		
		Stage 2	Stage 1	Stage 2	Stage 3
Geology	Tectonic setting	Volcanic-arc	Volcanic-arc		
	Host rock	Tuffaceous sandstone & dacitic porphyry	Andesite & volcanic breccia		
	Geological affinity	Calc-alkaline	Calc-alkaline		
	Host rock age	Early Carboniferous (tuffaceous sandstone) & Early Permian (dacitic porphyry)	Early Permian		
Mineralisation	Vein texture	Stockwork, crystalline & crustiform	Stockwork	Massive & brecciation	Veinlets
	Ore mineral	Pyrite, sphalerite, galena, chalcocopyrite, arsenopyrite, electrum, native gold	Pyrite, sphalerite, chalcocopyrite, electrum	Pyrite, sphalerite, galena, chalcocopyrite, native silver, stephanite	Pyrite, sphalerite, galena, chalcocopyrite, arsenopyrite, electrum, native silver
	Gangue mineral	Quartz, sericite, illite, adularia, chlorite	Quartz, calcite, chlorite, sericite, adularia, illite, chalcedony	Quartz, calcite, adularia, sericite, chlorite	Dolomite, ankerite, hematite,
	Structural control	E-W strike with northerly dipping?	E-W strike with northerly dipping	N-S strike with westerly dipping	N-S strike with westerly dipping
	Electrum fineness	520 to 867	317 to 558	0 to 167	0 to 267
	Sphalerite Fe content (mole %)	4.88 to 11.98	2.76 to 6.19	3.04 to 3.89	2.73 to 4.17
Pyrite geochemistry	Associated elements with Au	Ag, As, Pb, Cu, Co, Sb, Tl			
	Distinct elements	Au, Tl	Au, Ag, As	N/D	Au, Tl, Sb, Ag, As
	Au/Ag ratio	0.1 to 10	1 to 10	N/D	0.01 to 0.1
Isotope signature	S	-5.8 to -0.4 ‰	-8.2 to 3.3 ‰	-1.9 to -1.0 ‰	-26.8 to 0.9 ‰
	O* & H	-1.0 to -4.3 ‰, -79 to -55 ‰	0.3 to 7.3 ‰, -79 to -60 ‰	N/D	N/D
	Pb	Mixed crustal source			
Fluid inclusions	Homogenisation temperature	175 to 205 °C	190 to 215 °C	245 to 415 °C	240 to 315 °C
	Salinity (wt. % NaCl equiv.)	1.7 to 8.3	2.9 to 6.3	4.8 to 13.0	2.7 to 7.7

* calculated oxygen isotopic data at 200°C modeling temperature.

in epithermal systems, and it is known that boiling causes further metal deposition in epithermal systems, as it does decreasing temperature, loss of CO₂ and H₂S, and an increase of pH of ore-forming fluids (e.g., Reed and Spycher, 1985). However there was no fluid inclusion evidence of boiling (e.g., coeval vapour-rich and liquid-rich inclusions) at LCT and BHX. Nevertheless, the existence of boiling at LCT and BHX can not be totally ruled out, as the presence of abundant adularia is noted, which is still considered to be a product of boiling in a hydrothermal system (Lawless et al., 1999).

For the metal deposition at LCT and BHX, the water-rock interactions should be considered. It is noted that the syn-mineralisation veins are preferentially hosted in intermediate volcanic and sub-volcanic rocks such as the dacitic porphyry at LCT and the andesite at BHX (see Chapter 4 for details). The importance of the lithological control in epithermal deposits is revealed at the Coromandel volcanic zone in New Zealand, where the epithermal Au-Ag deposits are mostly (up to 87%) hosted in andesitic rocks (Christie et al., 2007). The water-rock interaction may have played an important role for metal deposition at LCT and BHX.

The fluid inclusion data also indicate that there were two fluid mixing processes during the formation of stockwork veins and structurally-hosted veins at LCT and BHX. The stockwork veins are characterised by isothermal mixing trends, whereas the structurally-hosted veins display surface fluid dilution trends (see Chapter 6 for details). These fluid mixing processes may have resulted in the different metal deposition (i.e., Au-rich in stockwork vein and Ag-rich in structurally-hosted vein).

9.4. Deposit models

Tables 9.2 and 9.3 summarise the mineralisation characteristics such as tectonic setting, host rock, ore texture, alteration, isotope and fluid inclusion data for the LCT and BHX deposits. The LCT deposit consists of one syn-mineralisation stage (Stage 2), whereas the BHX comprises three syn-mineralisation stages (Stages 1, 2 and 3). The structurally-hosted veins (i.e., Stages 2 and 3) appear to be the main mineralised system at BHX as indicated by a three dimensional model (Fig. 9.3). On this basis, the characteristics of the LCT (Stage 2) and BHX (Stages 2 and 3) deposits are compared with Au-rich and Ag-rich epithermal deposits, respectively. They include “typical” low-sulphidation epithermal deposits and epithermal Au-Ag deposits of the Hauraki Goldfield in New Zealand for LCT, and “typical” Mexican Ag-rich epithermal deposits and the Santo Nino epithermal deposit in Mexico for BHX.

LCT model: The Stage 2 mineralisation at LCT is comparable to the “typical” low-sulphidation epithermal deposit and the epithermal Au-Ag deposits of the Hauraki Goldfield in New Zealand (Table 9.2). The detailed correlations of the vein texture, ore and gangue mineralogy and fluid inclusion data with the model of Buchanan (1981) indicate that the LCT deposit is equivalent to the deeper part of his model (Fig. 9.4). In particular, the oxygen and hydrogen isotope data imply a stronger magmatic input compared with those of typical low-sulphidation epithermal deposits, and fluid inclusions show no unequivocal evidence of fluid boiling. These factors may indicate that the LCT deposit formed below the boiling zone in a deeper part of the system (Fig. 9.4). This interpretation is consistent with the presence of crystalline quartz with a lack of dominant crustiform-colloform banded texture and abundant sulphides (dark sphalerite and galena) within the LCT system. The occurrence of considerable CO₂ in the ore fluid of the LCT also corroborates with the deeper nature of the system and may suggest a transitional environment from epithermal to mesothermal conditions near an intrusive body.

BHX model: A comparison between the geological and geochemical characteristics of the Ag-rich structurally-hosted vein systems (Stages 2 and 3) of the BHX deposit with the Mexican Ag-rich epithermal and the Santo Nino epithermal systems are shown in Table 9.3. The geochemical data from BHX show similar characteristics to those from the Mexican Ag-rich epithermal and Santo Nino systems, particularly in metal content (i.e., Ag-rich) and fluid inclusion data. The fluid inclusion data from the BHX deposit, including homogenisation temperatures and salinity values, are comparable to the middle to deeper part of the system (Fig. 9.5).

Table 9.2. Comparison of the geological, geochemical and mineralisation characteristics of the LCT deposit (Stage 2 mineralisation) with typical low-sulphidation epithermal deposits and the epithermal Au-Ag deposits of Hauraki Goldfield in New Zealand.

	LCT (Stage 2)	Low-sulphidation epithermal deposits	Epithermal Au-Ag deposits of the Hauraki Goldfield, New Zealand
Tectonic setting	Volcanic-arc	Volcanic-arc	Volcanic-arc
Host rock	dacitic (calc-alkaline) porphyritic rock	Calc-alkaline volcanic rocks	Calc-alkaline volcanic (andesitic or dacitic) rocks
Ore texture	Stockwork, crystalline and crustiform veins	Veins, breccia, vein breccia, stockwork vein, dissemination	Breccia, stockwork vein, banded vein, massive vein, crystalline vein
Au-Ag signature	Au>Ag	Au>Ag	Au>Ag
Alteration	Sericitisation, chloritisation	Propylitic, argillic, advanced argillic	Propylitic, quartz±calcite±adularia±illite, argillic, advanced argillic
Isotopes	S; -26.8 to 0.9 ‰, O; -1 to -4.3 ‰, H; -79 to -55 ‰	S; centred on 0, O; -10 to 12 ‰, H; -130 to -40 ‰	S; -3.1 to 4.9 ‰, O; -7 to 3.8 ‰, H; N/D
Mineral assemblage	Pyrite, chalcopyrite, sphalerite, galena, arsenopyrite, electrum, quartz, sericite, adularia, chlorite, illite, calcite,	Pyrite, galena, chalcopyrite, sphalerite, pyrrhotite, quartz, calcite, illite, montmorillonite, chlorite, adularia	Pyrite, sphalerite, galena, chalcopyrite, sulphosalt minerals, electrum, acanthite, Te-bearing minerals, Se-bearing minerals, stibnite, cinnabar, quartz, calcite, adularia, illite
Fluids	175 to 205°C, 1.7 to 8.3 wt. % NaCl equiv.	150 to 270°C, <2 wt. % NaCl equiv.	180 to 250 °C, 0 to 6.1 (mostly <2) wt. % NaCl equiv.
Reference	This study	Buchanan (1981); Morrison et al. (1991); Cooke and Simmons (2000); Hedenquist et al. (2000);	Simpson et al. (2001); Christie et al. (2007)

Table 9.3. Comparison of the geological, geochemical and mineralisation characteristics of the BHX deposit (Stages 2 and 3) with the Mexican Ag-rich epithermal and the Santo Nino epithermal deposits.

	BHX (Stages 2 & 3)	Mexican Ag-rich epithermal system	The Santo Nino epithermal system, Mexico
Tectonic setting	Plate Margin (volcanic-arc)	Volcanic-arc	Volcanic-arc
Host rock	Andesite (calc-alkaline), volcanic breccia	Marine sedimentary rocks, volcanics, intrusions	Graywacke, shale, mafic volcanics, conglomerate
Ore occurrence	Vein, breccia, veinlet	Veins, breccia, stockwork vein, veinlet,	Vein, breccia
Au-Ag signature	Ag>Au	Ag>Au	Ag>Au
Structural control	N-S trending, steep westerly dipping fault zone	Regional normal block faults	Oblique deformation with right- lateral strike slip
Alteration	Sericitic	Propylitic, phyllic, argillic, advanced argillic	Silicific, argillic, propylitic, potassic
Isotopes	S; -26.8 to 0.9 ‰	S; centred on 0, O; -6 to 9 ‰, H; -61 to -115 ‰	S; N/D, O; 3.9 to 7.7 ‰, H; -43 to -75 ‰
Mineral assemblage	Pyrite, chalcopyrite, shalerite, galena, arsenopyrite, native silver, electrum, stephanite, ankerite, dolomite, quartz, adularia, sericite, chlorite	Pyrite, galena, chalcopyrite, sphalerite, pyrargirite, quartz, calcite, adularia, chlorite, chalcedony, calc- silicate minerals, clay	Pyrite, sphalerite, galena, pyrargyrite, polybasite, chalcopyrite, arsenopyrite, tetrahedrite, argentite/acanthite, stephanite, marcasite, proustite, antimonpearceite, pyrrotite, selenium polybasite, quartz, chalcedony, calcite, chlorite, clay
Fluids	240 to 440°C, 2.7 to 13.0 wt. % NaCl equiv.	200 to >300°C, <23 wt. % NaCl equiv.	170 to 260°C, 8.5 to 12 wt. % NaCl equiv.
Reference	This study	Simmons (1991); Albinson et al. (2001);	Simmons et al. (1988); Gemmell et al. (1988)

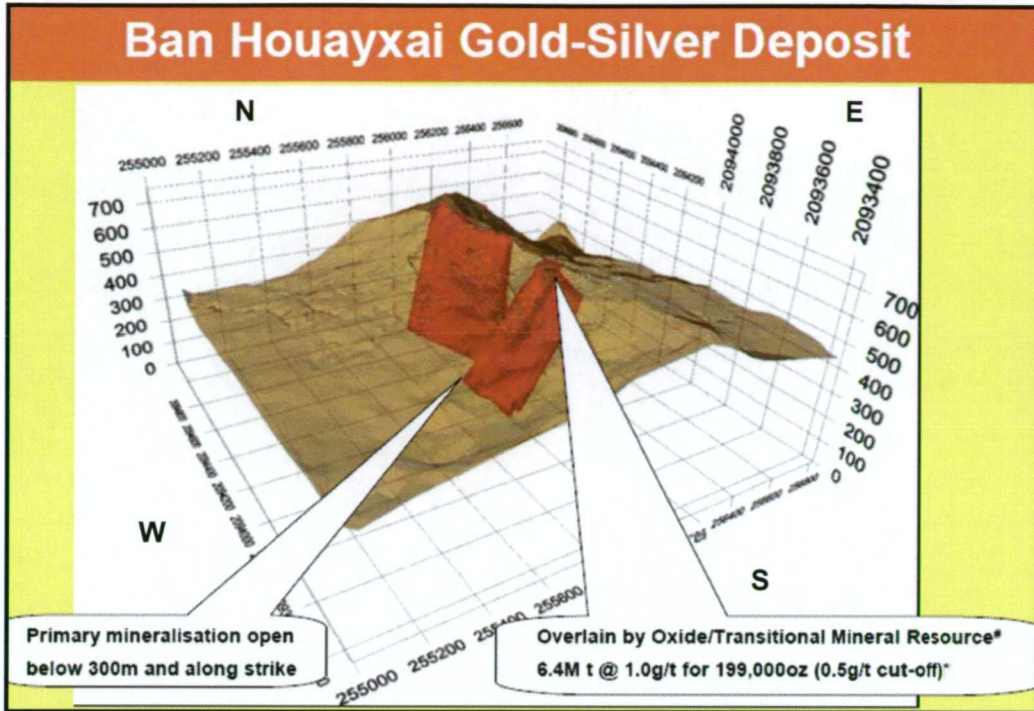


Fig. 9.3. Three dimensional ore model of the BHX deposit, looking NE (<http://www.panaust.com.au>). Note that the ore models trends N-S with a westerly dip and is separated by a late stage E-W trending fault in the central deposit area, resulting in two ore bodies in the south and north.

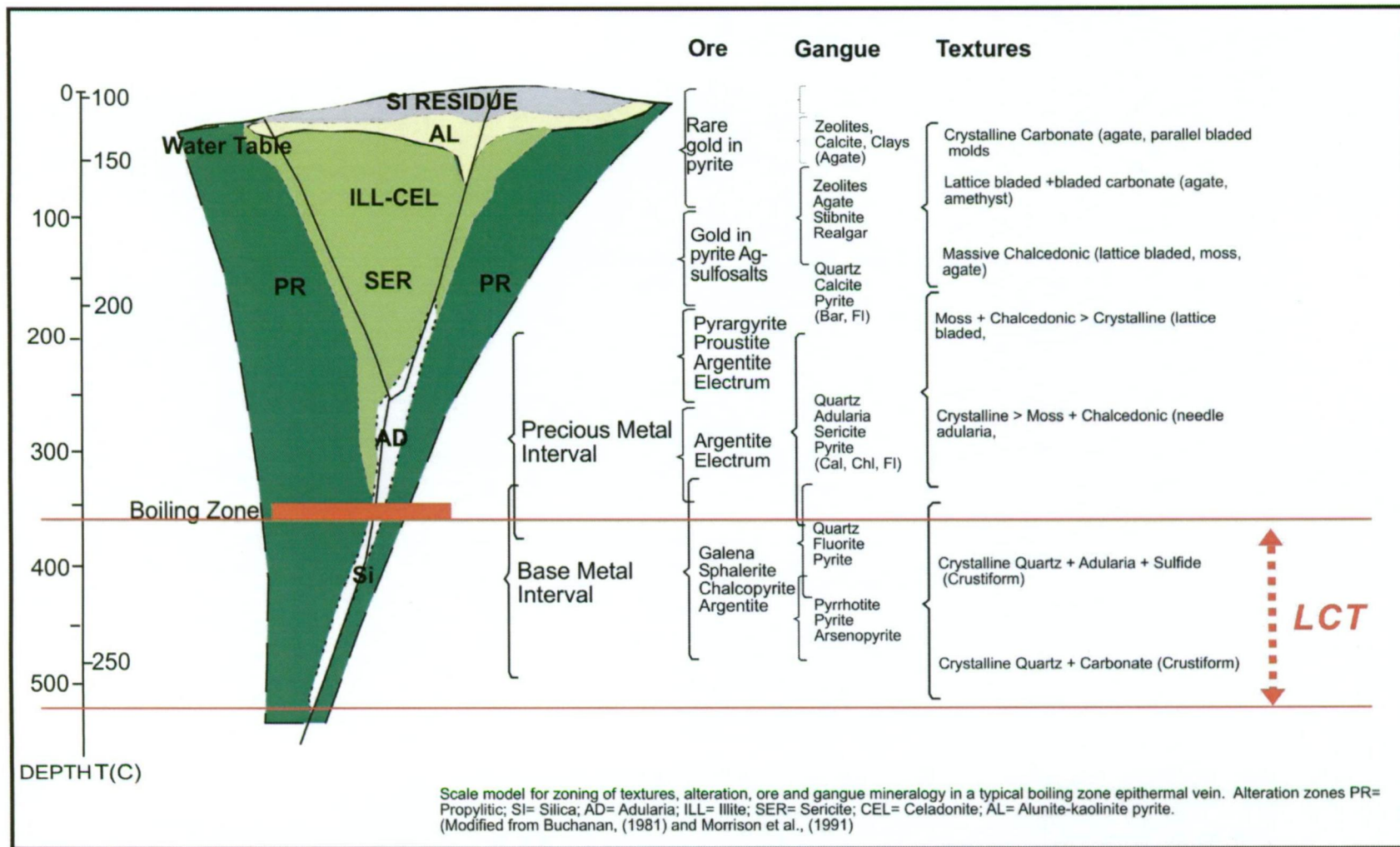


Fig. 9.4. Low-sulphidation epithermal model of Morrison et al. (1991) developed from Buchanan (1981) in comparison with the LCT mineralisation (Stage 2).

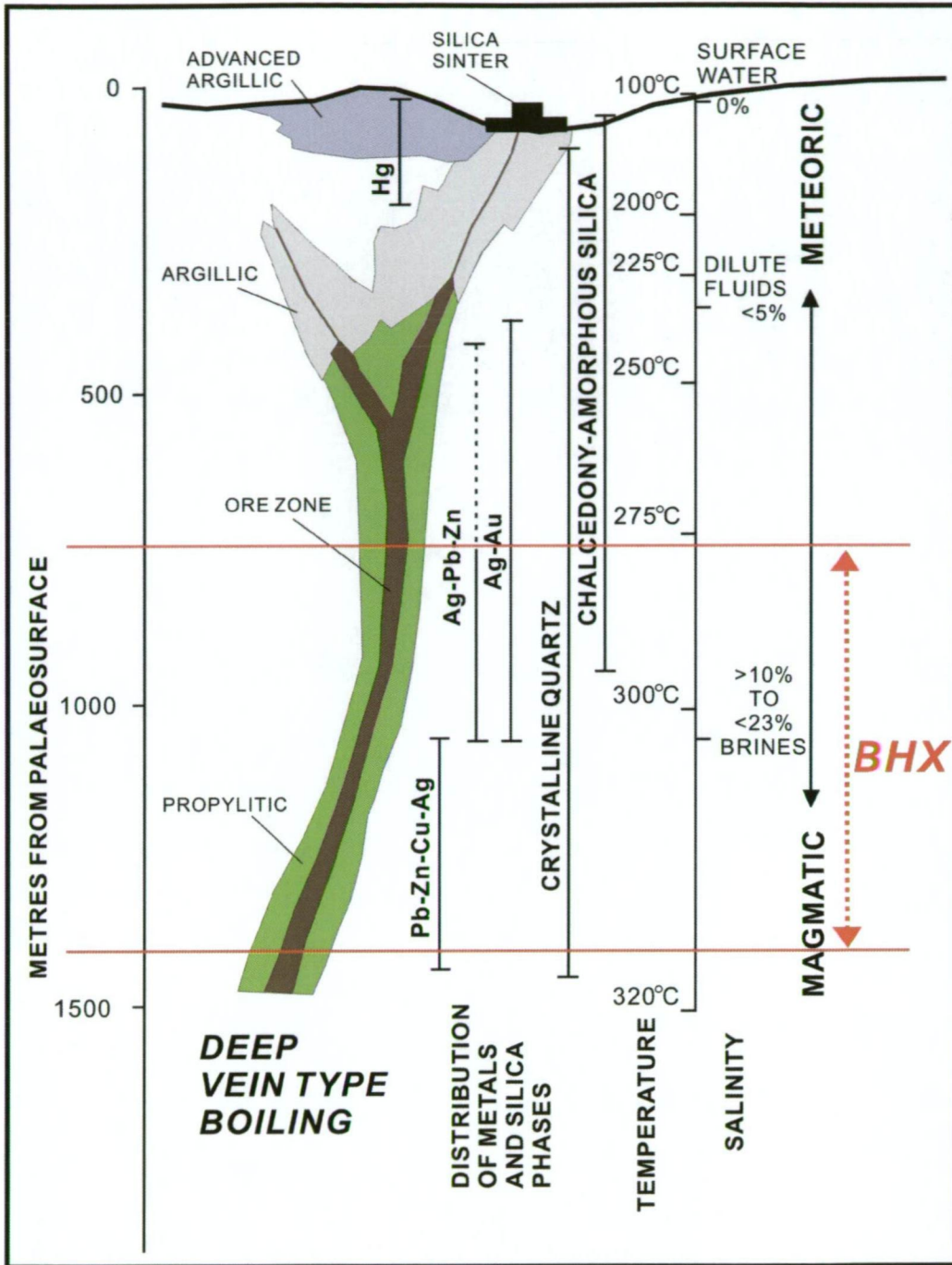


Fig. 9.5. Ag-rich Mexican epithermal model of Albinson et al. (2001) in comparison with the BHX mineralisation (Stages 2 and 3).

9.5. Conclusions

The main conclusions of this study on the geological setting and mineralisation characteristics of the LCT and BHX deposits are listed as below:

- The geology of the LCT deposit consists of an Early Permian Carboniferous sedimentary sequence intruded by Early Permian igneous rocks. The BHX deposit is predominantly hosted by an Early Permian volcano-sedimentary sequence. The red bed sedimentary rocks locally occurring at BHX are younger than the volcano-sedimentary sequence, with detrital U-Pb zircon ages as late as Triassic.
- The LCT deposit has five mineralisation stages including a single syn-mineralisation stage (i.e., Stage 2), whereas seven mineralisation stages are recognised at the BHX deposit including three syn-mineralisation stages (i.e., Stages 1, 2 and 3). The Stage 2 at LCT and Stage 1 at BHX mainly occur as stockwork veins, whereas Stages 2 and 3 of BHX occur as veins and veinlets in the N-S trending, westerly dipping fault zone.
- The alteration associated with the stockwork veins is dominantly developed at the LCT and BHX deposits, and consists of quartz, sericite, adularia, chlorite, illite and pyrite assemblages and chlorite, sericite and adularia assemblages, respectively. The alteration associated with Stage 2 of BHX is limited to the vein proximity (<1 m) comprising sericite, adularia and chlorite, whereas no significant alteration is associated with the Stage 3 mineralisation at BHX.
- The gold in the stockwork veins at LCT and BHX mostly occurs as electrum and some of the electrum occurring at LCT can be compositionally classified as native gold. In the structurally-hosted Stage 2 and 3 veins/veinlets at BHX, gold occurs as electrum and silver is present in electrum, native silver and stephanite. The occurrence of such gold- and silver-bearing minerals is intimately associated with pyrite, sphalerite, chalcopyrite, galena and arsenopyrite.
- Pyrite trace element analyses using LA-ICPMS reveal that the pyrites from the syn-mineralisation stages of the LCT and BHX deposits host variable concentrations of Au and Ag in the structure. A close association of Au with Ag, As, Sb, Tl, Pb and Co elements in pyrites was also found.

- The fluid inclusion data indicate that there are two different fluid mixing natures between the Au-rich stockwork veins and the Ag-rich structurally-hosted veins. The salinity values in the structurally-hosted Ag-rich veins are higher than those in the Au-rich stockwork veins.
- Bisulphide and chloride complexes may have played a significant role in the gold and silver transport, respectively. As fluid mixing processes are recognized, gold and silver were precipitated due to the mixing of fluids or the interaction of ore fluid with wall rocks. The boiling of ore fluids is considered to have played a minimal or insignificant role at LCT and BHX as there is a general lack of fluid inclusion evidence of boiling.
- The ore-forming fluids of Stage 2 at LCT and Stage 1 at BHX may have consisted of magmatic and meteoric water, evident by the stable isotope data (S, O and H). In particular, oxygen and hydrogen isotope data show there are stronger magmatic inputs at LCT and BHX compared with other low-sulphidation epithermal systems. This is further identified by the high salinity of fluid inclusions.
- The lead isotope data indicated that the lead at LCT and BHX may have been derived from a mixed crustal source.
- Based on geological and geochemical data, the mineralised system at LCT is comparable to the deeper part of the low-sulphidation epithermal deposit model of Buchanan (1981), whereas the main mineralised system at BHX as represented by a structurally-hosted vein system (Stages 2 and 3) may correspond to the middle to lower part of the Mexican Ag-rich epithermal deposit model developed by Albinson et al. (2001).

9.6. Implications for mineral exploration

The major results and outcomes of this study, and the genetic models of the LCT and BHX mineralised systems developed in this study, have several implications for mineral exploration in the PBCA and the adjacent area. They include:

- *Igneous rocks*: The existence of igneous rocks (e.g., porphyries, volcanics, volcanic breccia, tuff) are promising for hosting epithermal veins. This interpretation is supported by the fact that the mineralised veins are preferentially hosted in the dacitic porphyry at LCT and andesite at BHX. It is also noted that the intermediate compositions appear to be highly prospective.
- *Fluid inclusion data*: Fluid inclusion data of the mineralised vein samples are used to examine the conditions of ore-forming fluid at prospect-scale including fluid inclusion petrography, homogenisation temperature and salinity values. These data can be used for characterisation and indication for a comparison with other known epithermal deposits.
- *Pyrite geochemistry*: The Au/Ag ratios of the pyrites in the mineralised vein sample can discriminate whether samples from Au-rich or Ag-rich systems at BHX. The close association of Ag, As, Sb, Tl, Pb and Co elements with Au and the concentration of these elements in pyrites can provide geochemical vectors in exploration.
- *Stable isotopes*: The stable isotopic data such as oxygen, hydrogen and sulphur isotopes characterise the epithermal systems in the region. A strong magmatic fluid signature can be used to constrain the nature of mineralised systems for exploration.
- *Lead isotope*: The lead isotopic compositions of the Pb-rich minerals (i.e., galena and pyrite) provide information about the source of metals. Particularly in the area, the lead isotopic compositions have potential to discriminate between the mineralised systems of Loei and Truongson Fold Belts.

REFERENCES

- Albinson, T., Norman, D.I., Cole, D. and Chomiak, B., 2001, Controls on formation of low-sulfidation epithermal deposits in Mexico: constraints from fluid inclusion and stable isotope data. *Society of Economic Geologists*, vol.8, pp.1-32.
- Audley-Charles, M.G., 1983, Reconstruction of eastern Gondwanaland, *Nature (London)*, vol.306, pp.48-50.
- Black, L.P., Kamo, S.L., Allen, C.M., Aleinikoff, J.N., Davis, D.W., Korsch, R.J. and Foudoulis, C., 2003, TEMORA 1; a new zircon standard for Phanerozoic U-Pb geochronology, *Chemical Geology*, vol.200, no.1-2, pp.155-170.
- Bodnar, R.J., 1993, Revised equation and table for determining the freezing point depression of H₂O-NaCl solutions. *Geochemica et Cosmochimica Acta*, vol.57, pp.683-684.
- Bodnar, R.J., 2007, Fluid inclusions in magmatic and hydrothermal ore deposits, with applicants to exploration, in *Ores and Orogenesis 2007 short course manual*, 25, September, 2007, Tucson, Arizona.
- Buchanan, L.J., 1981, Precious metal deposits associated with volcanic environments in the southwest: *Arizona Geological Society Digest*, vol.14, pp.237-262.
- Bunopas, S., 1981, Paleogeographic history of western Thailand and adjacent parts of South-East Asia – A plate tectonic interpretation, Unpublished PhD dissertation, Victoria University of Wellington, New Zealand, pp. 1-810. (Reprinted 1982, Geological Survey Paper No. 5, Geological Survey Division, Department of Mineral Resources, Thailand).
- Bunopas, S., 1983, Paleozoic succession in Thailand, *Proceedings of workshop on stratigraphic correlation of Thailand and Malaysia*, Haad Yai, Thailand, pp.39-76.
- Charusiri, P., Daorek, V., Archibald, D., Hisada, K. and Ampaiwan, T., 2002, Geotectonic Evolution of Thailand; A new synthesis, *Journal of the Geological Society of Thailand*, no.1, pp.1-20.
- Christie, A.B., Pimpson, M.P., Brathwaite, R.L., Mauk, J.L. and Simmons, S.F., 2007, Epithermal Au-Ag and related deposits of the Hauraki Goldfield, Coromandel volcanic zone, New Zealand. *Economic Geology*, vol.102, pp.785-816.
- Cook, N.J. and Chryssouilis, S.L., 1990, Concentrations of invisible gold in the common sulphides. *Canadian Mineralogy*, vol.28, pp.1-16.
- Cooke, D.R., 1992, Numerical models of mineral deposition for the Acupan vein system, Philippines, in Kharaka, Y.K. and Maest, A.S. ed., *Proceedings of International Symposium on Water-Rock Interaction*, vol.7: Sug-Group on Water-Rock Interaction, International Association of Geochemistry and Cosmochemistry and Alberta Research Council, pp.1579-1582.
- Cooke, D.R. and Simmons, S.F., 2000, Characteristics and genesis of epithermal deposits. *Review in Economic Geology*, vol.13, pp.221-244.

- Corfu, F., Hanchar, J.M., Hoskin, P.W.O. and Kinny, P.D., 2003, Atlas of zircon textures, *Reviews in Mineralogy and Geochemistry*, vol.53, pp.469-500.
- Cromie, P.W., Manini, A.J. and Khin Zaw, 2004a, Geological setting and mineralisation characteristics of the gold and copper deposits in the Sepon Mineral District, Lao PDR, paper presented Predictive Mineral Discovery Under Cover Conference, SEG 2004, Perth, Western Australia, 27 September – 1 October 2004, pp.411.
- Cromie, P.W., Manini, A.J. and Khin Zaw, 2004b, The Sepon Mineral District, Lao PDR; an overview of the currently known geological setting and mineralisation, *Proceedings of 17th Australian Geological Convention*, Hobart, Tasmania, February, pp.64.
- Cromie, P.W., Khin Zaw, Smith, S., Cooke, D. and White N., 2007, Geological setting, gold-ore paragenesis and sulphur isotope geochemistry of the gold and copper deposits in the Sepon Mineral District, Lao PDR, *Proceedings of Asia Oceania Geosciences Society (AOGS) Conference*, 31 July - 4 August 2007, Bangkok, Thailand.
- Dedenczuk, D., 1998, Epithermal gold mineralisation at Khao Sai, Honours thesis (unpublished), University of Tasmania, Hobart, Australia.
- ESCAP, 1990, Lao People's democratic republic, *Atlas of mineral resources of the ESCAP region*, vol.7.
- Fan, P-F., 2000, Accreted terranes and mineral deposits of Indochina, *Journal of Asian Earth Sciences*, vol.18, no.3, pp.343-350.
- Fountain H. and Workman, D.R., 1978, Review of the geology and mineral resources of Kampuchea, Laos and Vietnam, *Proceedings of Third Regional Conference on Geology and Mineral Resources of Southeast Asia*, 14-18 November 1978, Bangkok, Thailand.
- Gatinsky, G.Y., 2005, Tectonics and geodynamic prerequisites of mineral resource distribution in the Indochina region, *Geology of Ore Deposits*, vol.47, no.4, pp.309-325.
- Gemmell, J.B., Simmons, S.F. and Zantop, H., 1988, The Santo Nino silver-lead-zinc vein, Fresnillo district, Zacatecas, Mexico: Part I. structure, vein stratigraphy, and mineralogy. *Economic geology*, vol.83, pp.1597-1618.
- Giggenbach, W.F., 1997, The origin and evolution of fluids in magmatic-hydrothermal systems, in Barnes, H.L. ed., *Geochemistry of hydrothermal ore deposits – third edition*: New York, John Wiley, pp.737-789.
- Grant, G.J. and Ruiz, J., 1988, The Pb-Zn-Cu-Ag deposits of the Granadena mine, San Francisco del Oro-Santa Barbara district, Chihuahua, Mexico. *Economic Geology*, vol.83, pp.1683-1702.
- Greener, S., 1999, Wall-rock alteration and vein mineralogy of C-Zone, a low sulphidation Au-Ag epithermal deposit in the Chatree Prospect, Thailand, Honours thesis (unpublished), University of Tasmania, Hobart, Australia.
- Groves, D.I., Goldfarb, R.J., Gebre-Marian, M., Hagemann, S.G. and Robert, F., 1998, Orogenic gold deposits: a proposed classification in the context of their crustal distribution and relationship to other gold deposit types. *Ore Geology Reviews*, vol.13, pp.7-17.
- Gulson, B.L., 1986, Lead isotopes in mineral exploration. *Developments in Economic Geology*, vol.23, pp.1-245.

- Hada, S., Bunopas, S., Ishii, K. and Yoshikura, S., 1999, Rift-drift history and the amalgamation of Shan-Thai and Indochina/East Malaya blocks, in Metcalfe, Ian; Ren Jishun; Charvet, Jacques; Hada S (ed.), Gondwana dispersion and Asian accretion. IGCP 321 final results volume, pp.67-87.
- Hall, R., 2002, Cenozoic geological and plate tectonic evolution of SE Asia and the SW Pacific; computer-based reconstructions, model and animations, *Journal of Asian Earth Sciences*, vol.20, no.4, pp.353-431.
- Hannington, M.D. and Scott, S.D., 1989, Sulphidation equilibria as guides to gold mineralisation in volcanogenic massive sulphides: evidence from sulphide mineralogy and the composition of sphalerite. *Economic geology*, vol.84, pp.1978-1995.
- Hedenquist, J.W., Antonio, A.R. and Eliseo, G-U., 2000, Exploration for epithermal gold deposits, *SEG Reviews*, vol. 13, pp.245-277.
- Hisada, K., Sugiyama, M. Ueno, K., Charusiri, P. and Arai, S., 2004, Missing ophiolite rocks along the Mae Yuam Fault as the Gondwana-Tethys divide in north-west Thailand, *Island Arc*, vol.13, pp.119-127.
- Hofstra, A.H. and Cline, J.S., 2000, Characteristics and models for Carlin-type gold deposit, *SEG Reviews*, vol.13, pp.163-220.
- <http://www.ggl.ulaval.ca/cgi-bin/isotope/generisotope.cgi>: Fractionation calculator website
- <http://www.oxiana.com.au>: Oxiana Ltd website.
- <http://www.panaustralian.com.au>: Pan Australian resources Ltd website.
- Huston, D.L., Bottrill, R.S., Creelman, R.A., Khin Zaw, Ramsden, T.R., Rand, S.W., Gemmell, J.B., Jablonski, W., Sie, S.H. and Large, R.R., 1992, Geologic and geochemical controls on the mineralogy and grain size of gold-bearing phases, eastern Australian volcanic-hosted massive sulphide deposits. *Economic geology*, vol.87, pp.542-563.
- Huston, D.L., Power, M., Gemmell, J., B. and Large, R., R., 1995, Design, calibration and geological application of the first operational Australian laser ablation sulphur isotope microprobe. *Australian Journal of Earth Sciences*, vol.42, pp.549-555.
- Hutchison, C.S., 1989, Geological evolution of South-east Asia, *Oxford Monographs on Geology and Geophysics*, vol.13, pp.368, Oxford University Press.
- Hutton, C.O., 1950, Sphene beach sand, Wainui inlet, N.W. Nelson, New Zealand: *Bulletin of the Geological Society of America*, vol.61, p.635.
- Intasopa, S., 1993, Petrology and geochronology of the volcanic rocks of central Thailand volcanic belt, PhD thesis at University of New Brunswick, pp.1-242.
- Irvine, T.N. and Baragar, W.R.A., 1971, A guide to the chemical classification of the common volcanic rocks, *Canadian Journal of Earth Sciences*, vol.8, pp.523-548.
- JOGMEC, 2005, Environmental research of mineral resource development in Lao People's Democratic Republic (in Japanese).
- Kamvong, T., 2006, Geology and genesis of porphyry-skarn Cu-Au deposits at the northern Loei Fold Belt, northeast Thailand and Laos – a progress report, Progress Report 5, Geochronology, metallogenesis and deposit styles of Loei Foldbelt in Thailand and Laos PDR, ARC Linkage Project.

- Kamvong, T., 2007a, Geology and genesis of porphyry-skarn Cu-Au deposits at the northern Loei Fold Belt, northeast Thailand and Laos – a progress report, Final Report, Geochronology, metallogenesis and deposit styles of Loei Foldbelt in Thailand and Laos PDR, ARC Linkage Project.
- Kamvong T., 2007b, Possible Aakitic Porphyries in Northeastern Thailand and Laos: Implications for the Evolution of the Loei Fold Belt, Proceedings of Asia Oceania Geosciences Society (AOGS) Conference, 31 July - 4 August 2007, Bangkok, Thailand.
- Khin Zaw, 1991, The effect of Devonian metamorphism and metasomatism on the mineralogy and geochemistry of the Cambrian VMS deposits in the Rosebery-Hercules district, western Tasmania. PhD thesis (unpublished), University of Tasmania, Hobart.
- Khin Zaw and Henderson, S., 1993, Geochemical and isotopic constraints for high grade gold mineralisation at Waitangi deposit, Thames district, Coromandel peninsula, north island, New Zealand. Proceedings of the 27th annual conference 1993, New Zealand branch of Australian Institute of Mining and Metallurgy, pp.133-141.
- Khin Zaw and Large, R.R., 1996, Petrology and geochemistry of sphalerite from the Cambrian VHMS deposits in the Rosebery-Hercules district, western Tasmania: implications for gold mineralisation and Devonian metamorphic-metasomatic processes. *Mineralogy and petrology*, vol.57, pp.97-118.
- Khin Zaw, Rodmanee, T., Thanasuthipitak, T. and Ruamkid, S., 2006, Mineralogy and paragenesis of Phu Thap Fah deposit, northeast Thailand: implication for reduced gold skarn formation, Proceedings of 18th Australian Earth Sciences Convention (AESC), 2-6 July, Melbourne, Australia.
- Khin Zaw and Meffre, S., 2007, Supplementary Report, Geochronology, metallogenesis and deposit styles of Loei Foldbelt in Thailand and Laos PDR, ARC Linkage Project.
- Khin Zaw, Meffre, S. and higher degree students, 2007a, Metallogenic relations and deposit-scale studies, Final Report, Geochronology, metallogenesis and deposit styles of Loei Foldbelt in Thailand and Laos PDR, ARC Linkage Project.
- Khin Zaw, Rodmanee, T., Khositantont, S., Thanasuthipitak, T. and Ruamkid, S., 2007b, Geology and genesis of Phu Thap Fah gold skarn deposit, northeastern Thailand: Implications for reduced gold skarn formation and mineral exploration, in Tantiwanit, W. (ed.). Proceedings of GEOTHAI'07 International Conference on Geology of Thailand, 21-22 November 2007, Bangkok, Thailand, pp.93-95.
- Khositantont, S., Khin Zaw and Ounchanum, P., 2007, Geology and mineralisation characteristics of Huai Kham On gold deposit, Sukhothai Fold Belt, northern Thailand, roceedings of Asia Oceania Geosciences Society (AOGS) Conference, 31 July - 4 August 2007, Bangkok, Thailand.
- Khositantont, S., Ounchanum, P., Panjasawatwong, Y., Thanasuthipitak, T., Khin Zaw and Meffre, S., 2008, Tectonic setting and evolution of Lampang-Phrae volcano-plutonic rocks in Sukhothai Fold Belt; Evidence from geochemical characteristics and LAICP-MS U-Pb zircon ages, Abstract of the Tectonics of Northwestern Indochina (TNI) International Conference, 6-8 February 2008, Chiangmai, Thailand.
- Kingsgate Consolidated Ltd website (<http://www.kingsgate.com.au>)
- Kohn, M. J., Riciputi, L.R., Stakes, D. and Orange, D.L., 1998, Sulfur isotope variability in biogenic pyrite; reflections of heterogeneous bacterial colonization? *American Mineralogist*, vol.83, no.11-12, Part 2, pp.1454-1468.
- Kosler, J. and Sylvester, P.J., 2003, Present trends and the future of zircon in geochronology; laser ablation ICPMS, *Reviews in Mineralogy and Gechemistry*, vol.53, pp.243-275.

- Kromkhun, K., 2005, Geological setting, mineralogy, alteration, and nature of ore fluid of the H zone, the Chatree deposits, Thailand, Master thesis (unpublished), University of Tasmania, Hobart, Australia.
- Lang, J. R. and Baker T., 2001, Intrusion-related gold system; the present level understanding, *Mineralium Deposita*, vol.36, no.6, pp.477-489.
- Large, R.R., 1992, A special issue devoted to Australian volcanic-hosted massive sulphide (VHMS) deposits and their volcanic environment. *Economic Geology and the Bulletin of the Society of Economic Geologists*, vol.87, no.3, pp.469-968.
- Large, R.R., Maslennikov, V.V., Scott, R.J., Danyushevsky, L.V. and Chang, Z., in press, Multi-stage sedimentary and metamorphic origin of pyrite and gold in the giant Sukhoi Log deposit, Lena Goldfield, Russia.
- Lawless, J.V., White, P.J., Bogie, I., Cartwright, A.J., 1999, Finding Mineralisation is Easy; Why is it so hard to find mine?, Kingstone Morisson, Short Course PacRim'99 Congress, Bali, 9-10 October, 1999, Indonesia.
- Lepvrier, C., Maluski, H., Nguyen, V.V., Rong, D., Axente, V. and Rangin, C., 1997, Indosinian NW-trending shear zones within the Truong Son Belt (Vietnam); (super 40) Ar- (super 39) Ar Triassic ages and Cretaceous to Cenozoic overprints, *Tectonophysics*, vol.283, no.1-4, pp.105-127.
- Manaka, T., Khin Zaw and Meffre, S., 2007a, Geological setting and mineralisation characteristics of LCT epithermal Au deposit, Lao PDR. Proceedings of Asia Oceania Geosciences Society (AOGS) Conference, 31 July - 4 August 2007, Bangkok, Thailand.
- Manaka, T., Khin Zaw and Meffre, S., 2007b, Mineralisation characteristics of the Long Chieng Track (LCT) gold deposit, Lao PDR, Proceedings of GEOTHAI'07 International Conference on Geology of Thailand, 21-22 November 2007, Bangkok, Thailand, pp.199-201.
- Maniar, P.D. and Piccoli, P.M., 1989, Tectonic discrimination of granitoids, *Geological Society of America Bulletin*, vol.101, pp.635-643.
- Mason, D., 1997, Petrographic descriptions and interpretation for eleven drill core rock samples, Long Chieng Track prospect (Lao PDR); Consultants Report for Phu Bia Mining Ltd.
- Meffre, S., unpublished, Pb isotopes in SE Asia.
- Meffre, S., Scott, R. J., Glen, R. A. and Squire, R. J., 2007 Re-evaluation of contact relationships between Ordovician volcanic belts and the quartz-rich turbidites of the Lachlan Orogen. *Australian Journal of Earth Sciences*, vol.54, pp.363-383.
- Meffre, S., Large, R.R., Scott, R., Woodhead, J., Chang, Z., Gilbert, S.E., Danyushevsky, L.V., Maslennikov, V. and Hergt, J.M., in press, Age and pyrite Pb-isotopic composition of the giant Sukhoi Log sediment-hosted gold deposit, Russia, *Geochimica et Cosmochimica Acta*, 2008.
- Metcalfe, I., 1996, Gondwanaland dispersion, Asian accretion and evolution of eastern Tethys, *Australian Journal of Earth Sciences*, vol.43, no.6, pp.605-623.
- Metcalfe, I., 1988, Origin and assembly of south-east Asian continental terranes; In Audley-Charles M.G. and Hallam A. (ed.), *Gondwana and Tethys*, Geological Society Special Publications, vol.37, pp.101-118
- Metcalfe, I., 1999, Gondwana dispersion, Asian accretion: an overview, in I Metcalfe (ed.), *Gondwana dispersion and Asian accretion*. IGCP 321 final results volume, pp.9-28.

- Morrison, G.W., Jaireth, S. and Guoyi, D., 1991, Textural zoning in epithermal quartz veins: James Cook University, Queensland.
- Nakano, N., Osanai, Y., Owada, M., Nam, T. N., Tsunogae, T., Toyoshima, T., and Binh, P., 2004, Decompression process of mafic granulite from eclogite to granulite facies under ultrahigh-temperature condition in the Kontum massif, central Vietnam, *Journal of Mineralogical and Petrological Sciences*, vol.99, no.4, pp.242-256.
- Norman, D.I., Moore, J.N. and Musgrave J.A., 1997, Gaseous species as traces in geothermal systems: Proceedings of workshop on Geothermal Reservoir Engineering, 22nd Stanford University, Stanford, California, 27-29, January, 1997, pp.419-426.
- Norman, M., Robinson, P. and Clark, D., 2003, Major- and trace-element analysis of sulphide ores by laser-ablation ICP-MS, solution ICP-MS, and XRF; new data on international reference materials. *The Canadian Mineralogist*, vol.41, Part 2, pp.293-305.
- Norrish, K. and Chappell, B.W., 1977, X-ray fluorescence spectrometry, in Zussman, J (ed): Acad. Press, London.
- Ohmoto, H. and Rye, R.O., 1979, Isotopes of sulphur and carbon. in Barnes, H.L. (ed): *Geochemistry and hydrothermal ore deposits*, Wiley, New York, pp.509-567.
- Osanai, Y., Nakano, N., Owada, M., Nam, T. N., Toyoshima, T., Tsunogae, T., and Binh, P., 2004, Permo-Triassic ultrahigh-temperature metamorphism in the Kontum massif, central Vietnam, *Journal of Mineralogical and Petrological Sciences*, vol.99, no.4, pp.225-241.
- Osanai, Y., Naskano, N., Owada, M., Nam, T. N., Binh, P., Miyamoto, T., Toyoshima, T., and Minh, N. T., 2007, UHT/UHP Collision Zone Metamorphism in Vietnam and Adjacent Southeastern Asia: Proposition of Trans Vietnam Orogenic Belt, Proceedings of Asia Oceania Geosciences Society (AOGS) Conference, 31 July - 4 August 2007, Bangkok, Thailand.
- Owada, M., Osanai, Y., Nakano, N., Matsushita, T., Tran Ngoc Nam., Tsunogae T., Toyoshima, T., Bonh. P. and Kagami, H., 2007, Crustal anatexis and formation of two types of granitic magmas in the Kuntum Massif, central Vietnam; implications for magma processes in collision zones, *Gondwana Research*, vol.12, no.4, pp.428-437.
- Pan Australian Resources Annual Report, 2003-04.
- Pearce, J.A. and Cann, J.R., 1973, Tectonic setting of basic volcanic rocks determined using trace element analyses, *Earth and Planetary Science Letters*, vol.19, pp.290-300.
- Pearce, J.A. and Gale, G.H., 1977, Identification of ore-deposition environment from trace element geochemistry of associated igneous host rocks, *Geological Society Special Publication*, vol.7, pp.14-24.
- Pearce, J.A., Harris, N.B.W. and Tindle, A.G., 1984, Trace element discrimination diagrams for the tectonic interpretation of granitic rocks, *Journal of Petrology*, vol.25, pp.956-983.
- Pearson, M.F., Clark, K.F. and Porter, E.W., 1988, Mineralogy, fluid characteristics, and silver distribution at Real de Angeles, Zacatecas, Mexico. *Economic Geology*, vol.83, pp.1737-1759.
- Petterson, J., 2005, Khathonglai (KTL) Cu-Au prospect Geological Model; Consultants Report for Phu Bia Mining Ltd.
- Reed, M. H. and Spycher, N.F., 1985, Boiling, cooling, and oxidation in epithermal systems: A numerical modelling approach. in Berger, B.R. and Bethke, P.M. (ed), *Geology and Geochemistry of Epithermal Systems*. *Reviews in Economic Geology*, vol.83, pp.1573-1596.

- Reich, M., Kesler, S.E., Utsunomiya, S., Palenik, C.S., Chryssoulis, S.L. and Ewing, R.C., 2005, Solubility of gold in arsenian pyrite. *Geochimica et Cosmochimica Acta*, vol.69, no.11, pp.2781-2796.
- Robinson, B.W. and Kusakabe, M., 1975, Quantitative preparation of SO₂ for ³⁴S/³²S analyses from sulphides by combustion. *Analytical Chemistry*, vol.47, no.7, pp.1179-1181.
- Roedder, E., 1984, Fluid inclusions. *Reviews in Mineralogy*, vol.12, pp.1-644.
- Rollinson, H., 1993, Using geochemical data: evaluation, presentation, interpretation. Longman Scientific Press. Chapter 7.
- Salam, A., Khin Zaw, Meffre, S., James, R. and Stein, H., 2007a, Geological setting, alteration, mineralisation and geochronology of Chatree epithermal gold-silver deposit, Phetchabun Province, central Thailand, Proceedings of Asia Oceania Geosciences Society (AOGS) Conference, 31 July – 4 August 2007, Bangkok, Thailand.
- Salam, A., Khin Zaw, Meffre, S., James, R., Stein, H., 2007b, Geological setting, alteration, mineralization and geochronology of Chatree epithermal gold-silver deposit, Phetchabun Province, central Thailand, Proceedings of Ores and Orogenesis, 24-30 September 2007, Tucson, Arizona, USA.
- Salam, A., 2007, Geological, geochemical and metallogenic study of the northern Chatree area, Phetchabun province, Loei Fold Belt, central Thailand - Progress report. Geochronology, metallogenesis and deposit styles of Loei Foldbelt in Thailand and Laos PDR, ARC Linkage Project, pp.9.1-9.45.
- Sengo, C. and Hsu, K.J., 1984, The Cimmerides of eastern Asia; history of the eastern end of Paleo-Tethys, in *Memoires de la Societe Geologique de France, Nouvelle Serie*, vol.147, pp.139-167.
- Sengo C., Altiner, D., Cin, A., Ustamomer, T. and Hsu, K.J., 1988, Origin and assembly of the Tethyside orogenic collage at the expense of Gondwana Land, in Aduly-charles, M.G. and Hallam, A. (ed), *Gondwana and Tethys Geological Society Special Publication no.37*, pp.119-181.
- Seward, T.M. and Barnes, H.L., 1997, Metal transport by hydrothermal ore fluids, in Barnes, H.L.(ed), *Geochemistry of hydrothermal ore deposits – 3rd edition*, New York, John Wiley, pp.435-486.
- Shepherd, T.J., Rankin, A.H. and Alderton, D.H.M., 1985, A practical guide to fluid inclusion studies.
- Sheppard, S.M.F., 1986, Characterization and isotopic variation in natural waters. Chapter 6, Review in *Mineralogy*, vol.16.
- Sherlock, R.L., Tosdal, R.M., Lehrman, N.J., Graney, J.R., Losh, S., Jowett, E.C. and Kesler, S.E., 1995, Origin of the McLaughlin mine sheeted vein complex: Metal zoning, fluid inclusion and isotopic evidence: *Economic Geology*, vol.90, pp.2156-2181.
- Simmons, S.F., Gemmill, B. and Sawkins, F.J., 1988, Santo Nino silver-lead-zinc vein, Fresnillo District, Zacatecas, Mexico: Part II. Physical and chemical nature of ore-forming solutions: *Economic Geology*, vol.83, pp.1619-1641.
- Simmons, S.F., 1991, Hydrologic implications of alteration and fluid inclusion studies in the Fresnillo district, Mexico: Evidence for a brine reservoir and a descending water table during the formation of hydrothermal Ag-Pb-Zn orebodies. *Economic Geology*, vol.86, pp.1579-1601.
- Simmons, S.F., Simpson, M.P. and Reynold, T.J., 2007, The significance of clathrates in fluids inclusions and the evidence for overpressuring in the Broadlands-Ohaaki geothermal system, New Zealand: *Economic Geology and the Bulletin of the Society of Economic Geologists*, vol.102, no.1, pp.127-135.

- Simpson, M.P., Mauk, J.L. and Simmons, S.F., 2001, Hydrothermal alteration and hydrologic evidence of the Golden Cross epithermal Au-Ag deposit, New Zealand: *Economic Geology and the Bulletin of the Society of Economic Geologists*, vol.96, no.4, pp.773-796.
- Singharajwarapan, S. and Berry, R., 2000, Tectonic implications of the Nan Suture Zone and its relationship to the Sukhothai Fold Belt, Northern Thailand, *Journal of Asian Earth Sciences*, vol.18, pp.663-673.
- Smith, S.G., Olberg, D. and Manini, A.J., 2005, The Sepon gold deposits, Laos: Exploration, Geology and Comparison to Carlin-type Gold Deposits in the Great Basin, Geological Society of Nevada Symposium, Reno, Nevada, 2005.
- Spycher, N.F. and Reed, M.H., 1989, Evolution of a broadlands-type epithermal ore fluid along alternative P-T paths: Implications for the transport and deposition of base, precious, and volatile metals. *Economic geology*, vol.84, pp.328-359.
- Srichan, W., Crawford, A.J. and Berry, R.F., 2006, Geochemistry and geochronology of the Chinag Khong-Lampang-Tak volcanic rocks, Northern Thailand. Proceedings of 2nd Symposium of IGCP 516 "Geological Anatomy and South Asia", 11-20 November Phillipines.
- Stacy, J.S. and Kramer, J.D., 1975, Approximation of terrestrial lead isotope evolution by a two-stage model. *Earth and Planetary Science Letters*, vol.26, pp.207-221.
- Sun, S.S. and McDonough, W.F., 1989, Geochemical and isotopic systematic of oceanic basalts; implications for mantle composition and processes, *Geological Society Special Publications*, vol.42, pp.313-345.
- Tate, N.M., 2003, Geology of the Long Chieng Track (LCT) Gold Deposit, Lao Peoples Democratic Republic; Consultants Report for Pan Mekong Exploration Pty Ltd.
- Tate, N.M., 2004, Mapping Notes for the Ban Houayxai Gold deposit, Lao Peoples Democratic Republic; Consultants Report for Pan Mekong Exploration Pty Ltd.
- Tate, N.M., 2005, Discovery, Geology and Mineralisation of the Phu Kham Copper-Gold Deposit Lao People's Democratic Republic, in JaB Mao, F. (ed.), *Mineral deposit Research: Meeting of the Global Challenge*, 8th Biennial SGA Meeting, 18-21 August 2005, Beijing, China, vol.2, pp.1077-1080.
- Tate, N.M., 2006, Mineralisation model for the Phu He gold prospect, Lao Peoples Democratic Republic; Consultants Report for Phu Bia Mining Ltd.
- Thompson, J.F.H. and Newberry, R.J., 2000, Gold deposits related to reduced granitic intrusions. Review in *Economic Geology*, vol.13, pp.377-400.
- Townsend, M., Long, R., Scott, G.F., and Gilbertson, R.R., 1988, Soil survey of Muskogee Country, Oklahoma, pp.1-188.
- Wilson, M., 1989, *Igneous Petrogenesis*, Unwin Hyman, London.
- Winchester, J.A. and Floyd, P.A., 1977, Geochemical discrimination of different magma series and their differentiation products using immobile elements, *Chemical Geology*, vol.20, pp.325-343.
- Wood, B.L. and Large, R.R., 2007, Syngenetic gold in western Victoria; occurrence, age and dimensions. *Australian Journal of Earth Sciences*, vol.54, no.5, pp.711-732.

-
- Yu, Z., Robinson, P., Townsend, A.T., Munker, C. and Crawford, A.J., 2000, Detection of geological materials for trace element determination of using ICP-MS. *Geostandards Newsletter: The Journal of Geostandards and Geoanalysis*, vol.25, pp.199-217.
- Zartman, R.E. and Doe, B.R., 1981, Plumbotectonics-The model, *Tectonophysics*, vol.75, pp.135-162.
- Zheng, Y-F., 1993, Calculation of oxygen isotope fractionation in anhydrous silicate minerals, *Geochimica et Cosmochimica Acta*, vol.57, no.5, pp.1079-1091.

Appendix I
Sample catalogue

Sample No.	Sample description	HS	Slab	TS	PST	FI	Mount	Py	XRF	REE	Zr	Stain	El	Sph	LRS	XRD	LA	S	O	H	Pb
LSD08@79.5m	Quartz-sulphide vein	X																X	X		
LSD08@83.4m	Sulphide vein cross-cut by calcite vein	X			X																
LSD08@83.7m	Quartz monzonite	X							X	X								X			
LSD08@99.3m	Tuffaceous sandstone	X			X																
LSD09@50.0m	Feldspar-phyric dacitic porphyry	X							X		X										
LSD09@88.0m	Carbonaceous limestone	X			X		X	X						X				X			X
LSD11@88.7m	Hydrothermal breccia consisting of limestone clasts with sulphide matrix	X	X															X			
LSD13@15.3m	Quartz-sulphide vein	X																X			
LSD13@35.2m	Hydrothermal breccia consisting of porphyritic clasts with dark fine-grained matrix	X																			
LSD13@55.0m	Quartz-sulphide vein	X													X			X	X		X
LSD13@96.6m	Quartz-sulphide vein	X			X									X							
LSD14@47.8m	Quartz-sulphide vein	X				X												X			
LSD14@88.1m	Sulphide-quartz vein	X			X													X			
LSD14@103.6m	Quartz-sulphide vein	X			X									X							
LSD15@97.3m	Quartz monzodiorite	X							X												
LSD15@99.1m	Quartz monzodiorite	X	X		X		X	X				X									
LSD15@96.6m	Quartz-sulphide vein	X																X	X		X
LSD16@36.1m	Quartz monzonite	X			X																
LSD16@99.2m	Quartz monzonite	X							X												
LSD16@101.0m	Quartz monzonite	X							X												
LSD16@107.1m	Quartz monzonite	X							X												
LSD18@70.7m	Quartz monzonite	X	X									X									
LSD23@57.3m	Tuffaceous sandstone. chloritised & sericitised	X														X					
LSD24@17.0m	Polymictic breccia	X																			
LSD24@36.5m	Tuffaceous sandstone. chloritised & sericitised	X					X	X													X
LSD24@69.6m	Sulphide vein	X																X			
LSD24@76.2m	Quartz-sulphide vein	X																	X	X	
LSD24@79.0m	Sulphide vein	X																X			
LSD24@86.0m	Hydrothermal breccia consisting of porphyritic clasts with sulphide matrix	X			X													X			
LSD24@94.2m	Sulphide vein in feldspar-phyric dacitic porphyry	X			X																
LSD24@99.2m	Quartz-sulphide vein	X																X			

Abbreviations: HS=hand specimen, TS=thin section, PTS=polished thin section, FI=fluid inclusion chip, Mount=polished mount, Py=pyrite geochemistry analysis, XRF=XRF analysis, REE=rare earth element analysis, Zr=Zircon U-Pb geochronology, Stain=K-feldspar staining, El=electron fineness analysis, Sph=sphalerite chemical analysis, LRS=laser raman spectrometry, XRD=XRD analysis, LA=laser ablation sulphur isotope, S=sulphur isotope, O=oxygen isotope, H=hydrogen isotope, Pb=lead isotopes

Sample No.	Sample description	HS	Slab	TS	PST	FI	Mount	Py	XRF	REE	Zr	Stain	El	Sph	LRS	XRD	LA	S	O	H	Pb
HSD04@75.2m	Crystal-rich volcanic breccia	X										X									
HSD04@75.3m	Sulphide vein	X															X	X			
HSD04@86.0m	Quartz-sulphide vein	X			X									X							
HSD04@96.4m	Quartz-sulphide vein	X																	X		
HSD05@39.4m	Feldspar-phyric andesite, sericited & chloritised	X					X	X													
HSD05@63.3m	Quartz-sulphide vein	X																	X	X	
HSD05@68.2m	Feldspar-phyric andesite	X							X												
HSD06@42.3m	Siliceous shale	X																			X
HSD06@42.3m	Shale, sericite-calcite-pyrite alteration	X					X	X													
HSD06@81.2m	Siliceous shale	X	X	X																	
HSD06@93.6m	Carbonaceous shale	X	X																		
HSD06@101.8m	Quartz-sulphide vein	X																	X	X	
HSD07@96.6m	Red bed sedimentary breccia	X									X										
HSD08@66.5m	Quartz-sulphide vein	X																	X	X	
HSD08@68.8m	Quartz-sulphide vein	X				X															
HSD08@77.0m	Quartz-sulphide vein	X			X									X							
HSD08@97.5m	Feldspar-phyric andesite	X							X	X								X			X
HSD09@56.2m	Feldspar-phyric andesite	X							X												

Abbreviations: HS=hand specimen, TS=thin section, PST=polished thin section, FI=fluid inclusion chip, Mount=polished mount, Py=pyrite geochemistry analysis, XRF=XRF analysis, REE=rare earth element analysis, Zr=Zircon U-Pb geochronology, Stain=K-feldspar staining, El=electron fineness analysis, Sph=sphalerite chemical analysis, LRS=laser raman spectrometry, XRD=XRD analysis, LA=laser ablation sulphur isotope, S=sulphur isotope, O=oxygen isotope, H=hydrogen isotope, Pb=lead isotopes

Appendix II

LA-ICPMS zircon U-Pb geochronological data

Appendix II. LA-ICPMS Zircon U-Pb geochronological data of the LCT and BHX deposits, Lao PDR.

Sample No.	comments	206Pb/238U age (207corr.)	+/-1s	206Pb/238U %rsd	age	+/-1s	208Pb/232Th %rsd	age	+/-1s	207Pb/206Pb %rsd	age	+/-1s	207Pb/235U %rsd	age	+/-1s	Nd	+/-1s	Hf	+/-1s	Pb	+/-1s	Th	+/-1s	U	+/-1s					
ACH066	ok	284	3.9	0.0450	1.3%	284	4	0.0135	3.5%	270	9	0.050	7%	187	155	0.319	7%	281	16	1.5	0.25	10280	455	36	2	419	35	719	46	
ACH066	ok	287	3.8	0.0454	1.3%	286	4	0.0133	3.4%	267	9	0.049	6%	149	149	0.316	6%	279	15	5.0	0.56	10547	466	43	3	550	45	860	54	
ACH066	ok	291	3.8	0.0462	1.3%	291	4	0.0136	3.6%	274	10	0.054	6%	360	140	0.360	6%	312	16	2.3	0.29	9994	440	43	3	515	42	860	54	
ACH066	ok	291	4.5	0.0460	1.5%	290	4	0.0136	3.1%	273	9	0.050	6%	202	142	0.345	6%	301	15	4.0	0.39	9115	408	39	3	584	49	736	49	
ACH066	common Pb rich inclusions at end slightly older at end	291	5.4	0.0461	1.8%	290	5	0.0126	5.2%	252	13	0.049	9%	143	207	0.323	8%	284	21	2.2	0.44	10512	488	46	3	561	47	951	61	
ACH066	ok	292	7.0	0.0467	2.3%	294	7	0.0141	6.1%	284	17	0.059	11%	150	232	0.373	10%	322	29	1.8	0.41	9935	465	28	2	325	28	567	37	
ACH066	ok	292	3.6	0.0463	1.2%	292	3	0.0138	2.9%	278	8	0.050	5%	190	124	0.335	5%	293	13	1.6	0.26	10665	470	56	4	646	53	1101	69	
ACH066	ok	293	4.1	0.0461	1.4%	291	4	0.0140	3.4%	282	10	0.046	7%	-13	160	0.295	6%	263	15	3.6	0.42	10514	464	39	3	546	46	760	50	
ACH066	ok	293	4.3	0.0463	1.4%	292	4	0.0137	3.9%	275	11	0.049	6%	153	148	0.324	6%	285	15	2.6	0.32	8301	371	31	2	435	36	613	38	
ACH066	ok	293	3.9	0.0463	1.3%	292	4	0.0137	3.2%	275	9	0.048	7%	86	158	0.310	6%	274	16	2.6	0.31	9276	405	39	3	513	43	762	48	
ACH066	ok	299	3.1	0.0475	1.0%	299	3	0.0141	2.2%	283	6	0.052	4%	276	93	0.354	4%	307	10	6.4	0.54	11438	510	144	10	2499	210	2523	165	
ACH066	ok	316	3.8	0.0500	1.2%	314	4	0.0150	3.1%	302	9	0.047	6%	70	133	0.354	5%	308	15	3.1	0.32	9641	425	48	3	544	45	871	55	
LSD9	ok	286.3	2.0	0.0455	0.7%			0.0142	2.4%			0.0534	1.5%									9886				756		860		
LSD9	ok	287.6	2.0	0.0458	0.7%			0.0142	2.4%			0.0543	1.4%									10772				609		689		
LSD9	ok	290.9	2.1	0.0463	0.7%			0.0147	2.8%			0.0552	1.8%									10982				293		408		
LSD9	ok	281.8	2.0	0.0463	0.7%			0.0140	2.4%			0.0527	1.4%									10009				459		621		
LSD9	ok	292.2	2.1	0.0464	0.7%			0.0141	2.5%			0.0526	1.5%									10145				443		638		
LSD9	ok	295.3	2.2	0.0469	0.7%			0.0142	2.7%			0.0532	1.7%									12609				261		487		
HSD01@63.8m	Pb rich inclusion at beginning	275	6.3	0.0444	2.2%			0.0158	5.8%			0.065	7.4%			0.370	8.2%				2.8	0.56	10632	483	19	1	218	14.2	372	24
HSD01@63.8m	ok	278	3.9	0.0449	1.4%			0.0152	2.8%			0.066	5.0%			0.396	4.7%				1.2	0.20	9815	438	27	2	284	18.1	541	35
HSD01@63.8m	ok	280	3.6	0.0443	1.3%			0.0132	3.0%			0.050	5.5%			0.300	5.5%				1.6	0.25	10470	467	27	2	362	23.6	568	37
HSD01@63.8m	ok	284	4.3	0.0452	1.5%			0.0141	3.0%			0.056	5.2%			0.339	4.7%				2.3	0.29	9700	432	29	2	331	21.2	588	38
HSD01@63.8m	ok	285	4.3	0.0456	1.5%			0.0146	3.3%			0.060	5.2%			0.367	5.0%				0.7	0.13	9574	426	24	2	222	14.1	504	33
HSD01@63.8m	ok	285	4.5	0.0454	1.5%			0.0157	3.6%			0.056	6.4%			0.346	6.5%				0.8	0.17	10014	452	18	1	179	11.6	369	24
HSD01@63.8m	Pb loss in high U zone at end	287	5.9	0.0467	2.0%			0.0150	4.7%			0.070	7.2%			0.454	6.9%				1.7	0.32	9743	461	25	2	311	21.1	491	33
HSD01@63.8m	ok	288	4.1	0.0458	1.4%			0.0143	3.2%			0.055	5.0%			0.337	5.0%				4.2	0.66	10139	450	27	2	343	22.2	550	36
HSD01@63.8m	ok	290	4.2	0.0464	1.4%			0.0151	3.2%			0.060	5.3%			0.378	5.1%				57.8	6.54	10264	459	26	2	294	18.8	506	33
HSD01@63.8m	ok	291	4.5	0.0462	1.5%			0.0148	3.3%			0.052	5.8%			0.314	5.8%				25.6	2.96	9766	443	25	2	279	18.4	496	32
HSD01@63.8m	ok	294	4.5	0.0467	1.5%			0.0144	3.5%			0.054	6.0%			0.330	5.6%				2.7	0.34	9874	442	23	2	274	18.1	467	31
HSD01@63.8m	ok	296	5.0	0.0475	1.6%			0.0157	3.4%			0.062	6.0%			0.393	5.7%				7.4	0.62	9901	448	20	1	210	14.3	392	26
HSD04@51.9m	ok but Pb rich inclusion in middle	279	4	0.0445	1.3%	281	4	0.0132	2.0%	264	5	0.058	3.4%	533	74	0.338	3.4%	296	9	2.1	0.16	9935	260	21	1	252	10.1	422	16	
HSD04@51.9m	ok	280	4	0.0444	1.4%	280	4	0.0131	2.2%	262	6	0.051	3.8%	241	87	0.303	3.7%	269	9	0.8	0.12	10243	273	18	1	201	8.0	372	14	
HSD04@51.9m	ok	284	3	0.0452	1.2%	285	3	0.0140	1.9%	280	5	0.055	3.6%	426	80	0.334	3.5%	293	9	34.4	2.76	9726	249	20	1	215	9.1	396	15	
HSD04@51.9m	ok	284	4	0.0451	1.3%	284	4	0.0134	2.0%	268	5	0.052	3.2%	294	74	0.320	3.2%	282	8	14.7	2.20	9535	251	24	1	275	11.5	472	18	
HSD04@51.9m	ok	286	4	0.0454	1.6%	286	4	0.0136	1.9%	274	5	0.052	3.4%	292	79	0.312	3.7%	276	9	8.0	1.13	10163	289	24	1	302	12.4	485	19	
HSD04@51.9m	ok	291	6	0.0466	2.1%	294	6	0.0149	4.1%	300	12	0.059	6.0%	566	130	0.359	6.0%	311	16	2.5	0.43	10146	300	15	1	147	6.2	312	13	
HSD07@96.6m	ok	257	6	0.0408	2.4%	258	6	0.0124	2.6%	250	7	0.053	5.8%	342	132	0.295	6.6%	262	15	4.2	0.31	9536	426	15	1	414	24.6	289	18	
HSD07@96.6m	ok	259	6	0.0408	2.5%	258	6	0.0124	2.7%	249	7	0.049	5.0%	162	117	0.268	5.2%	241	11	16.9	1.38	10399	454	15	1	331	19.3	331	20	
HSD07@96.6m	ok	261	5	0.0414	1.9%	261	5	0.0127	2.0%	255	5	0.051	3.4%	226	79	0.284	4.0%	254	9	2.4	0.23	10953	475	24	1	497	29.2	506	39	
HSD07@96.6m	ok	294	7	0.0464	2.5%	293	7	0.0143	4.0%	288	11	0.049	5.3%	152	123	0.303	5.4%	269	13	0.7	0.11	9901	435	6	0	36	2.1	138	8	
HSD07@96.6m	ok	326	8	0.0525	2.6%	330	8	0.0156	4.3%	312	13	0.063	6.8%	710	145	0.431	6.7%	364	21	0.4	0.09	11936	512	7	0	53	3.1	145	9	
HSD07@96.6m	ok	335	10	0.0533	2.9%	335	9	0.0163	4.1%	328	13	0.054	9.1%	355	205	0.357	8.4%	310	23	1.5	0.23	9780	439	5	0	50	2.9	94	6	
HSD07@96.6m	ok	338	8	0.0539	2.3%	338	8	0.0167	2.8%	335	9	0.055	4.5%	414	101	0.394	4.6%	337	13	0.7	0.11	10453	476	10	1	89	5.3	182	11	
HSD07@96.6m	ok	338	9	0.0540	2.6%	339	9	0.0154	3.3%	310	10	0.056	7.7%	442	171	0.389	6.9%	333	20	1.0	0.17	10486	440	11	1	176	10.1	186	11	
HSD07@96.6m	ok	355	8	0.0567	2.2%	355	8	0.0179	2.6%	359	9	0.054	4.0%	369	89	0.408	3.9%	348	12	1.7	0.21	5898	257	24</						

Appendix III

XRD results

DEPARTMENT OF INFRASTRUCTURE ENERGY AND RESOURCES

Mineral Resources Tasmania

Client: T. Manaka, CODES

Sample Source: Laos

MRT Job Number: M008/08

Analysis: Approximate Mineralogy

Method: X-Ray Diffraction

Results (approx wt %)

<i>Deposit/Sample</i>	<i>50%-65%</i>	<i>35%-50%</i>	<i>25%-35%</i>	<i>15%-25%</i>	<i>10%-15%</i>	<i>5%-10%</i>	<i>2%-5%</i>
BHX							
HSD01@98.4m			Quartz	Chlorite, Mica	K-Feldspar	Plagioclase, Pyrite	
HDD09@79.8m			Ankerite, Mica ¹	Quartz	K-Feldspar	Siderite	
HDD09@123.9m		Quartz	K-Feldspar, Mica ¹		Siderite	Ankerite	
HDD12@52.0m		Mica ¹ , Quartz				Siderite, K-Feldspar	Pyrite, Ankerite
LCT							
LDD03A@65.1m	Quartz		K-Feldspar				Kaolinite
LSD23@57.3m	Quartz		Mica ²		Chlorite		Plagioclase
LSD04@87.2m	Quartz	K-Feldspar					Pyrite, Calcite

¹ probably 1M Mica

² two types of Mica present (1M and 2M₁)

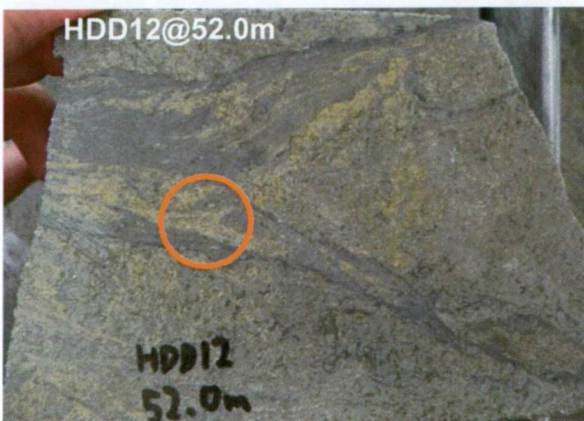
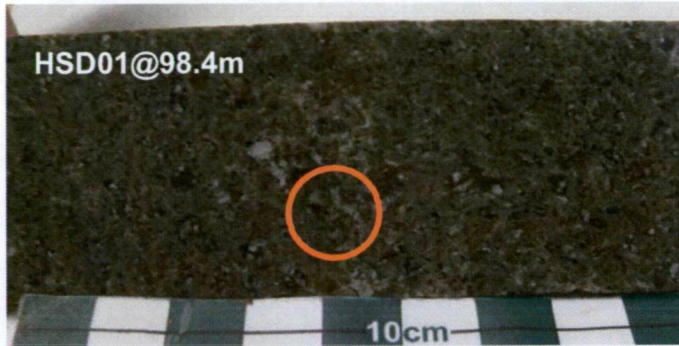
Peak overlap may interfere with identifications and quantitative calculations

Amorphous material (e.g. organic matter) and minerals present in trace amounts may not be detected

Analyst: R.N. Woolley

Date: 5 February 2008

BHX samples for XRD (circled parts were analysed)



LCT samples for XRD (circled parts were analysed)



Appendix IV

Sphalerite geochemical data

Appendix IV. Microprobe analysis of sphalerite chemical composition (wt.%) at the LCT deposit, Lao PDR. Number in red colour with blanket = under detection limit.

Sample No.	Zn	Cu	Fe	Mn	S	Ag	Cd	Se	Te	Au	Total	FeS mole%
LSD01@74.8m-A	59.46	0.03	6.69	(0.00)	34.08	0.01	0.26	(0.02)		0.15	100.71	11.09
LSD01@74.8m-B	60.90	0.03	5.03	0.01	34.08	0.00	0.25	(0.01)		0.22	100.58	8.38
LSD01@74.8m-C	61.50	0.04	4.84	0.02	33.65	0.04	0.24	(0.02)		0.17	100.51	8.03
LSD02@94.8m-A	59.36	0.00	6.03	0.02	33.98	0.01	0.04	(0.02)	(0.01)	(0.03)	99.44	10.12
LSD02@94.8m-B	59.08	0.01	6.93	0.02	34.20	(0.01)	0.03	(0.01)	0.00	0.01	100.29	11.50
LSD02@94.8m-C	57.01	0.02	7.53	0.16	35.95	0.00	0.14		0.03	(0.01)	100.83	12.77
LSD05@90.0m-A	58.24		6.60	0.04	33.05	0.00	0.25			(0.02)	98.18	11.16
LSD05@90.0m-B	60.12		5.73	0.03	33.12	(0.00)	0.24			(0.03)	99.24	9.55
LSD05@90.0m-C	60.47		5.62	0.03	33.31	0.01	0.25			(0.04)	99.69	9.34
LSD05@90.0m-D	60.73		5.30	0.02	33.20	0.01	0.24			(0.03)	99.50	8.82
LSD09@88.0m-A	63.56	(0.00)	2.62	0.11	33.82	0.01	0.32	0.00	0.02	0.01	100.47	4.36
LSD09@88.0m-B	63.60	0.00	2.56	0.16	34.02	(0.02)	0.28	(0.00)	(0.02)	0.01	100.64	4.27
LSD09@88.0m-C	62.41	(0.00)	3.05	0.17	33.94	(0.00)	0.36	0.01	0.01	(0.02)	99.94	5.14
LSD09@88.0m-D	63.07	0.00	3.11	0.17	33.75	0.01	0.37	(0.04)	(0.00)	0.00	100.48	5.18
LSD09@88.0m-E	63.01	(0.01)	3.27	0.18	33.74	(0.00)	0.35	(0.01)	(0.00)	(0.02)	100.56	5.44
LSD09@88.0m-F	62.90	0.00	2.91	0.14	33.98	0.02	0.38	(0.00)	0.00	(0.03)	100.35	4.88
LSD14@103.6m-A	63.99	0.01	2.75	0.02	33.76	0.02	0.31	(0.02)	(0.00)	(0.02)	100.87	4.54
LSD14@103.6m-B	63.91	0.00	2.69	0.03	33.95	0.02	0.36	0.01	(0.00)	(0.04)	100.98	4.46
LSD14@103.6m-C	60.65	0.01	5.61	0.03	34.51	0.00	0.28	0.00	(0.01)	(0.03)	101.10	9.30
LSD14@103.6m-D	61.36	0.02	5.21	0.01	34.38	0.01	0.31	(0.03)	0.02	(0.02)	101.32	8.60
LSD14@103.6m-E	60.70	(0.00)	5.80	0.02	34.19	0.01	0.32	0.00	0.02	(0.04)	101.07	9.58
LRD67@43.0m-A	59.22	0.01	4.51	0.08	34.11	0.02	0.28	0.02	0.01	(0.00)	98.26	7.78
LRD67@43.0m-B	59.49	0.02	4.44	0.08	34.47	0.03	0.30	(0.01)	(0.01)	0.03	98.86	7.65
LRD67@43.0m-C	61.41	0.02	4.49	0.09	34.24	0.00	0.27	0.01	(0.01)	0.00	100.54	7.50
LRD67@43.0m-D	61.65	0.03	4.48	0.10	34.25	(0.00)	0.31	(0.02)	(0.01)	(0.01)	100.81	7.45
LRD67@43.0m-E	61.73	0.02	4.33	0.07	34.24	0.00	0.29	0.01	0.01	(0.01)	100.70	7.21
LRD67@50.0m-A	58.32		6.88	0.20	33.07	0.00	0.24			(0.02)	98.70	11.56
LRD67@50.0m-B	58.28		7.03	0.24	32.97	(0.01)	0.26			(0.01)	98.77	11.79
LRD67@50.0m-C	58.04		7.40	0.22	32.98	0.01	0.25			(0.01)	98.90	12.39
LRD67@50.0m-D	58.20		7.30	0.22	33.38	0.00	0.24			(0.03)	99.33	12.20
LDD03A@75.0m-A	60.20	(0.00)	5.30	0.11	33.71	0.02	0.21	0.00		0.13	99.79	8.89
LDD03A@75.0m-B	60.84	0.01	5.37	0.06	33.77	(0.02)	0.26	0.02		0.23	100.66	8.91
LDD03A@75.0m-C	61.22	0.02	4.81	0.08	34.00	(0.00)	0.18	0.03		0.18	100.54	8.01
LDD03A@75.0m-D	62.69	0.08	3.54	0.01	33.73	0.03	0.32	0.01		0.25	100.71	5.89
LDD03A@75.0m-E	62.59	0.04	3.24	0.00	33.97	0.02	0.36	(0.02)		0.24	100.50	5.43
LDD03A@75.0m-F	62.39	0.01	3.68	0.06	33.69	(0.00)	0.33	(0.03)		0.17	100.42	6.14
LDD03A@75.0m-G	60.79	0.07	5.09	0.04	33.96	(0.00)	0.30	(0.01)		0.14	100.47	8.49
LDD03A@75.0m-H	61.43	0.00	4.74	0.05	33.87	0.00	0.32	(0.02)		0.16	100.60	7.88
LDD03A@75.0m-I	62.04	0.02	4.54	0.04	34.01	0.03	0.36	0.00		0.06	101.13	7.51
LDD03A@75.0m-J	59.97	0.02	5.86	0.07	33.87	0.01	0.33	0.02		0.24	100.51	9.77
LDD03A@75.0m-K	60.86	(0.01)	4.54	0.04	34.03	(0.01)	0.28	0.02		0.14	99.98	7.63
LDD03A@75.0m-L	59.84	0.01	5.98	0.07	34.16	(0.02)	0.33	0.01		0.25	100.69	9.98
LDD03A@75.0m-M	61.56	(0.03)	4.61	0.03	33.82	0.01	0.30	0.00		0.21	100.56	7.66
LDD03A@75.0m-N	61.17	0.01	5.10	0.08	33.99	(0.00)	0.29	(0.00)		0.10	100.74	8.46
LDD03A@75.0m-O	61.53	0.01	4.53	0.03	34.11	0.03	0.30	(0.02)		0.14	100.70	7.55

Appendix IV. Microprobe analysis of sphalerite chemical composition (wt.%) at the BHX deposit, Lao PDR. Number in red colour with blanket = under detection limit.

Sample No.	Zn	Cu	Fe	Mn	S	Ag	Cd	Se	Te	Au	Total	FeS mole%
HSD01@56.0m-A	63.37		1.64	(0.01)	33.15	0.01	0.05			(0.01)	98.22	2.79
HSD01@56.0m-B	62.42		2.80	0.01	33.40	0.01	0.04			(0.00)	98.68	4.74
HSD02@90.3m-A	64.38	0.06	1.90	0.00	33.76	0.02	0.32	0.00	(0.01)	0.00	100.44	3.16
HSD02@90.3m-B	55.92	3.65	4.92	0.00	34.09	0.03	0.24	0.01	(0.01)	0.01	98.87	8.89
HSD02@90.3m-C	63.84	0.21	2.05	(0.00)	33.85	0.01	0.30	0.01	(0.03)	(0.01)	100.27	3.44
HSD02@90.3m-D	63.81	0.10	1.48	(0.00)	34.07	0.02	0.31	(0.02)	(0.02)	(0.02)	99.80	2.51
HSD02@90.3m-E	63.15	0.02	2.15	0.00	33.95	0.02	0.26	(0.00)	(0.00)	(0.01)	99.57	3.64
HSD02@90.3m-F	63.62	0.05	2.37	(0.00)	34.33	0.00	0.30	0.01	(0.02)	(0.02)	100.68	3.97
HSD02@90.3m-G	63.30	0.18	3.11	(0.00)	33.93	(0.01)	0.29	0.04	(0.01)	0.03	100.90	5.17
HSD04@86.0m-A	63.77		2.77	0.00	33.40	0.01	0.49			(0.03)	100.44	4.59
HSD04@86.0m-B	64.59		1.45	0.01	33.18	0.00	0.43			(0.03)	99.65	2.42
HSD04@86.0m-C	64.93		1.49	0.00	33.47	(0.00)	0.43			0.02	100.33	2.48
HSD04@86.0m-D	64.18		1.46	0.01	33.38	0.02	0.44			(0.01)	99.49	2.46
HSD04@86.0m-E	64.58		1.10	(0.01)	33.57	0.00	0.42			(0.01)	99.68	1.86
HSD08@77.0m-A	56.00		8.09	0.01	35.46	0.02	0.67			(0.04)	100.25	13.80
HSD08@77.0m-B	63.51		2.04	0.01	33.17	(0.00)	0.76			(0.05)	99.49	3.44
HSD08@77.0m-C	62.47		1.80	0.00	33.16	0.01	0.74			(0.02)	98.18	3.09
HSD08@77.0m-D	63.28		2.65	0.02	33.02	(0.00)	0.75			(0.00)	99.71	4.43
HDD07@126.0m	63.54	0.16	1.65	0.01	33.61	(0.03)	0.36	0.01	(0.04)	(0.01)	99.43	2.79
HDD08@74.8m-A	64.61	0.04	1.63	0.00	33.08	0.02	0.29	(0.03)	0.00	(0.03)	99.68	2.71
HDD08@74.8m-B	64.04	0.04	1.60	(0.00)	33.14	0.05	0.55	0.02	(0.00)	(0.03)	99.48	2.70
HDD08@74.8m-C	61.16	0.76	2.73	0.00	32.93	0.13	0.51	0.02	(0.04)	(0.04)	98.27	4.72
HDD08@228.5m	63.85	0.02	1.81	0.03	33.08	(0.05)	0.36	(0.01)	0.00	(0.02)	99.16	3.04
HDD09@99.2m-A	63.43	0.08	2.41	0.01	33.21	(0.02)	0.32	(0.01)	(0.04)	(0.02)	99.48	4.04
HDD09@99.2m-B	63.34	0.04	2.57	0.00	33.23	0.03	0.33	(0.00)	(0.02)	(0.04)	99.55	4.31
HDD09@108.4m-A	63.80	0.00	2.00	0.07	33.29	0.05	0.23	(0.00)	(0.02)	(0.02)	99.44	3.35
HDD09@108.4m-B	65.13	0.01	1.27	(0.01)	32.81	(0.00)	0.25	(0.01)	0.05	(0.03)	99.55	2.12
HDD10@88.0m	63.94	0.02	2.28	0.00	33.24	0.05	0.43	0.01	0.01	(0.02)	100.01	3.80
HDD10@191.4m-A	63.77	0.02	2.50	0.02	33.12	(0.01)	0.28	(0.00)	(0.02)	(0.02)	99.74	4.17
HDD10@191.4m-B	63.34	0.02	2.14	0.01	32.79	(0.00)	0.30	0.00	0.01	(0.00)	98.63	3.61
HDD11@24.8m-A	64.69	0.04	1.65	0.00	33.68	(0.04)	0.40	0.00	(0.04)	(0.06)	100.47	2.76
HDD11@24.8m-B	63.38	0.33	2.16	0.01	32.94	0.21	0.45	(0.00)	(0.00)	(0.01)	99.68	3.64
HDD11@249.0m	64.24	0.10	1.94	0.03	33.79	0.06	0.37	0.00	0.05	(0.02)	100.60	3.24
HDD13@198.0m-A	63.49	0.03	2.68	(0.01)	33.54	0.07	0.37	(0.01)	(0.02)	(0.04)	100.22	4.47
HDD13@198.0m-B	63.49	0.02	2.75	(0.00)	33.69	0.05	0.22	0.01	(0.00)	(0.03)	100.23	4.58

Appendix V

LA-ICPMS pyrite geochemical data

Appendix V. LA-ICPMS pyrite trace element geochemistry data of the BHX deposit, Lao PDR

Sample No.	Pyrite location	Pyrite spot No.	Ti49	Mn55	Co59	Ni60	Cu65	Zn66	As75	Se77	Zr90	Ag107	Sb121	Ba137	Au197	Tl205	Pb208	Bi209	
HDD11@249.6m	Stage 3 vein	20	5.38	<0.91	14.68	1.93	18.51	<2.36	1993.2	2.5	<0.03	<0.24	<0.15	<0.2	2.13	<0.03	0.37	<0.04	
	Stage 3 vein	21	8.07	45.30	162.46	106.20	580.81	70.79	44365.3	<1.91	<0.07	802.26	8212.55	0.40	4.24	2399.41	989.59	0.40	
	Stage 3 vein	22-R	7.53	32.04	143.46	31.93	51.67	18.44	39162.2	<8.43	2.04	290.46	6388.43	41.64	0.34	961.94	1611.60	1.47	
	Stage 3 vein	22-I	7.71	46.18	1.65	18.33	534.76	14.65	50472.4	<9.03	<0.24	922.21	6969.20	0.88	3.27	1950.21	200.70	<0.17	
	Stage 3 vein	22-C	15.79	<4.2	15.01	<3.97	81.99	<9.7	10037.9	<9.64	<0.25	182.60	206.02	<0.89	3.67	96.89	38.49	<0.19	
	Stage 3 vein	23	7.20	58.01	610.55	169.70	734.40	855.24	44550.8	2.6	<0.09	840.23	4165.43	<0.2	8.79	899.81	2294.14	1.86	
	Stage 3 vein	24	<7.35	50.61	24.45	32.25	330.87	27.44	53925.6	<9.09	<0.3	824.81	5708.59	<0.63	2.78	1446.83	273.18	<0.16	
	Stage 3 vein	25-R	30.15	62.30	261.27	83.01	140.73	35.24	32037.9	<2.04	0.44	284.59	4838.90	25.83	0.97	718.87	930.24	0.65	
	Stage 3 vein	25-C	5.58	<1.69	136.95	2.07	17.98	<3.11	6412.7	4.8	0.09	1.81	0.39	0.27	1.99	0.08	3.09	0.08	
	Stage 3 vein	26	7.55	1.85	97.96	10.42	89.33	371.10	1344.7	2.4	<0.1	149.08	7.95	<0.25	0.31	0.31	49.33	0.06	
	Stage 3 vein	27	6.85	46.75	124.76	27.19	25.64	78.23	38788.5	4.3	0.15	66.51	4105.23	1.52	0.08	474.51	1984.05	1.11	
	Stage 3 vein	28-R	<9.55	23.91	66.85	10.50	59.80	18.09	40085.8	<6.3	<0.15	163.60	4741.07	1.37	<0.19	556.22	374.96	0.25	
	Stage 3 vein	28-I	<8.84	33.47	570.70	113.53	3004.10	62.22	37758.1	9.5	<0.13	728.38	5074.71	1.11	2.91	1017.84	5554.95	3.78	
	Stage 3 vein	28-C	<10.77	16.28	74.39	5.57	3714.33	21382.00	1165.5	<7.1	<0.16	4197.27	52.04	<0.52	502.39	2.31	5508.96	<0.26	
HDD09@108.3m	Stage 3 vein	31	53.01	4272.49	299.57	59.90	520.09	61820.75	7413.8	487.8	10.51	86197.81	624.56	2.07	13658.50	57.25	261.90	0.08	
	Stage 3 vein	32	6.13	<0.67	3.05	<0.58	7.03	<2.07	117.4	332.8	<0.05	99.58	<0.16	<0.21	0.20	0.12	0.23	<0.02	
	Stage 3 vein	33	7.97	47.23	40.98	13.11	191.36	2316.73	5297.9	<-85.46	0.05	190.38	2.03	0.22	0.77	0.18	3.90	<0.03	
	Stage 3 vein	34	5.44	6.64	42.56	59.11	150.65	<1.54	2215.3	<-33.43	<0.05	1480.55	42.31	<0.22	12.38	1.12	183.44	0.08	
	Stage 3 vein	35	6.20	<0.96	11.63	0.94	46.15	<1.57	9870.8	<-18.43	0.02	73.18	15.02	<0.09	4.47	2.71	9.74	<0.03	
HDD07@179.6m	Stage 3 vein	3	25.48	35.26	1137.90	349.20	7487.95	4651.06	31749.1	3.7	0.05	2248.71	8158.23	7.61	33.68	1155.33	1223.75	0.41	
	Stage 3 vein	4	5.95	20.86	165.42	29.94	419.69	57.30	24010.1	<2.21	<0.05	466.01	7115.95	<0.15	1.68	1631.28	599.42	0.13	
	Stage 3 vein	5	15.20	44.11	1360.22	412.36	3623.13	205.22	36104.1	4.0	<0.03	1715.01	7891.84	4.10	33.86	1259.49	1624.96	0.46	
	Stage 3 vein	6	14.63	47.42	2397.88	766.17	3434.05	109.93	30892.9	6.0	<0.05	2119.05	8932.53	5.08	40.49	1393.63	4172.92	0.98	
	Stage 3 vein	7	6.62	16.34	100.78	21.98	378.91	63.66	22586.2	<3.41	<0.05	460.53	7611.64	0.31	1.57	1951.99	564.05	0.10	
	Stage 3 vein	8	7.66	27.25	392.78	59.98	11460.60	34.12	24349.7	2.9	<0.05	580.74	3916.90	0.35	1.05	947.44	559.41	0.23	
	Stage 3 vein	9	9.20	3.85	129.81	80.23	6805.36	26.91	25919.9	<15.66	0.91	411.00	1516.77	<0.59	2.93	307.32	180.33	<0.15	
	Stage 3 vein	10	9.59	48.21	753.98	200.69	3563.63	198.43	28721.5	<3.74	0.22	2125.40	10950.62	1.68	9.48	2153.03	1178.08	0.22	
	Stage 3 vein	11	5.37	12.59	52.69	11.90	231.57	27.01	25271.0	<4.41	<0.06	370.26	6853.37	<0.23	1.08	1896.84	258.22	<0.05	
	Stage 3 vein	12	6.35	1.73	32.17	8.93	554.36	51.39	3108.2	6.4	<0.04	218.48	144.81	<0.2	4.95	33.50	766.69	0.75	
	Stage 3 vein	13	341.67	36.92	124.19	74.68	221.57	37.05	12088.8	<5.15	28.79	413.19	1877.45	1.21	0.82	1576.39	97.44	<0.05	
	Stage 3 vein	14	26.34	13.62	230.72	7.32	102.44	<2.08	1128.4	15.1	1.59	16.18	9.49	1.20	0.18	<0.1	230.15	0.16	
	HDD07@126.0m	Stage 1vein	38	6.02	22.34	70.02	13.69	40.66	<1.72	4710.7	8.7	3.17	13548.40	50.76	<0.13	16182.76	0.34	230.30	2.59
		Stage 1vein	39	17.58	<0.75	40.75	6.04	46.73	2.17	5397.6	11.4	2.94	5926.94	13.72	0.47	7617.60	0.11	89.51	0.73
Stage 1vein		40	31.36	1.29	20.05	9.14	67.38	<1.81	2274.5	1.8	118.58	404.28	5.22	33.54	576.81	0.07	15.12	0.18	
Stage 1vein		41	140.88	17.68	54.92	5.80	815.01	14825.84	2319.2	8.4	7.68	36.28	6.58	<0.2	0.95	0.04	2272.09	10.48	
Stage 1vein		42	51.84	28.99	68.79	20.85	5383.12	931.45	529270.6	25.7	3.89	44.40	1472.18	1.07	144.24	0.08	1402.25	7.85	
Stage 1vein		43	<5.34	<3.22	14.70	2.58	10.57	<5.69	12714.3	8.3	16.60	2.05	3.44	1.44	5.82	<0.05	14.47	0.17	
Stage 1vein		44	14.74	<3.54	11.21	3.89	16.74	<6.37	8276.7	16.7	<0.18	<0.59	1.76	1.72	6.72	<0.07	5.11	0.17	

Appendix V. LA-ICPMS pyrite trace element geochemistry data of the BHX deposit, Lao PDR

Sample No.	Pyrite location	Pyrite spot No.	Ti49	Mn55	Co59	Ni60	Cu65	Zn66	As75	Se77	Zr90	Ag107	Sb121	Ba137	Au197	Tl205	Pb208	Bi209
HDD07@78.3m	Wall Rock	79	561.11	10.34	3380.05	226.33	634.85	2.70	4134.1	14.4	4.93	53.03	86.33	7.94	0.26	16.55	450.84	32.75
	Wall Rock	80	12.00	8.12	770.84	37.08	131.99	2.31	6593.0	7.4	17.14	7.04	24.21	4.02	0.10	0.53	326.37	33.93
	Wall Rock	81	198.06	5.24	212.80	22.66	75.92	<1.53	4117.4	<4.97	20.43	18.66	15.57	2.08	0.44	0.09	117.66	3.86
	Wall Rock	82	10.15	8.62	308.65	18.30	690.99	2722.33	7027.7	6.7	0.31	34.84	41.29	<0.33	0.26	1.76	628.44	12.77
	Wall Rock	83	1603.42	29.79	3855.59	208.46	1748.77	62.04	1050.8	16.7	9.01	104.92	229.90	1.27	0.11	5.79	138.88	5.31
	Wall Rock	84	10017.79	32.58	1199.71	28.57	1234.80	5.88	6906.1	7.4	59.87	28.37	44.35	10.40	0.35	0.28	500.57	12.79
HDD13@47.5m	Wall Rock	57	6.85	31.48	174.95	36.22	79.66	<2.31	1285.9	4.0	0.12	10.04	2.54	0.53	0.10	0.02	14.42	<0.03
	Wall Rock	58	5509.94	66.97	62.25	18.26	126.65	46.52	1158.8	5.5	45.64	19.45	14.56	5.40	0.10	0.10	1285.10	0.25
	Wall Rock	59	9.41	24.29	488.84	16.90	234.12	73.32	2430.2	<3.39	3.39	7.67	15.47	40.68	0.11	0.12	200.24	0.22
	Wall Rock	60	6.28	83.86	6.39	4.27	15.71	3.77	1147.5	3.1	6.37	7.03	19.96	1.49	0.05	0.15	113.96	0.08
HSD01@98.4m	Wall Rock	87	154.98	79.92	1585.50	40.33	13517.99	34.81	3395.8	17.9	12.97	136.95	180.85	37.29	1.45	<-3.12	1994.67	122.71
	Wall Rock	88	4.87	5.44	529.95	44.22	1936.91	<1.35	637.9	7.3	0.85	12.91	17.92	1.62	0.10	<-1.6	187.44	10.14
	Wall Rock	89	5.72	30.62	1019.52	25.45	3315.50	7.83	3556.8	10.4	<0.05	82.66	153.43	1.31	2.63	<-1.22	3276.37	139.80
	Wall Rock	90	5.50	136.09	344.91	6.74	4020.43	86.33	1173.5	9.7	0.23	35.81	30.54	0.94	0.72	<-0.83	371.04	33.67
	Wall Rock	91	7.99	2.79	443.18	54.99	522.94	<1.3	1485.3	16.5	<0.07	11.57	22.99	1.06	0.65	<-0.54	329.10	15.74
	Wall Rock	92	23.69	31.93	111.22	36.86	1865.06	<1.32	1239.0	7.5	0.44	13.95	13.98	10.78	0.16	<-0.53	898.13	21.33
	Wall Rock	93-R	51.96	17.36	164.16	37.17	428.34	<8.36	720.4	<19.05	22.01	15.64	23.45	3.49	0.27	<-3.36	357.27	16.99
	Wall Rock	93-C	25.81	23.18	877.38	29.12	10559.93	9.78	1223.6	34.8	<0.38	101.99	119.89	218.10	0.54	<-3.94	3343.85	123.02
HSD04@57.9m	Wall Rock	47	12.30	10.79	156.47	128.93	41.94	<4.01	1731.7	293.6	5.67	7.57	34.06	<0.57	2.15	-0.78	739.16	129.18
	Wall Rock	48	10.40	<2.69	4.63	4.48	<8.63	<6.12	458.8	<13.13	22.96	<1.11	1.22	13.31	<0.15	-0.26	9.21	0.45
	Wall Rock	49-R	<12.44	<7.98	23.70	15.31	<19.44	<11.11	583.3	<31.6	23.20	<3.55	6.23	<1.17	0.34	-0.03	78.23	5.52
	Wall Rock	49-C	18.43	25.82	565.88	129.03	62.73	<7.42	2353.7	1223.9	48.94	5.09	38.51	<0.78	2.36	-0.03	619.39	117.66
	Wall Rock	50	190.24	21.46	124.67	70.46	89.02	<5.71	1451.3	320.1	10.61	38.95	23.12	125.79	1.53	<-0.62	311.00	239.65
	Wall Rock	51	220.48	6.22	108.40	37.87	14.14	<4.49	1015.5	12.4	13.92	4.81	11.93	0.75	0.88	<-0.3	185.71	10.66
	Wall Rock	52-C	514.21	13.57	358.85	122.27	79.16	<10.23	2283.2	471.9	20.78	12.38	33.94	113.29	2.90	-0.80	613.74	279.64
	Wall Rock	52-R	16.98	16.44	180.60	103.81	<27.64	<11.65	443.1	758.2	26.46	4.52	2.20	36.11	<0.41	-0.13	160.70	127.33
HDD12@65.3m	Wall Rock	63	23.93	6.98	170.50	20.87	361.48	31876.41	1095.0	-5.4	17.98	59.06	78.22	110.35	0.18	5.15	668.21	0.96
	Wall Rock	64	8.83	29.82	158.26	33.76	623.92	10348.86	3502.4	<-20.13	0.41	20.71	44.00	1.30	<0.04	0.27	2633.24	5.24
	Wall Rock	65	11329.58	15.47	126.50	27.83	191.13	393.56	960.3	<-13.18	215.43	15.78	17.79	9.09	0.09	0.66	3397.77	3.24
	Wall Rock	66	2624.37	4.14	25.47	24.29	14.47	3.24	3813.2	<-12.27	17.86	13.36	9.81	10.52	0.30	8.24	32.23	0.14
	Wall Rock	67	19.47	29.93	174.83	43.12	87.12	1.48	570.6	4.9	<0.06	0.33	8.07	0.63	<0.03	<0.2	166.15	0.55
HDD06@280.8m	Wall Rock	70	655.41	24.59	279.75	44.39	1929.38	69.59	9160.7	4.8	14.65	30.88	82.60	5.08	8.69	0.46	1144.94	92.71
	Wall Rock	71	7.79	28.10	38.36	18.24	139.30	32332.60	68.8	12.2	<0.04	151.96	1.65	<0.19	1.73	<0.07	40.25	0.79
	Wall Rock	72	38.76	14.77	658.71	25.17	17.83	<1.53	5671.4	7.0	0.64	7.65	6.32	<0.13	0.82	0.16	77.76	1.02
	Wall Rock	73	6.70	<1	253.06	34.35	<2.63	1.73	59.2	7.7	0.08	1.20	0.53	<0.18	<0.06	<0.09	8.12	0.11
	Wall Rock	74	7.72	<1.17	12.88	3.37	258.73	12.19	2352.6	8.5	3.69	1.95	2.43	0.59	1.01	<0.09	32.66	2.68

Appendix V. LA-ICPMS pyrite trace element geochemistry data of the BHX deposit, Lao PDR

Sample No.	Pyrite location	Pyrite spot No.	Ti49	Mn55	Co59	Ni60	Cu65	Zn66	As75	Se77	Zr90	Ag107	Sb121	Ba137	Au197	Tl205	Pb208	Bi209
HDD07@292.1m	Wall Rock	96	8.11	109.33	0.38	<0.43	48.97	84.97	7170.8	-1.0	0.71	584.60	20.10	0.54	1.46	1.83	125.22	3.51
	Wall Rock	97	6.50	55.21	0.98	0.64	5.43	<1.61	664.3	<-1.97	0.28	3.57	4.69	0.40	<0.03	0.46	31.81	0.78
	Wall Rock	98	6.65	17.33	7.36	2.24	4.12	<1.28	1314.5	<-2.08	0.06	1.03	2.90	9.64	0.06	0.48	17.97	0.92
	Wall Rock	99	39.52	269.39	21.65	8.00	7.30	389.21	1177.2	<-1.96	3.77	7.32	6.90	8.37	0.09	1.42	354.82	1.53
	Wall Rock	100	292.21	7.39	2383.17	163.15	98.19	<1.69	9094.7	<-1.9	9.29	8.83	26.53	2.99	0.30	8.44	254.98	102.18
HSD05@39.4m	Wall Rock	103	454.37	1.31	125.42	5.33	14.06	<1.5	374.0	<-1.39	4.53	3.03	3.27	4.45	0.03	0.29	24.34	0.55
	Wall Rock	104	354.98	9.55	86.84	21.47	4.95	4.48	554.0	<-2.03	3.75	1.43	6.25	12.88	<0.04	1.23	40.32	0.49
	Wall Rock	105	417.07	4.12	22.63	10.87	541.61	95.00	152.5	<-1.98	27.03	15.25	2.92	1.31	0.04	<0.42	367.43	0.61
	Wall Rock	106	2415.54	7.14	37.52	12.00	11.44	36.66	91.5	<-1.13	46.79	1.53	5.06	6.67	<0.03	0.53	27.82	0.44
	Wall Rock	107	689.02	35.62	394.40	37.34	54.73	1.72	457.5	<-1.68	28.98	8.02	16.54	0.96	0.10	2.92	278.24	1.38
BH-4	Wall Rock	3	6.78	13.43	87.74	13.54	66.11	102.54	859.0	5.7	7.29	5.83	7.20	251.39	0.08	0.08	213.58	16.11
	Wall Rock	4	1108.31	206.17	283.83	24.44	8.44	93.08	<46.48	7.1	69.75	9.81	2.21	2664.17	<0.03	0.08	<29.52	6.11
	Wall Rock	5	36.06	24.32	32.03	9.25	34.58	70.01	12.8	3.7	53.12	2.16	5.43	1467.50	<0.03	0.14	57.19	1.40
	Wall Rock	6	11.32	27.76	96.57	19.84	82.40	253.24	65.0	5.6	17.98	11.74	3.41	453.09	<0.03	<0.03	119.28	7.73
	Wall Rock	7	12.83	21.43	157.55	44.61	202.50	534.29	460.5	7.0	18.80	14.57	90.43	11.15	0.09	3.09	107.78	4.03
HSD06@42.3m	Wall Rock	8	9.12	42.58	102.10	28.71	2845.51	48.28	411.2	34.4	7.85	397.18	47.32	1.11	0.78	1.13	1311.88	15.17
	Wall Rock	9	6.22	4.58	3.51	11.72	1071.15	3.37	7434.5	25.2	9.96	216.77	32.81	0.81	6.42	0.13	11422.89	128.04
	Wall Rock	10	5.79	17.38	58.78	7.35	22.20	3.64	1076.8	17.6	36.68	1203.77	65.57	2.19	0.17	9.50	83.33	0.42
	Wall Rock	11	1889.64	9.58	63.89	21.52	606.24	43.18	14239.9	47.6	24.26	661.08	78.55	3.24	17.48	0.86	11544.26	90.56
	Wall Rock	12	16.00	7.42	30.02	6.44	15.85	14.36	446.3	28.5	15.92	5.36	5.14	12.22	0.14	0.44	212.32	2.80
	Wall Rock	13	15.61	<3.34	109.64	24.47	46.13	<3.87	1224.5	18.3	17.52	6.68	17.90	1.17	0.40	0.79	115.03	7.91
	Wall Rock	14	5.13	62.53	17.07	11.45	28.51	<5.27	1059.9	33.7	41.26	3.97	5.97	<0.49	0.36	<0.13	52.16	1.59

Appendix V. LA-ICPMS pyrite trace element geochemistry data of the LCT deposit, Lao PDR

Sample No.	Pyrite location	Pyrite spot No.	Ti49	Mn55	Co59	Ni60	Cu65	Zn66	As75	Se77	Zr90	Ag107	Sb121	Ba137	Au197	Tl205	Pb208	Bi209
LSD05@96.6m	Stage 2 vein	15	5.73	<1.37	0.04	0.32	1299.07	85.30	2304.0	26.7	<0.03	9.14	70.05	<0.1	4.76	0.02	844.21	16.81
	Stage 2 vein	16	7.02	5.10	2.50	3.09	19.48	2.25	5312.8	<2.42	<0.04	11.86	96.13	0.14	1.14	18.08	137.66	2.72
	Stage 2 vein	17	5.89	<0.9	6.04	0.32	8.08	0.74	1144.1	6.7	<0.06	3.29	12.90	<0.18	1.55	0.02	1683.88	11.39
	Stage 2 vein	18	5.29	13.01	0.05	0.40	1.54	2.86	89.9	<3.36	<0.04	4.34	2.31	<0.11	0.02	0.21	15.68	<0.02
	Stage 2 vein	19	3.31	435.79	2.05	1.36	335.81	225.13	2005.0	<2.24	<0.03	24.61	54.01	14.43	6.56	2.23	88.78	1.89
	Stage 2 vein	20	5.30	<0.94	317.82	0.42	1.19	0.77	466.6	190.4	<0.03	0.10	0.06	<0.23	0.02	0.02	0.25	0.12
	Stage 2 vein	21	4.19	<0.79	7.03	1.06	39.33	0.78	1010.0	7.3	<0.04	2.02	15.61	0.11	0.82	0.40	273.19	53.24
	Stage 2 vein	22	4.13	0.80	1.13	0.18	950.92	112.11	3633.0	11.0	<0.02	8.29	121.19	1.53	7.97	0.02	1345.92	46.70
	Stage 2 vein	23	4.67	<0.89	0.05	0.36	714.16	87.33	5165.2	14.0	<0.03	7.42	128.03	<0.11	10.98	0.03	1377.33	38.46
LDD81@78.1m	Stage 2 vein	28	20.47	2312.92	17.08	10.30	2471.21	26.87	2548.8	4.3	<0.05	106.46	114.24	11.24	20.44	10.20	3317.51	3.20
	Stage 2 vein	29	1704.39	442.19	166.83	31.98	2576.37	28.18	4718.6	<15.3	1.50	132.59	366.69	197.53	48.41	18.74	2645.62	2.82
	Stage 2 vein	30	18.20	647.79	1178.47	183.08	3216.33	52.26	12633.0	<17.09	8.33	44.38	482.42	1.51	40.89	14.09	1384.25	2.11
	Stage 2 vein	31	40.66	560.17	726.12	109.59	1011.72	51.21	8843.2	<16.53	2.99	74.17	569.16	13.06	82.79	6.24	5002.75	4.15
	Stage 2 vein	32	27.22	1165.23	112.70	25.90	2407.98	37.96	8450.6	<15.81	<0.14	43.46	236.13	4.77	177.50	8.09	2048.65	0.30
	Stage 2 vein	33	26.31	1165.91	52.32	16.86	5318.08	359.14	3735.0	<15.94	<0.1	71.41	257.46	<0.45	148.47	1.90	943.19	<0.07
LSD09@88.0m	Stage 2 vein	34	7.24	<3.25	24.77	17.61	199.14	7.56	428.1	<14.49	<0.1	3.30	36.57	<0.52	0.07	14.44	409.64	<0.08
	Stage 2 vein	35	<4.94	<3.22	12.69	45.32	23.85	5.00	1149.7	<13.72	0.21	2.35	29.37	<0.53	0.22	27.65	6955.29	0.14
	Stage 2 vein	36	14.27	6.65	26.59	90.78	307.32	668.32	2048.1	<18.84	1.81	9.12	61.42	<0.38	0.04	31.86	955.48	<0.06
	Stage 2 vein	37	8.95	3.94	13.36	95.72	363.92	613.90	1674.5	<18.81	<0.15	11.53	29.57	<0.46	0.06	98.47	403.40	0.07
	Stage 2 vein	38	<6.08	117.57	27.97	94.58	69.79	14.67	5035.9	<17.8	<0.13	9.12	76.80	<0.44	0.06	8.00	2972.74	<0.07
	Stage 2 vein	39	7.37	27.91	0.66	54.91	132.63	3.06	2972.2	<17.03	<0.08	4.56	75.64	<0.53	0.06	23.72	519.02	<0.07
	Stage 2 vein	40	6.57	<2.74	46.16	77.87	117.61	18.12	1526.4	<20.14	<0.14	1.89	47.65	<0.51	0.06	11.56	2950.50	<0.08
LSD15@99.1m	Wall Rock	63	6.13	5.67	105.35	8.42	12.62	2.20	607.8	27.2	<0.06	0.12	0.50	<0.13	0.02	0.04	6.01	13.91
	Wall Rock	64	12.72	5.38	848.87	36.06	20.74	0.66	2357.6	92.7	0.07	3.68	1.08	0.13	0.34	0.06	40.25	48.65
	Wall Rock	65	65.28	285.76	76.79	56.06	332.09	317.80	16345.7	<48.07	<0.48	47.10	109.34	30.78	5.22	14.92	554.68	196.21
	Wall Rock	66	3.16	4.11	12.21	1.05	2.33	0.75	2098.0	11.9	<0.07	0.19	0.45	3.91	1.11	0.03	10.83	2.62
	Wall Rock	67	2.52	2.43	231.03	3.21	13.90	1.67	1881.9	8.7	<0.07	2.58	3.98	<0.15	0.33	0.84	36.64	59.15
	Wall Rock	68	8.56	231.63	157.13	28.75	22.08	25.85	599.2	5.5	<0.04	3.10	10.49	7.12	0.13	1.75	65.22	9.79
	Wall Rock	69	5.49	8.45	40.35	6.04	39.73	5.97	3300.9	3.8	<0.04	8.50	2.40	<0.07	1.30	0.06	123.05	201.07
	Wall Rock	70	-0.63	-2.53	0.00	0.00	2022.95	137.07	897.1	9.0	-0.04	15.78	274.21	3.43	8.02	0.02	2467.46	-13.32
Wall Rock	71	5.55	18.82	2.44	0.69	970.06	1.52	269.8	4.4	<0.04	2.88	3.11	0.14	0.02	0.03	81.03	14.33	

Appendix V. LA-ICPMS pyrite trace element geochemistry data of the LCT deposit, Lao PDR

Sample No.	Pyrite location	Pyrite spot No.	Ti49	Mn55	Co59	Ni60	Cu65	Zn66	As75	Se77	Zr90	Ag107	Sb121	Ba137	Au197	Tl205	Pb208	Bi209
LDD03A@67.4m	Wall Rock	41	340.06	<4.77	1.00	1.50	55.07	16.51	239.1	<23.42	8.84	19.74	30.13	41.40	0.19	0.67	331.14	<0.06
	Wall Rock	42	375.25	9.28	0.29	1.58	194.17	13.45	262.9	<18.14	19.98	20.43	30.04	3.50	0.07	0.52	363.40	<0.1
	Wall Rock	43	387.32	6.21	12.22	1.47	290.18	2.38	148.8	<22.92	16.06	11.67	22.42	2.88	0.53	0.22	322.50	0.55
	Wall Rock	44	799.54	84.83	113.41	6.68	26.49	4.60	401.7	<25.67	153.76	1.85	8.93	1.57	0.27	0.08	55.62	2.36
	Wall Rock	45	18.75	19.99	36.70	2.00	34.08	6.57	593.8	<35.58	2.13	9.22	11.31	<0.75	0.21	0.06	98.87	0.19
	Wall Rock	46	498.95	173.42	275.70	22.34	1484.78	3.46	475.6	<31.46	13.82	4.98	12.31	5.11	0.24	0.27	157.13	2.60
	Wall Rock	47	948.88	92.12	2.36	1.75	37.99	3.01	85.5	<23.36	28.84	8.93	14.94	11.66	0.14	0.23	118.40	<0.09
	Wall Rock	48	<-44.13	-0.95	0.08	0.10	827.71	100.34	9097.4	30.8	<-1.4	3.31	160.57	0.97	6.91	0.00	1289.24	25.37
	Wall Rock	49	23.82	21.97	4.45	2.23	95.63	4.16	113.8	<41.32	19.17	6.48	16.00	2.24	0.08	0.07	217.65	<0.11
	Wall Rock	50	36.58	4.46	2.36	1.27	50.69	3.60	32.7	<24.32	21.88	10.95	15.47	52.11	0.08	0.39	156.96	<0.08
LSD24@36.5m	Wall Rock	53	16.33	8.78	37.32	46.97	742.22	8.97	87.9	<11.84	0.16	11.85	15.60	17.82	0.81	0.57	518.09	0.52
	Wall Rock	54	173.18	53.57	925.64	568.41	31598.15	103.59	2986.4	<24.53	0.32	408.26	585.98	158.37	0.88	2.93	6649.09	13.47
	Wall Rock	55-R	<9.06	<4.41	42.14	48.23	251.50	3.52	92.5	<20.27	<0.29	6.42	12.71	1.22	0.08	0.36	666.90	0.78
	Wall Rock	55-C	10.05	53.18	614.59	530.03	18155.62	27.01	1838.5	33.2	<0.24	283.96	495.71	6.17	0.67	1.08	16072.89	17.22
	Wall Rock	56	1878.28	104.27	25.58	73.83	3738.68	869.21	1202.8	<15.84	15.68	8.85	150.92	1.06	3.41	0.11	845.68	1.21
	Wall Rock	57	1129.29	536.16	5.33	11.93	8.39	14.12	97.9	<15.14	11.54	1.19	4.55	<0.73	0.07	0.12	77.13	0.32
	Wall Rock	58	53.46	14.38	17.81	40.23	74.40	16.48	255.4	<14.93	0.19	9.41	18.14	17.60	0.06	1.15	51.61	<0.11
	Wall Rock	59	29.93	9.15	42.97	72.01	471.18	21.58	440.0	<14.05	2.34	21.24	29.84	6.90	0.46	0.67	196.05	0.18
	Wall Rock	60	<-18.99	<-18.33	0.00	0.00	1014.60	71.19	3435.6	12.3	<-1.14	9.66	144.09	1.88	6.05	0.02	1320.82	30.02
	Wall Rock	61	1639.01	55.72	403.02	1032.73	100.75	62.96	326.6	<33.44	173.39	2.67	10.07	265.52	0.10	0.64	106.33	0.18
	Wall Rock	62	1502.10	62.94	6.40	6.52	16.92	3.47	65.6	4.0	122.16	0.62	6.76	6.35	0.00	0.11	122.30	0.31

Appendix VI

Fluid inclusion data

Appendix VI. Fluid inclusion petrographic and microthermometric data from the Stage 2 vein at the LCT deposit, Lao PDR

Deposit/ mineralisation stage	Sample No.	Inclusion No.	Host mineral	Inclusion type	Inclusion size (μm)	Homogenisation temperature (Th)	Last ice melting temperature ($^{\circ}\text{C}$)	Salinity (NaCl wt. % equiv.)
LCT Stage 2	LSD14@47.8m	1	Quartz	Liquid-Vapour	5	195.0	-3.3	5.4
		2	Quartz	Liquid-Vapour	5	206.7		
		3	Quartz	Liquid-Vapour	5	188.4	-5.3	8.3
		4	Quartz	Liquid-Vapour	5	199.8	-3.8	6.3
		5	Quartz	Liquid-Vapour	5	191.9		
		6	Quartz	Liquid-Vapour	5	203.8	-2.1	3.6
		7	Quartz	Liquid-Vapour	5	194.6	-1.9	3.2
		8	Quartz	Liquid-Vapour	5	182.3	-2.0	3.4
		9	Quartz	Liquid-Vapour	5	204.8	-1.0	1.7
		10	Quartz	Liquid-Vapour	<5	177.4	-2.7	4.5
		11	Quartz	Liquid-Vapour	<5	178.0	-2.6	4.4
		12	Quartz	Liquid-Vapour	5	189.3	-1.8	3.1
		13	Quartz	Liquid-Vapour	5	184.3	-2.6	4.3
		14	Quartz	Liquid-Vapour	5	191.6	-1.4	2.4
		15	Quartz	Liquid-Vapour	5	186.7	-3.4	5.6
		16	Quartz	Liquid-Vapour	5	187.7	-2.5	4.2
		17	Quartz	Liquid-Vapour	<5	175.2	-2.1	3.6
		18	Quartz	Liquid-Vapour	5	192.6		
		19	Quartz	Liquid-Vapour	5	192.1	-4.2	6.7
		20	Quartz	Liquid-Vapour	5	204.1	-3.0	5.0
		21	Quartz	Liquid-Vapour	5	186.3	-2.6	4.3
		22	Quartz	Liquid-Vapour	5	203.5	-2.9	4.8
		23	Quartz	Liquid-Vapour	5	187.1	-2.9	4.8
		24	Quartz	Liquid-Vapour	<5	184.7		
		25	Quartz	Liquid-Vapour	5	196.3		

Appendix VI. Fluid inclusion petrographic and microthermometric data from the Stage 1 vein at the BHX deposit, Lao PDR

Deposit/ mineralisation stage	Sample No.	Inclusion No.	Host mineral	Inclusion type	Inclusion size (μm)	Homogenisation temperature (Th)	Last ice melting temperature ($^{\circ}\text{C}$)	Salinity (NaCl wt. % equiv.)
BHX Stage 1	HSD08@68.8m	26	Quartz	Liquid-Vapour	<5	213.7	-2.4	4.0
		27	Quartz	Liquid-Vapour	<5	198.8	-3.1	5.0
		28	Quartz	Liquid-Vapour	<5	207.2	-3.9	6.3
		29	Quartz	Liquid-Vapour	<5	194.6	0.6	
		30	Quartz	Liquid-Vapour	<5	213.9	-2.6	4.3
		31	Quartz	Liquid-Vapour	<5	213.4	-3.4	5.4
		32	Quartz	Liquid-Vapour	<5	200.1	-1.9	3.2
		33	Quartz	Liquid-Vapour	<5	197.3	-1.9	3.2
		34	Quartz	Liquid-Vapour	<5	196.9	-2.2	3.7
		35	Quartz	Liquid-Vapour	<5	196.8	-1.7	2.9
		36	Quartz	Liquid-Vapour	<5	188.1	-2.2	3.7
		37	Quartz	Liquid-Vapour	<5	192.8	-2.6	4.3
		38	Quartz	Liquid-Vapour	<5	206.9	2.2	

Appendix VI. Fluid inclusion petrographic and microthermometric data from the Stage 2 vein at the BHX deposit, Lao PDR

Deposit/ mineralisation stage	Sample No.	Inclusion No.	Host mineral	Inclusion type	Inclusion size (μm)	Homogenisation temperature (Th)	Last ice melting temperature ($^{\circ}\text{C}$)	Salinity (NaCl wt. % equiv.)	
BHX Stage 2	HDD12@142.0m	39	Quartz	Liquid-Vapour	10	369.6	-4.0	6.5	
		40	Quartz	Liquid-Vapour	10	320.7	-4.4	7.0	
		41	Quartz	Vapour-Liquid	10	254.4	-3.7	6.0	
		42	Quartz	Liquid-Vapour	20	322.7	-4.8	7.6	
		43	Quartz	Liquid-Vapour	10	275.3	-3.9	6.3	
		44	Quartz	Liquid-Vapour	10	387.5	-9.1	12.9	
		45	Quartz	Liquid-Vapour	5				
		46	Quartz	Liquid-Vapour	10	398.5	-4.1	6.6	
		47	Quartz	Liquid-Vapour	20	304.3			
		48	Quartz	Liquid-Vapour	20	312.5	-2.9	4.8	
		49	Quartz	Liquid-Vapour	10	407.8	-4.1	6.6	
		50	Quartz	Liquid-Vapour	20	359.0	-3.4	5.6	
		51	Quartz	Vapour-Liquid	10	353.4			
		52	Quartz	Liquid-Vapour	10	356.7	-4.0	6.5	
		53	Quartz	Liquid-Vapour	10	341.8			
		54	Quartz	Liquid-Vapour	10	336.0	-4.6	7.3	
		55	Quartz	Liquid-Vapour	10	274.3	-3.7	6.0	
		56	Quartz	Liquid-Vapour	10	245.8	-4.1	6.6	
		57	Quartz	Liquid-Vapour	10	270.7	-3.9	6.3	
		58	Quartz	Vapour-Liquid	10	354.9	-4.7	7.5	
		59	Quartz	Liquid-Vapour	10	287.0	-5.0	7.9	
		60	Quartz	Liquid-Vapour	10	387.9	-3.9	6.2	
		61	Quartz	Liquid-Vapour	10				
		62	Quartz	Liquid-Vapour	10	413.1	-8.2	11.9	
		63	Quartz	Liquid-Vapour	10	392.2	-5.2	8.1	

Appendix VI. Fluid inclusion petrographic and microthermometric data from the Stage 3 vein at the BHX deposit, Lao PDR

Deposit/ mineralisation stage	Sample No.	Inclusion No.	Host mineral	Inclusion type	Inclusion size (μm)	Homogenisation temperature ($^{\circ}\text{C}$)	Last ice melting temperature ($^{\circ}\text{C}$)	Salinity (NaCl wt. % equiv.)
BHX Stage 3	HDD12@142.0m	64	Dolomite	Liquid-Vapour	10	298.3	-3.1	5.1
		65	Dolomite	Liquid-Vapour	10	315.8	-4.9	7.7
		66	Dolomite	Liquid-Vapour	10	268.2	-3.8	6.2
		67	Dolomite	Liquid-Vapour	20	340.4	-2.1	3.6
		68	Dolomite	Liquid-Vapour	5	245.1		
		69	Dolomite	Liquid-Vapour	10	347.9	-4.1	6.6
		70	Dolomite	Liquid-Vapour	10	327.0	-4.2	6.7
		71	Dolomite	Liquid-Vapour	10	258.5	-2.8	4.7
		72	Dolomite	Liquid-Vapour	10	283.1	-3.8	6.2
		73	Dolomite	Liquid-Vapour	5	273.1	-3.2	5.3
		74	Dolomite	Liquid-Vapour	10	298.4	-3.9	6.3
		75	Dolomite	Liquid-Vapour	10	338.5	-3.4	5.6
		76	Dolomite	Liquid-Vapour	5	257.5	-3.4	5.6
		77	Dolomite	Liquid-Vapour	10	238.7	-1.6	2.7
		78	Dolomite	Liquid-Vapour	5	315.7		
		79	Dolomite	Liquid-Vapour	10	310.0	-2.2	3.7
		80	Dolomite	Liquid-Vapour	10	356.0	-2.3	3.9
		81	Dolomite	Liquid-Vapour	10			
		82	Dolomite	Liquid-Vapour	10	323.3	-3.0	5.0
		83	Dolomite	Liquid-Vapour	10	377.0		
84	Dolomite	Liquid-Vapour	10	309.3	-2.6	4.3		